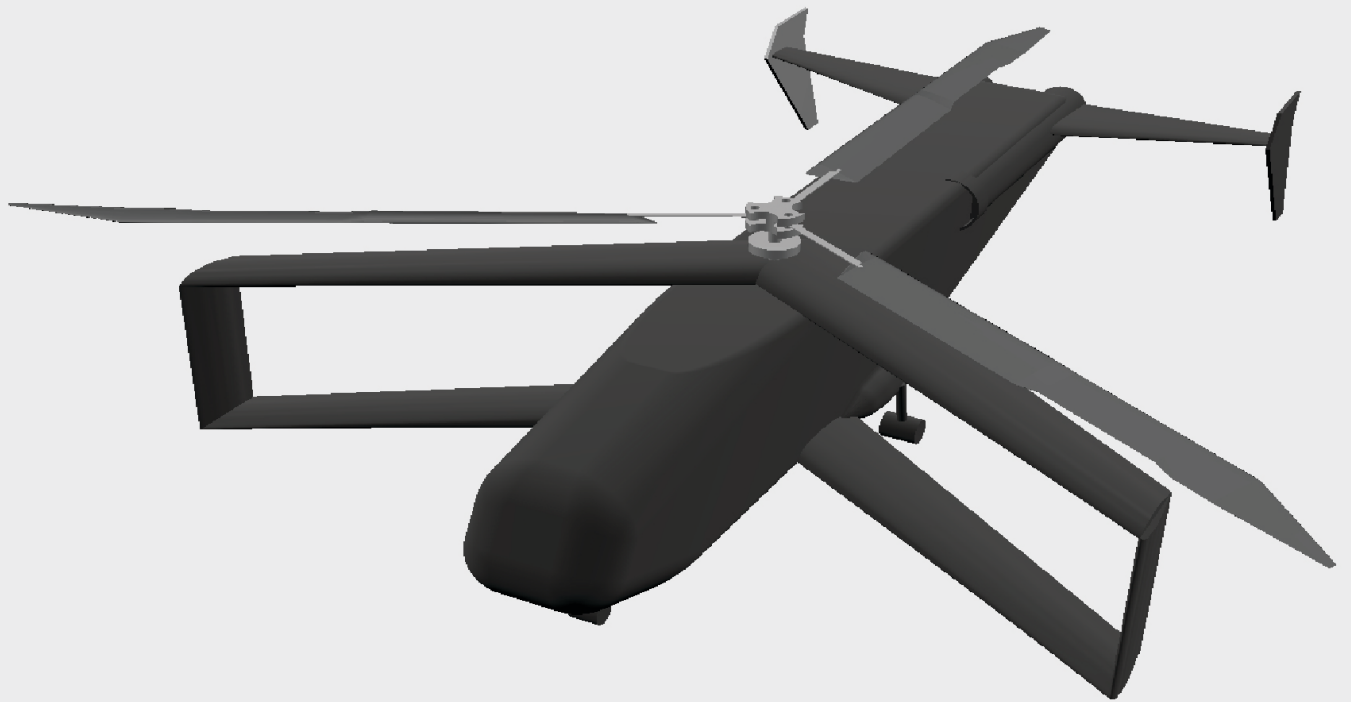# HIGH SPEED VERTICAL TAKE-OFF AND LANDING AIRCRAFT (HS-VTOL)

Final Report

AE3200: Design Synthesis Exercise
DSE Group 2

TUDelft

# HIGH SPEED VERTICAL TAKE-OFF AND LANDING AIRCRAFT (HS-VTOL)

Final Report

by

DSE Group 2

Student Name	Student Number	Sections
Edmundo Sanz-Gadea López	4553128	2.3, 5.1, 5.2, 7.3, 10.5, 10.7, Editing
Emmanouil Vasileiadis	4645707	7.2, 11.2, 11.5, 11.6, 11.7
Teun Wegkamp	4664620	Introduction, 9.2, 9.3, 9.4, 12.2
Dustin Holohan	4683463	ExecSum, 2.1, 2.2, 2.3, 2.4, 10.4, 10.5, 10.7, Editing
Lien-Ky Do	4780787	2.3, 3.1, 3.2, 3.3, 3.4, 5.3, 8.1, 8.2, 8.3, 12.2, Editing
Kunal Gupta	4998715	3.2, 3.3, 3.4, 8.1, Editing
Niklas Knöll	5006961	5.3, 6.1, 6.2, 10.1-10.4, 10.6, 10.8 - 10.10, 12.1, CAD
Ugo Coveliers-Munzi	5007631	Symbols, Intro., 2.3, 5.1, 5.2, 9.1, 9.4, 9.5, 12.2, Conclusion
Jasper van den Bosch	5074142	Abbr., 4.1, 4.2, 8.2, 8.3, 12.3, Ref.
Carlo Faulquier	5083877	7.1, 11.1, 11.2, 11.3, 11.4, 11.7, Ref

Tutor:	M. Pavel
Coaches:	G. Dacome, I. Akay
Teaching Assistants:	S. Van Dam, C. Mihalache
Project Duration:	10 weeks
Faculty:	Faculty of Aerospace Engineering
Institution:	Delft University of Technology

TUDelft

Executive Overview

This report details the outcome of ten weeks of design work by ten students in the final year of their bachelor of aerospace engineering degree. The design considerations and outcomes for the XV-25 Griffin showcased in Figure 1 are presented. The vehicle concept is an attempt at merging the worlds of vertical and horizontal flight.
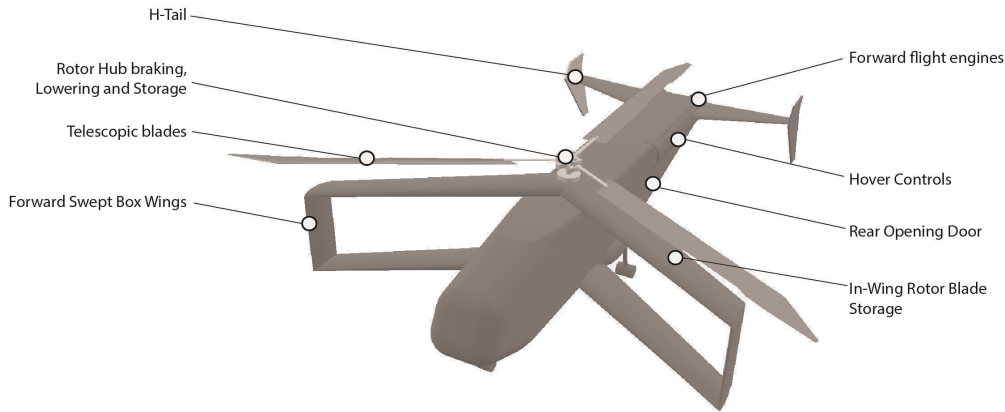
Figure 1: Detailed Design Concept

The objective of the design was to arrive at a vehicle that can meet the stated requirements. The team received the project brief from the Vertical Flight Society, which outlined a mission profile as the design consideration. The vehicle is required to carry 6,000 lbs (2,712 kg) of payload with a radius of action of 500 NM (926 km). The vehicle is required to be able to take off and land vertically with efficient hover capabilities. On top of this, the vehicle is required to maintain a cruise altitude of 20,000 ft (6,096 m) and a cruise speed of 450 kts (231.5 m/s). The project consisted of four phases, the initial planning phase, followed by the baseline. The third phase of the project concluded at the midpoint and consisted of conceptual design and trading off of these concepts. Following the first three phases a single concept was chosen and designed further, this last phase focused on the detailed design and analysis of the chosen concept.

In order to determine the viability of such a design, a market analysis was conducted to determine both the depth of the budget as well as the demand for such a vehicle. In the market analysis, the stakeholders identified were Governmental organizations such as the Military, Organisations in search and rescue, as well as the Commercial market where in particular the offshore industry is of interest. However, the key market is the military market. The breakdown of the expected cost can be characterized as can be seen in Table 1.

Table 1: Cost Breakdown Structure per Subsystem Adjusted for Inflation [in US $]

Airframe	Rotor	Propulsion	Electrical	Drive	Total $US \$$	Total $€$
21,226,100	9,114,430	18,000,200	1,677,686	1,033,113	51,051,529	47,000,000

From the baseline of the costs, a margin can be added and a sales price determined. Applying a margin of 13.1% yields a sales cost of US$ 57.7 million (€ 53.2 million). With a cadence of 12 vehicles per year leading to expected profits of US$ 80 million (€ 73.6 million) while capturing 1.7% of the total global military market. The features of the vehicle allowing it to reach the requirements set by the VFS and justify the sales price set can be overviewed in Figure 7.1. Specifically, the key technologies revolve around the main rotor being stowed in flight. This was deemed the most feasible way to reach the cruise speeds and as such drove the entire design. The forward-swept box wings, h-tail, and retracting rotors are also influenced by this decision. Several mechanisms were conceptualized and selected in accordance with the stowing including the storage compartments, blade retraction mechanisms, hub braking, rotor lowering, and compartment doors.

Once the final concept was chosen the different departments delved deeper into their respective analysis to

better characterize the design. The driving department was the Aerodynamics department where the blade and the wings were designed and the total vehicle drag was characterized. In the blade design a twist of $-5°$ was selected with different airfoils across the radius. Specifically for $0 < y/R < 0.55$, $0.55 < y/R < 0.75$, $0.75 < y/R < 0.85$, $0.85 < y/R < 1$, airfoils $V43012$, $SC1094 - R8$, $SC1095$, $OA206$ were respectively selected, generating a maximum thrust of 81.3 klbf (362 kN) in hover. The Wing design concluded with a Prandtl Box wing designed to limit the surface area under the blade and the span of the vehicle while providing a sufficient lifting surface to achieve equilibrium forward flight. The airfoils selected were NACA $65_2 - 415$ for the wings, NACA 0012 for the tail surfaces, and NACA 0012 for the wing tip joining structures. The main airfoil has a surface area of 631.4 ft^2 (29.3 m^2) and an aspect ratio of 8.73 and a quarter-chord sweep of -30 °. The drag coefficient of the entire vehicle was estimated to be $C_{D_{min}} = 0.0226$.

Following on from the Aerodynamics, the Power and Propulsion department delved into the power curves, the engine, and, fuel selection. For light the maximum required powers were determined as 16,110 hp (12,013 kW), 13,947 hp (10,400 kW), 18,345 hp (13,680 kW) for the hover, cruise, and max speed phases of the flight. Dual turbo fans were selected as engines for the vehicle, each a scaled version of the Pratt Whitney $F135 - PW - 600$ engine. The specific engine houses a drive shaft with a gear to translate the rotation 90 degrees for the main rotor, the engine also bleeds off pressurized air fed from the bypass and directs it out nozzles placed on the tail to control yaw in hover and counter the main rotor torque. From the power curves and engine selection, the mass of the fuel was estimated at approximately 18,000 lbs (8,160 kg) and facilitates a maximum ferry range of 2,700 mi (4,300 km).

The Structures and Materials department looked into the design of the main Rotor, wings, and fuselage. All elements were sized for a peak load factor of 3.8 and a safety factor of 1.5. The main rotor included the hub and blades, whose loads were characterized and analyzed. The hub is designed to withstand a load of 45 klbf (200 kN), determined as the maximum load expected from the cyclic behavior of the rotors in flight. The blades were analyzed in hover and found to require a minimum mass of 959 lbs (435 kg) per blade, in order to achieve a coning angle of $_0 = 5°$. For the wings, a detailed analysis of bending and torsion was performed employing an idealized structure and the load distributions obtained from the wing geometry and aerodynamic characteristics. Following the analysis, an optimization program was written to minimize the amount of material, and therefore the weight, required to sustain the loads present. The resulting trade-off lead to Aluminum 7075 as the structural material for all stiffeners, spars, and skin panels. The total cross-sectional area required to resist the normal stresses induced by bending varied from 1400 mm^2 at the wing root to 200 mm^2 at the tip; leading to a structural mass of 706 lbs (321 kg) for the bending mode. For torsion, the total weight required for the skin and spar webs came out to be 658 lbs (299 kg). The total mass of all four wings was therefore 5456 lbs (2480 kg). The Fuselage was estimated to internally carry a load of 40 kft-lbs (54 kNm). There were also several innovative mechanisms designed to facilitate the operational requirements of the vehicle. Finally, the estimated total weight of the vehicle was determined as 63,200 lbf (28.6 tons) and an empty mass ratio of 0.59.

The final department was the control and stability department which delved into the static and dynamic stability of the vehicle, sized the tail, and determined the controllers for stabilization. The main pitfall of having a winged helicopter compound vehicle is that the placement of the wing and its influence on the center of gravity has a negative effect on the stabilization of the helicopter at hover. In essence, what helps the fixed wing be stable destabilizes the helicopter. For that reason, iterations on wing placement were the key aspect of defining static stability with traditional methods of tail sizing having to follow, rather than vice versa. Therefore static stability was a true balancing act for the controls department. Using traditional stability and controllability diagrams indicated that this balance would make dynamic stabilization challenging. In order to determine the stability derivative for the linearized system for this novel configuration, there is no traditionally defined method. Therefore a numerical method was developed in order to determine the stability derivatives in compound configuration. Unsurprisingly the vehicle demonstrated negative dynamic stability which was beyond the limits of the vehicle requirements for that reason active stabilization using a pith rate feedback loo[p with effects on elevator deflection using a PD controller had to be implemented. In the end the vehicle was able to demonstrate good stability characteristics and fulfill the stability requirements.

This resulted overall in a vehicle concept that on paper can achieve all the requirements set by the Vertical Flight Society, though further analysis and optimization are required to bring this concept to the prototype phase.

Nomenclature

Abbreviations

Abbreviation	Definition		Abbreviation	Definition
BEM	Blade Element Method		ROC	Rate of Climb
BROC	Best Rate of Climb		MIMO	Multiple-input and Multiple-output
CAD	Computer-aided Design		MMGW	Mid Mission Gross Weight
CAGR	Compound Annual Growth Rate		MSL	Mean Sea Level
CFD	Computational Fluid Dynamics		MTOM	Maximum Take Off Mass
CG	Center of Gravity		MTOW	Maximum Take Off Weight
CMF	Controls Mixing Factor		NA	Non-applicable
CRUD	Cumulative Result of Undesirable Drag		NACA	National Advisory Committee for Aeronautics
DLR	German Space Agency		NASA	National Aeronautics and Space Administration
DOF	Degree of Freedom		NATO	North Atlantic Treaty Organization
EASA	European Union Aviation Safety Agency		OOS	Out-of-scope
EMS	Emergency Medical Service		PD	Proportional - Derivative
FAA	Federal Aviation Administration		PID	Proportional - Integral - Derivative
FARA	Future Attack Reconnaissance Aircraft		RDT&E	Research, Development, Testing and Evaluation
FBD	Free-body Diagram		RFP	Request For Proposal
FBS	Functional Breakdown Structure		ROA	Radius of Action
FFD	Functional Flow Diagram		S.M.	Stability Margin
FOD	Foreign Object Debris		SAF	Sustainable Aviation Fuel
HS	High-Speed		SAR	Search And Rescue
HIGE	Hover In Ground Effect		SFC	Specific Fuel Consumption
HOGE	Hover Out of Ground Effect		SDGW	Structural Design Gross Weight
HS-VTOL	High-Speed Vertical Take Off and Landing		SWOT	Strengths, Weaknesses, Opportunities, and Threats
ICAO	International Civil Aviation Organization		TOGW	Take Off Gross Weight
ISA	International Standard Atmosphere		TRL	Technology Readiness Level
LCN	Load classification number		VFS	Vertical Flight Society
LQR	Linear - Quadratic Regulator		VRS	Vortex Ring State
MCP	Maximum Continuous Power		VTOL	Vertical Take Off and Landing
MCT	Maximum Continuous Torque			
MEP	Mission Equipment Package			
MEW	Maximum Empty Weight			

Symbols

Symbol	Definition	Unit
AR	Aspect ratio of main wing	[-]
A_{blade}	Blade surface area	$[ft^2]$
A_{disk}	Rotor disk area	$[ft^2]$
A_{eq}	Equivalent flat plate area	$[ft^2]$
$A_{fuselage}$	Fuselage cross-sectional area	$[ft^2]$
CF	Control authority factor	[-]
C_D	Drag coefficient of the wing	[-]
C_L	Lift coefficient of the wing	[-]
C_d	Airfoil drag coefficient	[-]
C_f	Flat-plate skin-friction drag coefficient	[-]
C_l	Lift coefficient of the airfoil	[-]
$C_l\alpha$	Lift curve slope	$[1/rad]$
C_m	Moment coefficient	[-]
C_{D_0}	Zero-lift drag coefficient	[-]
C_{D_i}	Induced drag coefficient	[-]
C_{Dp}	Profile drag coefficient	[-]
C_T	Thrust coefficient	[-]
C_{fe}	Skin-friction drag coefficient	[-]
C_{int}	Internal fuel volume	$[gal]$
D	Drag	$[lbf]$
DL	Disk loading	$[lbs/ft^2]$
D_s	Diameter of landing gear strut	$[in]$
FF	Component form factor	[-]
FM	Figure of merit	[-]
F_x	Force in X axis	$[lbf]$
F_{MG}	Main gear force	$[lbf]$
$Freq_{Flap}$	Flap frequency of rotorblades	$[1/rev]$
G	Climb gradient	[-]
I_b	Blade moment of inertia	$[lbs \cdot ft^2]$
I_y	Mass moment of inertia about Y-axix	$[lbs \cdot ft^2]$
$I_{identifier}$	Moment of inertia	$[lbf \cdot ft \cdot s^2]$
L	Lift	$[lbf]$
M	Mach number	[-]
M_{cr}	Critical Mach number	[-]
M_{dd}	Drag-divergence Mach number	[-]
$P_{a_{max}}$	Maximum available power	$[hp]$
P_r	Required power	$[hp]$
$P_{ds_{lim}}$	Drive system limit power	$[hp]$
Q	Component inteference factor	[-]
ROC	Rate of climb	$[ft/min]$
Re	Reynolds number	[-]
S	Wing surface area	$[ft^2]$
$S_{identifier}$	Surface area of indicated variable	$[ft^2]$
S_{ref}	Wetted surface area of the wing	$[ft^2]$
S_{wet}	Wetted surface area of the aircraft	$[ft^2]$
T	Thrust	$[lbf]$
V	Velocity	$[kts]$
V_h	Horizontal velocity	$[ft/s]$
V_{BR}	Best range velocity	$[kts]$
V_H	Maximum velocity in level flight at maximum continuous power	$[kts]$

Symbol	Definition	Unit
V_{NE}	Never exceed velocity	$[kts]$
V_S	Stall velocity	$[kts]$
V_Y	Best rate of climb velocity	$[kts]$
V_{cr}	Cruise velocity	$[kts]$
V_{ind_h}	Rotor induced flow velocity at hover	$[ft/s]$
V_{ind}	Rotor induced flow velocity	$[ft/s]$
V_{tip}	Tip velocity of rotor	$[ft/s]$
W	Weight	$[lbf]$
a_1	Angle between the tip path plane and the control plane	$[rad]$
b	Wingspan	$[ft]$
c	Chord length	$[ft]$
e	Spanwise efficiency factor	$[-]$
f_{LGloc}	Modification factor for landing gear location	$[-]$
f_{LGret}	Modification factor for landing gear retraction	$[-]$
f_Q	Second rotor rated torque as fraction of total torque	$[-]$
f_{TR}	Modification factor for tail rotor location	$[-]$
f_{airind}	Air induction weight as fraction of engine weight	$[-]$
f_{bt}	Ballistic tolerance factor for fuel tanks	$[-]$
f_{cw}	Crashworthiness weight as fraction of fuselage weight	$[-]$
f_p	Second rotor rated power as fraction of total torque	$[-]$
f_{ramp}	Modification factor for ramp in fuselage	$[-]$
f_{tilt}	Modification factor for rotating rotors	$[-]$
h_{cg}	Height of center of gravity above ground	$[ft]$
h_w	Height between wings	$[ft]$
$i_{identifier}$	Incidence of the surface	$[deg]$
$k_{download}$	Download factor of rotor	$[-]$
$l_{fuselage}$	Length of fuselage	$[ft]$
l_m	distance of main gear to center of gravity	$[ft]$
l_n	distance of nose gear to center of gravity	$[ft]$
$m_{Identifier}$	Mass of indicated variable	$[lbs]$
n	Load factor	$[-]$
n_{blades}	Number of blades	$[-]$
$n_{identifier}$	Number of identified variable	$[-]$
q	pitch rate	$[rad/s]$
r	radius along the blade span	$[ft]$
t	Wing thickness	[ft]
$(\frac{t}{c})_r$	Thickness to chord ratio at root	$[-]$
u	instantaneous velocity along the X_B axis	$[ft/s]$
$u_{fuselage}$	Upsweep angle of aft fuselage	$[rad]$
w	instantaneous velocity along the Z_B axis	$[ft/s]$
x_{hub}	length of driveshaft between rotors	$[ft]$
ΔQ	Incremental Torque	$[lbf \cdot ft]$
Γ	Vortex strength	$[ft^2/s]$
Λ	Sweep angle	$[deg]$
Λ_{LE}	Sweep angle at leading edge	$[deg]$
$\Lambda_{c/4}$	Sweep angle at quarter-chord	$[deg]$
Ω	RPM of rotors	$[rpm]$
Ω_{Engine}	RPM of engines	$[rpm]$
α_c	angle of attack of the rotor control plane	$[rad]$
δ_e	Elevator angle	$[deg]$
η_p	Propeller efficiency	$[-]$

Symbol	Definition	Unit
η_s	Shock absorber efficiency	[-]
γ	Lock Number	$[1/rad]$
γ_{max}	Max climb angle	$[rad]$
λ	Taper ratio	[-]
λ_c	resultant velocity component normal to the control plane	[-]
λ_i	Non-dimensional induced velocity with omega*R	[-]
μ	advance ratio	[-]
$\overline{V_i}$	Non-dimensional induced velocity with $v_{ind_{hov}}$	[-]
$\overline{V}$	non-dimensional combined velocity, non-dimensionalized with $v_{ind_{hov}}$	[-]
ϕ	Inflow angle	$[deg]$
ϕ_l	Twist of the lower wing	$[deg]$
ϕ_u	Twist of the upper wing	$[deg]$
ϕ_t	Inflow angle at blade tip	$[deg]$
ψ	Azimuth of the blade along its rotation	$[deg]$
ρ	Air density	$[slugs/ft3]$
σ	Blade solidity	[-]
σ_a	Stress amplitude	$[PSI]$
σ_z	Normal Stress	$[PSI]$
θ_0	collective blade angle	$[rad]$
θ_c	cyclic angle	$[rad]$
θ_f	body pitch angle	$[rad]$

Contents

1
Introduction

The production of high-speed aircraft and vertical take-off and landing (VTOL) concepts have matured within the aerospace sector for many decades. The birth of the jet-powered aircraft coincided with the birth of the helicopter in September 1939. However, the thought of combining the two to create a high-speed VTOL vehicle has recently just surfaced due to its inherently complex design. Aircraft such as the Harrier, the F-35, or even the V-22 Osprey are all capable of performing VTOL operations in addition to forward flight. Nonetheless, they have to sacrifice efficiencies in both vertical and forward flight in order to overcome the barrier of combining high-speed forward flight with VTOL capabilities.

This report aims to generate a detailed conceptual design of a high-speed VTOL aircraft based on the requirements set out by the Vertical Flight Society's (VFS) Request for Proposals for its 40th Annual Student Design Competition[1]. This report is the last in a series of reports the team generated in order to arrive to a final detailed design of the concept vehicle dubbed the XV-25 Griffin. The Project Plan focused on the project organization, the Baseline report focused on generating high-level concepts after which a trade-0ff was performed and a final concept was selected in the Midterm report. This progression leads us to the current report where a detailed design of the different sub-systems found in the XV-25 Griffin was performed.

Chapter 2 covers the project management, design and development logic applied during the project as well as provide more detail on the mission profile. This is then followed by the market analysis, cost breakdown and resource allocation in chapter 3. Next, the technical risks and mitigation strategy are discussed in chapter 6, the requirements and constraints as were given to and set by the team in chapter 4 and the conceptual design, trade-off and sensitivity analysis in chapter 5. Furthermore the detailed description of the XV-25 Griffin's design, the operation and logistics description and functional analysis can be found in chapter 7.

After this, the design and analysis of the different department subsystems is performed. Concerning aerodynamics, as discussed in chapter 8, both the helicopter blade and fixed-wing are designed followed by a discussion about the aerodynamic and noise characteristics. This is followed by chapter 9, which elaborates on the power requirements, engine sizing, fuel required and performance. chapter 10 explains the loads on the aircraft as well as the required structural components and mechanisms. The final department discusses the control and stability of the vehicle in chapter 11. Additionally, all the departments mentioned above each discuss the verification and validation of the methods used. Finally, the report is concluded by the final system overview of the aircraft in chapter 12, followed by the conclusion and future recommendations in chapter 13.

2

Project Objective

This chapter outlines the purpose, structure, and logic associated with the development of the XV-25 Griffin Vehicle. The work done to date consists of a preliminary conceptual design of the vehicle with detailed analyses of the key departments and components required to enable designing the vehicle.

2.1. Project Statements

To define the project from inception the mission need statement and project objective statements were defined serving as the top-level objectives of the project and guide its development. These are as follows:

Mission Need Statement

Design a VTOL aircraft with high-speed, long-range, high altitude, efficient hover, and large payload capabilities.

Project Objective Statement

Over 10 weeks, 10 students will develop a preliminary design of a large payload high-speed VTOL aircraft with extreme range, altitude, and efficient hover capabilities to win the design competition by the vertical flight society.

The aim of these statements and the project is to develop a vehicle capable of carrying out a specific mission.

2.2. Mission Profile

The mission presented to the group can be seen in Figure 2.1. The mission has various phases and each phase has specific constraints attached from which design considerations stem.
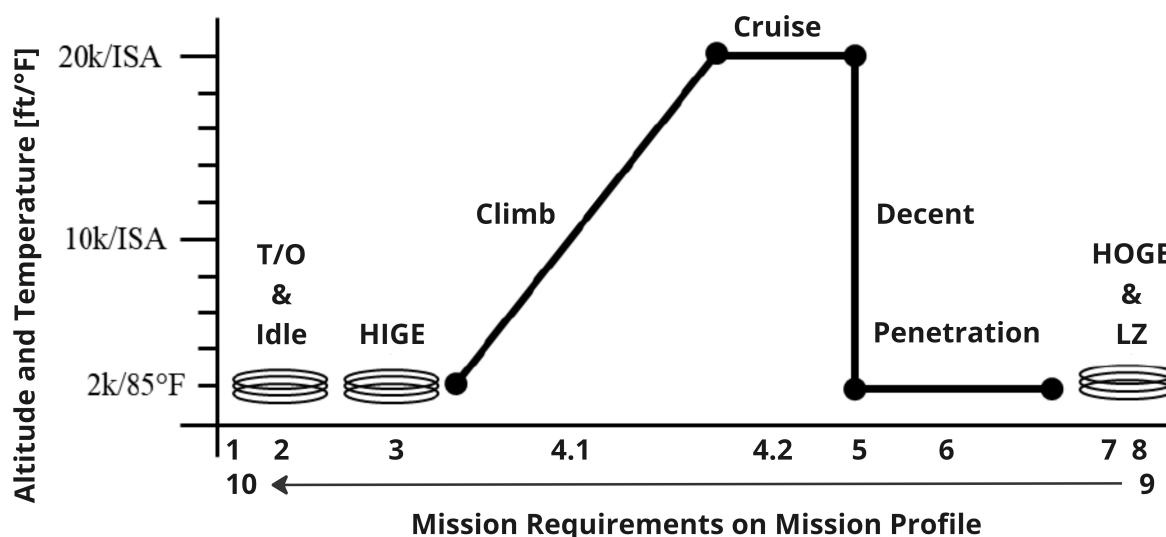
Figure 2.1: Mission Profile [1]

The mission requires that the vehicle be able to facilitate 5000 lbs (2258 kg) and 1000 lbs (454 kg) of payload and Mission Equipment Package (MEP) respectively, and 750 lbs (339 kg) allocated for three crew members. The Radius of Action (ROA) of the aircraft shall be 500 nm (926 km) made up of 450 nm (833 km) at cruise

altitude (climb phase included) and the remaining 50 nm (96 km) at 2000 ft (609.6 m). The cruise speed of the vehicle shall be greater than 450 kts (231.5 m/s).

2.3. Project Management

Before the team started on the design of the vehicle, a good project management plan had to be created to ensure the team adheres to all the non-technical requirements including deadlines and deliverables. This was done with the help of several different resources such as; an organogram, project development logic, workflow diagram, work breakdown structure, and a gantt chart. These diagrams gave the team a better understanding of how and when to prioritize different tasks throughout the course of the project cycle.

2.3.1. Organogram

As a first step, the team came up with roles and responsibilities for each individual team member. This was communicated in a clear and concise way as to prevent any miscommunications throughout the development of the project. A clear way of visually showing the team organization was created with the help of the organogram seen in Figure 2.2.
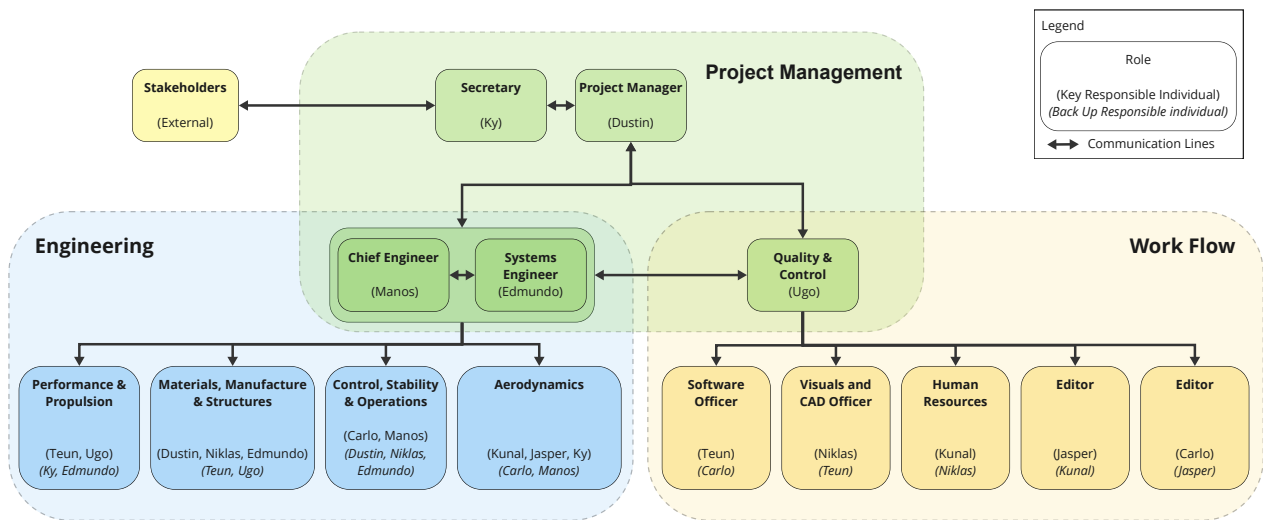
Figure 2.2: Organogram Visualizing the Team Organization.

2.3.2. Project Development Logic

The project has a given set of milestones for which deliverables were submitted. To ensure the deadlines were met and satisfactory results had been achieved the organization and logic of the project had to be understood. For this purpose, a project logic diagram was created giving an overview of the project flow and the main required deliverables at different stages of the project.
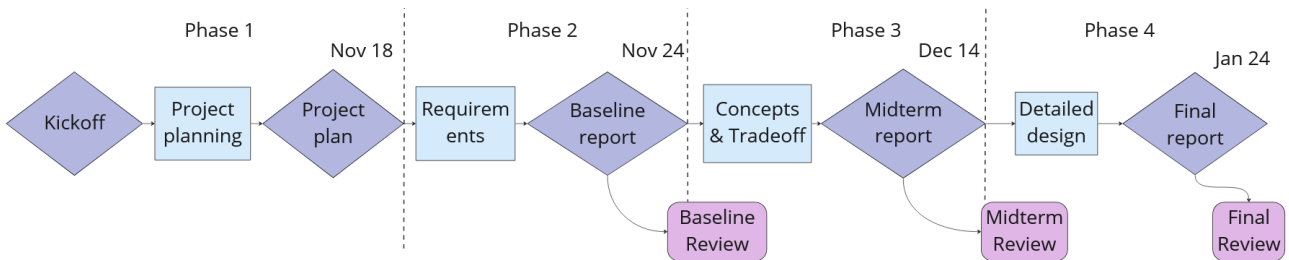
Figure 2.3: Project Logic Diagram

This laid the framework for a workflow diagram to fill out all the tasks and their sequence that were required to arrive at the deliverables for the milestones of the project. However, this project logic is only the highest level of the project flow. There will be more tasks than those just strictly related to the items mentioned in Figure 2.3.

Additionally, parts of the later phases were started before finishing all the tasks of the previous phases to ensure all team members were productively working on a task and the deadlines were met.

2.3.3. Work Flow Diagram

To have a clear understanding of how to proceed with the project a clear and concise diagram visually describing the expected flow of the project was required. This was done with a Work Flow diagram presented in Figure A in Appendix A. This diagram guided the team throughout the whole project by providing a visual description of when different tasks had to be completed as well as showing the interdependence between tasks which will give the team a better understanding of which tasks can be done in parallel and which must be done sequentially.

2.3.4. Work Breakdown Structure

The Work Breakdown Structure offers the team a more detailed view of the work to be performed. This contains the activities outlined in the Work Flow Diagram. The Work Breakdown Structure diagram presented in Figure A structures the specific tasks hierarchically and employs an "AND" logic. The specific contents of each block are referred to as Work Packages. Each work package allows the team to allocate tasks for members to work through. The work packages are designed so that the global task is only completed when every work package is concluded.

2.3.5. Gantt Chart

The Gantt chart is a visual tool that assists in project management and planning. The Gantt chart, presented in Figure A in Appendix A, presents the work packages across the duration of the project. The tasks were given start and end dates and fit into the duration of the project life, indicating the possible time for each work package in order to arrive at a complete project. This chart acted as a living tool throughout the project, allowing the team to track performance and maintain the schedule. As well as the time for each work package, the number of individuals working on each work package was also incorporated. On top of indicating the effort allocated to each work package the chart also allowed for efficient distribution of the team across the project, monitoring the total input from each member.

2.4. Design and Development Logic

The Design and Development Logic diagram found in Appendix A showcases the flow of stages and milestones between the end of this project and the vehicle in operation. There are various milestones the project needs to meet to progress. Along the path, there are yes/no logic tests to determine success or failure and the ability to progress or not. The main phases consist of concluding the detailed design followed by the development of the prototype, this is preceded by the testing phases and only once this is complete can the vehicle be certified for flight, finally the commercial phase will begin when the vehicle is certified.

3

Market Analysis

Understanding the development of different markets and establishing a base unit cost is crucial in developing any engineering project, especially when it involves multiple stakeholders. A detailed market analysis can provide the team with better insights and make it possible to prepare the product for the future market from the development phase to the final stage. In this chapter, the economical aspect of the XV-25 Griffin as well as its selling feasibility is thoroughly analyzed. The structure of this chapter is as follows:

3.1. Industry Research

A necessary measure before introducing a significant product like the XV-25 Griffin into the current market is to examine whether such markets are active and in favor of an upward trend. Firstly, the global VTOL market is analyzed in subsection 3.1.1. Secondly, the regional VTOL market is studied in subsection 3.1.2.

3.1.1. Global Market

In the past decade, VTOL vehicles have become more recognizable thanks to their unique characteristics and increasing safeness. Even though the COVID-19 pandemic severely halted the aviation industry in 2020, the market still quickly recovered afterward as shown in Figure 3.1. According to a report published by Fortune Business Insights [1], the global helicopter market is estimated to grow from US$ 42.67 Billion in 2020 to US$ 68.34 Billion by 2027 which visualizes a stable Compound Annual Growth Rate (CAGR) of 6.24%. Considering how fast the market has recovered after COVID-19, it is safe to conclude that the worldwide VTOL market is stable and subjected to positive annual growth, which reveals the possibility for project XV-25 Griffin to develop.
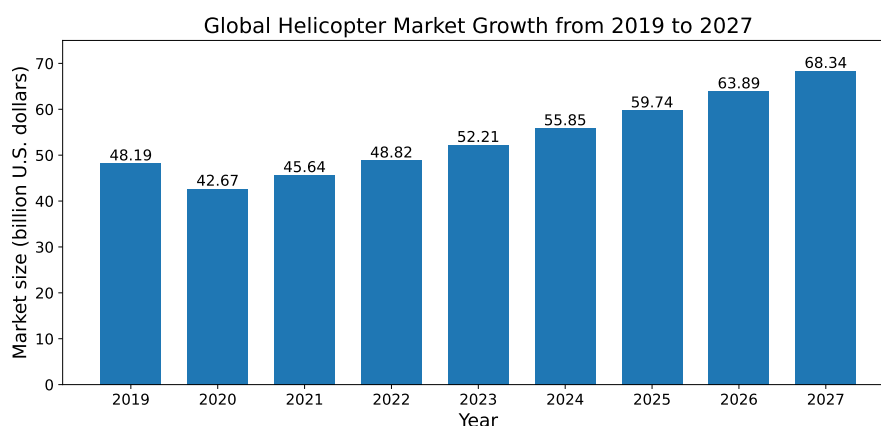
Figure 3.1: Global Helicopter Market Growth from 2019 to 2029

3.1.2. Regional Market

When the market demonstrates promising signals, it is time to drill down to the regional level to obtain more understanding of the low-level market and uncover potential customers. As illustrated in Figure 3.2 and Figure 3.3, North America has the highest possession in terms of units for both categories in consideration, commercial and military. Accordingly, Europe and Asia-Pacific share the runner-up positions in both rankings, which is arguably reasonable since developed countries in the two regions understand the importance of investing in helicopters for multiple applications and long-term benefits. On another note, it is worth noticing that Russia & the CIS region holds third place for military helicopters but is not among the top seventh commercial helicopter regions.

---

[1]https://www.statista.com/statistics/1117653/global-helicopter-market-size-end-use/ - 24/11/2022

Therefore, if the team decides to commercialize the XV-25 Griffin, the market in Russia & the CIS region is visibly not tempting. Nevertheless, considering the size and operational type of the perspective XV-25 Griffin, the team tends to shift its attention to bigger regions of developed countries where the design can be used to its full potential at different segments.
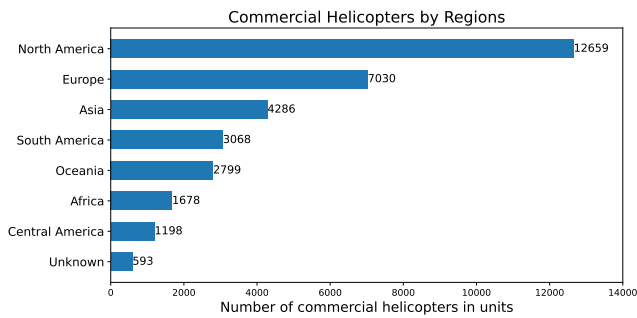
Figure 3.2: Commercial Helicopter by Regions[2]
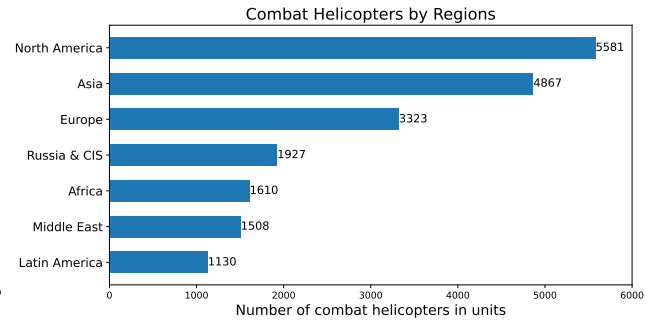
Figure 3.3: Combat Helicopter by Regions[3]

3.2. Competition Analysis

Based on the key characteristics of the XV-25 Griffin, the team goes one step further by considering different segments where it can become a competitive product. At first sight, the current market seems somewhat missing a vehicle that holds essential features of VTOL vehicles - the ability to take off and land vertically and hover, and aircraft - the large capacity with high cruise speed. Eagerly, the XV-25 Griffin aims to be the first to merge the two ends of the aviation spectrum by designing a VTOL vehicle with a minimum cruise speed of 450 kts and a large payload capacity of 5000 lbs. While the requirements and constraints are further analyzed in chapter 4, how the XV-25 Griffin performs compared to its competitor in different segments is investigated in this section.

3.2.1. Military Market

Military operations often require aircraft capable of attaining high speeds and altitudes, carrying large payloads, having a long range, and accessing remote locations. In times of global instability such as the current situation with Russia and Ukraine, there is often an increased need for these types of capabilities, as military and humanitarian organizations may need to quickly respond to crises in remote or hard-to-reach locations. Currently, large planes such as the Lockheed C-5 or Boeing C-17 are often used in addition to a second land vehicle, but an alternative approach is using heavy-lift helicopters like the Chinook CH-47 or Sikorsky CH-53. These helicopters can access remote locations by themselves but are slower and lower-flying, making them more vulnerable to surface-to-air missiles. As an alternative, tilt-rotor aircraft offer a compromise by combining the advantages of both planes and helicopters. Daringly, the new XV-25 Griffin is designed to compete with and replace the V-22 Osprey and similar military aircraft as shown in Figure 3.6.
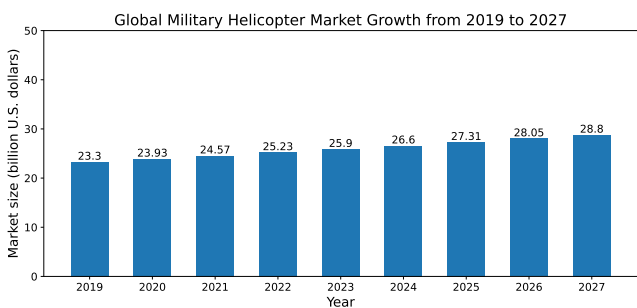
Figure 3.4: Global Military Helicopter Market Growth from 2019 to 2027 [4]
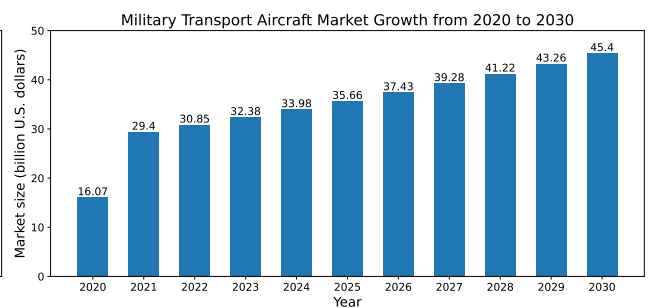
Figure 3.5: Military Transport Aircraft Market Growth from 2020 to 2030 [5]

---

[2]https://www.statista.com/statistics/778319/commercial-helicopters-fleet-size-region/ - 24/11/2022
[3]https://www.statista.com/statistics/1117595/global-combat-helicopter-fleet-region/ - 24/11/2022

The global military helicopter market recorded in 2019 amounted to US$ 23.3 Billion. It is expected to grow up to US$ 28.8 Billion by the end of 2027[6]. Figure 3.4 also indicates a constant growth in the demand for military helicopters in the future. Similarly, the military transport aircraft market shows an increase in demand as the market grows from US$ 16 Billion in 2022 to US$ 45 Billion by 2030[7]. Figure 3.5 shows a 4.8 percent growth in the market from 2022 until 2030.

The tilt-rotor aircraft market deserves special attention since the XV-25 Griffin is directly competing with the V-22 Osprey. The market itself is much smaller than that of conventional aircraft and helicopters due to its newer technology and North America is the largest market for tilt-rotor aircraft, with a global revenue of US$ 986.1 Million in 2020. It is the fastest-growing market among aircraft and helicopters and is expected to have a CAGR of 7.47% during 2020-2028[8]. The military is also showing interest by organizing competitions like FARA (Future Attack Reconnaissance Aircraft) which highlights the future demand for tilt-rotor aircraft.
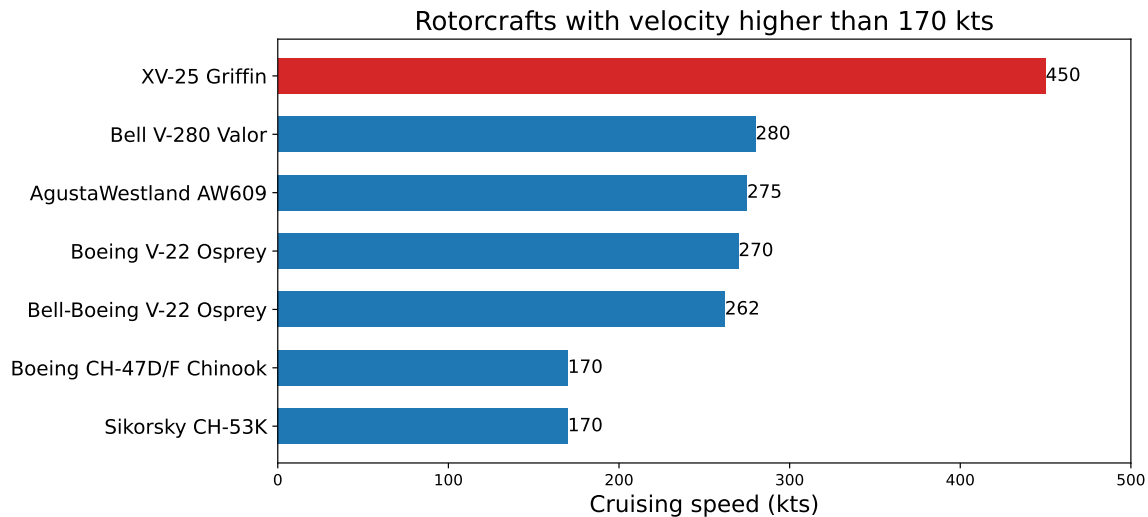
Figure 3.6: Cruising Speed of Fastest Military Helicopters vs. XV-25 Griffin. [9]

3.2.2. SAR/EMS Market

While the XV-25 Griffin is originally designed to satisfy military operational conditions, the team realizes the potential of introducing the design into different markets, namely the Search And Rescue (SAR) and the Emergency Medical Service (EMS). In 2021, the SAR market value is estimated at US$ 1.91 Billion [10] while the EMS market size is valued at US$ 4.89 Billion [11]; both markets are anticipated to have a stable positive growth rate of 4.1% and 8.56%, respectively. SAR operations aim to prepare for emergency situations, and quickly search for and provide support to people who are in distress or danger. Common circumstances requiring SAR can be disasters, mountain rescues, combat rescues, air-sea rescues, or accidents. On the other hand, EMS operations are meant to provide medical support where land-based assistance would take too long to arrive. While serving different purposes, the two operations require almost the same characteristics from the vehicle: safe, quick, efficient, hovering ability, and payload capacity. The critical requirements quickly eliminate aircraft in the competition since they cannot hover and strictly require airdromes to properly function.

The main competitor of the XV-25 in this market can be the Leonardo AW101 - notably used by the British Royal Navy as a rescue vehicle, the Sikorsky S-92 which is preferred by the South Korean Coast Guard, or the Airbus H225 which is currently in use by the State Emergency Service of Ukraine. With Table 3.1 summarizing the key characteristics of the XV-25 Griffin and its competitors in the SAR/EMS market, it can clearly be seen

---

[4]https://www.statista.com/statistics/1117792/global-military-helicopter-market-size/ - 2/12/2022

[5]https://www.alliedmarketresearch.com/defense-transport-aircraft-market-A13461 - 2/12/2022

[6]https://www.statista.com/statistics/1117792/global-military-helicopter-market-size/ - 20/01/2023

[7]https://www.einnews.com/pr_news/601547139/ - 20/01/2023

[8]https://www.researchandmarkets.com/reports/5354374/ - 22/11/2022

[9]https://www.statista.com/statistics/614301/cruising-speed-of-fastest-military-helicopters/ - 24/11/2022

[10]https://www.grandviewresearch.com/industry-analysis/search-rescue-helicopter-market-report - 24/11/2022

[11]https://www.fortunebusinessinsights.com/homeland-security-and-emergency-management-market-102743 - 24/11/2022

that the XV-25 Griffin significantly outperforms its contestants in terms of cruise speed (averagely three times higher).

Table 3.1: Comparison between XV-25 Griffin and Its Competitors on the SAR/EMS Market

Model	Manufacturer	MTOW	Payload Capacity	Flight Ceiling	Cruise Speed	Range
Units	-	*lbs (kg)*	*lbs (kg)*	*ft (m)*	*kts (m/s)*	*nm (km)*
XV-25 Griffin	TBD	62,361 (28,286)	6,000 (2,722)	20,000+ (6,096+)	450+ (231+)	1000 (1,852)
AW101	Leonardo	32,187 (14,600)	6,724 (3,050)	15,000 (4,572)	150 (77.2)	466 (863)
S-92	Sikorsky	26,500 (12,020)	7,417 (3,364)	14,000 (4,267)	151 (77.7)	547 (1,013)
H225	Airbus	24,692 (11,200)	11,907 (5,400)	19,400 (5,913)	141 (72.5)	454 (841)

3.2.3. Civil Transport and Offshore Market

Other than the previously mentioned markets, the team does not exclude the possibility of using the XV-25 Griffin as an offshore or civil transport vehicle. International organizations and companies like the WHO, UN, Airbus, Antonov, and UPS use large aircraft for the transportation of goods[12]. However, these operations require a good level of infrastructure, including an airstrip for take-off and landing. Project Griffin aims to overcome these difficulties and restrictions by utilizing VTOL while carrying a significant payload at a speed of 450 kts.

Recent years also demonstrate high demands and reveal certain opportunities for the XV-25 Griffin with respect to the offshore market. While the oil and natural gas industries become less tempting, new possibilities are opening up in the market, for instance, the wind energy market or the aquaculture market. Approximately 6000 wind turbines have been installed offshore over the period from 2018 to 2022 [13]. The XV-25 Griffin can help with accelerating the installation process and promoting clean energy production and usage. The growing aquaculture market also presents a potential opportunity for the XV-25 Griffin as it may be used to transport equipment and large amounts of food products quickly. The demand for aquatic food production is also expected to increase by 15% by 2030 giving more reason[14].

3.2.4. Stakeholders

Obviously, introducing the XV-25 Griffin to the market involves different stakeholders. With the major segments have been scrutinized, it is predicted to have the following stakeholders:

- Government: the government publishes the regulation and certification that the XV-25 Griffin has to satisfy in order to come to the manufacturing stage and operation.

- Military: the military is the key focus and biggest potential customer of the XV-25 Griffin.

- Air ambulance service providers: air ambulance service providers (both public and private) are potential customers of the XV-25 Griffin.

- Organizations (UN, UNICEF, WHO): potential customers of the XV-25 Griffin.

- Manufacturers/Competitors/Investors (Sikorsky, Leonardo, Bell, Boeing): XV-25 Griffin would directly compete with current manufacturers and affect their market shares or become a part of their existing ecosystem.

- Suppliers and maintenance: XV-25 Griffin would require a tailor-made supply chain and maintenance services for different subsystems: interior, power, aerodynamic, etc.

- Pilots: they are required to operate the aircraft.

3.3. Market Capitalization

When the markets, as well as the stakeholders, have been identified, the team can perform a unit cost estimation to predict a potential future market capitalization. The unit cost per each XV-25 Griffin is based on the cost of its subsystem which is reported in subsection 3.3.1. After finishing the evaluation, the team look at different parameters that could grow during the development phase and set an upper limit for them so as to prevent a so-called

---

[12]https://www.unicef.org/supply/stories/ -24/11/2022

[13]https://www.helicopterinvestor.com/articles/offshore-opportunities-739/ - 02/12/2022

[14]https://www.fao.org/state-of-fisheries-aquaculture - 02/12/2022

snowball effect from happening. The resource allocation/budget breakdown is explained in subsection 3.3.2.

3.3.1. Cost Breakdown Structure

In order to get an estimate of the unit price for the XV-25 Griffin, a cost estimation was done for all the subsystems of the aircraft with the help of a Ph.D. thesis by Johnny J. Gilliland from Denton, Texas [2]. The study presented multiple equations to estimate the subsystem weights of a compound helicopter and analyzed them to arrive at the most accurate equations for different subsystems. Each subsystem consisted of multiple parts as listed below:

- Airframe Cost: forward fuselage, mid-fuselage, wings, tail boom, and horizontal & vertical fin assembly.
- Rotor Cost: blades, hub, and rotating controls.
- Drive Cost: main transmission gearbox, drive shafts.
- Propulsion Cost: engines, engine mounts, air management, firewalls, fuel system.
- Electrical Cost: electrical equipment, wiring, instruments, and navigation equipment.

Since the cost estimation was done for the year 1978, an inflation factor was applied to find the costs for 2023[15]. Furthermore, for the propulsion subsystem, the F-35 engines were used as a starting point with a cost of US$ 15.4 million per engine[16]. The cost was then linearly scaled down with the maximum thrust of the engine to arrive at the cost for Griffin engines.

Table 3.2: Cost Breakdown Structure per Subsystem Adjusted for Inflation

Airframe	Rotor	Propulsion	Electrical	Drive	Total US $
US $					
21,226,100	9,114,430	18,000,200	1,677,686	1,033,113	51,051,529

Similarly, another study was conducted by the Institute for Defence Analysis, USA in 1984 to estimate the cost of Soviet aircraft [3]. The flyaway cost (FLY) of a rotary-wing aircraft is heavily dependent on the shaft horsepower (SHP) of the rotor and can be estimated using Equation 3.1. This includes the production and tooling cost only and the shaft horsepower is estimated using the torque and the rotational speed of the rotor in Equation 3.2.

$$FLY = 2.6 \cdot 10^{-3} \cdot SHP^{0.93} \qquad (3.1) \qquad\qquad SHP = Torque_{max} \cdot \Omega \qquad (3.2)$$

This gives a flyaway cost of US$ 18.57 million for 1985. When adjusted with inflation for the year 2023, the unit cost comes up to US$ 50.5 million which lines up with the previously estimated sum of subsystem costs. In addition to the flyaway cost, an estimate for the research, development, testing, and evaluation (RDT&E) cost was also done with Equation 3.3 where ATK = 1 for attack helicopter; 0 elsewhere and MOD = 1 for helicopter modification; 0 elsewhere. So the ATK and MOD are set to zero for XV-25 Griffin since it's neither an attack helicopter nor does it have any modifications. This yields an RDT&E cost of US$ 2.66 billion for the year 1985, which when adjusted with the inflation factor for 2023 results in an RDT&E cost of US$ 7.23 billion.

$$RDT\&E_{cost} = 3.34 \cdot SHP^{0.7} \cdot 2^{ATK} \cdot 0.16^{MOD} \qquad (3.3)$$

Even though the unit cost of the XV-25 Griffin is around US$ 51 million, a profit margin of 13.1% is applied much like the Bell helicopters[17]. This results in the sale price of one unit being around US$ 57.7 million. The combined market value for tilt-rotor aircraft, military helicopters, and military transport aircraft in 2020 was US$ 40.9 billion, and with a production of 12 machines per year, the team expects US$ 700 million in sales. This allows the team to capture at least 1.7% of the military market shares.

---

[15]https://www.usinflationcalculator.com/ - 24/01/2023

[16]https://www.defensenews.com/air/2022/06/15/pratt-whitney-wins-44b-contract-for-f-35-engines/ - 24/01/2023

[17]https://www.statista.com/statistics/609756/ - 24/11/2022

3.3.2. Resource Allocation and Budget Breakdown

Obviously, the unit cost has a strong correlation with the size and technology the aircraft is equipped with. There-fore, without pre-set limitations during early design phases, the cost of the project could increase and deviate significantly compared to the early estimations. For that reason, the technical budget of the most important resources is established as follows:

- Mass: The aircraft mass inarguably plays a critical role in the whole designing process as it provides input to all other subsystems [4]. If the mass of the XV-25 Griffin increases beyond the allowable budget, it could trigger an accelerating growth of magnitude in everything. As one of the requirements provided by the VFS already includes a structural contingency factor of 5% (see REQ-STK-SIK-10 in chapter 4), only 5% will be added to the mass budget margin. This is due to the fact that at later designing phases, weight estimations can make use of more accurate and detailed methods, which typically results in less weight.

- Power: To simplify the budget allocation process, power-related performance indicators such as range or endurance are considered together. Exceeding the power budget could lead to a heavier engine or an issue of over-designing a subsystem. Similar to weight, as the power section itself (see chapter 9) already included safety factors where applicable for the calculations, only 10% will be added to its budget. The reason for a higher margin value compared to mass is that numerical calculation usually underestimates the actual frictions or the engines could produce less power than the provided specifications. It is also due to the fact that multiple subsystems are exploiting the available power; thus, a higher margin to make sure separated changes is taken into account.

- Cost: Cost is also an important factor in deciding the financial success of the project and determining the possible life of the project. While little information can be found regarding cost estimation for the specific case of the XV-25 Griffin, because it is supposed to compete directly with the V-22 Osprey, the team decides to place the cap based on the price of the V-22 Osprey (72 mil. U.S. dollars) with a margin of 5%. If the unit cost of the XV-25 Griffin exceeds this margin, even with better performance, it would be difficult to introduce the product into the market.

3.4. SWOT Analysis

As a final remark, the team performs a SWOT analysis to identify different factors from both the external environment - the market, and the internal environment - the team, which can both affect the outcome of the project. As shown in Figure 3.7, the opportunities, threats, strengths, and weaknesses are visualized to assist the team in further advancing the project.

Opportunities
- Support from professors and experts of the field.
- University resources at disposal
- A growing market for compound vehicles.
- Very few competitors
- RFP from a market leader for VFS competition

Threats
- High price compared to existing products.
- Field with low TRL
- Changes in Federal/Govt. laws
- Constrained to a single market
- Possibility of new competitors

External

Internal

Strengths
- Pilot experience from the team's member.
- Actual practices from multiple Student Dream Teams: AeroDelft, DARE, and Formula Student.
- Different skill sets from minors and internships: sustainability, computer science, business management, etc.
- Full-time working principles.
- Balanced synergy and good cooperation among team members.
- Designs combining advantages from high-speed and VTOL vehicles.

Strategies to make use of **Opportunities** through our **Strengths**
- Making use of different skill sets and available resources to produce a competitive design.
- Use pilot experience to ground designs in reality.
- Capitalize on the advantages of a combination of high speed and VTOL design in a market with few competitors.

Strategies to prevent **Threats** through our **Strengths**
- Make use of high motivation and team spirit to keep up with tight working conditions.
- Leverage Multiple Discipline Knowledge to Build Group Capability
- Use the combination of a high speed and VTOL design to explore multiple market.

Weaknesses
- Lacking knowledge designing rotorcraft with such challenging requirements.
- Lacking experience in project management and system engineering.
- Conflicts of interest among team's members.
- Limited time and personnel (10 students in 10 weeks).
- No budget and funding during development phase.

Strategies to make use of **Opportunities** to minimize **Weaknesses**
- Utilize university resources to its full potential and over the lack of funding.
- Create a productive and professional working environment throughout the project.
- Use the support from professors and experts to improve our knowledge on rotor craft design.

Strategies to minimize the potential dangers lying in sectors where **Weaknesses** meet **Threats**
- Establish expert network at an early stage for proper guidance.
- Maintain sharing of knowledge to mitigate knowledge expert absentness
- Establish a strict schedule to combat the limited time and meet the challenging requirements.

Figure 3.7: SWOT Analysis of Project XV-25 Griffin

4

Requirements and Constraints

This chapter details the requirements and constraints that were established at the start of development. Based on the requirements from the project's different stakeholders as well as the required mission profile, the set of constraints and technical system requirements was derived using a requirements discovery tree as detailed in the Baseline Report [5]. The stakeholder and mission requirements are listed in Table 4.1 and Table 4.2, respectively. The full list of system requirements is omitted here for brevity but can be found in the Baseline Report.

4.1. Stakeholder Requirements

The stakeholder requirements (STK) showcase the higher-level requirements set by the different stakeholders of the design. These requirements define the global capability of the design to be delivered. The different stakeholders that were identified are: Sikorsky Aircraft (SIK) [1], the military (MIL), the EASA Certification Body (EASA) [6], the Federal Aviation Administration (FAA) [7] and the Technical University of Delft (TUD).

Table 4.1: Stakeholder Requirements

ID	Requirement
REQ-STK-SIK-1	The aircraft shall be able to perform the mission as stated in the mission requirements.
REQ-STK-SIK-2	The aircraft shall minimize the effect of the downwash environment on ground personnel.
REQ-STK-SIK-3	The aircraft shall minimize the susceptibility of the propulsion system to foreign object debris.
REQ-STK-SIK-4	The aircraft shall use no more than 100% MCP or 100% MCT from the primary propulsion system at SDGW.
REQ-STK-SIK-5	The aircraft shall be able to transition from cruise to hovering in flight.
REQ-STK-SIK-6	The landing gear shall be designed for a sink rate of 10 f/s (3.0 m/s) with $\frac{2}{3}$ rotor lift.
REQ-STK-SIK-7	The aircraft shall accommodate a 3-man crew at 250 lb (113 kg) each.
REQ-STK-SIK-8	The aircraft shall carry a payload of 5000 lb (2258 kg).
REQ-STK-SIK-9	The aircraft shall carry a mission equipment package of 1000 lb (454 kg).
REQ-STK-SIK-10	The aircraft weight shall include a 5% contingency margin.
REQ-STK-SIK-11	The airframe limit load factor shall be 3.5g at SDGW.
REQ-STK-MIL-12	The aircraft shall be able to operate in a military environment.
REQ-STK-EASA-13	The aircraft shall adhere to certification standards as outlined in CS-29.
REQ-STK-FAA-14	The aircraft shall adhere to certification standards as outlined in 14 CFR Part 25.
REQ-STK-TUD-15	The preliminary design of the aircraft shall be delivered by the 25th of January 2023.

4.2. Mission Requirements

The mission requirements (MSN) outline the different phases of the mission that the design shall adhere to. These stem from the Sikorsky stakeholder and are linked to REQ-STK-SIK-1 directly.
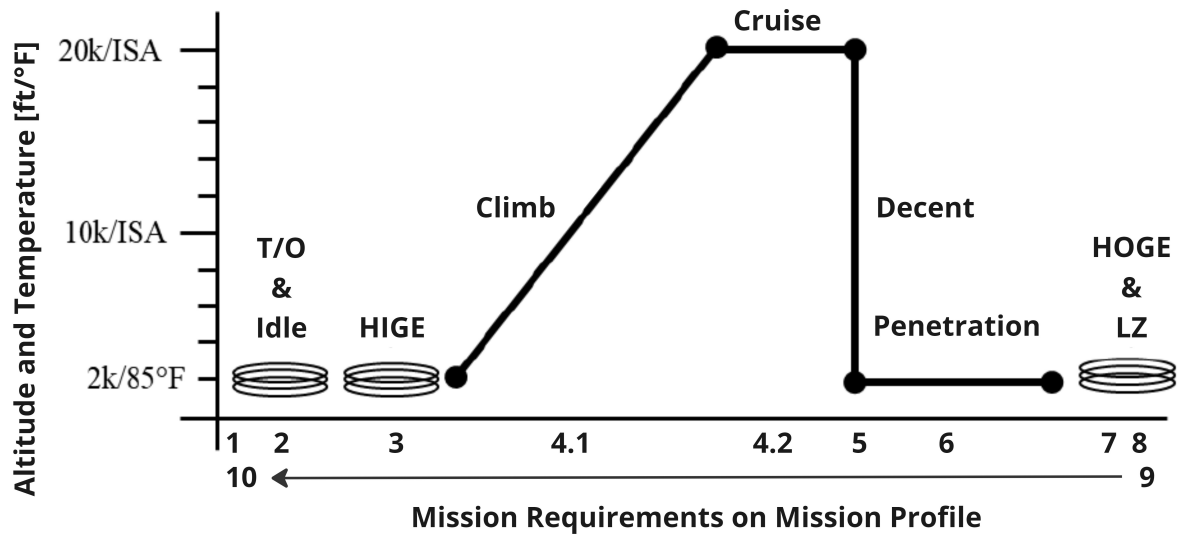
Figure 4.1: Mission Profile [1]

Table 4.2: Stakeholder Requirements

ID	Requirement
REQ-MSN-1	The aircraft takeoff condition shall be 2000 ft (609.6 m) pressure altitude and 85°F (24°C) air temperature.
REQ-MSN-2	The aircraft shall perform an idle for 10 min after ignition.
REQ-MSN-3	The aircraft shall perform a 2-minute hover in ground effect.
→ REQ-MSN-3-1	The engine power shall be no greater than 90% Maximum Rated Power at hover conditions.
→ REQ-MSN-3-2	Motor and gearbox torque shall be no greater than 100% continuous transmission torque at hover conditions.
REQ-MSN-4	The aircraft shall cruise 450 nm (833 km/h).
→ REQ-MSN-4-1	The cruise climb at best climb speed shall be included in the aircraft cruise range.
→ REQ-MSN-4-2	The aircraft shall cruise at an altitude of no less than 20.000 ft (6093 m).
REQ-MSN-5	The aircraft shall perform a vertical descent from cruise conditions to 2000 ft (610 m) MSL 85°F (24°C).
REQ-MSN-6	The aircraft shall cruise with full power or torque at 2000 ft (609.6 m).
REQ-MSN-7	The aircraft shall hover out of ground effect at MMGW.
REQ-MSN-8	The aircraft shall perform a 2 min landing at MMGW.
REQ-MSN-9	The mission profile shall be repeated in reverse order.
REQ-MSN-10	The energy reserves shall be 20 min at V_{BR} and 2k/85°F.

<div align="right">

5

</div>

Conceptual Design, Trade-Off

In this chapter, an overview of the whole conceptual design process is presented. As a first step, a design option tree was generated [4] which was used to generate 3 different concepts that meet the requirements outlined in chapter 4. After this, a preliminary analysis was performed for each concept whose outcome was then used to trade off the three concepts to arrive at a final concept the team thought was the best given the required mission. Finally, a sustainable development strategy is presented to ensure both the design process as well as the vehicle itself adhere to the sustainability requirements.

5.1. Conceptual Design Overview

The first step in realizing three concepts that could fit the mission requirements was to generate a design option tree where all possible options for our vehicle were collected. Once the tree was generated, the team went over all the presented options and eliminated options that were either unrealistic or would prevent the vehicle from meeting the key requirements. The complete tree can be found in the Midterm report[4].

As a next step, the team generated three preliminary concepts with the help of the design option tree. The three selected concepts are shown in Figure 5.1. The fan-in-wing concept is shown on the left. It features a blended wing body with a single central ducted fan-in-wing for hover. During high-speed forward flight, the rotor is covered and thrust is provided by jet engines located on top of the body. Winglets are located at the wing ends for directional stability during forward flight. For torque control during hover, either a coaxial rotor system can be used or the winglets can be outfitted with ducted vertical fans. The cargo bay is located forward of the fan and placed at an angle of $90°$ to the longitudinal axis, it can be accessed from the side of the aircraft.

(a) Fan-in-Wing Concept

(c) Compound Concept

(b) Tilt-Rotor Concept
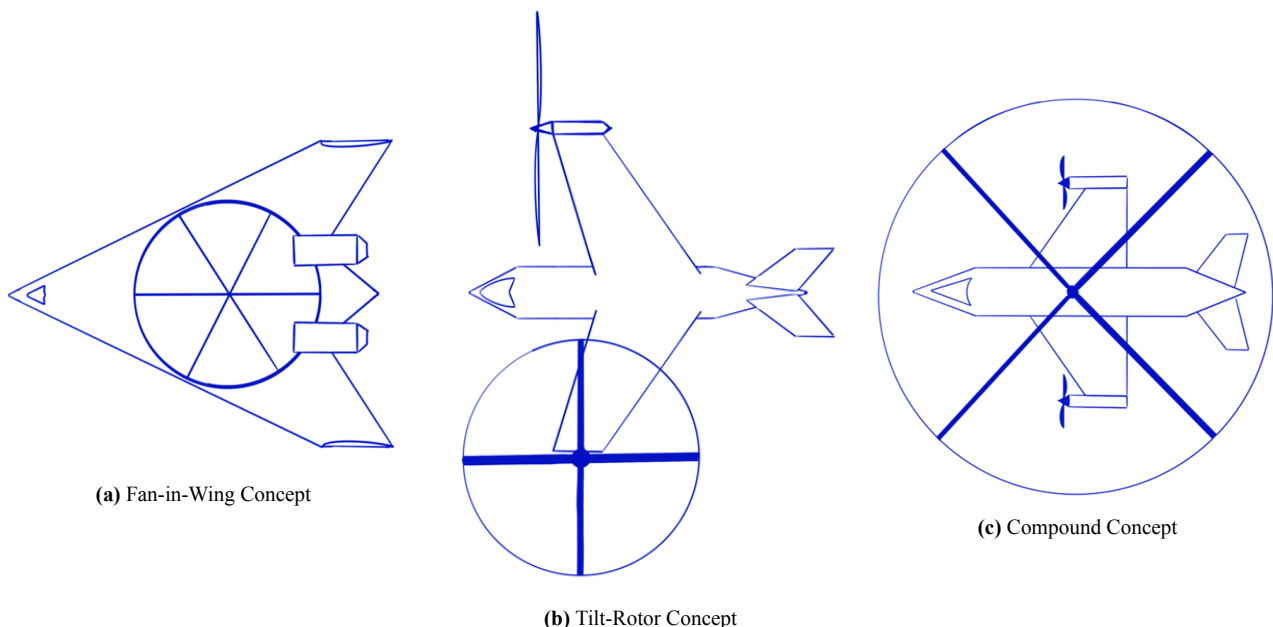
Figure 5.1: Top View Sketches of the Selected Concepts

The second concept, shown in the middle, is a dual tilt-rotor aircraft. The rotors have variable-diameter to allow for low disk loading during hover as well as high propulsive efficiency in forward flight. The wings are swept forward to achieve the required transonic performance while also leaving space for the rotors. Because the rotors are counter-rotating, no additional torque control is needed. The concept has a V-tail configuration.

The third concept is a compound aircraft. The main rotor is used for vertical flight while dedicated propeller

engines located at the wingtips provide horizontal thrust during forward flight. The propellers also use differential thrust for torque control during hover. It features a closed-wing design for greater aerodynamic efficiency, a stronger structure, and less aerodynamic interference between the rotor and wings although interference between the wings themselves could become an issue. The tail only has horizontal surfaces, as yaw stability is provided by the vertical components of the wings. During the high-speed flight, the rotor is stowed away in the fuselage and wings to improve the drag coefficient of the aircraft. Variable blade length technologies might be used to reduce the rotor diameter during the cruise, making it easier to store.

5.2. Trade-off

After having generated three concepts, a trade-off was performed using some preliminary analysis results to drill down to a final concept. To ensure the best design was selected, each concept was scored on a number of weighted criteria to obtain a numerical score that could be used to compare the different concepts. Five criteria were defined on which the concepts were scored. The criteria are "Power", "Structures", "Control", "Operations", and "Risk". Under each criterion, multiple aspects were considered which are shown in Figure 5.1. The detailed justification for the selected categories along with their respective weights chosen for the final trade-off can be found in [4].

Table 5.1: Trade-off Criteria and Associated Weights

Power	Structures	Control	Operations	Risk
4.0	2.3	2.4	3.0	2.1
Energy Budget	Dimensions	Control in Hover	Operation Safety	System Redundancy
Maximum Power	Weight	Control in Cruise	Footprint	Technology Readiness Level
Efficiency in Hover	Structural Complexity	Ease of Transition	Downwash	Autorotation Capabilities
Efficiency in Cruise	Mechanical Complexity	Control Redundancy	Noise	Gliding Capabilities

For each criterion, the most important values or aspects for that score are stated, which result in the scores represented by the colors of that box where boxes colored in blue represent an excellent score, grey represents a good score, yellow represents a poor score and red represents an unacceptable score. This resulted in the scores stated in the final column of the trade-off table. Both the compound and tilt-rotor concepts did not have any unacceptable scores meaning that both concepts could be taken into a more detailed design. The final concept chosen by the team was the compound concept due to it having a slightly higher total score when compared to the tilt-rotor.

Table 5.2: Trade Off Results

Concept	Power	Structures	Control	Operations	Risk	Score
Fan In Wing	3 Grey Hover: 13MW, Cruise 6.5MW	1 Red MEW: 48k lbs, Structure: Challenging	1 Red Hover: Challenging, Transition: Challenging	1 Red Downwash: Large Footprint: Unacceptable	4 Blue Gliding: Good Autorotation: Good	**4.22**
Tilt Rotor	4 Blue Hover: 8MW, Cruise 11MW	4 Blue MEW: 28k lbs, Structure: Well Understood	2 Yellow Hover: Demonstrated, Transition: Demonstrated	3 Grey Downwash: Medium Footprint: Excellent	2 Yellow Gliding: Possible Autorotation: Unfeasable	**5.22**
Compound	2 Yellow Hover: 10MW, Cruise 14MW	3 Grey MEW: 40.7k lbs, Structure: Well understood	4 Blue Hover: Efficient, Transition: Simple	5 Green Downwash: Small Footprint: Acceptable	3 Grey Gliding: Good Autorotation: Difficult	**6.22**
Weight	*4.4*	*3.8*	*3.1*	*3.2*	*2.2*	

5.2.1. Sensitivity Analysis

To confirm the findings and ensure there is no sensitivity to any specific parameter chosen a sensitivity analysis was performed. The sensitivity analysis will change the weighting of the different criteria to find out the changes in the trade-off results as a consequence. As the weighting of the criteria can never be completely objective

and subjective opinions will thus influence the weight determination process, this sensitivity analysis allows engineers to check their biases. If the sensitivity analysis shows that the winner of the trade-off will also win in cases where the weights have changed it shows that the concept and trade-off are robust and a good choice. However, if it is discovered that the winning concept in the original trade-off seldom achieves an acceptable score the process should be reconsidered.

In this case, The trade-off was manipulated by changing the weights of the different sections. Each weight was changed from 1 through to 5 at intervals of 0.5. Each concept received a new score while the other categories maintained their weights. In Figure 5.2 the results of the sensitivity are illustrated. The results show the variance of the total score for each concept as the weights per category are changed from 1 through 5.
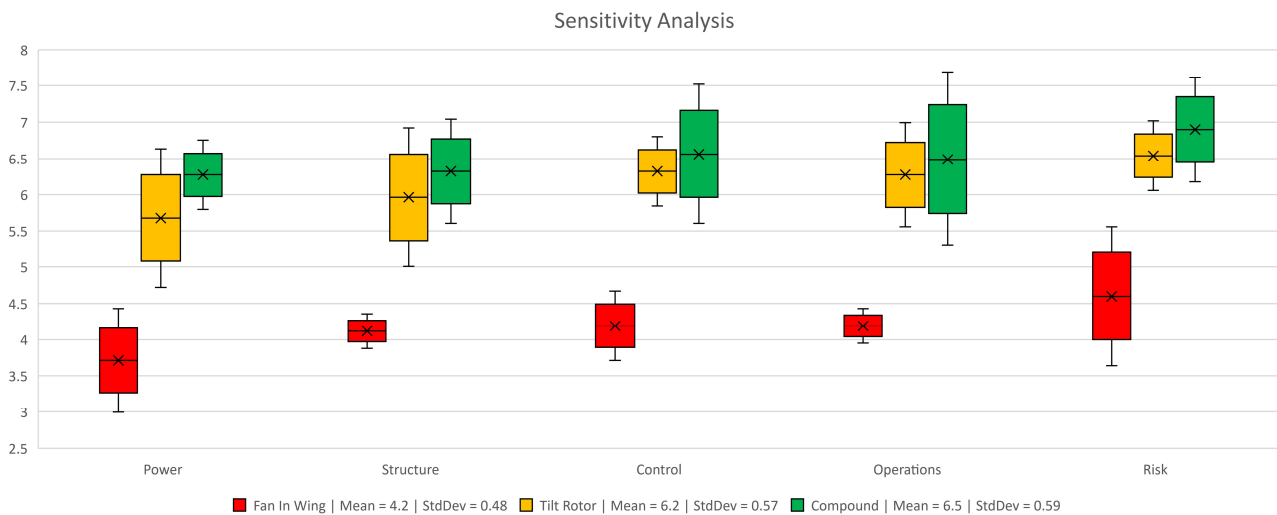
Figure 5.2: Sensitivity Analysis

As seen in Figure 5.2 the Compound concept repeatedly held the higher mean, however, the standard deviation was the largest. This stems from the variance in Control and operations suggesting these weights had the largest effect on the Compound result. Conversely, the Structure and Power had the largest influence on the Tilt Rotor concept and the Power and Risk on the Fan in Wing.

5.2.2. Final Concept

From the trade-off, the final selection is the compound aircraft. The concept employs a box wing, the main rotor to generate vertical lift, and two wing-mounted engines for forward flight. This is illustrated in Figure 5.3. In order to facilitate the high velocities of cruise, the main rotor will be designed such that it can both vary its radius as well as lower vertically, these capabilities will allow it to be stowed away for the cruise portion of the mission. Thus the vehicle will utilize the main rotor for hover and vertical take-off and landing while using the box wings for the cruise. In transition, the main rotor will be stopped once the wings are carrying the weight, retract to decrease their diameter, and then lower into the body.

It must be noted that the final concept selected in the Midterm report [4] has been slightly modified. Namely, the turboprops on the wings were switched to turbofan engines which will be placed at the back of the fuselage. In addition, the wings were changed to rectangular wings instead of triangular wings. Justifications for these changes can be found in chapter 9 and chapter 8, respectively.

5.3. Sustainable Development Strategy

As the concept was finalized, a plan for the long-term development of the project had to be considered, of which the sustainability aspect can not be disregarded. In principle, a sustainable project oversees the long-term vision and is a considerable task to guarantee stakeholders' requirements. For project XV-25 Griffin, several critical parameters are considered as suggested by Chawla et. al [8]: profitability, safety, transparency, ethicality, nature-friendly, and social acceptability. The parameters are grouped into three pillars and investigated separately: environmental in subsection 5.3.1, social in subsection 5.3.2, and economic in subsection 5.3.3.
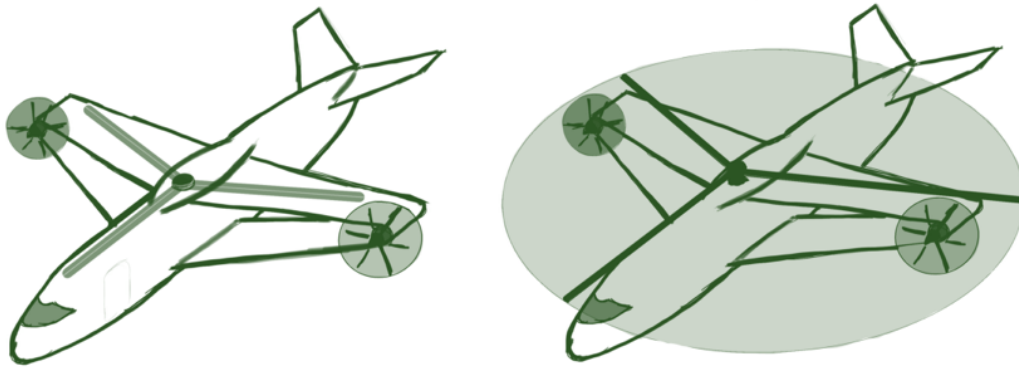
Figure 5.3: Visualized Final Concept

5.3.1. Environmental Sustainability

It is undeniable that climate change is increasingly prominent and becoming a true crisis of the century. According to a report published by the ICAO [9], traffic growth is expected in all sectors and international aviation can grow up to 280% by 2050. Consequently, it will have an important impact on the overall emission of CO2, NOx, etc. Noticeably, the ICAO also creates several theoretical scenarios which assume different technology developments and none of them are able to help with achieving net-zero emissions by 2050.

To combat climate change and its impacts, in the 26th United Nations Climate Change (COP26) conference in Glasgow, 153 countries put forward new 2030 emissions targets and aim to achieve net-zero emissions by 2050 [1]. To accomplish that, the military is no exception to new regulations as they typically account for a large proportion of governments' emissions. Among developed countries, the UK was the first to take action on its military sectors by applying sustainable fuel to its fighter jets [2].

The new regulations could pose several challenges to project XV-25 Griffin since it requires a large amount of power (as elaborated in chapter 9) to properly execute the mission profile. Although the current Technology Readiness Level (TRL) may prevent immediate changes from taking place, the team still considers multiple actions that could make XV-25 Griffin as sustainable as possible by the time it will be introduced to the market in 2035. The following methods are considered by the team:

- Deploying Sustainable Aviation Fuel (SAF): SAF can be made from agricultural waste, cooking oil, or carbon captured from the air. As previously mentioned, by substituting 30% of conventional fuel with SAF, the UK government expects a CO2 emission reduction by 18% [2]. When SAF becomes widely available and applicable, the team will test its compatibility with the XV-25 Griffin.

- Electrification and hybridization: Airbus proposes combining a conventional thermal engine with an electric propulsion system to optimize energy consumption and reduce unwanted emissions [3]. The team does not exclude the possibility of hybridizing the XV-25 Griffin if it can deliver the amount of needed power sufficiently.

- Hydrogen: Airbus also reveals a project to develop a hydrogen-powered zero-emission engine with an operational range of 1000 nautical miles which matches the XV-25 Griffin's requirement [4]. The team strictly follows the status of such projects and considers if changes can be applied to the XV-25 Griffin before its production phase.

In terms of TRL and application, SAF seems to be the most viable solution that can be integrated into the XV-25 Griffin to achieve the sustainable goal. This will be re-iterate after the subsystems' analyses have been

---

[1] https://ukcop26.org/wp-content/uploads/2021/11/COP26-Presidency-Outcomes-The-Climate-Pact.pdf - 14/12/2022

[2] https://www.gov.uk/government/news/sustainable-fuels-to-power-raf-jets - 14/12/2022

[3] https://www.airbus.com/en/sustainability/respecting-the-planet/decarbonisation/decarbonising-helicopters - 14/12/2022

[4] https://www.airbus.com/en/innovation/zero-emission/hydrogen/zeroe - 14/12/2022

performed, together with other vehicle environmental characteristics like noise and emission in chapter 12.

5.3.2. Social Sustainability

Social sustainability relates to the lives around the project, spanning through different phases like the development, manufacturing, or operation of the XV-25 Griffin. Each phase will have unique aspects about it that will impact different groups in society. The goal of social sustainability is to establish a balance boundary between the community surrounding the vehicle and the growth of the project.

- During manufacturing, it is important to look at the material sources and suitable locations where workers' rights are guaranteed whilst keeping the cost at an optimal range. It is also worth mentioning that the XV-25 Griffin is meant to be a military vehicle, which indicates globalization and spreading the supply chain to developing regions is not viable. Consulting the Global Rights Index given by the International Labour Organization [5], European countries like France, Italy, Portugal, Spain, or Poland are good candidates since the workers' rights are respected and they are part of the NATO Alliance. Localizing the manufacturing process within the European Union also offers multiple benefits: the quality of the materials, the consistency of the product, and in case of prolonged conflicts, it poses less vulnerability to the whole process.

- During operation, the influence of the XV-25 Griffin depends heavily on the exact customer or mission which is yet to be finalized at this stage of the project. However, as indicated in section 3.2, the SAR/EMS and Offshore applications seem to improve the quality of lives around the XV-25 Griffin. Another consideration is the noise created which is computed in subsection 8.1.3 and in case of exceeding the EASA limit, solutions are proposed in subsection 12.2.3. One final concern is the disposal of the system at the end of its life cycle. To avoid pollution, the team's objective is to recycle the retired vehicles as much as possible. According to a study conducted by Zhao et al. [10], the majority (800 - 1000 components) of retired vehicles can be repurposed through recycling, especially parts made with alloys like aluminum or titanium, or composites like carbon fibers. Additionally, other functional parts like landing gears or flaps can also be sold secondhand.

5.3.3. Economic Sustainability

In the first place, the market analysis created in chapter 3 indicates a high probability of earning profit from the XV-25 Griffin with annual revenue of approximately US$ 700 million. Noticeably, the current revenue is only based on the military market and there are other markets that with simple modifications, the XV-25 Griffin can soon become a competitor. Therefore, sustaining the project and examining the economic sustainability aspect is one of the priorities of the team. To achieve the long-term goal, the product should promote the economy surrounding it. In the case of the XV-25 Griffin, with the initial plan of centering the supply chain within Europe, it is expected to elevate the regional economy by creating jobs and manufacturing based on regional products.

In addition, the request for proposal, provided for a military customer by the VFS allows the assumption that the military will obtain a large amount of this type of aircraft [1]. This can draw the positive attention of the public and create a good effect when introducing the very first HS-VTOL vehicle into the market; thus, generating future funding for research, and possibly increasing the gross domestic product of every country joining the program.

---

[5] https://www.ilo.org/global/docs/WCMS_851377/lang--en/index.htm - 24/1/2023

6

Technical Risk Analysis

Any development of an engineering project will contain parts that are uncertain and could impact the operation of the resulting system. To deliver a successful final result, these uncertainties and risks need to be identified at an early stage and tracked during the entirety of the project's duration. The identified risks are presented in section 6.1. Following the identification mitigation strategies need to be worked out to reduce either the likelihood, the impact, or both of each risk. This tracking and managing of risks ensure that the project's completion has the highest probability of success possible.

6.1. Identified Risks

The risks for the aircraft are identified using a unique ID to be able to track them across time. Furthermore, each risk is assigned a probability that describes how likely it is that the event described by that risk occurs. The impact of each risk is described by the impact rating of each risk and specifies what the consequence of the event identified by each risk would have. These two parameters are each given on a scale from 1-5 as specified in Table 6.1 and Table 6.2.

Table 6.1: Risk Probability Scale

Score	Description	
1	Very low	$p < 5\%$
2	Low	$p < 15\%$
3	Medium	$p < 40\%$
4	High	$p < 60\%$
5	Very high	$p > 60\%$

Table 6.2: Risk Impact Scale

Score	Description
1	Negligible
2	Small performance reduction
3	Medium performance reduction
4	Large performance reduction
5	Mission failure

The risks identified with a small description including their probability and impact scores are documented in Table 6.3.

Table 6.3: Technical Risks

ID	Risk	Description	Probability	Impact
TR-1	Exceeding the structural margins	When flying at the edges of the structural envelope there might be points where a gust or the requirements to perform evasive maneuvers could push the aircraft past the structural margins, causing the breakup of the structure	4	5
TR-2	High-speed Rotor Flow Interference	During forward flight with the rotors activated there might be complex interactions between the downwash of the rotor, the wing as well as the engine intakes located under the rotor, causing reductions in lift or issues with the engines.	3	3
TR-3	Instability during transition	During transition a special maneuver needs to perform to allow the rotor to stop and transfer the lift responsibility to the wings, followed by the retraction of the blades	3	4
TR-4	Certification not granted	As this aircraft is a complicated hybrid between conventional airplanes and helicopters it is not certain under which certification regulations it would be assessed by the regulating agencies. This makes it uncertain which exact requirements need to be met	3	4

TR-5	Rotorblades collide with other components	During the rotor-powered flight, the blades of the rotor can move and bend to provide control forces as well as a result of gusts. This could lead to the rotor blades moving downwards far enough to contact other parts of the aircraft such as the wings or tail.	3	5
TR-6	Failure of hydraulics	As large parts of the control surfaces and swashplate are actuated through hydraulic actuators, the loss of hydraulics would mean the loss of control leading to a crash.	3	5
TR-7	Failure of fly-by-wire system	The fly-by-wire system is required to control the aircraft during the transition parts operational envelope. Failure of this system could in many situations lead to a loss of control	3	4
TR-8	Engine failure during transition	In case the engine fails during transition, the loss of thrust can interrupt that transition. The loss of power will thus, depending on the exact state of the aircraft, cause the loss of complete lift. Due to the low time spent transitioning this is considered to be a very low probability.	2	5
TR-9	Engine failure during hover	During hover, the entire lift of the aircraft is coming from the rotor powered by the engines, thus a failure of the engine might bring the aircraft to crash.	3	5
TR-10	Engine failure during cruise	During cruise an engine failure would turn the aircraft into a glider. However, depending on the landing gear it might not be possible to perform a typical aircraft landing instead of a vertical one.	4	5
TR-11	Rotor retraction mechanism jams	If the rotor retraction mechanism jams, this will not allow the rotor to be retracted into the wings and fuselage. This will result in the rotor staying exposed, causing large drag and preventing the achievement of the desired cruise speed. However, in the reverse case when trying to extend the rotor blades, landing as a rotorcraft will still be possible. During transition back to rotor craft, a landing will still be possible with reduced lift, due to the lower radius.	3	2
TR-12	Hub lowering mechanism jams	Similar to the failure of the hub lowering mechanism, this will prevent the nominal cruise. However, in contrast to the blade retraction mechanism, if this mechanism jams on the transition to rotorcraft a normal vertical landing is no longer possible	4	2
TR-13	Bird strike	A bird strike usually happens at low altitude, and can destroy the parts the bird hits, possibly causing a crash.	4	4
TR-14	Premature fatigue failure	If the operation environment and usage of the aircraft is not estimated correctly this can cause unforeseen numbers of load cycles to be applied to the structure, thus causing a premature breakup in flight.	3	5
TR-15	Jet blast damages surrounding equipment or personnel	The jet engines produce powerful jetblast that can damage both equipment and personnel that is working around the aircraft during takeoff or idle. This is especially important on cramped environments such as aircraft carriers.	4	3

TR-16	FOD Ingestion into engines	During operation in adverse environments there is the possibility of ingesting objects into the intakes of the engines generating suction. This will cause damage to the engines, possibly even making the engine fan, compressor or turbines shatter and cause damage to surrounding components.	3	4

All the risks identified are placed into a risk map to visualize the relative score of each risk. The risk map is shown in Figure 6.1.
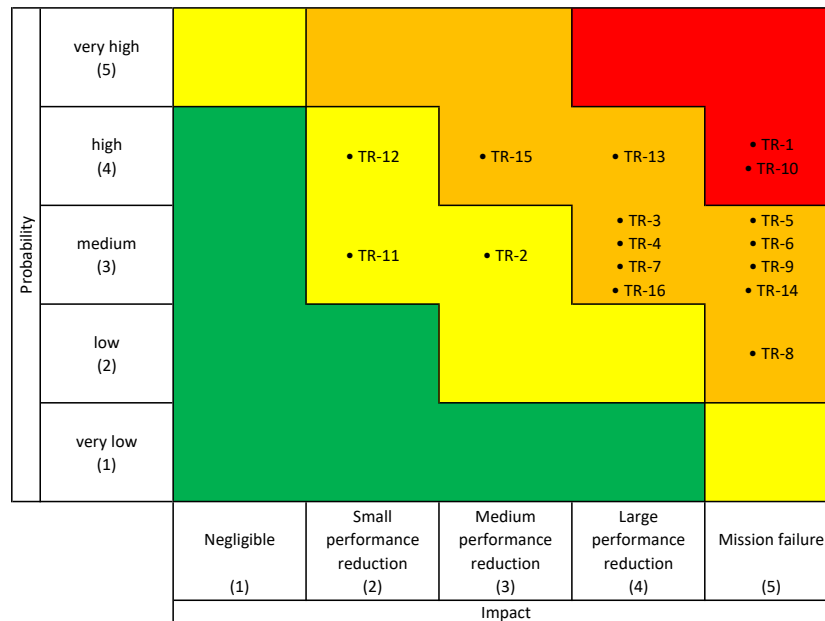
Figure 6.1: Risk Map before Mitigations

There are a number of risks in the upper right corner, having both a high probability with their impact resulting in large performance reductions or even mission failures. Thus, especially for these risks a mitigation strategy was developed to ensure the project becomes a successful aircraft with a high probability.

6.2. Mitigation strategy

For as many risks as possible a mitigation strategy is developed, that aims to reduce the probability or the impact, or both of that risk. These risks will then continue to be tracked in a risk map. During the development of the engineering project these risks will be monitored to ensure that none of these risks become too large and to monitor the implementation of the risk mitigation strategies. The mitigation strategies are documented in Table 6.4.

Table 6.4: Technical Risk Mitigations

ID	Mitigation	Reduced Probability	Reduced Impact
TR-1	Adding standard safety factors to the different components loaded by the flight loads ensures that even if the flight envelope is exceeded no immediate failure will occur. This reduces the probability of this risk dramatically	1	5

TR-2	To ensure this risk does not occur, thorough analysis on the flow fields around the wings, rotor and engine intake shall be performed using CFD and wind tunnel tests. This ensures an optimal design that minimizes performance losses of these components will be achieved	1	3
TR-3	A fly-by-wire system should implement different types of control laws depending on the flight state and simplify the controllability for the pilots. It should also allow for recovery of failed transitions. To aid in that, transition should only be attempted with enough altitude to recover from this failure, be it in helicopter or plane mode	2	3
TR-4	To ensure certification is as likely as possible, thorough research into the different types of certification categories that could apply to such aircraft as the XV-25 Griffin shall be performed. In addition, other vertical take-off planes should be investigated to gain a better understanding of the certification criteria. Once these are known, all the requirements set by these certification guidelines should be considered early in the design so they can be met.	2	4
TR-5	To ensure the rotor does not hit the tail, wing or other parts of the fuselage, sufficient stiffness of the blades, as well as a minimum distance between the rotor and potentially interfering components shall be defined. In addition, the flapping hinges allowing for the up and down movement of the blades shall have appropriate end stops set.	1	4
TR-6	Using redundant hydraulic circuits in such a layout that even if one circuit fails the aircraft stays controllable is a relatively simple way to mitigate the impact in case the hydraulic circuit does break.	3	3
TR-7	To prevent the fly-by-wire system to stop working due to singular issues with components, all sensors, computers and actuators will be laid out in a redundant fashion. This ensures that in case a component does fail the remaining parts can identify that and use the remaining good components to continue a safe flight.	3	2
TR-8	A failure of the engines during the transition can be mitigated by only transitioning at a sufficient altitude, that would allow the aircraft to start gliding by converting the altitude to velocity. In addition, for a safe recovery of the vehicle it needs to be designed to be able to perform a gliding landing.	2	3
TR-9	To ensure safety during an engine failure during hover, two engines are installed. Thus, enough power remains to perform an emergency landing using the single engine. In addition, if there is sufficient altitude or velocity allowing for autorotation or a gliding landing will further increase safety even in case both engines fail.	3	3
TR-10	A single engine failure during cruise will only reduce the cruise speed with two engines installed. In addition, transition and a vertical landing would become risky or impossible. Thus, the gear is designed for a horizontal landing like a conventional aircraft.	4	2
TR-11	-	3	2
TR-12	-	4	3
TR-13	To mitigate the risks of bird strikes the aircraft will be operated as little as possible in lower altitudes where birds are more common. In addition, the frontal surfaces as well as the engine intakes are designed to not sustain catastrophic damage that will cause the aircraft to crash.	2	3

TR-14	During deployment close monitoring of both the usage and the operational profile of the aircraft as well as the corresponding fatigue progression of the fatigue life limited components shall be implemented. This allows the correction of assumptions during design about the usage by the operators, thereby giving a better understanding of the recommended life of the parts. Monitoring the components also allows premature wear to be detected and to be corrected before it causes any issues during flight	1	5
TR-15	Preventing jet blast damage is achieved by using engine exhausts that are elevated at a sufficient level above the ground to gain clearance from most equipment on the ground. In addition, maintaining a cleared area for equipment behind the vehicle can prevent damage.	2	3
TR-16	Similar to the jet blast, the engine is placed at a certain height above the ground, which prevents most FOD to enter the engines. In addition, no personnel or equipment shall be allowed to enter the area in front of the engine intakes when the aircraft is running.	1	4

The risks are fitted into a new riskmap that visualizes the new state of the risks of the project with the mitigation plans incorporated. It is shown in Figure 6.2.
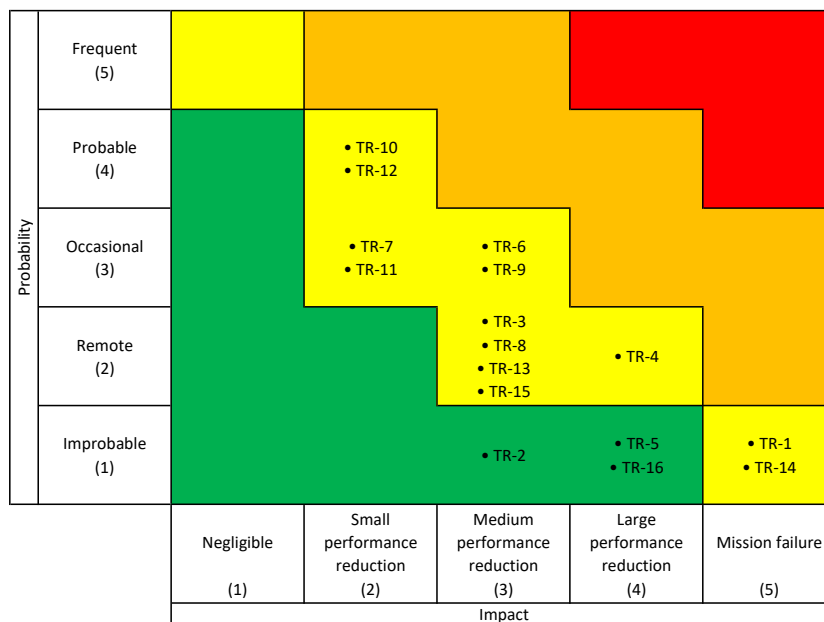
Figure 6.2: Risk Map After the Mitigation

It can be observed that there are no risks left in the orange area. However, not all risks are mitigated to an entirely satisfactory level, with many remaining at an intermediate level. These will be continuously monitored during the further development process to ensure they will no threaten the planned operation.

7

Design and Integration

To arrive at the final design all the different subsystems were integrated to perform the desired tasks. The results as well as the tools used to arrive at these results are presented in this chapter.

7.1. Detailed Design

The detailed designed has been established and showcased in Figure 7.1. This includes the key elements of the concept aircraft.
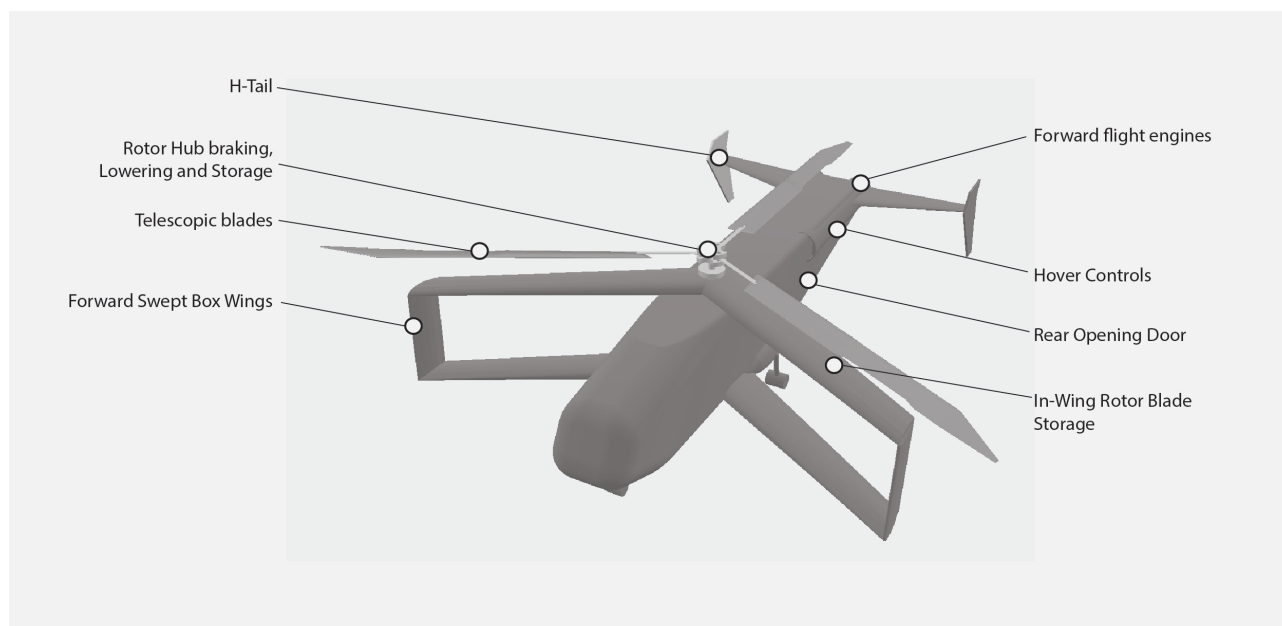
Figure 7.1: Detailed Design Concept

Telescopic Blades: During hover, the blades are fully extended in order to provide efficient hover and low down-wash. The specifics are determined in section 8.1. The blades are designed such that the outmost section can retract within the innermost section of the blade in a telescopic manner. The mechanism is showcased in section 10.7.

Forward flight engines: The engines provide the thrust required for cruise speed in forward flight. Furthermore, they allow the aircraft to reach transition velocity from hover. This allows the minimal downward pitch of the compound when the rotor is used. The specific engine is established in section 9.2.

Rotor Hub braking, Lowering and Storage: Once in flight with sufficient velocity, the wings of the aircraft generate lift. The Rotor is then slowed down proportionally to the lift generated from the wings until it completely stops in order to maintain level flight. Upon which the rotor hub system is disconnected. The rotor is fully stopped and locked in the desired position. The rotor hub is then lowered down into the fuselage. The mechanism is showcased in section 10.7.

Forward Swept Box Wings: The wings are swept forward in order to store the rotor blades within, such that they are fully concealed while reaching cruise speed. Furthermore, the box wing allows the rotor blades to function with reduced impact from the wing area required for flight. Flaps are placed in order to further minimize the perceived area of the wing when fully deflected for hover. The specifics are determined in section 8.2.

In-Wing Rotor Blade Storage: Simultaneously, as the main rotor hub has been lowered into the fuselage, the rotor blades are lowered into the wings. The rotor blades are then concealed under retractable skin doors for cruise flights. This mechanism is developed in section 10.7.

Hover Controls: During Hover, the Griffin makes use of a conventional swash plate to allow pilot inputs to be translated into vehicle motions. In order to control the yaw axis of the aircraft in addition to counteract the torque generated by the main rotor, high-pressure gas is diverted from the engine bypass to the tail of the aircraft. The controls are described in section 11.1.

H-Tail: The compound has an unconventional H-Tail in order to provide conventional aircraft controls once the airspeed is sufficient. The H-Tail has a lowered Vertical Stabilizer in order to provide additional clearance from the rotor blades. The H-Tail provides static stability in the longitudinal and lateral directions.

Rear Opening Door: The payload bay is easily accessible from the rear of the aircraft. This allows cargo bay access to large-volume elements within the payload limit.

7.2. Operation and Logistics Concept Description, Mission Analysis

Ground Operations: In terms of ground operations, the XV-25 Griffin is no different than any other conventional helicopter. Because the fixed wings are entirely underneath the main rotor, the ground footprint is no different than a conventional helicopter of similar size. Additionally, the ground crew is protected from the main rotor, as it is placed high above the ground and there is no hazard of the engines for inspecting, loading, and unloading the aircraft while in operation, as the engines are positioned high above the cargo compartment. Similarly, there is no danger of injuries due to the lack of a tail rotor.

Taxi, Hover, Takeoff and Landing: As the XV-25 Griffin has a relatively low disk loading, there is no need for special provisions for the protection of life around the vehicle, as people and objects should not face any issues standing near the vehicle when taxiing on the ground, hovering, or departing. Any operations in compound mode are done with the wing flaps set to the fully deflected position in order to reduce the download factor from the wing area under the rotor. Due to the low induced velocity of the rotor, operation above dirt, water, or sand is possible. Because of the lack of a tail rotor, the risk of VRS (Vortex-Ring State) of the tail rotor due to crosswinds or main rotor turbulence is eliminated.

Acceleration and Transition: When accelerating in compound mode, the angle of attack is kept constant at $3°$ in order to have the optimal angle for the fixed wings to generate lift, in order to improve efficiency and be able to unload the rotor as soon as possible. At a velocity of 135 kts the wings are able to support the vehicle entirely, hence at that speed the rotor is disengaged from the engines and slowed down for storage. At 150 kts the rotor is fully stopped and stowed into the upper wing.

Climb and Cruise: As the aircraft has very powerful engines to support hover, all the excess power provides an exceptional rate of climb in fixed-wing flight as described in section 9.5. That means that the XV-25 is able to get up to cruising altitude in a very short time and then cruise efficiently at that altitude.

Descent: The main drawback of steep, rapid descent using the rotor system is the susceptibility of the rotor to VRS (Vortex-Ring State). Considering the non-dimensional horizontal velocity V_H/V_{ind_h} and non-dimensional vertical velocity V_Z/V_{ind_h} Basset et. al. [11] the region of VRS susceptibility varies approximately from $0 \leq V_H/V_{ind_h} \leq 1$ and $-2 \leq V_Z/V_{ind_h} \leq 0$. Having a relatively low disk loading, but still higher than a vast number of conventional helicopters, the risk of encountering VRS occurs at very steep descents at relatively low speeds. Thus, it is recommended to avoid such operations as much as possible and thoroughly assess the characteristics of a possible Vuichard recovery from VRS.

Pilot Training: As indicated in chapter 11, operations at speeds up to 65kts are no different than flying a conventional helicopter and the aircraft is dynamically stable until transition. Furthermore, after transitioning into the fixed-wing flight, the aircraft can operate as a conventional airplane that is stable. For that reason, any pilot trained in helicopters should be able to operate the XV-25 Griffin with minimal additional training, as any differences encountered with a conventional helicopter are only at cruise, which is not a demanding phase of flight in terms of handling. Emphasis should be placed on emergency landings in fixed-wing mode as the approach and landing speed are rather high and the placement of the landing gear is not favorable for high-pitch

angles.

Storage: When the main rotor is stowed into the upper wing, the footprint of the helicopter is the lowest and similar to a small to a medium-sized airliner. For that reason, parking and storage are possible at any conventional aircraft stand, or even off the field.

Overweight Operations: In principle, the XV-25 is not able to hover when the loaded mass exceeds the maximum take-off mass, due to power limitations. However, the possibility of performing a running take-off from a runway by tilting the rotor tip-path-plane forward using cyclic on the ground to accumulate speed exists for overweight departures. This can work because the power required at speed is much lower than the power required at hover. However, as the landing gear is not positioned to allow for excessive rotation angles, takeoff using flaps is recommended in order to be able to lift without rotating the body of the craft. Using rough estimates, the forward thrust that can be produced using this method is $19800 lbf$ ($88kN$), easily enough to accelerate the XV-25 Griffin forward. Using this technique, the MTOM can be increased by approximately $5200 lbs$ ($2400kg$).
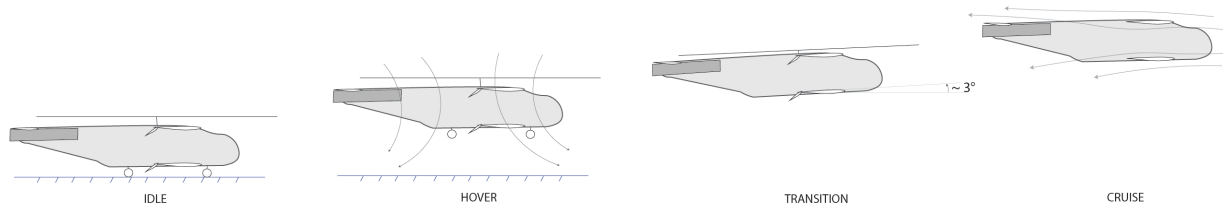
Figure 7.2: Flight Mode Diagram

7.3. Functional Analysis

To show the logical order of functions from systems and sub-systems, a Functional Flow Diagram (FFD) was created and described in subsection 7.3.1. In addition, a Functional Breakdown Structure (FBS) is illustrated in subsection 7.3.2 to represent the hierarchy of functions within the system.

7.3.1. Functional Flow Diagram

The FFD helps the team gain a better understanding of the functionality of the system from the top-level functionality all the way down to the functionality of detailed sub-systems where each function has a unique identifier. As can be seen in Figure 3.1, the system functionality is described in the sub-tree "Perform Mission", the design and production process is described in the "Provide Aircraft" sub-tree and the end-of-life process is described in the "Disposal" sub-tree. The top-level functions in the "Perform Mission" sub-tree are taken from the mission profile and are then expanded, in chronological order, into more detailed functions which must be performed in order to be able to complete the top-level function. This diagram provided a detailed description of the system functionality which the team can always look back on to gain a clearer bird's-eye-view of the system.

7.3.2. Functional Breakdown Structure

The FBS presents an overview of the system functions in a similar manner to the FFD. However, the FBS presents a hierarchical categorization, showing all the sub-functions which the main functions can be divided into.

The main functions are the design, construction, disposal of the aircraft, mission fulfillment, and safety guarantee. The main functions are presented filled with light green and the sub-functions are presented in different levels, colored in red, yellow, and white as the levels progress to finer detail. The use of arrows was avoided in the lower details to prevent the cluttering of the diagram.

The FBS provided the team with a good high-level overview of all the functions the system needs to perform. The FBS, together with the FFD, proved to be invaluable tools to clarify the task at hand and complete the other sections of the report.

Legend
- Top level functions
- Level 1
- Level 2
- Level 3

Provide Aircraft 1.0 — **Perform Mission 2.0**

Define Mission 1.1 — Design Aircraft 1.2 — Produce Aircraft 1.3

Define Mission 1.1 — Determine Mission Statement 1.1.1 — Determine Stakeholders 1.1.2 — Determine Requirements 1.1.3

Determine Mission Statement 1.1.1 — Analyze request for proposal 1.1.1.1 — Formulate Mission Statement 1.1.1.2

Determine Stakeholders 1.1.2 — Determine Customers 1.1.2.1 — Determine auxiliary stakeholders 1.1.2.2

Determine Requirements 1.1.3 — Define Mission Requirements 1.1.3.1 — Define System Requirements 1.1.3.2 — Define Sub-System Requirements 1.1.3.3

Design Aircraft 1.2 — Conceptual Design 1.2.1 — Preliminary Design 1.2.2 — Detailed Design 1.2.3 — Verify and Validate 1.2.4

Conceptual Design 1.2.1 — Generate Concepts 1.2.1.1 — Perform Trade-Off 1.2.1.2 — Choose best concept 1.2.1.3

Preliminary Design 1.2.2 — Perform Preliminary Sizing 1.2.2.1 — Perform Preliminary Sub-System Design 1.2.2.2 — Analyse Preliminary Design 1.2.2.3

Detailed Design 1.2.3 — Finalize Sub-System Design 1.2.3.1 — Integrate Sub-Systems 1.2.3.2 — Iterate over design to optimise 1.2.3.3

Verify and Validate 1.2.4 — Perform V & V on analysis Tools 1.2.4.1 — Verify all requirements are met 1.2.4.2

Produce Aircraft 1.3 — Generate Production Plan 1.3.1 — Create Production Facility 1.3.2 — Produce Aircraft 1.3.3 — Test Product 1.3.4

Dispose of Aircraft 3.0

Disassemble 3.1 — Reuse 3.2 — Scrap 3.3

Disassemble 3.1 — Seperate into subsystems 3.1.1 — Test performance of subsystems 3.1.2 — Reuse subsystem 3.1.3 — Disassemble subsystem into parts 3.1.4 — Test performance of parts 3.1.5 — Reuse parts 3.1.6 — Dispose of parts 3.1.7

Reuse 3.2 — Put system/part into storage 3.2.1 — Assemble into existing aircraft 3.2.2

Scrap 3.3 — Seperate into materials where possible 3.3.1 — Recycle materials 3.3.2 — Discard the rest 3.3.3

Perform Mission 2.0

Enable pre flight loading 2.1 — VTOL take off 2.2 — Hover in ground effect 2.3 — Cruise at 450 kt, 20k ft 2.4 — Hover out of ground effect 2.5 — Vertical Landing 2.6

Enable pre flight loading 2.1 — Load payload 2.1.1 — Load fuel 2.1.2 — Crew Boarding 2.1.3 — Assess aircraft condition 2.1.4

Load Payload 2.1.1 — open payload bay 2.1.1.1 — Move payload onboard 2.1.1.2 — Fasten payload 2.1.1.3

Load fuel 2.1.2 — Check level 2.1.2.1 — Fill fuel 2.1.2.2 — Check level 2.1.2.3

Crew Boarding 2.1.3 — Allow boarding 2.1.3.1 — Provide seating 2.1.3.2

Assess aircraft condition 2.1.4 — Check engine condition 2.1.4.1 — Check control surface function 2.1.4.2 — Visual inspection 2.1.4.3

VTOL take off 2.2 — Startup aircraft 2.2.1 — Create vertical thrust 2.2.2 — Maintain stability in vertical flight 2.2.3

Startup aircraft 2.2.1 — Startup energy source 2.2.1.1 — Establish communication with ATC 2.2.1.2

Create vertical thrust 2.2.2 — Provide power 2.2.2.1 — Transmit power/torque to lift device 2.2.2.2

Maintain stability in vertical flight 2.2.3 — Provide attitude and position feedback 2.2.3.1 — Adjust lift distribution 2.2.3.2

Hover in ground effect 2.3 — and — Maintain Stability in Hover 2.3.1 — Maneuver 2.3.2

Maintain Stability in Hover 2.3.1 — Maintain straight flight 2.3.1.1

Maneuver 2.3.2 — Control Thrust vector 2.3.2.1 — Give pilot control over thrust vectoring 2.3.2.2

Cruise at 450 kt, 20k ft 2.4 — Transition to forward flight 2.4.1 — and — Maintain stability at high speed 2.4.2 — Maneuver 2.4.3 — Navigate 2.4.4

Transition to forward flight 2.4.1 — Translate vertical thrust to forward thrust 2.4.1.1 — Create lift to replace vertical thrust 2.4.1.2 — and — Accelerate to cruise speed 2.4.1.3 — Climb to cruise altitude 2.4.1.4

Maintain stability at high speed 2.4.2 — Maintain Steady/Straight Flight 2.4.2.1 — Trim out aircraft 2.4.2.2

Maneuver 2.4.3 — Ensure adequate control surfaces on wing 2.4.3.1 — Give pilot control over control surfaces (e.g. fly by wire) 2.4.3.2

Navigate 2.4.4 — Avoid obstacles 2.4.4.1 — Maintain heading 2.4.4.2 — Maintain altitude 2.4.4.3 — Avoid traffic 2.4.4.4

Hover out of ground effect 2.5 — Transition to Vertical flight 2.5.1 — and — Maintain Stability in Hover 2.5.2 — Maneuver 2.5.3

Transition to Vertical flight 2.5.1 — Descend to transition altitude 2.5.1.1 — Decelerate to transition speed 2.5.1.2 — Translate forward thrust to vertical thrust 2.5.1.3 — Decelerate to 0 forward speed 2.5.1.4

Maintain Stability in Hover 2.5.2 — Maintain straight flight 2.5.2.1

Maneuver 2.5.3 — Control Thrust vector 2.5.3.1 — Give pilot control over thrust vectoring 2.5.3.2

Vertical Landing 2.6 — Reduce vertical thrust 2.6.1 — Deploy Landing Gear 2.6.2 — Land 2.6.3 — Shut down aircraft 2.6.4

Reduce vertical thrust 2.6.1 — Reduce engine power 2.6.1.1

Deploy Landing Gear 2.6.2 — Open landing gear doors 2.6.2.1 — Extend Landing Gear 2.6.2.2 / 2.5.3.1

Land 2.6.3 — Absorb landing loads 2.6.3.1 — Stop movement 2.6.3.2

Shut down aircraft 2.6.4 — Follow aircraft shutdown procedure 2.6.4.1

Design, build and dispose of aircraft

Define Mission (1.1)
- Determine Mission Statement (1.1.1)
  - Analyze request for proposal (1.1.1.1)
  - Formulate Mission Statement (1.1.1.2)
- Determine Stakeholders (1.1.2)
  - Determine Customers (1.1.2.1)
  - Determine auxiliary stakeholders (1.1.2.2)
- Determine Requirements (1.1.3)
  - Define Mission Requirements (1.1.3.1)
  - Define System Requirements (1.1.3.2)
  - Define Sub-System Requirements (1.1.3.3)

Design Aircraft (1.2)
- Conceptual Design (1.2.1)
  - Generate Concepts (1.2.1.1)
  - Perform Trade-Off (1.2.1.2)
  - Choose best concept (1.2.1.3)
- Preliminary Design (1.2.2)
  - Perform Preliminary Sizing (1.2.2.1)
  - Perform Preliminary Sub-System Design (1.2.2.2)
  - Analyse Preliminary Design (1.2.2.3)
- Detailed Design (1.2.3)
  - Finalize Sub-System Design (1.2.3.1)
  - Integrate Sub-Systems (1.2.3.2)
  - Iterate over design to optimise (1.2.3.3)
- Verify and Validate (1.2.4)
  - Perform V & V on analysis Tools (1.2.4.1)
  - Verify all requirements are met (1.2.4.2)

Produce Aircraft (1.3)
- Generate Production Plan (1.3.1)
- Create Production Facility (1.3.2)
- Produce Aircraft (1.3.3)
- Test Product (1.3.4)

Dispose of Aircraft (3.0)
- Disassemble (3.1)
  - Seperate into subsystems (3.1.1)
  - Test performance of subsystems (3.1.2)
  - Reuse subsystem (3.1.3)
  - Disassemble subsystem into parts (3.1.4)
  - Test performance of parts (3.1.5)
  - Reuse parts (3.1.6)
  - Dispose of parts (3.1.7)
- Reuse (3.2)
  - Put system/part into storage (3.2.1)
  - Assemble into existing aircraft (3.2.2)
- Scrap (3.3)
  - Seperate into materials where possible (3.3.1)
  - Recycle materials (3.3.2)
  - Discard the rest (3.3.3)

Perform Mission (2.0)

Enable pre flight loading (2.1)
- Load Payload (2.1.1)
  - Open Payload Bay (2.1.1.1)
  - Move Payload Onboard (2.1.1.2)
  - Fasten Payload (2.1.1.3)
- Load Fuel (2.1.2)
  - Check Level (2.1.2.1)
  - Fill Fuel (2.1.2.2)
  - Check Level (2.1.2.3)
- Crew Boarding (2.1.3)
  - Allow Boarding (2.1.3.1)
  - Provide Seating (2.1.3.2)
- Assess Aircraft Condition (2.1.4)
  - Check Engine Condition (2.1.4.1)
  - Check Control Surface Function (2.1.4.2)
  - Visual inspection (2.1.4.3)

VTOL take off (2.2)
- Startup Aircraft (2.2.1)
  - Startup Energy Source (2.2.1.1)
  - Establish Communication with ATC (2.2.1.2)
- Create Vertical Thrust (2.2.2)
  - Provide Power (2.2.2.1)
  - Transmit Power/Torque to Lift Device (2.2.2.2)
- Maintain Stability in Vertical Flight (2.2.3)

Hover in ground effect (2.3)
- Maintain Stability in Hover (2.3.1)
  - Maintain straight flight (2.3.1.1)
- Maneuver (2.3.2)
  - Control Thrust vector (2.3.2.1)
  - Give pilot control over thrust vectoring (2.3.2.2)

Cruise at 450 kt, 20k ft (2.4)
- Transition to Forward Flight (2.4.1)
  - Translate vertical thrust to forward thrust (2.4.1.1)
  - Create lift to replace vertical thrust (2.4.1.2)
  - Accelerate to cruise speed (2.4.1.3)
  - Climb to cruise altitude (2.4.1.4)
- Maintain Stability in Forward Flight (2.4.2)
  - Maintain Steady/Straight Flight (2.4.2.1)
  - Trim out aircraft (2.4.2.2)
- Maneuver (2.4.3)
  - Ensure adequate control surfaces on wing (2.4.3.1)
  - Give pilot control over control surfaces (e.g. fly by wire) (2.4.3.2)
- Navigate (2.4.4)
  - Avoid obstacles (2.4.4.1)
  - Maintain heading (2.4.4.2)
  - Maintain altitude (2.4.4.3)
  - Avoid traffic (2.4.4.4)

Hover out of ground effect (2.5)
- Reduce Vertical Thrust (2.5.1)
  - Descend to transition altitude (2.5.1.1)
  - Decelerate to transition speed (2.5.1.2)
  - Translate forward thrust to vertical thrust (2.5.1.3)
  - Decelerate to 0 forward speed (2.5.1.4)
- Maintain Stability in Hover (2.5.2)
  - Maintain straight flight (2.5.2.1)
- Maneuver (2.5.3)
  - Control Thrust vector (2.5.3.1)
  - Give pilot control over thrust vectoring (2.5.3.2)

Vertical Landing (2.6)
- Transition to Vertical Flight (2.6.1)
  - Reduce engine power (2.6.1.1)
- Deploy Landing Gear (2.6.2)
  - Open landing gear doors (2.6.2.1)
  - Extend Landing Gear (2.6.2.2)
- Land (2.6.3)
  - Absorb landing loads (2.6.3.1)
  - Stop movement (2.6.3.2)
- Shut down aircraft (2.6.4)
  - Follow aircraft shutdown procedure (2.6.4.1)

Guarantee Safety (4.0)

Guarantee Aircraft Safety (4.1)
- Detect internal failures (4.1.1)
- Maintain Weather Awareness (4.1.2)
- Avoid threats (4.1.3)
  - Detect Threats (4.1.3.1)
  - Fly at threat avoidance altitude (4.1.3.2)
- Mitigate Potential risks (4.1.4)
- Ensure redundancy of critical components (4.1.5)
- Maintain stability through all fly phases (4.1.6)

Maintain Subsystem Integrity (4.2)
- Powerplant (4.2.1)
  - Provide Emergency Power (4.2.1.1)
  - Mitigate engine failure (4.2.1.2)
  - Restart engine in flight (4.2.1.3)
  - Automatically disengage failed engine (4.2.1.4)
  - Detect fuel tank and lines ruptures and leaks (4.2.1.5)
  - Mantain flight condition in case of one engine failure (4.2.1.6)
  - Maintain thermal balance (4.2.1.7)
  - Provide hydraulic power (4.2.1.8)
  - Provide electrical power for instrumentation and devices (4.2.1.9)
- Structure (4.2.2)
  - Monitor vibrations (4.2.2.1)
  - Avoid resonance (4.2.2.2)
  - Guarantee structural integrity (4.2.2.3)
  - Transfer loads from propulsion unit, landing gear, wings or rotors, etc to airframe (4.2.2.4)

Guarantee Crew Safety (4.3)
- Maintain Crew Support Systems (4.3.1)
- Perform safe emergency landing when required (4.3.2)
- Enable pilot control (4.3.3)
  - Display flight information to pilots (4.3.3.1)
  - Alert of emergencies (4.3.3.2)
  - Perform Communications (4.3.3.3)
  - Integrate with air traffic control (4.3.3.4)

Guarantee Ground Crew and Assets Safety (4.4)
- Minimize noise at landing and take-off (4.4.1)
- Avoid FOD (4.4.2)
  - Preserve ground integrity at site (4.4.2.1)
- Minimize downwash (4.4.3)
- Integrate with existing ground infrastructure (4.4.4)

Facilitate Maintenance (4.5)
- Facilitate component inspection (4.5.1)
- Facilitate accessibility to subsystems (4.5.2)

Legend
- Top level functions
- Level 1
- Level 2
- Level 3

8

Aerodynamics

To assure that the XV-25 Griffin can properly execute the mission profile, the aerodynamics aspect of the aircraft has to be examined carefully. Aerodynamics also plays an essential role in predicting the performance of the aircraft and selecting a suitable engine. This chapter is dedicated to studying the rotary wing system for the VTOL operation and the fixed-wing system that will be used during cruise. The structure of this chapter is as follows: first, section 8.1 focuses on the rotor blades; second, section 8.2 explains the fixed-wing configuration which includes the wing planform, the airfoil, lift and drag estimations; finally, the verification and validation procedures are reported in section 8.3.

8.1. Rotary Wing Analysis

This section details the rotor blade design process which is the most crucial component to performing the VTOL operation. The rotor blades have to be carefully designed in order to meet the requirements outlined in chapter 4. The preliminary rotor design is recapped in subsection 8.1.1. Blade design which includes the blade twist and airfoil selection per section are shown in subsection 8.1.2. The noise created by the blades is estimated in subsection 8.1.3.

8.1.1. Preliminary Rotor Design

The first step in designing the rotor is to perform a preliminary sizing from which the radius, chord length, number of blades, and rpm of the rotor.

As a first step, a disk loading (DL) must be assumed to then calculate the required blade radius as per Equation 8.1 (T=W). After this, the rotational speed of the rotor can be calculated with an assumed maximum Mach number at the tip of 0.95 with Equation 8.2 which can then be used to calculate the never exceed advance ratio ($\mu_{V_{NE}}$) with Equation 8.3 where V_{NE} can be assumed to be equal to the transition speed as specified in section 2.2.

$$R = \sqrt{\frac{T}{DL \cdot \pi}} \qquad (8.1) \qquad \Omega = \frac{M_{tip} \cdot c - V_{max}}{R} \qquad (8.2) \qquad \mu_{V_{NE}} = \frac{V_{NE}}{\Omega R} \qquad (8.3)$$

With the advance ratio calculated, a value of $\frac{C_T}{\sigma}$ of 0.16 can be estimated based on statistics. This value can now be used to calculate the blade solidity, σ with the equations below considering $T = k_{download} \cdot W$ where the value of the download factor can be taken from subsection 9.1.1.

$$\sigma = \frac{C_T}{\frac{C_T}{\sigma}} \qquad (8.4) \qquad C_T = \frac{T}{\rho \cdot \pi \cdot (\Omega R)^2} \qquad (8.5)$$

With the value of the blade solidity calculated, the number of blades can be found based on an iterative process with the constraints being the aspect ratio of the blade having to be larger than 14 to prevent aerodynamic losses while having to be lower than 20 to prevent structural integrity issues.

$$c_{const} = \frac{\sigma \cdot \pi \cdot R}{n_{blades}} \qquad (8.6) \qquad AR = \frac{R}{c_{const}} \qquad (8.7)$$

Table 8.1: Preliminary Sized Parameters of the Rotor

Disk Loading	Number of Blades	Blade Radius	Constant Chord	Aspect Ratio
DL	n_{blades}	R	c_{const}	AR
lbs/ft^2 (N/m^2)	-	ft (m)	ft (m)	-
13 (622)	3	40.7 (12.4)	2.6 (0.8)	15.5

8.1.2. Blade Design

Blade design for the rotor of a compound aircraft involves balancing a lot of factors to optimize performance. The rotor blades for these aircraft need to be designed to be efficient both in hovering and high-speed forward flight. One of the key considerations in blade design for compound aircraft is aerodynamics. The blades need to be designed to provide lift and minimize drag in both hover and forward flight. However, the XV-25 Griffin has a telescopic mechanism that retracts the blades and stores them within the upper wing of the Prandtl box wing after a transition speed of 150 kts. This allows the team to focus more on optimizing the blade for hover rather than high-speed forward flight.

Blade Twist

Blade twist in helicopter rotors is crucial for hover efficiency as it helps to optimize the lift distribution across the rotor blade. The blades of a helicopter rotor are twisted so that the angle of attack is less at the tip of the blade than at the root. This helps reduce the induced drag at the blade's tip, improving the rotor system's overall efficiency. To optimize for hover flight, the ideal twist curve should be followed, which dictates the local blade pitch based on the percentage of the radius length.
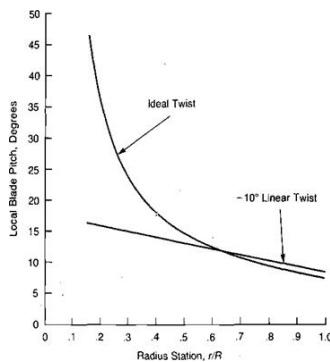
Figure 8.1: Ideal Blade Twist Curve[12]
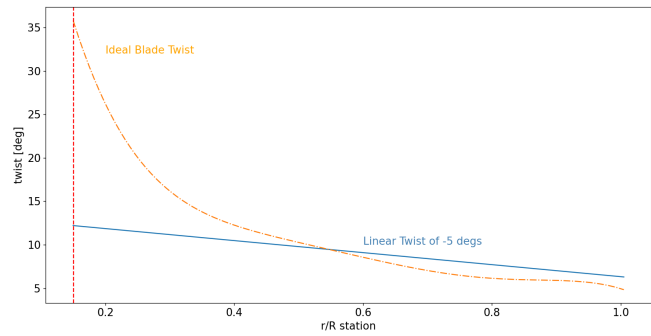
Figure 8.2: Linear Twist at -5°

However, implementing an ideal twist in a rotor blade leads to a few problems. One of the main issues is that it can increase the structural loads on the blade, which can cause it to fail more quickly. Moreover, the manufacturing process for blades with an ideal twist is more complex and costly. Hence, many helicopter manufacturers use linear twists across the blades to achieve a reasonable balance in performance between hover and forward flight. Similarly, a $-5°$ linear twist was chosen for XV-25 Griffin and is presented in Figure 8.2 along with the ideal twist curve. The equation for the ideal twist curve was estimated by fitting a 6-degree polynomial over Figure 8.1 where y is the local blade pitch in degrees and x is the radius station (r/R). The vertical line in Figure 8.2 is set at 15% of the radius where the airfoil of the blade starts.

$$y = 21.865 \cdot x^6 - 897.13 \cdot x^5 + 2801.6 \cdot x^4 - 3519.1 \cdot x^3 + 2185 \cdot x^2 - 687.58 \cdot x + 100.29 \qquad (8.8)$$

The next step was to estimate the pitch of the blade at the tip (θ_t). Raymond Prouty presents a formula in the book "Helicopter Performance, Stability, and Control" that calculates θ_t as a function of the thrust coefficient, blade solidity, and slope of the lift curve per radians [12].

$$\theta_t = 57.3 \cdot \left(\frac{4}{c_{l_\alpha}} \cdot \frac{C_T}{\sigma} + \sqrt{\frac{\sigma \cdot \frac{C_T}{\sigma}}{2}} \right) \quad [\text{deg}] \qquad (8.9)$$

The C_{l_α} for most airfoils is very similar and estimated to be equal to 5.73 per radians [12]. However the C_T & σ can be calculated based on Equation 8.10 and Equation 8.11 respectively.

$$C_T = \frac{T_{rotor}}{\rho \cdot A_{disk} \cdot (\Omega \cdot R)^2} \qquad \begin{cases} T_{hover} = (1 + k_{download}) \cdot MTOW \\ T_{max\ allowed} = (1 + k_{download} + 0.18) \cdot MTOW \end{cases} \qquad (8.10)$$

$$\sigma = \frac{A_{blade}}{A_{disk}} \tag{8.11}$$

Since the aircraft has wings placed under the rotor, it is important to account for the download factor ($k_{download}$) which was taken to be 0.11 based on the reasoning in subsection 9.1.1. This means that the thrust required for hover is 0.11 times the aircraft weight as seen in Equation 8.10. Moreover, by changing the collective angle of the blades, an extra thrust equivalent to 18% of MTOW can be produced. Nevertheless, due to the large radius of the blades and a relatively large C_T/σ value, the pitch angle at the blade tip was very large and increased towards the hub. Therefore, a θ_t of 6.3° was manually set for hover. This along with a linear twist of -5° resulted in a pitch angle at the hub (θ_0) of 13.2° for hover.

Airfoil Selection

Unlike the wing of an aircraft, the helicopter blade must adapt to a wide range of airspeeds and angles of attack during each revolution of the rotor. Symmetrical airfoils provide acceptable performance under these alternating conditions. They are also easier to manufacture and therefore cost less. This is the main reason why many helicopters in the early days of helicopter flight, used symmetrical airfoils. However, they tend to produce a lot of drag and have a lower lift-to-drag ratio in comparison to their non-symmetrical counterpart. There are three main criteria to consider while choosing an airfoil for the rotor blades [12].

- Low pitching moment to minimize the torsion moments and control loads on the blade.
- Low drag at moderate lift coefficients to minimize the power in normal flight.
- High drag divergence Mach number to allow flight at high advancing tip Mach numbers without prohibitive power losses or noise.

Since no single airfoil is considered optimum along the span of a blade, the blade was split into 4 different sections as seen in Figure 8.3 to meet the requirements above [12].
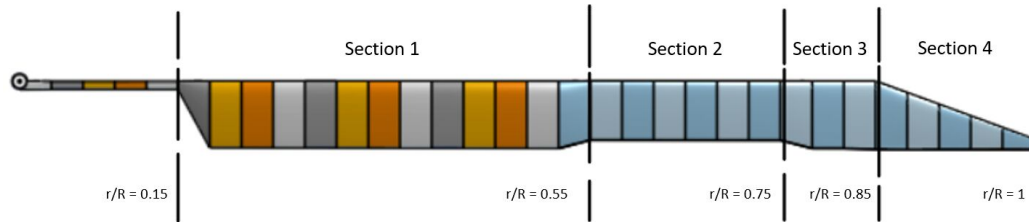
Figure 8.3: Sections of the Rotor Blade.

The airfoil only starts at 15% of the blade radius as the flapping hinge is located at that point. The first section of the blade ranges from 15% to 55% of the blade radius. This is also the section with the highest twist and pitch angle but has a relatively low speed in comparison to the outer portion of the blade. Hence an airfoil with a high $C_{l_{max}}$ value was required while also limiting its moment coefficient C_m. The drag divergence was not a leading factor in the selection of an airfoil for this section. Another important requirement for the first section was the thickness. It had to be thick enough to house the telescopic mechanism and the other sections of the blade after the transition speed was reached. A few airfoils were selected as potential candidates for the first section, namely the Boeing-Vertol V43012-1.58, Boeing-Vertol VR-7, and ONERA/Aerospatiale OA213. These airfoils were also examined by ONERA and SNIAS in 1974 as part of a joint research program [13]. It was seen that the OA213 airfoil performed best overall by having a relatively high value for drag divergence Mach number of 0.75, a low drag coefficient, and a moment coefficient of less than 0.01. Similarly, the Boeing-Vertol VR-7 airfoil also had a M_{dd} higher than 0.7 and a $C_{m_{0.25}}$ less than 0.02. Nevertheless, neither of these airfoils could produce enough C_l at low speeds. Therefore, the Boeing-Vertol V43012-1.58 airfoil, which had a $C_{l_{max}}$ of 1.7 at M = 0.3 and a Reynolds number of 6.5 million, was chosen for the first section of the blade. The maximum thickness to chord ratio was increased from 12% to 14.42% and a chord length of 0.825 was set in order to house the other sections. However, this came with an extremely low M_{dd} of about 0.65 which limited the length of the section to only 55% of the radius.

The second section of the blade lies between 55% to 75% of the blade radius. With a rotational speed of almost 187 rpm or $\omega = 19.6$ rads/sec and a maximum forward speed of 150 kts, the highest speed achieved by the second section is 0.75 Mach at 2000 ft. Much like the UH-60A Black Hawk helicopter, the SC1094-R8 airfoil was used for the middle section of the blade. At a Reynolds number of 8.5 million and the previously mentioned Mach number, the airfoil showed excellent performance with a C_d value of less than 0.01 before the stall angle at $12°$, a smaller $C_{m_{0.25}}$ value than V43012 and a M_{dd} of 0.78 [14]. It is important to note that the t/c_{max} for the airfoil was reduced from 9.4% to 8% for telescopic purposes. This reduced the $C_{l_{max}}$ from 1.6 to 1.4 at an angle of attack of $12.5°$. The reduction in C_l is not considered a big loss as the maximum twist angle in section 2 at hover is $9.4°$ which is almost $3°$ less than its stall angle and the twist only decreases as the r/R increases.

The airfoil chosen for the 3rd section of the blade was also taken from the UH-60A Black Hawk. The highest speed achieved by this section of the blade is 0.82 Mach at transition speed. Hence the SC1095 Sikorsky airfoil was used as it has a drag divergence Mach number of 0.82 [14]. It also has a very low moment coefficient of less than 0.02 in addition to a C_d value of 0.01 below the stall angle of $10°$. Once again, this is not a problem as the highest twist angle for this section is $8°$ which is still in the linear part of the C_l/α curve. Similar to the second section, the t/c_{max} ratio was changed from 9.5% to 8% to allow this section to fit inside the 1st section of the blade. Reducing the thickness-to-chord ratio of the airfoil lowers the $C_{l_{max}}$ and the stall angle to 1 and 9.8 deg respectively from the original $C_{l_{max}}$ of 1.14 and a stall angle of $11.2°$.

Finally, 3 different airfoils were considered for the last 15% of the blade. Since the radius of the blade is on the upper side of the helicopter blade radius spectrum, the high M_{dd} value was the leading factor in the choice of an airfoil. Onera OA206, OA207, and Boeing Vertol VR-7 were the 3 airfoils chosen for the 4th section. All three of these airfoils showed a very low value for the drag and moment coefficient at around 0.01. This left the M_{dd} to be the deciding factor, and the OA206 airfoil had the highest drag divergence Mach number of about 0.9 [15]. However, a leading edge sweep was added to the section to reduce the velocity experienced by that section from 0.93 Mach to below the M_{dd}. The t/c_{max} ratio also had to be altered to 8% to have a uniform lift distribution over the blade which will be discussed in more detail in Figure 8.1.2 along with the leading edge sweep.

Lift Distribution Over The Blade

The blade element method was used to estimate the lift distribution over the blade. The blade was first split into 124 dr sections of 0.1 m each. Next, the lift produced by a dr section at a given radius r and for a given chord length was calculated by estimating its rotational speed and simply using the lift formula in Equation 8.12. Similarly, the drag was calculated from C_d where C_{d_0} was extracted from the airfoil using Javaprop, the Oswald efficiency factor was set at 0.8, and C_d was calculated with Equation 8.13. This was done for all dr sections along the span.

$$L_{dr} = C_l \cdot \frac{\rho \cdot (\Omega \cdot r)^2 \cdot c \cdot dr}{2} \tag{8.12}$$

$$C_d = C_{d_0} + \frac{C_l^2}{\pi \cdot e \cdot AR} \qquad D_{dr} = C_d \cdot \frac{\rho \cdot (\Omega \cdot r)^2 \cdot c \cdot dr}{2} \tag{8.13}$$

Performing this calculation for every dr along the span of the blade produces the lift distribution vs radius curve as seen in Figure 8.4. An initial estimate for the chord was taken from the preliminary sizing in Table 8.1. The chord was then varied to ensure a relatively continuous lift distribution over the blade. However, it can be seen that there is a large discontinuity from section 1 to section 2 of the blade. This is because section 1 of the blade was made much thicker than other sections to house them inside. This discontinuity in lift creates vortices that induce drag [16]. This is a penalty that the team accepts in exchange for the stowing mechanism of the blades which offers a more efficient cruise flight constituting the largest part of the mission. Similarly, the thicknesses of the airfoils were modified not only for packaging purposes but also so they would produce the desired C_l value and have a continuous lift distribution over them.
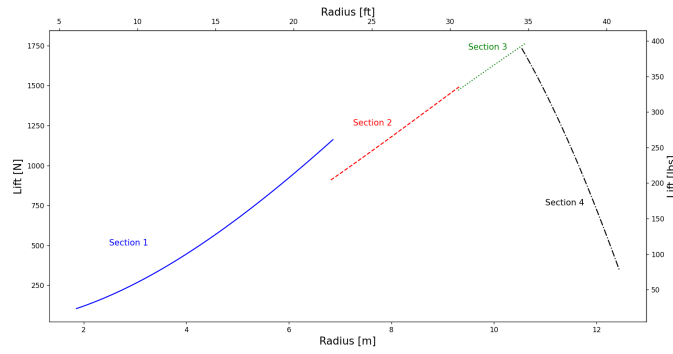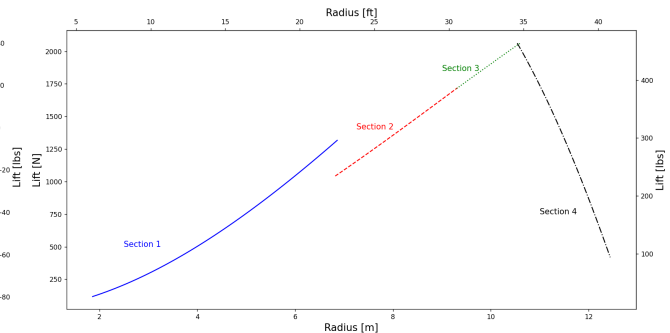
Figure 8.4: Lift Produced by Elements of Length $dr = 0.1$ m Along the Span of the Blade.
In hover, Collective angle: $8.65°$

The collective angle was calibrated such that at $0°$, the blades produce almost no lift (-2.8N) for a constant rpm of 187 as seen in Figure 8.5. At $8.65°$ the aircraft is able to produce enough lift to hover with a thrust of 312.5 kN and the maximum allowed collective angle is set at $10.02°$. This allows for a maximum thrust of 361.9 kN which can also be seen in Figure 8.6. The thrust for the rotor is simply the lift produced by the blades which was calculated using Equation 8.12.
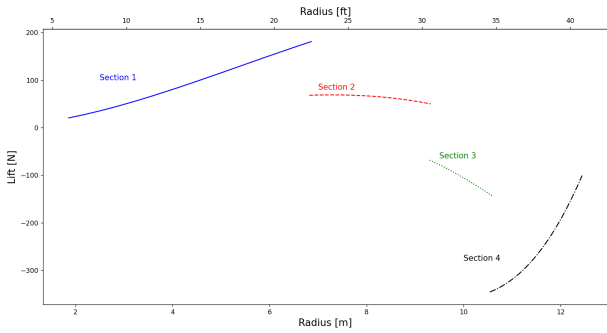
Figure 8.5: Lift Produced by Elements of Length $dr = 0.1$ m Along the Span of the Blade.
In Zero Lift, Collective Angle: $0°$

Figure 8.6: Lift Produced by Elements of Length $dr = 0.1$ m along the Span of the Blade.
In the Max Rate of Climb with Rotors, Collective Angle: $10.02°$

The torque of the blades was calculated using the inflow angle (ϕ). First, the inflow angle at the blade tip (ϕ_t) was calculated via Equation 8.14. Based on ϕ_t, the inflow angle was calculated [12].

$$\phi_t = \sqrt{\frac{C_T}{2}} \qquad \phi = \frac{\phi_t}{r/R} \tag{8.14}$$

With values for ϕ and ϕ_t available, the incremental torque (ΔQ) could be calculated with Equation 8.15. This when summed over the span of the blade and multiplied by the number of blades gives the rotor torque [12]. In addition to the torque calculation, the new disk loading at hover was also calculated using Equation 8.1 to be $13.5\ lbs/ft^2$.

$$\Delta Q = r \cdot \left[\frac{\rho}{2} \cdot (\Omega \cdot r)^2 \cdot C_l \cdot c \cdot \Delta r \cdot \phi + \frac{\rho}{2} \cdot (\Omega \cdot r)^2 \cdot C_d \cdot c \cdot \Delta r \right] \tag{8.15}$$

An overview of performance and aerodynamic parameters for the three aforementioned collective angles is presented in Table 8.2. The blade design can be further improved by accounting for the tip losses and other mechanical losses. Better results and confidence can be obtained with the use of rotor-craft aerodynamic software and computational fluid dynamics (CFD) analysis such as CAMRAD and Ansys Fluent.

Table 8.2: Aerodynamic and Performance Parameters of the Rotor.

Collective angle deg	Thrust lbf (N)	Drag lbf (N)	Torque lbf-ft (Nm)	C_T/σ
0	0.63 (-2.8)	649 (2,887)	24,521 (33,246)	-
8.65	70,243 (312,458)	4,066 (18,088)	326,696 (442,940)	0.17
10.02	81,368 (361,946)	5,151 (22,913)	391,446 (530,730)	0.20

8.1.3. Noise

Noise plays an important role in both civil and military operations of the XV-25 Griffin. For the civil case, the XV-25 Griffin has to satisfy sustainability (SYS-CO-SUS-1) and legal (SYS-CO-LEG) requirements which include the EASA and FAA regulations in order to be certified. On the other hand, while military operations are usually exempted from regulations, the far-field noise gives unnecessarily early warning of the aircraft's approach [17].

The origin of helicopter noise has been studied thoroughly both from experimental [17], [18], and theoretical [17], [19] perspectives. Though using different methods and approaches, researchers all agree that vortex noise, rotational noise, and blade slap are the main aerodynamic sources of helicopter noise. While being mentioned individually, it has been concluded that it is complicated to draw a clear distinction between the three sources as they are interconnected [17]. The characteristics of each source can be described as follows:

- As for vortex noise, rotor wake plays an influential role because each blade can be considered a wing during flight and leaves a vortex wake behind as they generate lift. The vortex wake tends to roll up into concentrated vortices and when the blade has to pass over vortices created by the previous blades [17], it creates a substantial amount of noise.

- As for blade slap, it is a worse scenario of vortex noise when the vortex wake goes very near the rotor or the blades go locally supersonic at high rotor speed [17]. This creates a specific slapping or banging noise.

- As for rotational noise, it originates from the fluctuating forces along the blades and these forces also rotate with the blade [17]. Commonly, a program has to be made to simulate and estimate the noise of this source, such as the FORTRAN model depicted by Schlegel et al. in literature. [18]

It can be seen that all noise sources have an interconnection with rotor wake; thus, according to reference [18], vortex noise is the most consequential factor in estimating helicopter noise. By means of experiment, Hubbard [20] proposed Equation 8.16 and Equation 8.17 to estimate vortex noise. The first equation is based on multiple experiments to measure the Sound Pressure Level (SPL) and the second equation is to provide a distance correction term since the original experiment was conducted 300ft away from the rotor. In both equations, A_B is the effective blade area, $V_{0.7}$ is the velocity at the 7th station of the blades, and d is the distance at which the noise needs to be estimated. Assuming the noise created during hover is the same as take-off and landing, the noise estimation of the XV-25 Griffin in different flight phases is summarized in Table 8.3. Further discussion regarding the noise estimation results can be found in chapter 12 together with other characteristics of the whole design for the sake of completeness.

$$SPL = 10 \log \frac{6.1 \times 10^{-27} A_B (V_{0.7})^6}{10 \times 10^{-16}} + 20 \log \frac{C_L}{0.4} \quad (8.16) \qquad \Delta SPL = 20 \log \frac{300}{d} \quad (8.17)$$

8.2. Fixed Wing Analysis

As indicated in requirement REQ-MSN-4 in chapter 4, the most important requirement that the XV-25 Griffin has to achieve is a cruise speed of at least 450 kts (231.5 m/s). To achieve the mentioned requirement, the analysis starts with the preliminary estimations of the wing surface area, lift, and drag as explained in subsection 8.2.1. The outputs of this step are used as inputs for the detailed wing design in subsection 8.2.2. After obtaining the wing details, an airfoil is selected through a simple trade-off elaborated in subsection 8.2.3. When the airfoil is finalized, predictions regarding the lift and drag of the aircraft can be made in subsection 8.2.4 and subsection 8.2.5, respectively.

Table 8.3: Noise Estimation of the XV-25 Griffin in Different Phases

Parameter	Unit	Hover	Transition
A_b	$ft^2\ (m^2)$	107 (92)	
$C_{L_{0.7}}$	-	1.113	
$V_{0.7}$	$ft/s\ (m/s)$	558 (170)	810 (247)
d	$ft\ (m)$	150 (45.7)	2000 (610)
ICAO Noise (MTOW based)	dB	102	101
Hubbard Noise	dB	97.8	85

8.2.1. Preliminary Sizing and Estimation

Before being able to perform a detailed analysis of the wing, an initial estimation of the wing sizing must be performed based on the estimated MTOW. By generating thrust loading vs wing loading diagrams, an optimal design point can be chosen. From this design point, both the surface area of the wing (S) and the maximum engine thrust (T_{TO}) will be found. In the same manner, lift and drag are also conceptually estimated based on statistical methods to provide inputs to other departments.

Wing Loading constraint

As a first step, an upper limit on the wing loading is found based on the stall speed. The wing loading is related to the stall speed through Equation 8.18. The design stall speed was assumed to be 0.9 times the transition speed whereas the design maximum lift coefficient was assumed to be 1.8. These assumptions are necessary to generate an initial wing sizing although these values will be updated after a detailed analysis is performed further in this chapter.

$$\left(\frac{W}{S}\right)_{stall} = \frac{1}{2} \cdot \rho \cdot V_S^2 \cdot C_{L_{max}} \tag{8.18}$$

Thrust Loading constraint

Maximum Speed

The maximum speed for an aircraft in steady, straight, and horizontal flight is defined as the speed where $T_{max} = D$. In other words, the maximum speed is reached when the engine can not provide enough thrust to overcome the drag. A relationship between the thrust loading and wing loading based on the maximum speed (at cruise conditions) can be found in Equation 8.19 where the maximum speed, V_H, was assumed to be 1.1 times the cruise speed.

Climb Gradient

As prescribed in 14 CFR Part 25 [7], a two-engine aircraft (with retracted landing gear) must be capable of a climb gradient, G, of at least 3%. Based on this requirement, a limiting thrust loading can be found with Equation 8.20.

$$\frac{T}{W} = \frac{C_{D_0} \cdot \frac{1}{2} \cdot \rho \cdot V_H^2}{\frac{W}{S}} + \frac{W}{S} \cdot \frac{1}{\pi \cdot AR \cdot e \cdot \frac{1}{2} \cdot \rho \cdot V_H^2} \quad (8.19) \qquad \frac{T}{W} \geq G + 2\sqrt{\frac{C_{D_0}}{\pi \cdot AR \cdot e}} \quad (8.20)$$

At the preliminary stage, values for C_{D_0} and AR were assumed based on statistics but after a detailed analysis was performed this process was repeated for the calculated values.

Loading Diagram

With the above equations, a loading diagram can be generated as can be seen in Figure 8.7. The design point was chosen so that the wing loading was maximized, to maximize the amount of weight the wing can lift, while the thrust loading was minimized, to reduce the amount of thrust required to lift a specific weight, while staying inside the design space (area shaded in green). Maximizing the wing loading while minimizing the thrust loading brings us to the bottom right corner possible in the design space (marked with a red cross on the diagram).
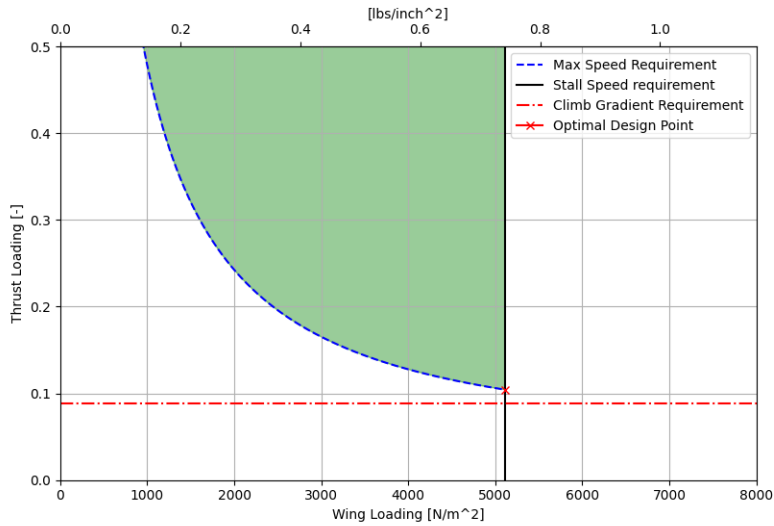
Figure 8.7: Loading Diagram

Finally, based on the design point, the required thrust at cruise conditions as well as the surface area of the wing based on the stall speed can be found by dividing/multiplying by the MTOW. The required thrust must be corrected to sea level with Equation 8.21 as it was calculated at cruise conditions [21]. The resultant values generated from this process can be found in Table 8.4

Table 8.4: Preliminary Sizing Results

$$T = T_{TO} \cdot \left(\frac{\rho}{\rho_0} \right)^{\frac{3}{4}} \quad (8.21)$$

Variable	Unit		Value	
S	ft^2	(m^2)	624.3	(58)
T_{TO}	lbf	(N)	10736	(47755.9)

Lift and Drag

While an initial value for the lift coefficient $C_{L_{des}}$ is chosen to be 0.29, the class I method is used to obtain a value for drag-related coefficients. The most important parameter is the zero-lift drag or parasite drag coefficient C_{D_0} - the drag with no lift present (skin drag). According to Raymer [22], C_{D_0} can be approximated using Equation 8.22 in which C_{fe} is the skin-friction drag coefficient, S_{wet} is the wetted area of the whole aircraft, S_{ref} is the wing reference area. Specifically, the variable C_{fe} is derived from statistics and only based on the aircraft type. Compared to the available reference aircraft types from Raymer's textbook [22], the XV-25 Griffin is assumed to be a civil transport with C_{fe} equals to 0.0030 and S_{wet}/S_{ref} is estimated to be 5 which leads to a total C_{D_0} of 0.015.

$$C_{D_0} = C_{fe} \frac{S_{wet}}{S_{ref}} \quad (8.22)$$

8.2.2. Wing Configuration and Planform

Compared to the original concept that is used in the trade-off, the wing planform undergoes several significant improvements. The most noticeable modification is the change from a triangular closed wing to a rectangular closed wing as shown in Figure 8.8, which is expected to offer a number of advantages. Aerodynamics-wise, the change helps with increasing the span efficiency factor e; thus, lowering the induced drag. Additionally, it minimizes the aerodynamic interference between the wing itself and the rotor. There are also structural benefits that are clarified in chapter 10.
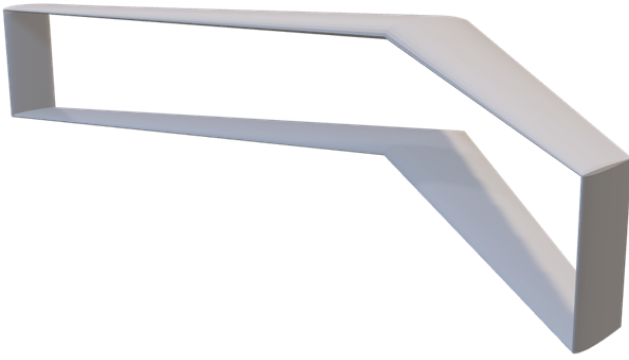
Figure 8.8: Wing Geometry of the XV-25 Griffin

Parameter	Unit	Value
S	ft^2 (m^2)	315.71 (29.33)
b	ft (m)	52.49 (16.00)
AR	-	8.73
h_w	ft (m)	10.50 (3.20)
c_r	ft (m)	7.43 (2.27)
c_t	ft (m)	4.59 (1.40)
λ	-	0.62
$\Lambda_{c/4}$	°	-30
c_{mac}	ft (m)	6.14 (1.87)

Table 8.5: Planform Parameters for Each Wing.

The wing configuration and planform were to a large extent driven by structural considerations. In particular, the requirement that the rotor blades could be lowered into the upper wing proved to be an important factor. Because the rotor has 3 blades a wing quarter-chord sweep $\Lambda_{c/4}$ of 30° aft or forward was required, where forward was chosen so that the third blade could fit in the back of the fuselage. The wingspan b was set such that the blades, which are retractable to 2/3 of their original radius, could be stowed. Similarly, the c_t was chosen to be greater than the rotor blade chord at that point. The height h_w between the two wings is based on the fuselage structure. All other planform parameters are calculated based on these and given in Table 8.5.

8.2.3. Wing Airfoil Selection

The goal of the airfoil selection process is to optimize the aerodynamic performance of the wing during critical flight phases while ensuring that all structural and performance requirements can be met.

Selection Criteria

In order to perform a trade-off of different airfoils, the most important selection criteria are established. The aerodynamic performance should be optimized for the most fuel-intensive mission segment, which for this vehicle is the cruise phase as it takes the longest time. To this end, the drag should be minimized while still meeting the lift coefficient required for cruise flight, $C_{L_{des}}$. The airfoil's minimum drag $C_{d_{min}}$ should be as small as possible and be located at a C_l close to the $C_{l_{des}}$ for optimal benefits during cruise. The drag bucket around $C_{d_{min}}$ should also be as large as possible to allow for low drag over the full range of weight and CG values.

Furthermore, the airfoil should have as high a maximum lift coefficient, or $C_{l_{max}}$, as possible. At the very least it should be high enough that the requirements on stall speed are met, which stem from the speed at which the transition into fixed-wing mode must be completed. In the event that stall is reached, airfoils with a gradual decrease in C_l beyond $C_{l_{max}}$ are desirable, as this leads to benign stall characteristics for the aircraft.

The value of the airfoil's pitching moment coefficient $C_{m_{c/4}}$ has significant implications for the trim drag during cruise, as a more negative C_m will lead to greater trim drag. Its value in cruise should thus be as low as possible. While this criterion is less important than those previously mentioned as it can be countered through the sizing of the horizontal tail, this will also have negative consequences for the weight and is ideally avoided.

The most efficient flight occurs where the lift-to-drag ratio is maximized (L/D_{max}) so this value should be as high as possible. However, in practice, this occurs at an angle of attack different from that of the $C_{l_{des}}$. It is therefore desirable to have as small a margin between these two angles of attack as possible.

Structurally, the wing should be as thick as possible because this allows for a taller spar, lowering the bending stresses and ultimately leading to a lighter wing structure. It also allows for a greater volume of fuel to be stored in the wings. A high thickness over chord ratio t/c is thus wanted.

Finally, the airfoil's transonic performance should be considered. The requirements for a cruise speed of 450 kts and an associated maximum speed of 495 kts at cruise altitude lead to values of the free-stream Mach number M_∞ located firmly within the transonic regime. Care must be taken that the drag divergence Mach number M_{dd} of the airfoil is not exceeded as this would lead to a massive increase in drag. Although this effect is to some extent mitigated by the large sweep angle applied to the wing, which lowers the flow velocity seen by the

airfoil, it is still an important factor to keep in mind. Practically, the transonic performance sets an upper limit on the wing thickness as thicker wings have a lower critical Mach number M_{cr}. It also calls for investigation into supercritical airfoils that offer higher M_{cr} values at the same t/c and wing sweep.

Flight Conditions

In order to compare the performance of different airfoils across the criteria established above, a number of requirements must be calculated.

The first of these is the design lift coefficient $C_{L_{des}}$. As mentioned before, this is the wing lift coefficient required for the most fuel-intensive mission segment, cruise for the current case. It is calculated using Equation 8.23. The mission profile contains two cruise phases, the first starting shortly after takeoff and the second ending shortly before landing. Because of this, there will be a significant weight difference that leads to a variation in the required lift coefficient. For this reason, $C_{L_{des}}$ is calculated at the start and end of the cruise phase and a range of values is specified. Note that this is the value for an unswept wing. To account for the sweep, the airfoil lift must be higher following Equation 8.24.

$$C_{L_{des}} = \frac{1}{q} \left\{ \frac{1}{2} \left[\left(\frac{W}{S} \right)_{start,cruise} + \left(\frac{W}{S} \right)_{end,cruise} \right] \right\} \qquad (8.23)$$

$$C_{L_{swept}} = C_L / \cos \Lambda_{c/4}^2 \qquad (8.24)$$

To properly compare different airfoils, their parameters must be considered at Reynolds numbers comparable to the actual flight condition. In this case, the values during the transition, climb, and cruise were calculated, using Equation 8.25. For transition and climb, the take-off conditions of 2000 ft and 85 F are considered, whereas for cruise the cruise altitude is used. The average chord $\bar{c}$ is used for C. The required maximum lift coefficient $C_{L_{max}}$ is calculated based on the condition immediately after the rotor has been stowed using Equation 8.26, with W equal to the MTOW and the velocity V_{trans} of 150 kts.

$$Re = \frac{\rho V C}{\mu} \qquad (8.25) \qquad\qquad C_L = \frac{2 \cdot W}{\rho \cdot V^2 \cdot S} \qquad (8.26)$$

Finally, the Mach number at the design maximum speed of 495 kts is calculated to be 0.81. Correcting for the sweep angle with $M_{swept} = M / \cos \Lambda_{c/4}$, the airfoil must thus reach drag divergence no earlier than $M = 0.7$. From Torenbeek, it can be approximated that $M_{dd} = M_{cr} + 0.03$ so M_{cr} should be at least 0.67.

Airfoil Tradeoff

As the number of existing airfoil profiles is nearly limitless, a structured approach had to be taken to come up with a shortlist of viable candidates for this aircraft's wings. Based on the aerodynamic requirements, several airfoil databases as well as literature were searched for airfoils with good transonic performance. Two sources proved particularly useful. The *Theory of Wing Sections* by Abbott and Van Doenhoff contains a large collection of NACA airfoils alongside their experimentally determined polars, which allowed for a rapid evaluation of an airfoil's potential in the current application [23]. The *UIUC Airfoil Coordinates Database* also listed many airfoils with good transonic performance that have seen commercial application [1].

The NACA 4- and 5-digit series were quickly eliminated as they did not have the required transonic performance at the thicknesses that were needed [24]. However, the 6-series showed promise due to its low drag at the design condition, which is a result of a larger part of the chord experiencing laminar flow. The nomenclature of the 6-series allowed for a rapid selection of candidates, as it specifies the airfoil's design lift coefficient, drag bucket width, and thickness. Ultimately, profiles were considered with a $t/c = 15 - 18\%$, to take advantage of the structural benefits of thicker wings while still having good enough transonic performance. By choosing the $C_{l_{des}} = 0.4 - 0.6$, the minimum drag point is located around the cruise condition. Where possible, the drag bucket parameter was chosen to be as high as possible. Experimental data on these airfoils was retrieved from Abbott and Van Doenhoff [23].

---

[1]`https://m-selig.ae.illinois.edu/ads/coord_database.html-22-1-2023`

The RAE2822, NLR7301 [25] and CAST 10-2/DOA-2 [26] were all designed specifically to have good transonic performance. As such, they were included in this comparison. The BACXXX airfoil was designed by Boeing for NASA's Energy Efficient Transport Program [27], and therefore served as a good candidate for a transonic transport aircraft. Lastly, the NLF(1)-0416 natural laminar flow airfoil was considered as it was designed to have low drag at a cruise $C_l = 0.4$ similar to the current design, but with a reasonable thickness and relatively high $C_{l_{max}}$ [28]. For the RAE2822, NLR7301 and BACXXX, not all of the required experimental data could be found. In these cases, the airfoil profile was imported into XFOIL, and analysis was run using comparable Reynolds and Mach numbers [29].

To find the M_{cr} of the airfoils where no transonic performance data was available, the method from Gudmundsson was used [24]. First, the low-speed, incompressible minimum pressure coefficient C_{p0} is calculated using XFOIL. Then, a compressibility correction is applied to find the minimum pressure coefficient C_{pmin} at higher Mach numbers. The Karman-Tsien correction, given by Equation 8.27, was chosen for its greater accuracy than other methods [24]. Lastly, the whole is set equal to Equation 8.28, which gives the pressure coefficient at which the minimum pressure point reaches $M = 1$, and solved for M_{cr}.

$$C_p = \frac{C_{po}}{\sqrt{1-M^2} + \left(\frac{M^2}{1+\sqrt{1-M^2}}\right)\frac{C_{po}}{2}} \quad (8.27) \quad C_{p_{cr}} = \frac{2}{\gamma M_{cr}^2}\left\{\left[\frac{2}{1+\gamma}\left(1 + \frac{(\gamma-1)}{2}M_{crit}^2\right)\right]^{\frac{\gamma}{\gamma-1}} - 1\right\}$$
$$(8.28)$$

The final tradeoff is performed in Table 8.6, based on the method by Gudmundsson [24] where rows ID are used for scoring and winning cells are colored green. Note that when comparing C_l to the desired C_L values, they must be lowered by a factor of 0.85-0.9. Scores are given for the different selection criteria established previously. In the end, the airfoil with the greatest total score is selected as the winner, with the caveat that the M_{cr} must meet its target value. If this is not the case, the aircraft will experience drag divergence below its design maximum speed and not achieve the required performance.

While the scores are very close, the NACA 65_3618 airfoil comes out as best. However, due to its t/c of 18%, it has a rather low M_{cr} which fails to satisfy the requirement. Therefore, the next best candidate is chosen that does have viable transonic performance: the NACA 65_2415.

The only requirement for the winglet airfoil is that it is symmetric so that the lift being generated follows the optimal lift distribution. For this reason, NACA 0012 is chosen.

8.2.4. Lift Estimation
With the airfoil profile of the wings being known, a first version of the wing $C_L - \alpha$ curve can be generated. As a first step, the 3D wing lift curve slope is estimated. Compared to the 2D airfoil case, its value is reduced due to the influences of aspect ratio, compressibility, and sweep. These factors are taken into account in Equation 8.29, which is a semi-empiric relation based on the DATCOM method [30]. It is accurate up until the drag divergence Mach number. The parameter β is found using Equation 8.30. For the airfoil efficiency factor η, a standard value of 0.95 is taken in lieu of experimental data on the relation between C_{l_α} and M. The wing lift curve slope is 5.174 1/rad at cruise and 4.299 1/rad at stall.

$$\frac{dC_L}{d\alpha} = C_{L\alpha} = \frac{2\pi AR}{2 + \sqrt{4 + \left(\frac{A\beta}{\eta}\right)^2 \cdot \left(1 + \frac{\tan^2 \Lambda_{0.5C}}{\beta^2}\right)}} \quad (8.29) \qquad \beta = \sqrt{1 - M_\infty^2} \quad (8.30)$$

The linear part of the wing $C_L - \alpha$ curve can now be generated using Equation 8.31, where α_{0_L} is equal to the previously found value for the airfoil of -2.6°. In order to determine the wing incidence, the design trim angle was found using Equation 8.32. It varies between -0.5 and 0.5°, depending on the point along the cruise phase being considered.

$$C_L = C_{L_\alpha} \cdot (\alpha - \alpha_{0_L}) \quad (8.31) \qquad \alpha_{trim} = \frac{C_{L_{des}}}{C_{L_\alpha}} + \alpha_{0_L} \quad (8.32)$$

The maximum lift coefficient for the wing $C_{L_{max}}$ is initially estimated using the DATCOM method [30]. First, the aspect ratio is compared to Equation 8.33 to see if the high aspect ratio procedure should be used, where C_1

Table 8.6: Airfoil Selection Trade-off for the Wings

ID	Parameter	63(2)-615	65(2)-415	65(3)-618	RAE2822	BACXXX	CAST-10-2	NLR7301	NLF(1)-0416
	Re_{stall}	$8.7 \cdot 10^6$							
	Re_{cruise}	$17.4 \cdot 10^6$							
	Target $C_{L_{max}}$	1.41							
	$C_{L_{des}}$	0.26-0.36							
	Target M_{cr}	0.67							
1	t/c	0.15	0.15	0.18	0.121	0.113	0.12	0.165	0.16
	Re for data below	$9 \cdot 10^6$	$9 \cdot 10^6$	$9 \cdot 10^6$	$9 \cdot 10^6$	$9 \cdot 10^6$	$30 \cdot 10^6$	$9 \cdot 10^6$	$9 \cdot 10^6$
2	$C_{l_{\alpha=0}}$	0.4	0.3	0.45	0.23	0.21	0.31	0.3	0.44
	$\alpha_{L=0}$	-3.7	-2.6	-4	-1.9	-1.8	-2	-2.3	-3.7
3	$C_{l_{max}}$	1.67	1.57	1.66	1.66	1.69	1.03	2.14	1.92
4	α of $C_{l_{max}}$	15.5	16.5	21	15.6	16.5	6.5	21	15.5
5	Stall characteristics (A, B, C)	A	A	A	B	B	A	B	C
6	$C_{d_{min}}$	0.0048	0.0042	0.0044	0.0047	0.005	0.0073	0.006	0.0052
7	$C_{l_{minD}}$	0.41	0.38	0.5	0.1	0.3	0.3	0.3	0.6
8	$(C_l/C_d)_{max}$	133	144	183	115	133	61	122	155
9	C_l of $(C_l/C_d)_{max}$	0.8	0.65	0.95	1.1	1.1	0.52	1.48	0.93
10	$C_{m_{cruise}}$	-0.113	-0.07	-0.112	-0.066	-0.04	-0.072	-0.079	-0.11
	Drag bucket start C_l	0.15	0.2	0.2	-0.01	0.17	0	0.2	0.36
	Drag bucket end C_l	0.7	0.6	0.8	0.2	0.4	0.5	0.35	0.9
11	$C_{L_{des}}$ in drag bucket?	Y	Y	Y	N	N	Y	N	N
12	M_{cr}	0.658	0.681	0.625	0.715	0.656	0.77	0.75	0.628
	Total Score	3	4	7	0	1	3	2	1

is a correction factor based on the taper that is found from Figure 8.9 to be 0.486.

$$A > \frac{4}{(C_1 + 1) \cos \Lambda_{LE}} \tag{8.33}$$

For a NACA 65-series airfoil, the leading edge sharpness parameter Δy is equal to $19.3 t/c$, giving a value of 2.895 [22]. With the leading edge sweep Λ_{LE} of 27.5 °, the ratio of the maximum wing lift coefficient to the maximum section lift coefficient $C_{L_{max}}/C_{l_{max}}$ can be found along the $\Delta y \geq 2.5$ curve and has a value of 0.799. This is multiplied with the 2D maximum lift coefficient $C_{l_{max}}$ of 1.6 for a $C_{L_{max}}$ of 1.28.

$$C_{L\,max} = \left[\frac{C_{L\,max}}{C_{l\,max}} \right] C_{l\,max} + \Delta C_{L\,max} \tag{8.34}$$
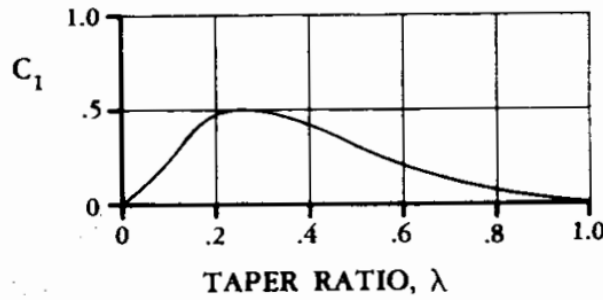
Figure 8.9: Taper-Ratio Correction Factors for Low-Aspect-Ratio Wings [30].
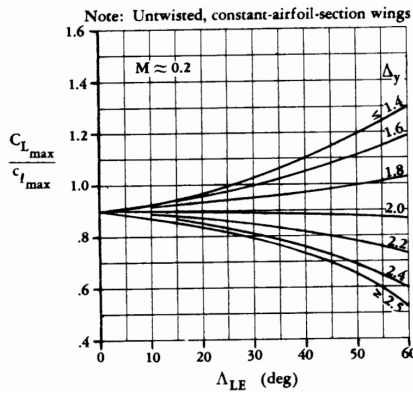
Figure 8.10: Ratio of Maximum Wing to Section Lift of High-Aspect-Ratio Wings [30].
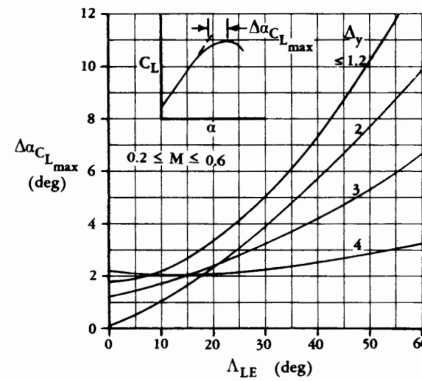
Figure 8.11: Angle of Attack Increment for Subsonic Maximum Lift of High-Aspect ratio wings [30].

The corresponding wing stall angle α_s can be calculated using Equation 8.35. Here, the value of C_{L_α} must be taken at the stall Mach number. The third term on the right accounts for the curved part of the lift curve and is found from Figure 8.11 to be $3°$. This results in an α_s of $17.4°$.

$$\alpha_s = \frac{C_{L\,\text{max}}}{C_{L\alpha}} + \alpha_{0L} + \Delta\alpha_{C_{L\,\text{max}}} \tag{8.35}$$

High-lift devices

The aircraft requires the highest lift coefficient around the transition phase, as this is the point where velocity is the lowest. During the wing sizing, a design $C_{L_{max}}$ of 1.8 and design stall speed of 135 kts V_s were assumed. The speed at which transition is completed, V_{trans}, is directly linked to the stall speed with a safety factor and is equal to 150 kts. Using the lift equation and the MTOW at take-off conditions, the required C_L at the transition speed of 150 kts is 1.39. When comparing the calculated value of $C_{L_{max}}$ to the lift coefficients required at the stall and transition speeds, it is clear that the clean wing does not produce enough lift. The maximum lift coefficient also occurs at an α of $17.4°$ and so would require a strong pitch-up maneuver to go from rotary-wing to fixed-wing mode. To solve these problems, the use of high-lift devices is investigated.

There are many different mechanisms to increase the $C_{L_{max}}$ of a wing, that can be broadly categorized into leading- and trailing-edge devices. The latter do so through the effect of delaying stall, which mainly makes them useful at high angles of attack that are preferably avoided during the transition phase. This leaves trailing-edge flaps, of which there are several different types. Non-extending flaps tilt to increase the camber, which shifts the zero-lift angle of attack left and increases the maximum lift. Extending flaps have the additional benefit of increasing the effective area of the wing, increasing the lift curve slope [22].

Two other criteria restrict the choice of high-lift devices: weight and rotor download on the wing. The most effective flaps are mechanically complex, making them heavy and thus undesirable. More important, however, is the rotor download. As is detailed in subsection 9.1.1, the rotor performance during hover flight is affected by the wing below it, with approximately 18% of thrust being lost to download. This loss of efficiency can be

lowered to 11% by deflecting flaps, as this decreases the area of the wing located below the rotor. For this reason, any extending flaps are undesirable, since these have the opposite effect of increasing the wing area. With split flaps, the area impinging on the rotor downwash remains the same so they are also not desired. Finally, plain flaps were chosen over slotted flaps as the former proved sufficient and use a simpler mechanism.

Experimental data on the aerodynamic characteristics of the NACA 65_2415 with a split flap deflected $60°$ are directly available [23]. Split flaps produce lift increases that are nearly identical to those of plain flaps, so this data gives good insight into the performance of the flapped wing [22]. The zero-lift angle of attack $\alpha_{L=0}$ moves to $-14°$, the zero-angle of attack lift $C_{l_{\alpha=0}}$ increases to 1.75 and the $C_{l_{max}}$ increases to 2.6. When using the previously found section-to-wing lift ratio $C_{L_{max}}/C_{l_{max}}$ of 0.799, this results in a $C_{L_{max}}$ of 2.08. Because this is greater than the design value of 1.8, the actual stall speed will be lower than the assumption of 135 kts with a new value of 121.6 kts. It is evident that the lift coefficients at both the design stall and transition speeds can easily be reached with the current airfoil and flap combination, at relatively low angles of attack.

One final issue concerns the short segment of the transition maneuver when the stowage mechanism in the wing opens its doors as the rotor is being lowered into it. This will lead to a temporary disruption of the flow over the upper wing and consequently a loss of lift. While it is difficult to quantitatively assess the effects of this lift reduction without a detailed computational fluid dynamics (CFD) analysis, a qualitative estimate can still be made.
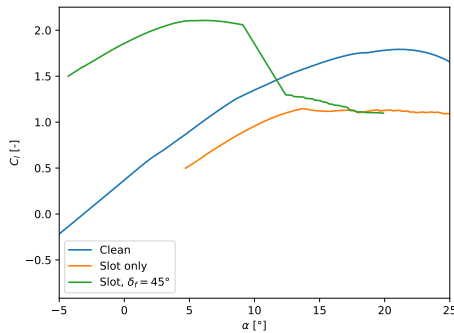
Figure 8.12: Lift Curves for the NACA 65_2415 Profile in Clean Configuration, with a Slot Cutout for the Rotor Blade and with both a Slot and a Plain Flap Deflected by $45°$, $Re = 8.7 \cdot 10^6$, $M = 0.146$
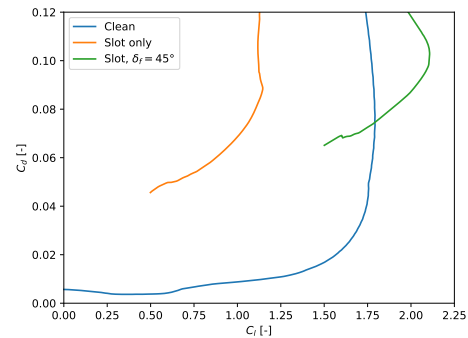
Figure 8.13: Drag polar for the NACA 65_2415 Profile in Clean Configuration, with a Slot Cutout for the Rotor Blade and with both a Slot and a Plain Flap Deflected by $45°$, $Re = 8.7 \cdot 10^6$, $M = 0.146$

To do this, the upper wing's NACA 65_2415 airfoil is loaded into the XFLR5 *Direct Foil Design* interface. A slot is then cut into the upper surface, using the size comparison between the average rotor blade chord $\bar{c}_{blade}$ and the upper wing c_{mac} as shown in Figure 8.14. The edges are smoothed to remove any sharp corners that will strongly affect the aerodynamic analysis. On the slotted profile, a plain flap is added along a length of $0.2c$. Flap deflections from 30 to $60°$ were considered. All variants beyond $40°$ showed similar $C_{l_{max}}$, but a δ_f of $45°$ was chosen as this offered the greatest α range with high lift. An aerodynamic analysis was then run on the three airfoils at the stall speed conditions of $Re = 8.7 \cdot 10^6$ and $M = 0.146$.

Figure 8.14: Geometry of the NACA 65_2415 Airfoil with the Slot for the Rotor Blade Cut Into It, Compared to the Original Profile.

The resulting lift curves from this comparison are shown in Figure 8.12. As expected, the slotted profile has

lower C_l values over the entire range of α and stalls at a lower $C_{l_{max}}$. However, with the deflection of flaps the C_l increases again, up to values higher than for the unslotted and unflapped profile. From Figure 8.13, it can be seen that the slot causes the drag to increase by one order of magnitude compared to the clean configuration.

The $C_{L_{max}}$ associated with the slotted wing would be lower than the value of 1.4 required to fly at the transition speed, making the maneuver impossible. However, as the flaps are deflected C_L will increase up to and beyond the required value. While there will be a very significant increase in drag this is not a cause for concern because there is a great excess of thrust at the transition speed, the increased drag is limited to the upper wing, and there is an allowed deceleration margin of more than 25 kts before the stall speed is reached.

In the future, the effects of carving a slot into the wing should be quantified using high-fidelity CFD analysis and wind tunnel testing.

Wing Twist Optimization

The distribution of lift over a wing is not uniform but varies along the span as each section produces a different lift coefficient. By modifying the lift distribution, an aircraft designer can improve the aerodynamic efficiency of a given wing planform, achieve a more beneficial load distribution and improve the stall behavior [24].

In the "best wing system" box-wing, as originally devised by Prandtl, minimum induced drag is achieved when each wing generates the same amount of lift and the distribution over the winglets is butterfly-shaped so that they produce a net lift of zero and no induced drag [31]. This was confirmed by Frediani, and the lift distribution on the wings consists of an elliptical and constant part [32]. According to Kroo and Demasi, the lift share can also be unequal and still achieve minimum induced drag, but for the purposes of this analysis, the simpler solution of an equal lift share was desired [33], [34].

To influence the lift distribution towards the optimal case, a wing twist is employed. There are two types of twist: geometric twist, where different sections of the wing are placed at a different angle of incidence compared to the root, and aerodynamic twist, where different airfoils are used across the wing [24]. For simplicity, only the geometric twist ϕ_G was considered here. The difficulty in optimizing the aerodynamics of a box wing lies in the fact that different twist distributions are needed across the lower and upper wings, due to the effects their down and upwash have on each other.

To determine what the optimal wing twist is for this aircraft, the lift distribution must first be determined. Typically, this is done using CFD analysis but these require detailed grids which makes them computationally expensive and thus time-sensitive. Instead, a method will be used based on lifting-line theory, requiring only a fraction of the computational power.

In Prandtl's classical formulation of this theory [35], the wing is represented by a large number of horseshoe vortices, consisting of bound vortices being located along a lifting line and a trailing vortex sheet. These trailing vortices generate induced velocities at points along the wing according to the Biot-Savart law (Equation 8.36) [16]. The lift generated by each spanwise section of the wing is considered equivalent to that generated by an infinite wing with the same circulation and found using the two-dimensional Kutta-Joukowski theorem (Equation 8.37). The first analytical solution, consisting of a series of sines, was given by Glauert [36]. Anderson provided a numerical scheme and incorporated non-linearity of the relation between α and C_l [37].

$$\mathbf{dV} = \frac{\Gamma}{4\pi} \frac{\mathbf{dl} \times \mathbf{r}}{|\mathbf{r}|^3} \qquad (8.36) \qquad\qquad L'(y) = \rho_\infty \cdot V_\infty \cdot \Gamma(y) \qquad (8.37)$$

However, these methods become inaccurate for wings with sweep and dihedral. Phillips and Snyder were able to mitigate this problem and come up with a new numerical lifting-line method by applying the three-dimensional vortex lifting law and taking into account the velocities induced by the bound vortices [38]. Their method is particularly useful because it can be generalized to multiple lifting surfaces, such as two wings placed on top of each other, and was therefore chosen to be used here. A brief description is given below.

$$\boldsymbol{V}_j = \boldsymbol{V}_\infty + \sum_{i=1}^{N} \frac{\Gamma_i \boldsymbol{v}_{ij}}{\bar{c}_i} \qquad (8.38) \qquad\qquad \alpha_i = \tan^{-1}\left(\frac{\boldsymbol{V}_i \cdot \boldsymbol{u}_{ni}}{\boldsymbol{V}_i \cdot \boldsymbol{u}_{ai}}\right) + \alpha_t + \alpha_g \qquad (8.39)$$

First, a span-wise grid of nodes is generated using cosine clustering to efficiently handle the large change in vorticity near the wing tips and root. Horseshoe vortices are placed between the nodal points and control points

are placed midway between the nodes, on the lifting line. The total velocity at a control point on a horseshoe vortex is the vector sum of the free-stream velocity and the induced velocity of all vortices acting on this point, given by Equation 8.38. v_{ij} is a dimensionless induced velocity defined in [38].

$$\boldsymbol{dF}_i = \rho\Gamma_i\boldsymbol{V}_i \times \boldsymbol{dl}_i \qquad (8.40) \qquad\qquad |\boldsymbol{dF}_i| = \frac{1}{2}\rho V_\infty^2 C_{l_i}(\alpha_i)dA_i \qquad (8.41)$$

The local angle of attack α at i is found using Equation 8.39, where $\boldsymbol{u}_{ni}$ and $\boldsymbol{u}_{ai}$ are defined in Figure 8.16. This α is used to find the sectional lift coefficient C_l from 2D airfoil data. Using the relations given by Equation 8.40 and Equation 8.41 for the differential force on a section and non-dimensionalizing with the free-stream velocity, the system of non-linear equations given by Equation 8.42 can be derived, with one equation per control point. To get the vector of residuals $\boldsymbol{R}$ below the convergence threshold, the Newton corrector equation given by Equation 8.43 is used. $[\boldsymbol{J}]$ is the matrix of partial derivatives $\frac{\partial \mathcal{R}_i}{\partial G_j}$. An improved estimate of the dimensionless vortex strength $\boldsymbol{G}$ is then found with Equation 8.44, where Ω is a relaxation factor.
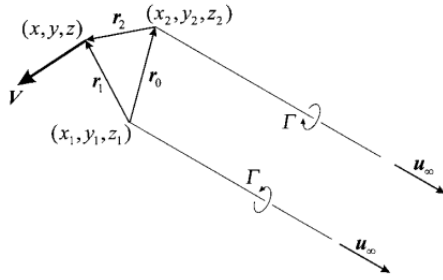
Figure 8.15: Geometric Definitions for a Horseshoe Vortex [38].
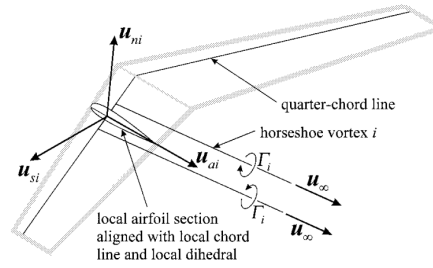
Figure 8.16: Orientation of Vectors on the Local Airfoil Section [38].

$$\boldsymbol{R} = 2\left|\left(\boldsymbol{v}_\infty + \sum_{j=1}^{N}\boldsymbol{v}_{ji}G_j\right) \times \boldsymbol{\zeta}_i\right|G_i - C_{\ell i}\left(\alpha_i, \delta_i\right) \qquad (8.42) \qquad\qquad [\boldsymbol{J}]\Delta\boldsymbol{G} = -\boldsymbol{R} \qquad (8.43)$$

$$\boldsymbol{G} = \boldsymbol{G} + \Omega \cdot \Delta\boldsymbol{G} \qquad (8.44)$$

In this form, the method returns unexpected results for the region around the wing root, as described in more detail in section 8.3. Phillips and Snyder ignore this behavior as it does not affect the convergence of their results, which are still largely correct. However, in the case of forward-sweep, the method diverges so a solution must be found. After careful consideration and validation with wind tunnel data, detailed in section 8.3, a correction method was determined. From 40 to 60% of the span, the value of α is set equal to that at the 40% point. This correction is based on the approximate value seen in actual lift distributions of forward-swept wings [24] but currently has no theoretical foundation.

Although the current lifting-line method should theoretically be capable of analyzing a fully closed box-wing, there will be discrepancies at each intersection of surfaces that strongly influence the resulting distribution, the effects of which cannot currently be validated. Instead, a biplane configuration is considered, as this leads to very similar distributions over the wing with only a slightly reduced span efficiency factor of 1.36 compared to 1.46, as illustrated in Figure 8.17 and Figure 8.18. The value of e obtained by the numerical method is thus an underestimate of the actual efficiency achieved when the winglets are taken into account.

The method is repeated for a linearly varying ϕ_G and optimized to find the ideal wing twist. To determine what the optimum distribution is, the objective function of the spanwise efficiency factor e is taken as given by Equation 8.45 [40]. As the twist of the upper and lower wing are different, this is now a multi-variate function. Another factor to keep in mind is the stall behavior. If the tips stall before the root, this can result in a loss of control.
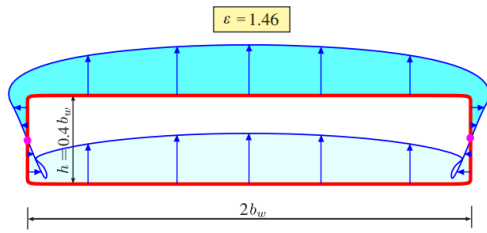
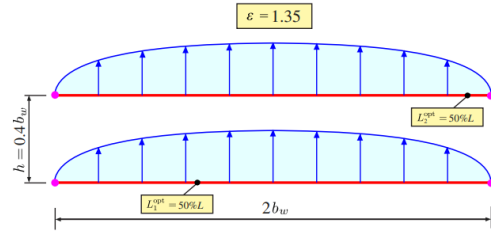**Figure 8.17:** Lift Share Over Box Wing for $h/b = 0.2$ [39].

Figure 8.18: Lift Share Over Biplane with $h/b = 0.2$ [39].

$$e = \frac{C_L^2}{\pi \cdot AR \cdot C_D} \tag{8.45}$$

Figure 8.19 shows the distribution of circulation over the two wings for the cruise condition, where the aircraft flies at α_{trim}, without any twist applied. The section lift coefficients are shown in Figure 8.20. It can be seen that the lift on the lower wing is mostly located inboard, as is expected for a forward-swept wing [24]. On the upper wing, the lift is higher due to the upwash caused by the lower wing. This is also reflected in the lift coefficients. In its untwisted state, this wing would experience poor stall behavior. Note the straight lines around the wing root, which are caused by the correction method that was used.
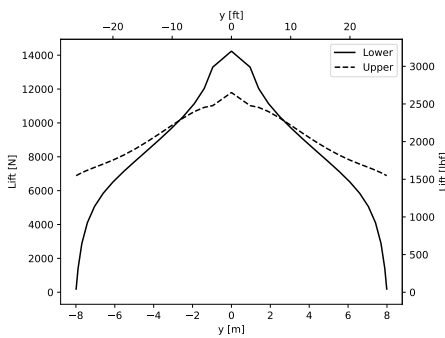
Figure 8.19: Lift Distribution Over the Upper and Lower Wings for the Cruise Condition and No Wing Twist.
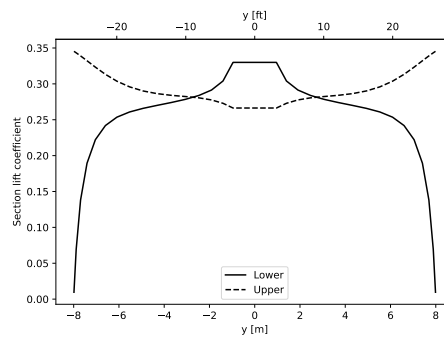
Figure 8.20: Section Lift Coefficients Over the Upper and Lower Wings for the Cruise Condition and No Wing Twist.

The optimal twist distribution consists of a $1.1°$ washout on the upper wing and $0.7°$ washing on the lower wing. To ensure that the lift shared by each wing is similar, the upper wing is placed at a relative incidence angle i_u of $0.65°$ greater than the lower wing, which shifts the lift distribution up by a constant value. Figure 8.21 shows that the lift distributions of both wings are now much more similar and the lift has shifted inboard for the upper wing compared to the untwisted case. From the section lift coefficients, plotted in Figure 8.22, it is confirmed that this solution is fairly close to the ideal case, where the sectional lift coefficient is constant. Importantly, however, care was taken to ensure that the inboard lift coefficients are greater than the outboard and will thus stall earlier.
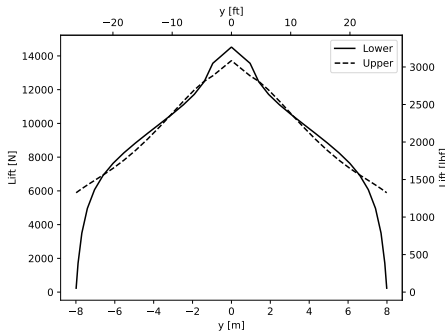
Figure 8.21: Optimized Lift Distribution Over the Wings for the Cruise Condition with $1.1°$ Washout on the Upper Wing and $0.7°$ Washin on the Lower Wing.
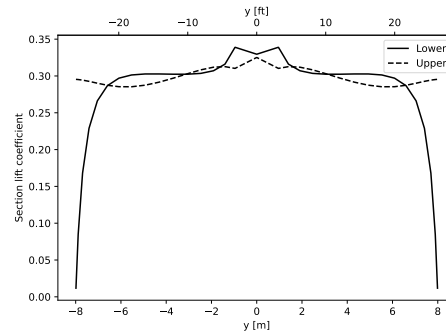
Figure 8.22: Optimized Section Lift Coefficients Over the Wings for the Cruise Condition with $1.1°$ Washout on the Upper Wing and $0.7°$ Washin on the Lower Wing.

Finally, the lift curve slope of the wing was calculated and found to have a value of 5.116 1/rad. This is very close to the cruise value of 5.174 1/rad from the DATCOM method presented in subsection 8.2.4. The C_L at cruise was found to be 0.299. These results indicate that the lift estimates provided by the lifting-line method are fairly accurate for this aircraft. The same cannot be said for the induced drag coefficients, however, as these are an order of magnitude too low. This is again an artefact of the ill-defined lifting-line definition near the root that caused previous issues, as detailed in section 8.3. Unfortunately, this means that the spanwise efficiency factor e cannot be accurately calculated at this time.

In the future, it is recommended that a twist distribution parameterized by more variables is implemented. The greatest potential for improvement, however, lies in a better definition of the lifting line near the root as this is the main cause of errors in the results. In this regard, recent research by Goates and Hunsaker is promising [41]. If this issue is solved, the analysis can likely be extended to the full box-wing geometry. Other areas of improvement include adapting the analysis to beyond stall [37], [42], better account for transonic effects, and considering the interactions of fuselage, tail, and wings [43].

8.2.5. Drag Estimation

Similar to lift, drag is an aerodynamic force but instead of pushing the moving body forward, drag provides resistance that prevents the object from moving. Typically, it is objective to minimize the drag, especially during climb and cruise. Consequently, it also has a negative snowball effect on the structural and fuel weight of the aircraft. This section introduces a basic drag model that is used to estimate the drag of the XV-25 Griffin. According to Gudmundsson [24], different kinds of drags can be classified into pressure drag C_{D_0}, skin friction drag C_{D_f}, induced drag C_{D_i}, wave drag C_{D_w}, and miscellaneous drag $C_{D_{misc}}$. Usually, except for induced drag, the other terms are combined and referred to as minimum drag coefficient $C_{D_{min}}$ as shown in Equation 8.46 so the final drag model can be described using Equation 8.47.

$$C_{D_{min}} = C_{D_0} + C_{D_f} + C_{D_w} + C_{D_{misc}} \quad (8.46) \qquad C_D = C_{D_{min}} + C_{D_i} \quad (8.47)$$

Minimum Drag Coefficient

The whole procedure to utilize the Component Buildup Method described by Raymer [22] to perform the drag estimation is summarized in Figure 8.23. In the mentioned method, the aircraft is divided into different components such as the wing, the fuselage, and the tails, and each of them is evaluated separately as formalized in Equation 8.48 [22]. In Equation 8.48, the subscript c indicates that the values are meant for each component. From left to right, C_f is the flat-plate skin friction drag coefficient, FF is the component form factor, IF is the component interference factor, S_{wet} is the wet surface area and S_{ref} is the wing surface area. Apart from those, $C_{D_{wave}}$ is the wave drag on projectiles moving at transonic or supersonic speeds due to the presence of shock waves, and $C_{D_{misc}}$ considers miscellaneous drag resulting from non-smooth surfaces or the upswept aft fuselage.

$$C_{D_{min}} = \frac{\Sigma C_{f_c} FF_c IF_c S_{wet_c}}{S_{ref}} + C_{D_{wave}} + C_{D_{misc}} \quad (8.48)$$
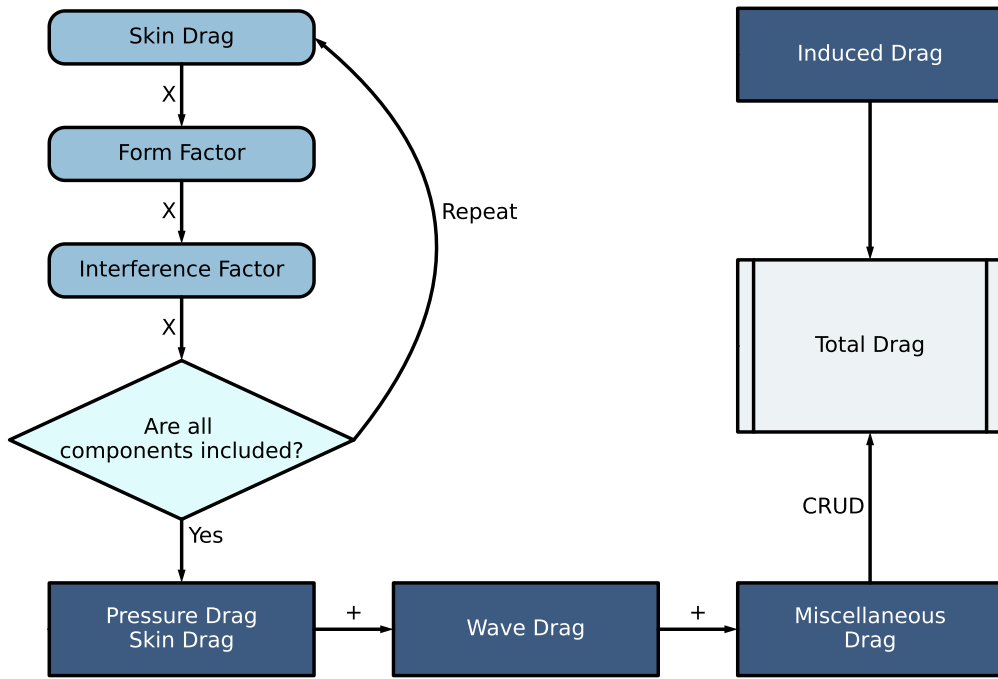
Figure 8.23: Procedures to Perform Drag Estimation

The flat-plate skin friction drag coefficient C_f heavily depends on the Reynolds number and the type of the boundary layer. The laminar boundary layer ($Re < 2300$) is characterized as a thin layer with lower friction while the turbulent boundary layer ($Re > 4000$) is thicker and has higher friction [23]. To perform the calculation shown in Equation 8.50, the first step is to determine the viscosity of air so the Reynolds number can be obtained using Equation 8.49 and Equation 8.25 where T is the temperature in Kelvin and C denotes the characteristic length. It should be pointed out that the characteristic length is different between the root chord and the tip chord for the wing, so they consequently have different Reynolds numbers.

$$\mu = 1.458 \cdot 10^{-6} T^{1.5} \frac{1}{1 + 110.4} \qquad (8.49) \qquad C_f = \begin{cases} \frac{1.328}{\sqrt{Re}} & \text{Laminar} \\ \frac{0.455}{(\log_{10} Re)^{2.58}(1+0.144M^2)^{0.65}} & \text{Turbulent} \end{cases}$$
$$(8.50)$$

In Equation 8.50 [22], it is worth noticing that the coefficient is either completely laminar or turbulent while there also exists the transition process when the laminar boundary layer becomes turbulent which results in a mixed boundary layer. Therefore, assumptions regarding the proportion of each boundary layer as well as the transition point have to be made.

- For the wings, the NACA $65_2 - 415$ airfoil is chosen; since the NACA 6-series airfoils are designed with an emphasis on maximizing laminar flow, literature [24] suggests that it can maintain up to 60% of laminar flow for the upper surface and up to 50% for the lower surface.

- For the tails, the symmetrical NACA0012 is chosen with the motivations further clarified in chapter 11, but it is assumed to have a laminar proportion of 50%.

- For the fuselage, only the weighted average of the laminar and turbulent proportion is used because the majority (about 90-95% [44]) of the boundary layer is turbulent so the effect of the transition process is negligible.

The transition point and skin friction coefficient of the mixed region can be calculated using Equation 8.51 and Equation 8.52 [24] with X_{tr}/C is the assumed laminar flow coverage and X_C/C is the exact location of the transition point along the chord. Then the total skin friction drag coefficient of the component is simply the average of the upper and lower surfaces of the wing, or the left and right surfaces of the tail.

$$\frac{X0}{C} = 36.9 \cdot (\frac{X_{tr}}{C})^{0.625}(\frac{1}{Re})^{0.375} \quad (8.51) \qquad C_f = \frac{0.074}{Re^{0.2}}(1 - (\frac{X_{tr} - X_0}{C}))^{0.8} \quad (8.52)$$

The next factor in the Component Buildup Method is the form factor FF which takes into account the geometric shape of the components. For the wings and tails, the form factor is based on the thickness-to-chord ratio t/c with a compressibility correction term as shown in Equation 8.53. For the fuselage, Raymer [22] presents the fineness ratio $f = l_{fuselage}/d_{fuselage}$ to calculate the form factor by using Equation 8.54. The values for these calculations are taken from subsection 8.2.2 and chapter 7.

$$FF = (1 + \frac{0.6}{(x/c)_{max}}\frac{t}{c} + 100(\frac{t}{c})^4) \cdot (1.34 M^{0.18}(\cos \Lambda_{tmax})^{0.28}) \qquad FF = 1 + \frac{60}{f^3} + \frac{f}{400} \quad (8.54)$$
$$(8.53)$$

There is also the effect of one component on another, for instance, the connections between the wings and the fuselage, which is corrected in the Component Buildup Method by the interference factor IF. However, this factor has to be multiplied for each component (so the lower and upper wing has to be multiplied separately) and it does not take into account additional drag due to early flow separation because of poorly designed wing or fuselage [24]. The values for IF are determined statistically from reference [22], [24].

The wetted surface area of the components is estimated based on the actual exposed area with an area booster factor as shown in Table 8.7. The exposed areas are estimated by exploiting the created CAD model which was impossible during earlier design phases since a concept was not finalized before the trade-off. Correspondingly, the results are more accurate and comparable to real aircraft because the XV-25 Griffin has a very specific shape rather than the ones used in the statistical method (paraboloid cockpit, elliptic cylinder fuselage, and cone tail).

Table 8.7: Basic Drag Calculation

	Unit	Upper Wing	Lower Wing	Horizontal Tail	Vertical Tail	Fuselage
C_f	-	0.00165	0.00165	0.00171	0.00172	0.00178
FF	-	1.644	1.644	1.473	1.454	1.358
IF	-	1	1.4	1.13	1.13	1
S_{wet}	ft^2 (m^2)	533(49.5)	533(49.5)	362(33.6)	95.4(8.862)	2260(210)
C_{D_0}	-	0.00229	0.00321	0.00163	0.000427	0.00866

Table 8.7 summarizes the basic minimum drag coefficient C_{D_0} of different components. When summing them up, the value of the vertical tail is multiplied by three to take into account the drag contribution of the vertical connection between the upper and lower wings which both have an approximately similar surface area (45.2 ft^2 vs 47.4 ft^2).

Generally, when the aircraft approaches the speed of sound, the corresponding drag coefficient increases significantly. While the exact location (drag-divergence Mach number M_{dd}) depends on the geometry of the aircraft, a relative factor $C_{D_{wave}}$ has to be taken into account for this effect. The wave drag can be calculated using Equation 8.55 [45] and Equation 8.56 [44]. Applying the formulas gives a wave drag value of 0.008 which is considered acceptable since the XV-25 Griffin is not designed to be a supersonic vehicle and the cruise speed is only in the subsonic regime.

$$M_{dd} = M_{cruise} + 0.03 \quad (8.55) \qquad C_{D_{wave}} = 0.002(1 + 2.5\frac{M_{dd} - M}{0.05})^{-1} \quad (8.56)$$

The miscellaneous drag $C_{D_{misc}}$ is finally added to compensate for details that are overseen in the calculations of each component. Specifically, it originates from the fuselage where the form factor formula (Equation 8.54) only considers the maximum length and diameter of the fuselage but the actual geometry has a notable upsweep angle at the aft of the fuselage to load the payload which could produce a large amount of drag if it is not designed properly. Additionally, the drag that comes from the cockpit window can also be calculated separately.

- Aft fuselage upsweep drag is evaluated based on the method described by Kroo [46]. The correlation between the mentioned drag and the fuselage geometry can be characterized by the vertical displacement of the fuselage centerline in the tail cone above the fuselage reference plane as shown in Figure 8.24. To minimize the effects of modifications at the very end of the fuselage, the measurement is performed at

75% of the total upsweep length as shown in Equation 8.57. Using the parameters obtained from the CAD model, $C_{D_{upsweep}}$ is estimated to be 0.00181.

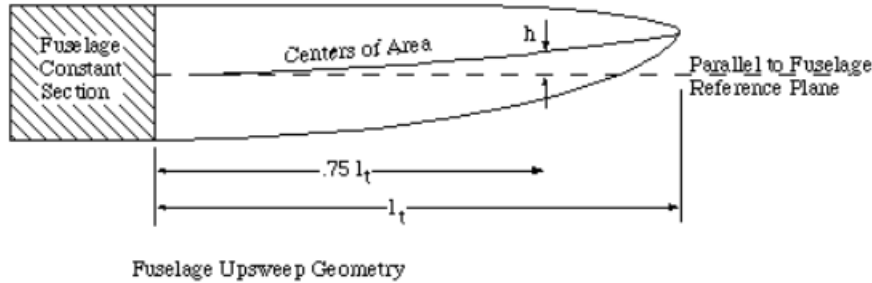$$C_{D_{upsweep}} = 0.075(h/l)_{0.75lt} \tag{8.57}$$

Figure 8.24: Geometry of Fuselage Upsweep Drag Estimation [46]

- Similarly, the front of the fuselage has to be designed to fit conventional cockpit windows as visualized in Figure 8.25. It provides the crews with visibility and makes it safer to operate the aircraft, especially during the hovering stage of the mission profile. However, a high-pressure region is created due to discontinuity resulting from the geometry's reduced speed. The additional drag to correct this issue can be computed using Equation 8.58 where C_{D_S} depends on the type of window and A_{max} is the maximum frontal area of the fuselage. For the XV-25 Griffin, it is assumed to have curved windscreens with a round upper edge whose C_{D_S} value is estimated to be 0.002 [24]. Eventually, the drag raises by approximately 0.000310.

$$C_{D_{window}} = C_{D_S} \cdot \frac{A_{max}}{S_{ref}} \tag{8.58}$$
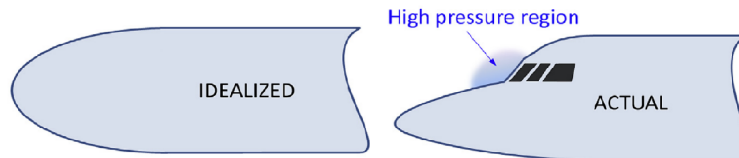
Figure 8.25: Ideal and Actual Front Fuselage Geometry [24]

- An obvious drawback of the Component Buildup Method is that it only isolates the major components of the aircraft for drag estimation whereas the actual assembly consists of several other design details such as landing gears, antennas, or connection joints. At this design phase where the low-level designs (number of antennas or surface finish) are yet to be decided, these details are taken into account by the Cumulative Result of Undesirable Drag (CRUD) factor which is suggested to be 20 to 25% by references [24]. Considering the wave drag and extra drags from the fuselage have been calculated separately, a factor of 15% is used for the XV-25 Griffin.

To conclude the section, the overall results of the minimum drag coefficient analysis are tabulated in Table 8.8 and the final drags breakdown structure among the components is illustrated in Figure 8.26. It is here assumed that the blades are successfully stowed in the fuselage and the upper wing so there are no rotor-related drags. By adding C_{D_w} into $C_{D_{misc}}$ for visualization purposes and acknowledging that a large portion of $C_{D_{misc}}$ also comes from the fuselage, it can be pointed out that the majority of the drag contribution originates from the wing and the fuselage where the fuselage is the draggiest component. This contradicts conventional airliners where the wing usually contributes the most to the drag but seems reasonable for the specific case of the XV-25 Griffin since it has a relatively small wing surface area compared to passenger aircraft. Nevertheless, at the clean configuration during cruise, the $C_{D_{min}}$ of the XV-25 Griffin is comparable to 0.024 of the Boeing-737 or 0.023 of the Airbus-A320 [47].
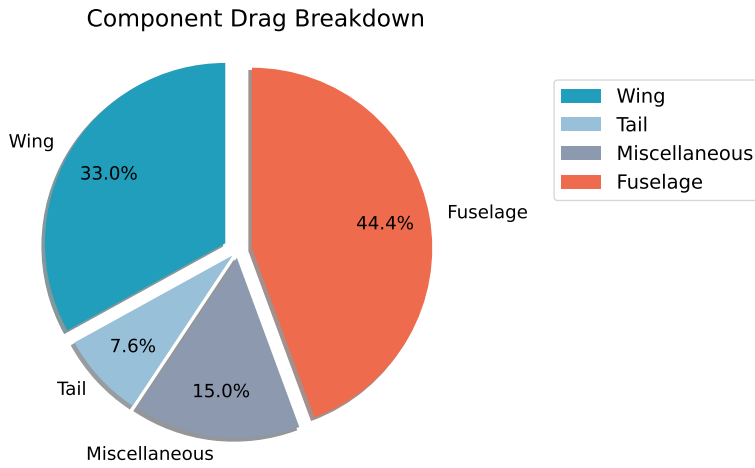
Component Drag Breakdown

Figure 8.26: Component Drag Breakdown Structure of the XV-25 Griffin

Drag	Value
$C_{D_{upper-wing}}$	0.00229
$C_{D_{lower-wing}}$	0.00321
$C_{D_{horizontal-tail}}$	0.00163
$C_{D_{vertical-tail}}$	0.000472
$C_{D_{fuselage}}$	0.00866
ΣC_{D_f}	0.0166
$C_{D_{wave}}$	0.0008
$C_{D_{misc}}$	0.00212
ΣC_D	0.0195
$CRUD$	15%
$C_{D_{min}}$	0.0226

Table 8.8: Drag Analysis Results

Induced Drag

To visualize the drag polar and complete the drag estimation, it is necessary to also analyze the induced drag C_{D_i} which is the drag due to lift. For a conventional fixed-wing system, the induced drag can be calculated using Equation 8.59 where $C_{L_{minD}}$ is to calculate the effect of cambered airfoils if existed, and Equation 8.60 [22] where e is the span efficiency factor to include the 3D wing effects.

$$C_{D_i} = \frac{(C_L - C_{L_{minD}})^2}{\pi ARe} \quad (8.59) \qquad e = 1.78(1 - 0.045AR^{0.68}) - 0.64 \quad (8.60)$$

However, since Prandtl's "best wing system" as described in subsection 8.2.2 was integrated into the XV-25 Griffin, the value of e changes considerably. In 1924, Prandtl proposed Equation 8.61 [31] to calculate e without further explanation where G is the vertical distance between the upper and lower wings as visualized in Figure 8.27 to identify the vertical aspect ratio G/b. Similarly, in 2005, Kroo [33] introduced a span efficiency value of 1.46 for rectangular closed wings assuming a vertical aspect ratio of 0.2 and designs are optimally twisted. To double-check these values, a new formula proposed and validated in the wind tunnel by Demasi et al. [48] as shown in Equation 8.62 was utilized. In order of appearance, the results of the span efficiency factor are 1.47, 1.46, and 1.46, respectively. It can be seen that there is little deviation among studies for the span efficiency factor; for further calculation, 1.46 is used.

$$\frac{1}{e} = \frac{1 + 0.45 \cdot \frac{G}{b}}{1.04 + 2.81\frac{G}{b}} \quad (8.61) \qquad \frac{1}{e} = \frac{1}{1 + 1.7433(\frac{G}{b})^{0.823}} \quad (8.62)$$
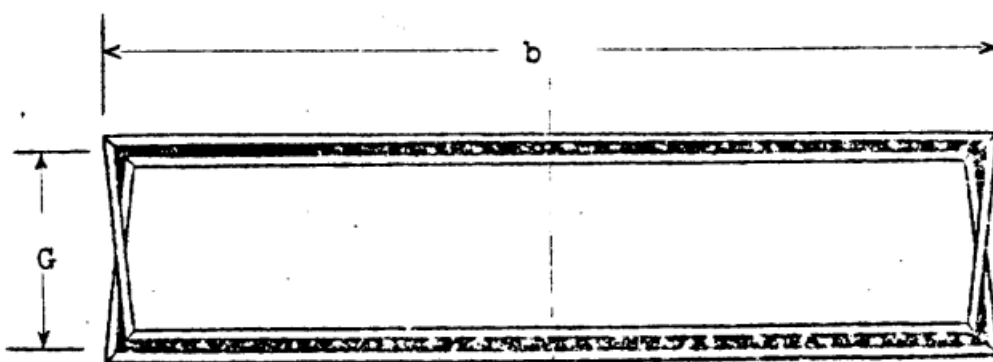

Figure 8.27: Prandtl's Best Wing System [31]

Assuming the weight does not vary significantly during cruise, the drag curve of the XV-25 Griffin after the transition was visualized in Figure 8.28 where the relationship between $C_{D_{min}}$ or C_{D_i} and the velocity can clearly be seen. Although the curves are not similar to that of conventional aircraft, as the whole design process is specifically focused on the high-speed performance of the XV-25 Griffin, the combination of the rectangular

closed wing and laminar cambered airfoil makes the design very efficient at high speed where the main contribution of the total drag originates from the parasite drag. Similarly, the drag polar describes the relationship between C_L and C_D as illustrated in Figure 8.29. At the chosen design cruise point whose lift coefficient is 0.3, the ratio of C_L/C_D is approximately 13.5.
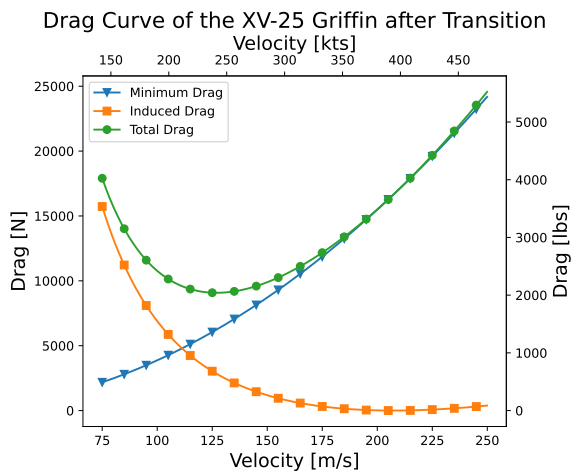

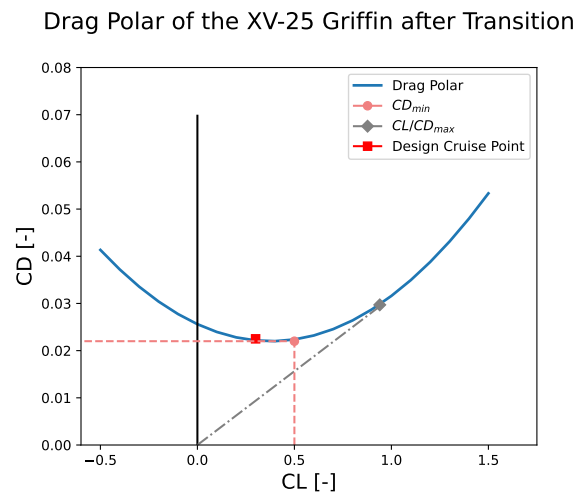**Figure 8.28:** Drag Curve of the XV-25 Griffin after Transition

Figure 8.29: Drag Polar of the XV-25 Griffin

8.3. Verification and Validation

Verification and validation maintain a prominent role in engineering projects, especially ones that involve a simulation model to replicate the physical responses of a system. This section explains the verification (in subsection 8.3.1) and validation (subsection 8.3.2), and recommendations if it is unfeasible to perform such processes at this phase of the project.

8.3.1. Verification

Throughout the project, especially within the Aerodynamic department, several scripts were created to assist the team in analyzing different related aspects. Therefore, these codes have to be verified to ensure that there were no errors within themselves. While the majority of the scripts were created within a compiler with the ability to spot and check for errors, the team also generated extra unit tests and subsystem tests to guarantee that no errors exist in the system. Additionally, inputs were changed separately to see if the codes behaved as they expected to, for instance, changing the span efficiency factor would lead to a decrease in the induced drag.

The code for blade design used equations from the book of Raymond Prouty [12] which are widely used by many institutions and projects and are therefore considered true. Furthermore, the lift distributions over the blades were compared to other models such as the CAMRAD2 and the small-scale rotor model developed by Hyun-Ku Lee and their team in joint research with Seoul National University and Korea Aerospace Research Institute [49].

8.3.2. Validation

Lifting line method

The numerical lifting line method, described in subsection 8.2.4, was extensively verified and validated. As a first test, its results were compared to those obtained with the classical Prandtl method, for wings of various aspect ratios. From Figure 8.30, there is a near-perfect agreement between the two methods.

Next, in order to validate the method, its results were compared to wind tunnel experiment data of rectangular and aft-swept wings. The rectangular wing data with an aspect ratio of 6.57 comes from McAlister and Takahashi [50]. The swept-wing data comes from Weber and Brebner and concerns a wing with a sweep of $45°$ and an aspect ratio of 5. Figure 8.31 and Figure 8.32 show the results of this comparison.

For the rectangular wing, the numerical lifting line method again accurately predicts the lift and induced drag coefficients. In the swept-wing case, the lift coefficients are also accurately predicted, but there is a discrepancy

in the drag coefficients. According to Phillips and Snyder, this is likely caused by the step change in the direction of the lifting line at the wing root for a swept wing, which causes a singularity in the induced velocity and leads to an overestimated drag coefficient [38]. This result does serve as a verification against their method, as they achieved similar results.
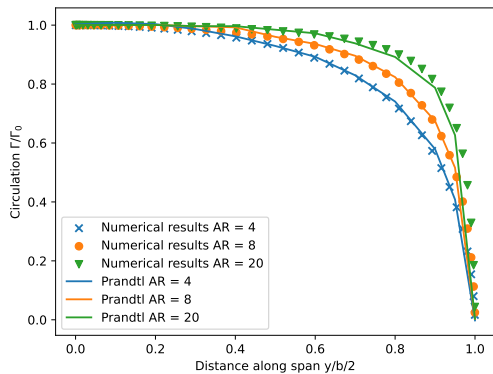

Figure 8.30: Comparison of the Numerical Lifting-Line Method for Rectangular Straight Wings of Different Aspect Ratios to Prandtl's Classical Theory
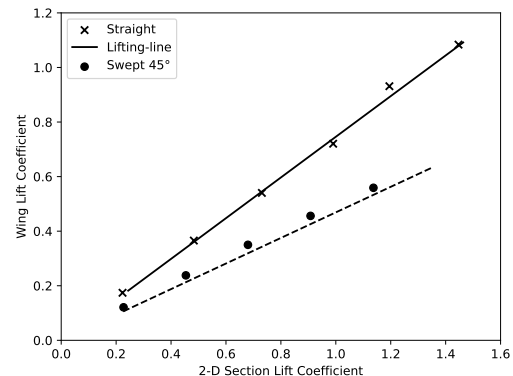
Figure 8.31: Comparison of the Lift Coefficients Calculated by the Lifting-Line Method to Experimental Data, for a Straight Wing and a Wing Aft-Swept by $45°$.
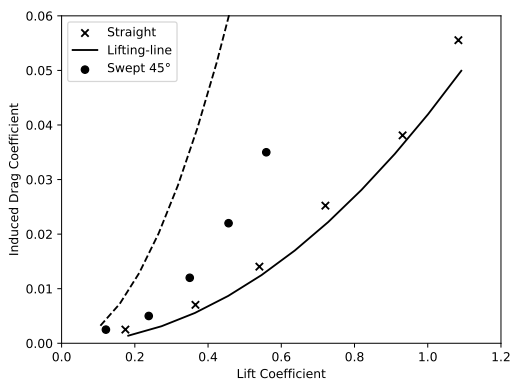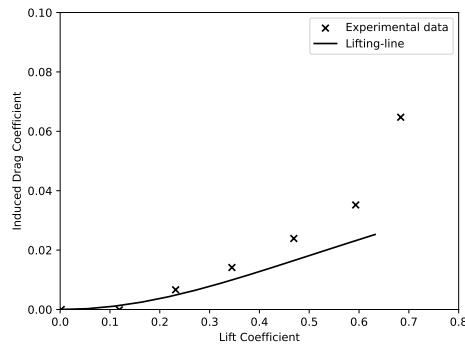

Figure 8.32: Comparison of the Drag Coefficients Calculated by the Lifting-Line Method to Experimental Data, for a Straight Wing and a Wing Aft-Swept by $45°$.
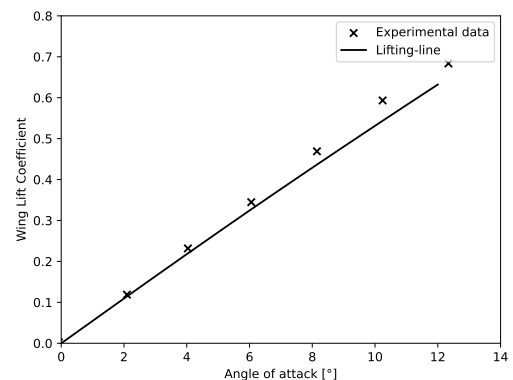
Figure 8.33: Comparison of the Lift Coefficients Calculated by the Lifting-Line Method, Corrected for the Discrepancy at the Wing Root, to Experimental Data for a Forward-Swept Wing.

Problems arise when a forward-swept wing is considered. Like the previous case, there is again a singularity located at the root of the wing, but this singularity now causes the solution to diverge. This behavior was apparently not caught by the authors of the method. To counter this issue, several different remedies were considered. First, the section lift coefficients were simply restricted to an arbitrary range of reasonable values. While this did have the desired effect of converging to a solution, the lift coefficient was overestimated as the region near the root experiences $C_{l_{max}}$, which is not the case in real life. Next, the region near the root was set to have a constant C_l distribution equal to a point slightly removed from it, at 40% of the span. This significantly reduced the total calculated C_L values, providing a better estimate of the true lift. The correction was then validated against wind tunnel data of a $30°$ forward-swept wing with an aspect ratio of 5.2, determined by Purser and Spearman [51]. Results are shown in Figure 8.33 and Figure 8.34. The lift is reasonably accurate, but the drag is significantly underestimated, likely as a result of the correction to the root region where the induced velocities are greatest.

Because the calculated coefficients for swept wing configurations are likely to be inaccurate, the lift distribution should not be used for structural calculations of the spanwise loads or for an exact calculation of the wing lift and drag. However, the validation above demonstrates that the lifting line results follow the same pattern as

Figure 8.34: Comparison of the Drag Coefficients Calculated by the Lifting-Line Method, Corrected for the Discrepancy at the Wing Root, to Experimental Data for a Forward-Swept Wing.

the actual values. This is also noted by Phillips and Snyder, who remark that the aerodynamic interactions found through this method are at least qualitatively correct. The results are therefore considered valid enough to determine the optimum twist distribution.

Noise

Hubbard's noise model mentioned in subsection 8.1.3 was thoroughly validated by Schlegel et al. [18]. The results of the experiments for two helicopters CH-3C and CH-53A can be found in Table 8.9 with little to no deviations between the calculations and the actual measurements. However, it is worth noticing that several atmospheric conditions such as pressure, temperature, humidity, or wind may affect the experiments and lead to inconsistencies. Therefore, for future analysis, it is suggested that a more stable and error-proofed model is exploited, like the HELENA model created by FRIENDCOPTER - a project funded by the EU Community Research and Development Information Service [2].

Table 8.9: Vortex Noise Levels Experiment Result [18]

Rotor Speed (rpm)	SPL Calculated (dB)	SPL Measured (dB)
CH-3C		
183	78	76
203	82	81
213	81	81
CH-53A		
166	82	80
185	83	83
215	84	85

Drag

Drag poses the most challenging validation process where the comparison to similar experiments is not convincing because every vehicle is different, especially in the case of the XV-25 Griffin where the model is the first to push the limitations of helicopters. The team proposes the validation process to take place at a later stage of the project where resources can be put into CFD analysis like the Airbus RACER [52] or prototype wind tunnel testing like Russo et. al performed for their box wing [48].

---

[2]https://cordis.europa.eu/project/id/502773/reporting - 24/1/2023

9

Performance & Propulsion

With the aerodynamic analysis having been performed, the team must now ensure that the XV-25 Griffin's propulsion unit is adequately designed to ensure it can meet both the mission profile and the performance requirements. As a first step, the power requirements will be analyzed over the different phases of the mission with the help of power curves. After this, an engine will be sized based on the power requirements which will then allow the team to perform an energy and fuel budget estimation. Finally, a performance analysis of the XV-25 Griffin will be performed.

9.1. Power Required

This section will present how the team arrived at the required power at different conditions for the final compound concept. This section can be split into 3 main parts; rotor power, aircraft power, and finally, the combined power required for the compounded vehicle.

9.1.1. Rotor Power

The final design parameters of the rotor calculated in subsection 8.1.2 will be used in the following section to calculate the power required for a pure rotorcraft. The method presented below is a combination of momentum theory and Blade Element Method (BEM) [12].

Advance ratio

It is assumed that in the helicopter condition of flight, the rotational speed of the rotor shaft, Ω, is constant. This value can be calculated based on the assumed maximum tip Mach number of 0.95. Using the calculated rotational speed, the tip speed can be calculated. Finally, the advance ratio, μ, is calculated which will be used later on in the rotor power calculations.

$$\Omega = \frac{M_{tip} \cdot c - V_{max}}{R} \quad (9.1) \qquad V_{tip} = \Omega R + V \quad (9.2) \qquad \mu = \frac{V}{\Omega R} \quad (9.3)$$

Where c is the speed of sound and V_{max} can be set equal to the transition speed as the rotor will be stowed into the wing after the transition.

Relation of Thrust to Weight

In helicopter mode, the thrust required by the rotor can be set equal to the MTOW along with a factor to account for the download of the rotor onto the vehicle immersed in its wake.

$$T = (1 + k_{download}) \cdot MTOW \quad (9.4)$$

Where $k_{download}$ is a factor to take into account the download due to the fuselage and wing being in the rotor wake. At 0 forward speed, the download factor is equal to 0.11. This value was based on typical values for similar compound aircraft including a reduction factor of about 40% to account for the flaps being extended to 60° causing a lower download. The download factor then decreases with forward velocity using the following equation [53].

$$k_{download} = k_{download_{V=0}} \cdot [1 - sin^2(\pi \cdot \frac{V}{2V_{max}})] \quad (9.5)$$

Induced Velocity

The first step to calculating the power required is by finding the induced velocity at different forward velocities. In hover, the induced velocity can be found with Equation 9.6.

$$V_{ind_h} = \sqrt{\frac{T}{2\rho\pi R^2}} \tag{9.6}$$

In forward flight, the induced velocity can be related to the induced velocity at hover by using a piece-wise function.

$$V_{ind} = V_{ind_h} \cdot \overline{V_{ind}} = V_{ind_h} \cdot \begin{cases} \frac{\sqrt{\sqrt{\overline{V}^4+4}-\overline{V}^2}}{\sqrt{2}} & \text{for } \overline{V} < 2 \\ 1/\overline{V} & \text{for } \overline{V} \geq 2 \end{cases} \tag{9.7} \qquad \overline{V} = \frac{V}{V_{ind_h}} \tag{9.8}$$

A curve showing the variation of the induced velocity using Equation 11.48 (at take-off conditions) can be found in the figure below. As can be seen in Figure 9.1, the induced velocity is maximum at hover and decreases substantially up to the transition speed where the rotor will be stopped and stored. The induced velocity is an important parameter of the rotor as it gives a good idea of the downwash produced by the rotor. It is important to minimize the downwash of the rotor to prevent foreign object debris (FOD) as well as to allow ground personnel to safely operate under the rotor.
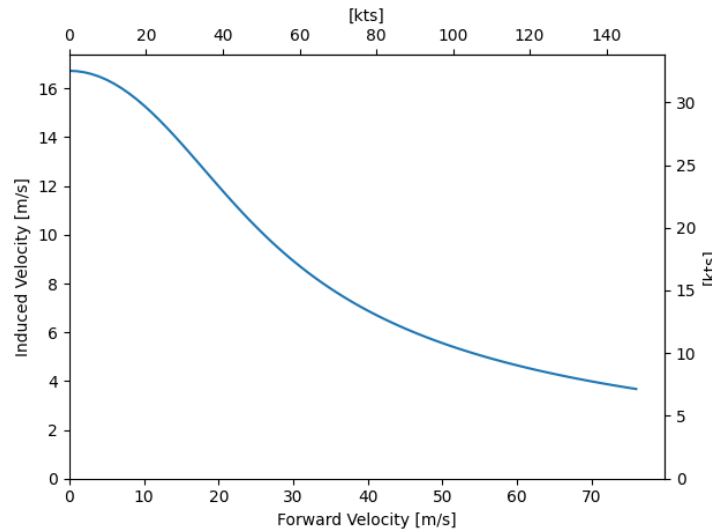

Figure 9.1: Variation of Induced Velocity with Airspeed

Induced Power
With a relation between forward velocity, V, and V_{ind} having been established, the induced power can be calculated. Induced power is defined as the power required to overcome the drag created due to the thrust generated by the rotor [12]. It can be calculated with the following equation.

$$P_{ind} = TV_{ind} \tag{9.9}$$

Profile Power
The profile power is defined as the power required to overcome the air friction drag on the blades.

$$P_{profile} = \rho A_{blade}(\Omega R)^3 \cdot \frac{\overline{C_d}}{8}(1 + 3\mu^3) \tag{9.10}$$

Where A_{blade} is the area of the blades found in chapter 8, $\overline{c_d}$, assumed to be constant, is the average drag coefficient of the blade as prescribed in chapter 8 and μ can be found with Equation 11.40.

Parasite Power
The last contribution to the power required by the rotor is the power required to overcome the drag of the rotor-less vehicle. This can be calculated with the following equation.

$$P_{parasite} = D_{parasite}V = f\rho V^3 \tag{9.11}$$

Where f is the equivalent flat plate area of the rotor-less vehicle and V is the forward velocity.

Total Power

All the individual power contributions are added up to arrive at a total power required value.

$$P_{tot} = P_{ind} + P_{profile} + P_{parasite} \tag{9.12}$$

The total power is calculated over a range of velocities (up to the transition velocity) to generate the power curve seen in Figure 9.2.
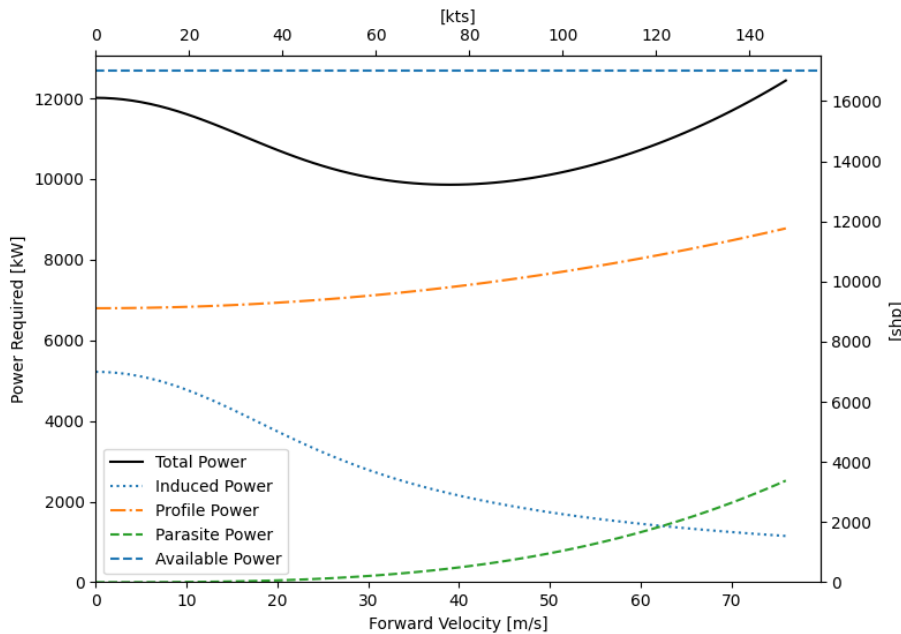
Figure 9.2: Power Curve for Pure Helicopter at Take-Off Conditions Prescribed in section 2.2

As can be seen in Figure 9.2, the power curve follows the classic 'bucket shape' seen in all helicopter power curves. The horizontal line is the available power the engine can transfer to the rotor shaft which is a constant value deriving from the fact that the engine was sized in section 9.2 to account for the extra power needed to climb vertically. The induced power decreases with airspeed due to the fact the induced velocity decreases with airspeed. The profile power slightly increases with airspeed due to there being more friction drag on the blades at higher speeds. Finally, the parasite power also increases with airspeed due to the drag experienced by the rotor-less vehicle increasing quadratically with airspeed.

In vs Out of Ground Effect

As can be seen in section 2.2, the vehicle is required to hover both in (HIGE) and out (HOGE) of ground effect. When hovering in ground effect, the induced velocity at the rotor disc is reduced proportionally to Z/D where Z is the height from the ground to the rotor and D is the rotor diameter [12]. The reduction in induced velocity at the rotor reduces the amount of induced power required as per Equation 9.9. The ratio of $\frac{V_{ind_{IGE}}}{V_{ind_{OGE}}}$ ranges from 0.55 at a Z/D ratio of 0.05 and reaches a value close to 1 at a Z/D ratio of approximately 1.2. These values are taken from a full-scale flight test performed for multiple rotors [12].

$$\Delta P = T \cdot V_{ind_{OGE}}(1 - \frac{V_{ind_{IGE}}}{V_{ind_{OGE}}}) \tag{9.13}$$

9.1.2. Aircraft Power

The final design parameters of the wing calculated in section 8.2 will be used in the following section to calculate the power required for a pure aircraft.

Drag

In order to be able to calculate the required power, the drag of the aircraft must first be calculated. As a first step, the lift coefficient required for a specified airspeed must be calculated using Equation 9.14 which can then be used in Equation 9.15 to calculate the drag coefficient. Finally, the drag coefficient can be dimensionalized using Equation 9.16 to arrive at a total drag value. In jet engines, the thrust required by the engines can be set equal to the drag of the vehicle.

$$C_L = \frac{MTOW}{qS} \qquad (9.14) \qquad C_D = C_{D_0} + \frac{C_L^2}{\pi ARe} \qquad (9.15) \qquad D = qSC_D \qquad (9.16)$$

Where q is the dynamic pressure, C_{D_0} is the profile drag coefficient of the vehicle, AR is the aspect ratio of the wing, e is the Oswald efficiency factor and S is the surface area of the wing. All the values were taken from chapter 8.

Total Power

With the drag being calculated, arriving at the total required power is straightforward.

$$P_{req} = DV \qquad (9.17)$$

Where D is the drag calculated in Equation 9.16 for the prescribed velocity.

The total power is calculated over a range of velocities to generate the power curve seen below where the power available is based on the maximum thrust the engine can provide at the prescribed take-off conditions. This value is equivalent to the engine thrust at the high-speed penetration condition which can be found in section 9.2.
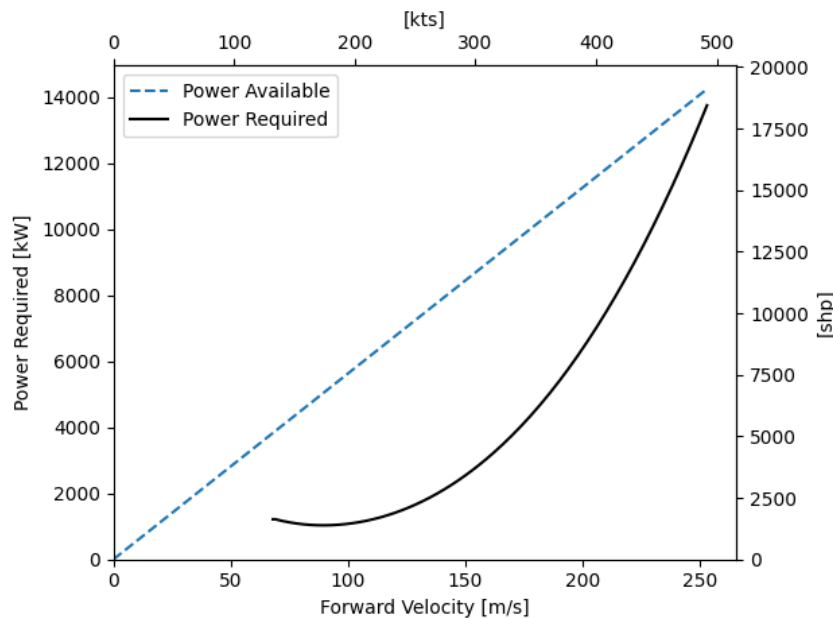

Figure 9.3: Power Curve for Conventional Aircraft at Take-Off Conditions Prescribed in section 2.2

9.1.3. Power for Compound concept

Now that the separate methodologies calculate the power for helicopter and aircraft separately, a method must be laid out to combine these into a single power requirement for the XV-25 Griffin.

Lift Distribution

Due to our vehicle having a wing, in the 'helicopter' phase of the flight, the wing will still provide a certain

amount of lift even if not enough to sustain the weight by itself. This means that whatever lift the wing produces can be subtracted from the rotor thrust required using Equation 9.18

$$T_{rotor} = MTOW - L_{wing} \tag{9.18}$$

Where the lift of the wing is calculated by dimensionalizing the lift coefficient calculated in Equation 9.14 with the assumption that for speeds lower than the design stall speed, a constant C_L value of 1.8 is used due to the flaps being extended as explained in chapter 8.

Power Distribution
With the required rotor thrust and the lift of the wing, and consequently the drag, having been calculated for different airspeeds, the total power for the XV25 Griffin can be calculated with the following equation.

$$P_{tot} = P_{ind_{rotor}} + P_{profile_{rotor}} + P_{AC} \tag{9.19}$$

Where $P_{ind_{rotor}}$ is calculated with Equation 9.9 based on the thrust requirement calculated in Equation 9.18, $P_{profile_{rotor}}$ is calculated with Equation 9.10 and P_{AC} is calculated with Equation 9.17. The parasite power contribution to the rotor power is neglected in Equation 9.19 as it is assumed the jet engines will provide the power to overcome the drag of the vehicle.

Transition
For our vehicle, the transition occurs between the design stall and transition speed. Once V_{stall} is reached, the wing provides enough lift to sustain the entire vehicle weight. Consequently, the required rotor thrust becomes 0 after V_{stall} meaning that the only power contribution for the rotor is the profile power. In addition to this, the rotational speed of the rotor is linearly decreased starting at V_{stall} reaching a value of 0 at the transition speed. This is to simulate the braking of the rotor drive shaft in order to be able to stop it and lower it into the wings at the transition speed. After the transition speed, it is assumed the rotor is stowed in the wing and thus the only remaining power contribution is P_{AC}.
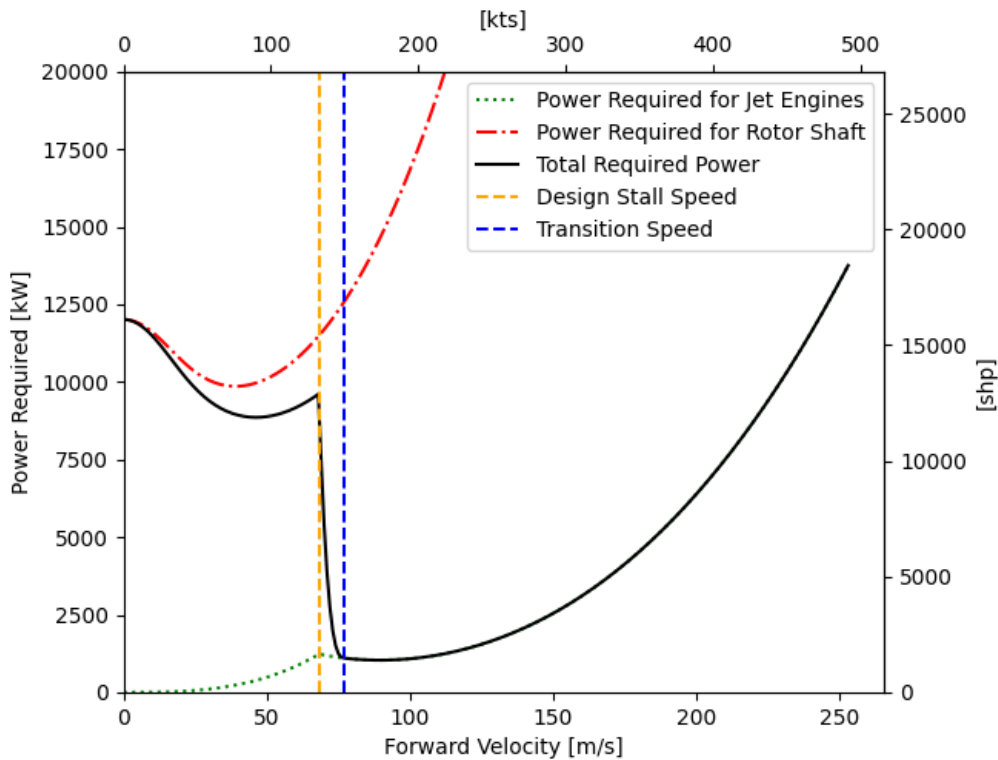

Figure 9.4: Compounded Power Curve at Take-Off Conditions Prescribed in section 2.2

Power Curve
The method presented above is now used to generate the power curve for the XV25 Griffin at the take-off conditions prescribed in section 2.2.

In Figure 9.4, the black curve represents the power required for the compounded vehicle, the red curve represents the power requirement for a pure helicopter (neglecting the lift provided by the wing and the extra thrust provided by the jet engines), the green power curve represents the power required for a pure aircraft and the two vertical lines represent the design stall and transition speed, respectively. The reduction in power (before transition) of the compound power required compared to the pure helicopter power requirement can be accredited to the fact that the induced power for the rotor reduces the more lift the wing produces and a wing is much more efficient in providing lift when compared to a rotor. Between the design stall and transition speed, the sharp decline in power can be accredited to the fact that Ω is linearly decreased until it reaches a value of 0 at the transition speed as well as the fact that after V_{stall}, the induced power of the rotor is 0 due to wing being able to provide enough lift. After transition, the rotor is stowed and thus, the total power is equal to the power requirement of the jet engines to overcome the drag. Finally, the change in slope at V_{stall} in the power required for the jet engines curve is due to the fact that up until that point, C_L is at a constant value of 1.8 whereas after V_{stall}, C_L varies based on the airspeed as per Equation 9.14.

9.2. Engine Selection & Sizing
This section will describe the inputs, processes, and outputs involved that led to the selection of an engine and the available performance of that engine.

9.2.1. Engine Selection
Firstly a type of engine has to be selected. Choosing a propulsion system is one of the most critical tasks when it comes to aircraft design, as the performance of the vehicle is highly dependent on the thrust-to-weight ratio of the engine. The options on the table were turboprop, turboshaft, and turbofan. Turbo propeller and turboshaft engines were ruled out due to a combination of factors:

- Airflow interference from the main rotor with propellers.

- Clearance between the main rotor and wing-mounted propellers.

- Using these engines would likely require three engines working in tandem which would make the vehicle overweight, unless engines like the Europrop TP400 (with a propeller diameter in excess of five meters) used on the Airbus A400M Atlas (Figure 9.5b) would have been selected.

- Turbofans are more efficient at mission altitudes and velocities.

(a) Lockheed Martin F35B Lightning II About to Take-Off from Aircraft
Carrier HMS Queen Elizabeth [1]

(b) Airbus A400M Atlas in Low Altitude Flight [2]

Figure 9.5: Aircraft in current service featuring different propulsion systems.

[1]https://theaviationist.com/2019/10/24/interesting-photo-shows-british-f-35b-in-beast-mode-aboard-hms-queen-elizabeth-aircraft-carrier/

[2]https://www.airbus.com/en/products-services/defence/military-aircraft/a400m

After coming to the conclusion to use turbofans for the compound aircraft the search began for combining a turbofan with VTOL operations. This is without using downward thrust vectoring because it would make it unable to achieve the disc loading requirement of 40 $\frac{lb}{ft^2}$ maximum [1]. To resolve this problem the team started looking into ways of powering a stowable rotor with a turbofan engine. With this in mind, the propulsion system of the F35 Lightning II Joint Strike Fighter aircraft was examined, especially the VTOL system of the F35B variant (Figure 9.5a) with its Pratt & Whitney (P&W) F135 engine and Rolls-Royce (RR) LiftSystem.

After doing a simple trade-off of turbofan engines the team decided to select this (type of) engine based on the following reasons:

- Proven combination of VTOL and turbofan propulsion.
- Relatively modern engine.
- High thrust-to-weight ratio.

This choice was later backed up by the report 'Future applications of the JSF Variable Propulsion Cycle', by the engineer who designed the F35 concept and propulsion system for Lockheed Martin, which specifically theorizes the successful application of the fighter jet's propulsion system to compound helicopters. [54]

9.2.2. Performance Estimation

With the selection of the type of engine complete the team moved on to resizing the existing P&W F135 Turbofan engine for its own thrust and power required. In order to properly estimate the new dimensions of the engine given the requirements a thermodynamic engine model was created. For this, the general workings of the engine, the RR LiftSystem, and engine specifications had to be studied.

General Engine Overview

The Pratt & Whitney F135-PW-600 engine (variant used on the F35B) is a twin-spool, low bypass ratio, mixed flow, afterburning turbofan, which in VTOL-mode powers a lifting fan in front on the engine and redirects most of the bypass airflow to ducts on the wing for roll control. The first shaft, driven by the high-pressure turbine, powers both the fan, at the entrance to the engine and the high-pressure compressor, at the start of the core. The ducted fan, which during VTOL operations provides the same amount of thrust as the thrust vectored nozzle of the engine, is powered by a low-pressure, second turbine. During all operations, some of the airflow through the engine is bled off to use for cooling. [55]
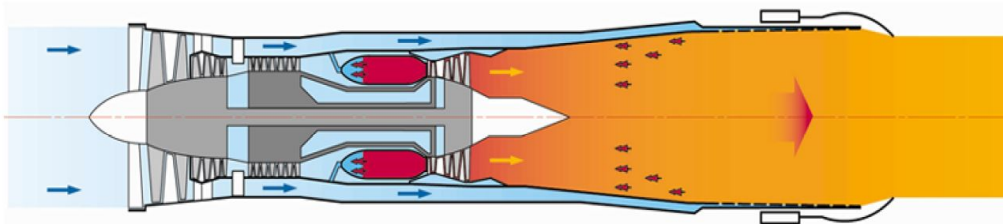

Figure 9.6: Pratt & Whitney F135 Engine Schematic [54]

The bypass, which receives part of the airflow coming from the fan at the start of the engine, in the F135-PW-600 engine has a multitude of functions, which can be grouped under the two distinct flight modes: VTOL and forward. During VTOL operations it has a bypass ratio of 0.51, Table 9.2, all of the bypass airflow is redirected to the nozzles in the wing for roll control and connection to the aft of the engine shut off. Meanwhile, in conventional flight, the bypass ratio is 0.56 (Table 9.2), and the bypass airflow is mixed into the core flow after the turbines and before the afterburner. Conclusively in VTOL mode, the bypass thrust is used for roll control and as a boost in conventional operation.

For the development of the lifting fan system (Figure 9.7) Pratt & Whitney outsourced to Rolls-Royce. The majority of the take-off thrust is delivered in half by the swiveling exhaust of the engine and the other half by the shaft-driven ducted fan. A minority is powered by the bypass exhausts in the wings, which are mainly used for roll control.
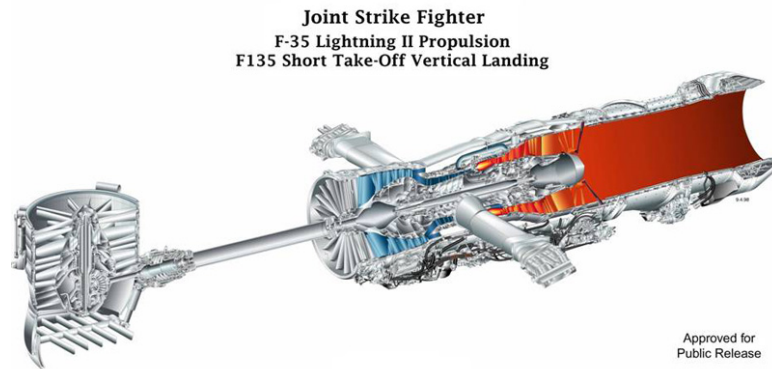
Figure 9.7: Propulsion System of Lockheed Martin F35B Lightning II [55]

Lastly the F135 engine features an afterburner (Figure 9.8a) after the remixing of the bypass and core flows. These add fuel to the exhaust of the turbine stages, adding combustion and energy to the flow and thereby increasing the thrust. In the case of the F35, it increases by around 50 % compared to conventional thrust.

Thermodynamic Model

Using the information in the previous section a thermodynamic model of the F135-PW-600 was created by the team, with the goal of resizing and reconfiguring the engine later down the line in mind. In order to verify the principles firstly a more general turbofan model of the General Electric GE9X was derived, and then adapted to the F35's engine to be able to validate this specific type. To start this off the engine was divided into stages as shown below, for each of which at least the pressure and temperature had to be calculated.

- Stage 0: Ambient
- Stage 1: Pre-inlet
- Stage 2: Inlet
- Stage 3: Fan
- Bypass exhaust (active during VTOL mode)
- Stage 4: Low-Pressure Compressor (not installed)
- Stage 5: High-Pressure Compressor
- Stage 6: Combustion Chamber
- Stage 7: High-Pressure Turbine
- Stage 8: Low-Pressure Turbine
- Stage 9: Bypass Remixing (active during conventional and afterburner operation)
- Stage 10: Afterburner (active in maximum thrust)
- Stage 11: Core exhaust

Then, using the pressure ratios for the different stages [56] and Equation 9.20 (example: fan stage), the temperatures and pressures in all but the combustion and turbine stages have been calculated. Equation 9.20 uses the temperature before, the efficiency, and the pressure ratio of the stage as inputs to calculate the temperature after. For the temperatures in the combustion chamber and afterburner estimations [56] have been applied as this is not publicly available data.

$$T_3 = T_2 * (1 + (\frac{1}{\eta}) * ((\frac{P_3}{P_2})^{\frac{\gamma-1}{\gamma}} - 1)) \qquad (9.20) \qquad P_{fan,req} = \frac{\partial m_{flow}}{\partial t} * C_{P_{air}} * (T_3 - T_2) \qquad (9.21)$$

Next the power required to operate the fan and compressor stages has been determined with Equation 9.21 (example: fan stage), which is a multiplication of the mass flow, the air pressure coefficient, and the temperature difference across the compression stage. Having found the power required by the compression sections this

power has to be delivered by the turbines, taking into account the efficiency of the shaft. The temperature and pressure after the turbine were computed by rewriting Equation 9.21 (and switching out the air pressure coefficient for the exhaust gas pressure coefficient) and Equation 9.20 respectively.

$$\frac{\partial m_{fuel}}{\partial t} = \frac{\frac{\partial m_{flow}}{\partial t} * C_{P_{gas}} * (T_6 - T_5)}{\eta_{CC} * LHV_{fuel}} \quad (9.22) \qquad T_9 = \frac{(\frac{\partial m_{flow}}{\partial t})_{core} * C_{P_{gas}} * T_8 + (\frac{\partial m_{flow}}{\partial t})_{bypass} * C_{P_{air}} * T_{bypass}}{(\frac{\partial m_{flow}}{\partial t})_{total} * C_{P_{gas}}} \quad (9.23)$$

The fuel mass flow was quantified by Equation 9.22 which, on top of the variables already known, takes into account the efficiency and temperature of a combustion stage and the heating value of the fuel (LHV_{fuel}). In case the afterburner is active the fuel of the combustion chamber and the afterburner fuel were added for the specific fuel consumption (SFC) calculation.

When it came to the remixing of the bypass and core flow in stage 9 two assumptions were made; the first being that the pressure in the bypass duct would gradually build up to match the pressure of the core flow and the second that the new temperature of the combined flow could be estimated by the use of isentropic relations in the form of Equation 9.23.

$$(\frac{P_{11}}{P_0})_{critical} = \frac{1}{(1 - \frac{1}{\eta} * \frac{\gamma-1}{\gamma+1})^{\frac{\gamma}{\gamma-1}}} \quad (9.24) \qquad T_{engine} = \frac{\partial m_{flow}}{\partial t} * (V_{exhaust} - V_0) + A_{nozzle} * (P_{11} - P_0) \quad (9.25)$$

Finally, Equation 9.24 was utilized to determine if the exhaust flow is choked in the last stage (and in the bypass nozzle). If the actual pressure ratio of the nozzle pressure over the ambient pressure is higher than this critical pressure ratio the gas flow is choked. Practically this means that there is a pressure force contribution to the generated thrust, in addition to the thrust gained from the acceleration of the mass flow through the engine. Conclusively the thrust of the engine was computed with Equation 9.25 in which the two components of thrust can be seen; first, the gas acceleration, followed by the pressure force (only active if the exhaust is choked).

9.2.3. Model Verification & Validation

This subsection first specifies how the principles of the developed thermodynamic model were verified before providing evidence for the validity of the model for the exploitation of the F35's propulsion system.

Verification

As previously stated the principle workings of the engine model were verified by correctly calculating the pressures, temperatures, powers, exhaust velocities, thrust, fuel flows, and specific fuel consumption of the General Electric GE9X engine (Figure 9.8b) and compared with values obtained from the Power & Propulsion course in the Bachelor Aerospace Engineering at the Delft University of Technology.

(a) Lockheed Martin F35C Lightning II about to Take-Off from Aircraft Carrier with Afterburner. [3]

(b) General Electric GE9X Engine on a Boeing 747 Aircraft During an Engine Test Flight [4]

Figure 9.8: Engines Used for Validation and Verification.

Table 9.1: Design Parameters for F135 Engine from Thesis Report [56].

Parameter	Symbol	Value	Unit
Inlet mass flow	W	147	kg/s
Pressure ratio inlet	PR_i	0.9	[-]
Pressure ratio fan (core)	PR_{cj}	4.7	[-]
Pressure ratio fan (duct)	PR_{df}	5.1	[-]
Fan efficiency	η_f	0.9	[-]
Shaft 1 rotational speed	N_1	10080	RPM
Bypass ratio	BPR	0.57	[-]
Engine core mass flow	W_{25}	93.63	kg/s
Pressure ratio compressor	PR_c	6	[-]
Compressor efficiency	η_c	0.85	[-]
Shaft 2 rotational speed	N_2	15200	[-]
Fuel flow	W_f	3.15	kg/s
Combustor efficiency	η_{comb}	0.995	[-]
Turbine inlet temperature	TIT	2175	K
Turbine efficiency (HPT)	$\eta_{turb,HPT}$	0.9	[-]
Turbine efficiency (LPT)	$\eta_{turb,LPT}$	0.91	[-]
Mechanical efficiency	η_{mech}	0.995	[-]
Mixer area	A_6	0.54	[-]
Thrust	FN	125903	N
Overall pressure ratio	OPR	28.2	[-]
Nozzle velocity coefficient	C_v	0.985	[-]
Thrust specific fuel consumption	TSFC	0.090	kg/Nh

Table 9.2: Pratt & Whitney F135 SVTOL Engine Specifications [58]

Short Take Off and SVTOL Propulsion System Vertical Landing Design	
Maximum Thrust Class	41,000 lbs (182.4 kN)
Intermediate Thrust Class	27,000 lbs (120.1 kN)
Short Take Off Thrust Class	40,740 lbs (181.2 kN)
Hover Thrust	40,650 lbs (180.8 kN)
Main Engine	18,680 lbs (83.1 kN)
Lift Fan	18,680 lbs (83.1 kN)
Roll Post	3,290 lbs (14.6 kN)
Length	369 in (9.37 m)
Main Engine Inlet Diameter	43 in (1.09 m)
Main Engine Maximum Diameter	46 in (1.17 m)
Lift Fan Inlet Diameter	51 in (1.30 m)
Lift Fan Maximum Diameter	53 in (1.34 m)
Conventional Bypass Ratio	0.56
Powered Lift Bypass Ratio	0.51
Conventional Overall Pressure Ratio	28
Powered Lift Overall Pressure Ratio	29

Validation

In order to validate the model for the F135's type engine the model had to be adjusted from the GE9X, as this is a twin-spool, high bypass ratio, separated flow, non-afterburning turbofan, and compared to the engine specifications from Pratt & Whitney, Table 9.2. To this end engine parameters for our thermodynamic model were taken from a report that analyzed the engine of the Lockheed Martin F35A [56], such as the pressure ratios, stage efficiencies, air mass flow, and afterburner temperature and pressure. As well as variables such as the lifting fan power [57] and bypass ratios [58]. Our own estimations were done on the combustion chamber exit / high-pressure turbine inlet temperature and the remixing chamber.

The main value utilized for validation is thrust, as this is also the main requirement of an engine. Simulations of the three distinct operating modes, VTOL, conventional, and afterburning were done and compared with the values from the manufacturer, as can be seen in Table 9.3. Which shows the model is able to quite accurately simulate the thrust of the F35B's engine. There is a small deviation during VTOL mode which mostly comes down to the overestimation of the roll posts thrust.

Table 9.3: Thrust Validation of Pratt & Whitney F135-PW-600 Thermodynamic Engine Model.

Propulsion Mode	Thrust Model	Thrust Actual	Difference
VTOL	190.7 kN / 42871 lbs	180.8 kN / 40650 lbs	5.48 %
Conventional	120.1 kN / 27000 lbs	120.1 kN / 27000 lbs	0.41 %
Afterburner	180.4 kN / 40556 lbs	182.4 kN / 41000 lbs	-1.12 %

Additionally, the fuel flow and specific fuel consumption were compared to the numbers in Table 9.1, as validating with the engine manufacturer, in this case, was not an option. This validation is limited by the fact that models of two different versions of the same engine are being evaluated, yet the results in perspective suggest reliability. For our model of the F35B engine, the nominal fuel flow was calculated at 3.02 kg/s at a thrust level of 120.1 kN, while in the F35A model, it went to 3.15 kg/s at a thrust setting of 125.9 kN. Meanwhile, both of the models come down to a specific fuel consumption of 0.090 kg/Nh.

9.2.4. Engine Sizing

For our own exploitation of the F35B's engine, some psychical changes were made to the engine layout to facilitate optimal performance for our mission:

---

[3]https://www.youtube.com/watch?v=kNO1Kqm$_j$d4

[4]https://www.bizjournals.com/seattle/news/2018/03/15/ge-aviation-tests-ge9x-engine-boeing-777x-747.html

- Increase in bypass ratio for counteraction of main rotor torque by adapting the roll control posts of the F35B to yaw control posts in the tail of our compound helicopter.

- Separate bypass and core flow to achieve better specific fuel consumption.

- Remove afterburner as no need for supersonic speeds and better specific fuel consumption.

- Change lifting fan with its required power to a helicopter rotor with its different required power, section 9.1.

- Remove swiveling exhaust for disc loading requirements and no necessity for it.

- Variable air intake diameter to limit airflow going in and thrust coming out of the engine.

Using the equations in subsection 9.2.2 and the aforementioned changes to the engine layout the internal engine parameters are shown in Figure 9.9 for a simulated thrust scenario at a horizontal, sea level take-off from zero speed. The engine model amongst other variables uses the forward speed of the vehicle to model the engine behavior so at small speeds, the program estimates a sucking capacity of the compression stages of Mach = 0.2. This estimate is based on Bernoulli's equations.
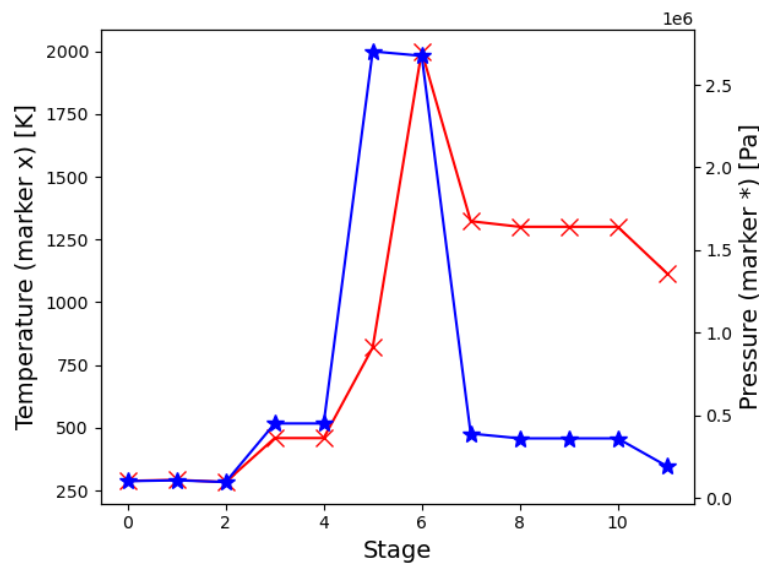
Figure 9.9: Simulated Engine Parameters.

The bypass ratio was increased to 2, mainly so that in helicopter flight enough thrust out of the yaw control nozzle is generated to counteract the torque from the main rotor. The critical phase for this was the climb in VTOL. During pure horizontal flight, the bypass ratio decreases to 1.5.

Furthermore, the model assumes that when VTOL mode is not active and the low pressure, second, the turbine is disconnected it still consumes 10% of the maximum power it absorbs during VTOL operations from the gas flow.

Next, the team decided on a variable inlet to minimize the thrust at higher speeds, as the need to oversize for the helicopter phases would also mean a great excess of thrust in the high-velocity regime. To this end until speeds of 150 m/s are reached the inlet per engine equals 1.1 m^2, between that and 200 m/s 0.3 m^2 and for speeds in excess of 200 m/s the inlet comes down to 0.2 m^2. The effect of this can be observed in Figure 9.10. Optimally the team imagines a completely variable inlet that adapts during flight to fit the situation as best as possible, yet this might be limited by the possible complexity of such a system.
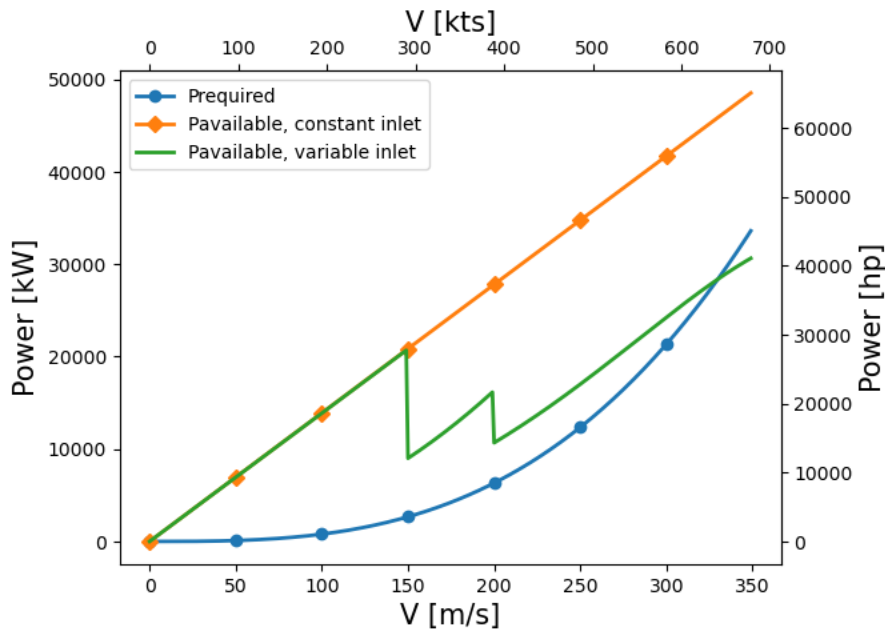
Figure 9.10: Power Required and Power Available at Sea Level Thrust

Finally to further illustrate the thrust levels at the critical phases of flight; Table 9.4.

Table 9.4: Thrust produced by one of the two engines to be installed on the XV-25 Griffin.

Flight phase	Forward velocity	Altitude	Inlet area	Thrust
Maximum take-off	0 m/s / 0 kts	0 m / 0 ft	1.1 m^2 / 12 ft^2	69.4 kN / 15602 lbs
VTOL	0 m/s / 0 kts	600 m / 2000 ft	1.1 m^2 / 12 ft^2	T_{yaw} = 28.5 kN / 6407 lbs, T_{core} = 10 kN / 2248 lbs
Climb	159.2 m/s / 309 kts	600 m / 2000 ft	0.3 m^2 / 3 ft^2	28.2 kN / 6340 lbs
Cruise	231.5 m/s / 450 kts	6096 m / 20000 ft	0.2 m^2 / 2 ft^2	14.4 kN / 3273 lbs
High speed, low altitude penetration	255 m/s / 495 kts	600 m / 2000 ft	0.2 m^2 / 2 ft^2	30.4 kN / 6834 lbs

It also should be said that for further calculations certain assumptions were made, based on our engine's expected similarity to the F135:

- Thrust-to-weight is assumed to be the same so that would present us with a weight of about 983 kg / 2163 lbs per engine.
- RPM of the engine shafts are for now assumed to be equal as detailed design, verification, and validation are needed.
- Costs are scaled with thrust available.

9.3. Vehicle Power Distribution

Figure 9.11 shows the preliminary power distribution layout of the vehicle. Some of these power values are mentioned in this report while others will still need to be determined during further design.
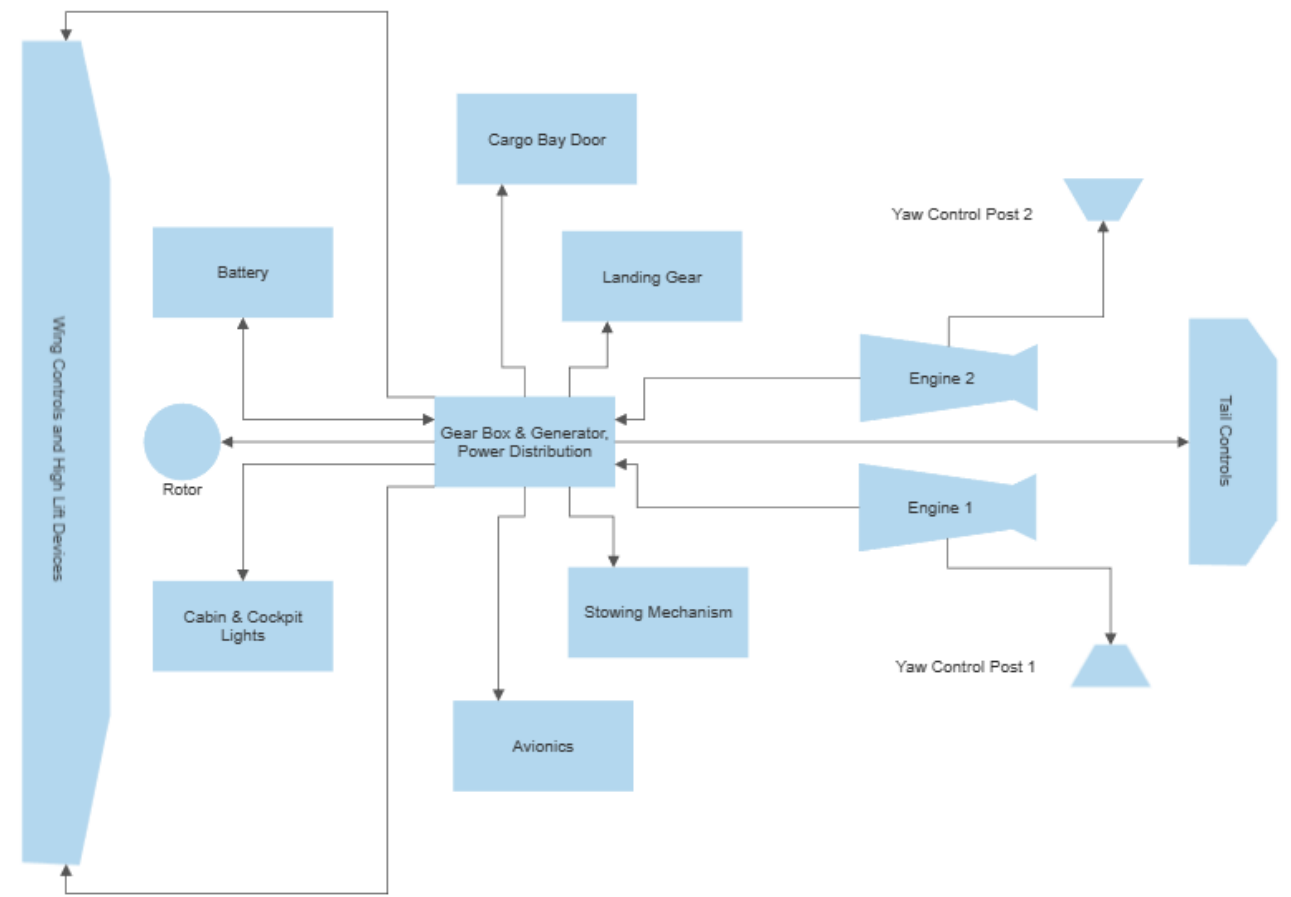
Figure 9.11: Power Distribution Schematic.

9.4. Energy & Fuel Budget

After having calculated the power requirements for different conditions as well as having sized an engine, an estimation of the energy budget and the fuel mass can be performed.

9.4.1. Energy Budget

With the times for each mission phase calculated based on the performance calculations performed in section 9.5, calculating the energy budget is as simple as multiplying the required power at each mission phase by the time of the phase as per the following equation. It was assumed that the 'Idle', 'Descent' and 'Landing' phases do not contribute to the total budget as their contribution would be very minimal.

$$E = P_{req} \cdot t \tag{9.26}$$

The resulting energy budget can be found by adding up the energy required for each phase. This results in a total energy budget of $61309 MJ$.

9.4.2. Fuel Mass

Following a similar process as was done for the energy budget, the fuel mass for the whole mission can be calculated by adding the fuel required for each mission phase. The fuel mass for each phase can be found by using the following formula.

$$m_{fuel} = SFC \cdot T \cdot t \tag{9.27}$$

Where SFC is the specific fuel consumption, T is the engine thrust and t is the time of each phase. The SFC as well as the thrust values for the different flight phases are calculated in section 9.2 while the times of the different phases are found in section 2.2. The reduction in the vehicle weight due to the usage of fuel throughout

the mission is also accounted for in this calculation. Using kerosene, the total fuel mass was calculated to be $8158kg$. This fuel mass is close to what was estimated in the class I estimation ($8800kg$) which gives the team a good indication that the fuel mass was correctly estimated. A breakdown of the fuel mass at each phase can be found in the table below.

Table 9.5: Fuel Budget Breakdown per Phase

Mission Phase	Units	HIGE	Climb1	Cruise1	Penetration1	HOGE	Climb2	Cruise2	Penetration2	HIGE	Reserves
Fuel Mass	lbs (kg)	643 (292)	1071 (486)	5126 (2325)	1171 (530)	798 (361)	896 (406)	4683 (2124)	1102 (499)	578 (261)	1920 (871)

9.4.3. Fuel Selection

With a method for calculating both the energy and fuel budget having been defined, a trade-off can be performed between kerosene, (liquid) hydrogen combustion and hydrogen fuel cells by comparing their total fuel weight and storage volume as well as storage weight.

For kerosene and hydrogen combustion, these parameters can be found by using the method to calculate the fuel mass described above whereas, for fuel cells, the total mass is found by calculating the energy required for the mission and dividing that by the specific energy of the fuel cell taking efficiencies into account. The resultant values can be found in the table below.

Table 9.6: Fuel Trade-Off

Parameter	Unit		Kerosene		Hydrogen Combustion		Fuel Cell	
Mass	lbs	(kg)	17985	(8158)	6945	(3150)	5622	(2550)
Tank volume	ft^3	(m^3)	360	(10.2)	1568	(44.4)	1268	(35.8)
Tank weight	lbs	(kg)	939	(426)	6466	(2933)	4246	(1926)
Propulsion system weight	lbs	(kg)	5051	(2291)	5051	(2291)	150135 (3900 + 64200)	

As can be seen in Table 9.6, kerosene is the most favorable option due to its storage capabilities. Liquid hydrogen combustion is a possibility worth exploring although the main advantage of being less heavy is quickly counteracted by the fact that a much heavier fuel tank is required due to the low temperatures and high pressures [59] as well as additional safety measures such as a firewall resulting in a significant weight increase. In addition to this, the fact that it must be stored in cylindrical tanks leads to the vehicle having to be significantly extended to be able to fit such a large tank leading to an even higher weight and drag. For these reasons, hydrogen combustion was neglected by the team. Using fuel cells does lead to a reduction of liquid hydrogen needed due to the increased efficiency when compared to hydrogen combustion (60% efficiency [59]) although the added weight and storage volume for the fuel cells themselves will increase the weight and size of the vehicle significantly. The propulsion system weight is significantly higher (3900kg) due to turboprops (Europrop TP400 [60]) having to be used with fuel cells which goes against what was said in subsection 9.2.1 and the weight of the fuel cells required to output 12MW of power is a staggering 64200kg. These values completely rule out fuel cells for our vehicle.

Hydrogen combustion could become a viable option in the next decade when significant technological advancements have been made to reduce both the weight required to store the hydrogen as well as the storage volume although at the present moment, the technology is not mature enough for it to be taken into consideration.

9.5. Performance

Now that the power requirements have been analyzed and an engine has been sized for the vehicle, a performance analysis must be performed to verify the vehicle meets the performance requirements. This section will be split into the performance of the vehicle when in helicopter and aircraft mode.

9.5.1. Helicopter Performance

The helicopter performance analysis of the XV-25 Griffin will focus mostly on its hovering and climb capabilities as those will be the most critical phases in the mission.

Hover Performance

In conventional helicopters, hover performance is a highly dictating factor in the design of the rotor blades. For

the XV-25 Griffin's specific mission as outlined in section 2.2, the total time spent hovering is a minimal 6 minutes. This led to the team putting less emphasis on the hover capabilities of the vehicle while still ensuring acceptable performance.

A good indication of hover performance is the figure of merit FM of the vehicle. The figure of merit is the ratio between the ideal power required to hover (this is equal to the induced power as outlined in Equation 9.9) and the actual power required for hover (this is equal to the total power as outlined in Equation 9.12) as seen in Equation 9.28. This ratio gives the team a good idea of how well the blade is designed for hover.

$$FM = \frac{P_{ideal}}{P_{actual}} \tag{9.28}$$

For the XV-25 Griffin, this value comes in at around 0.44 indicating a poor hover efficiency when compared to conventional helicopters (0.6 to 0.8 [12]). This discrepancy can be explained by the fact that the rotor has to provide high amounts of lift due to the unusual requirements imposed on the vehicle leading to a high induced drag. Namely, the weight of the XV-25 Griffin is high when compared to conventional helicopters but, more importantly, the restriction of having only 3 blades to ensure stowage into the vehicle after transition leads to a situation where the lift per blade needs to be extremely high leading to high values of induced drag. As mentioned before, the team found the above-mentioned value acceptable due to the limited time the vehicle will spend in the hover phase.

Vertical Climb Performance
The rotor was designed in chapter 8 to be able to produce more thrust than required to hover to be able to climb vertically. This extra thrust is obtained by increasing the collective angle of the blades. Based on the maximum thrust the rotor can provide at take-off conditions, the power required for producing the specified thrust can be calculated with the method outlined in subsection 9.1.1. The engine was sized so as to be able to deliver the required power when the rotor is at a maximum collective angle. The power required for hover was also calculated in subsection 9.1.1. Setting the maximum rotor power equal to the available power, the vertical rate of climb can be calculated with Equation 9.29 where P_H is the power required for hover at MTOW.

$$ROC = \frac{P_{available} - P_H}{W} \tag{9.29}$$

For the XV-25 Griffin, this results in a maximum vertical rate of climb when hovering, at take-off conditions and MTOW, of $2.92 m/s$. This value can increase to $4.66 m/s$ at end of the mission considering most of the fuel has been expelled and the payload is removed.

Having calculated the rate of climb at take-off conditions, the theoretical ceiling of the XV-25 Griffin when in helicopter mode can be found by using Equation 9.29 while varying the available power as well as the required power to hover with altitude. As can be seen in Figure 9.12, the theoretical ceiling of the XV-25 Griffin when in helicopter mode is about 1845m.
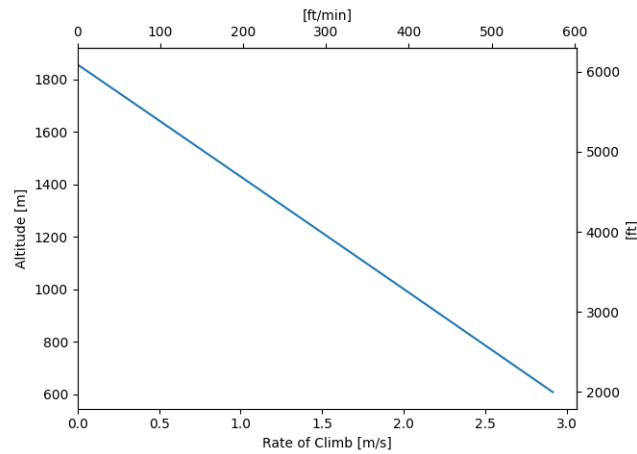
Figure 9.12: Varying Vertical Rate of Climb with Respect to Altitude.

9.5.2. Aircraft Performance

In this section, the performance of the vehicle when in pure aircraft mode, after transition, will be analyzed.

Climb Performance

The climb performance can be broken down into three main parts; the best rate of climb (BROC), the maximum climb angle, and finally the climb performance diagram.

The best rate of climb of the aircraft can be calculated based on the power curves with the following equation where the best rate of climb is when the difference between available and required power is maximum.

$$ROC = \frac{P_{available} - P_{req}}{W} = \frac{TV - DV}{W} \tag{9.30}$$

According to section 2.2, the climb phase will start at 2000ft. Assuming a steady climb with a weight equal to MTOW, the best rate of climb is 15.35 m/s at a forward velocity (V_Y) of 157.16m/s. Based on these values, the climb angle when climbing at V_Y is about 5.58°.

Finding the maximum climb angle follows a similar process to the rate of climb calculation although this time the drag curve will be analyzed. The maximum climb angle can be found by finding the point on the curve where the difference between the available engine thrust and the drag is maximum.

$$\gamma_{max} = \frac{T - D}{W} \tag{9.31}$$

Once again the maximum climb angle is found at the take-off conditions and a weight equal to MTOW. This leads to a climb angle of 7.9° at a speed of 105.2m/s.

Having established the climb characteristics of the XV-25 Griffin, it is now possible to find the theoretical ceiling when in aircraft mode. This can be done by calculating the ROC for different altitudes (thus densities) while also adjusting the available power due to the increase in altitude. Although the power required decreases with altitude due to the decrease in drag, the available thrust decreases at a faster rate, and thus, at a certain density, there will no longer be enough power to climb. This point is called the theoretical ceiling of the aircraft.
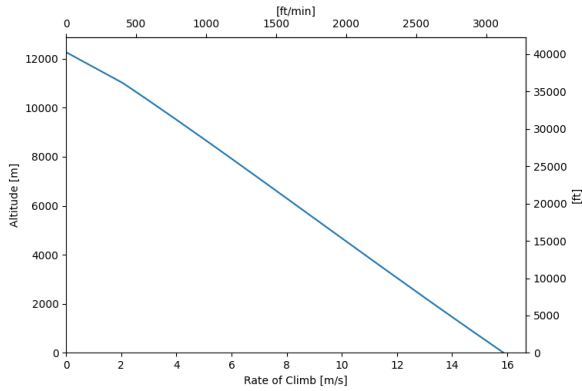
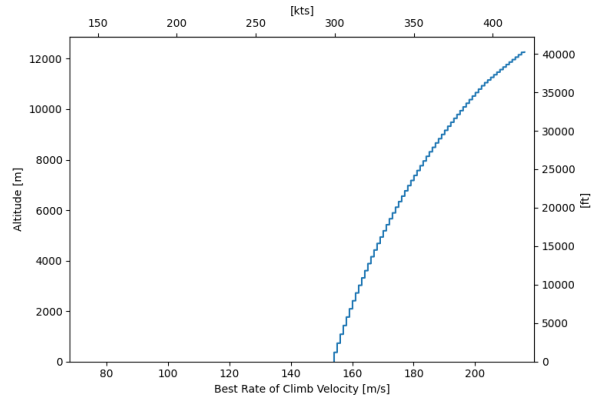**Figure 9.13:** Variation of Rate of Climb with Altitude

**Figure 9.14:** Variation of Best Rate of Climb Velocity with Altitude.

Figure 9.13 shows that the theoretical ceiling of the XV-25 Griffin when in aircraft mode is about 12100m, the point where the ROC approaches 0. Figure 9.14 shows the variation of the Best Rate of Climb velocity, V_Y, with altitude.

Payload-Range

As established from literature [21] the maximum range and endurance for a jet-powered aircraft can be found for maximum lift over drag, which can be brought down to $(\frac{C_L}{C_D})_{max}$. In our case, this value can be calculated from Figure 9.15a to be 31.1. Next using Equation 9.32 and Equation 9.33 the range and endurance respectively can be calculated, resulting in Figure 9.15b.

$$Range = \frac{V_{average} \cdot (\frac{C_L}{C_D}) \cdot ln(\frac{W_{start}}{W_{final}})}{g} \quad (9.32)$$

$$Endurance = \frac{(\frac{C_L}{C_D}) \cdot ln(\frac{W_{start}}{W_{final}})}{g} \quad (9.33)$$
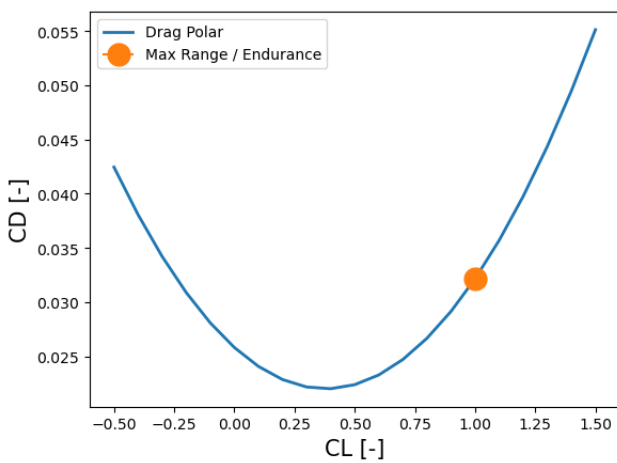
(a) CL vs CD Curve of the Aircraft.
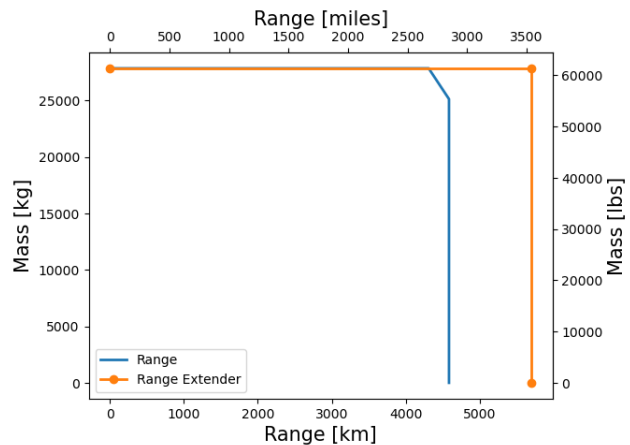
(b) Mass vs Range diagram. Range Extender Considered is Replacing Payload Mass with Extra Fuel

Figure 9.15: Performance graph of the XV-25 Griffin.

From Figure 9.15b certain ranges can observed:

- Missions range: 1852 km / 1150 miles + hover time, reserves.
- Continuous fixed-wing cruise starting at MTOW, maximum fuel and payload: 4309 km / 2678 miles taking 10.9 hours.
- Ferry (continuous fixed-wing cruise starting at MTOW, maximum fuel and zero payload): 4585 km / 2849 miles taking 12.4 hours.

- Ferry with range extender (extra fuel tank, same weight as maximum payload): 5698 km / 3541 miles taking 15.6 hours.

It should be noted that the last three ranges in the list above assume optimal conditions for lift-over-drag and velocity and a cruise altitude equal to the mission cruise altitude.

Maximum Speed

From the same literature [21] the maximum speed can be calculated for a certain altitude as the decrease in density has an effect on the drag and thrust, the variable inlet is not taken into account for this calculation. Using Equation 9.34 Figure 9.16 was derived.

$$V_{max} = \sqrt{(\frac{T}{C_{Do} * \rho * S}) \cdot (1 + \sqrt{\frac{4 * C_{Do}}{\pi * AR * e} * (W/T)^2})} \tag{9.34}$$
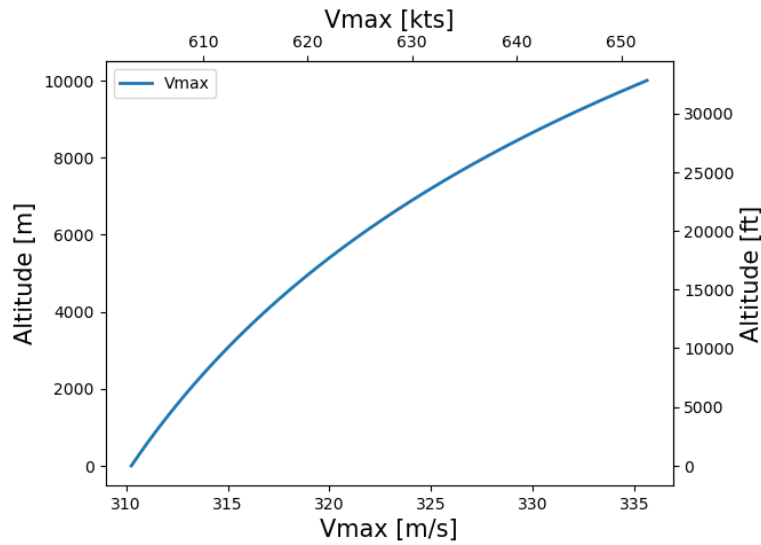
Figure 9.16: Maximum Theoretical Speed Based on Altitude.

Combining Figure 9.16 and Figure 9.10 it can be deduced that the maximum attainable speed, purely based on engines, would be around 340 m/s at an altitude of just over 10 km.

<div align="right">

10

</div>

Structures & Materials

This chapter will deal with the loads, structures as well as the materials of the aircraft. First, the general flight envelope and the associated load factors are introduced in section 10.1, followed by a more thorough treatment of the key components. Finally, in section 10.8 the center of gravity during different loading conditions is calculated, followed by the component weights in section 10.9.

10.1. Flight load envelope

The flight envelope defines the loads that the aircraft will need to endure. There are different envelopes for helicopters and aircraft. The airplane portion of the flight envelope is shown in Figure 10.1 with both the maneuver loads and gust loads shown. From the diagram, it is apparent that the gust loads at cruise produce the highest load factors.
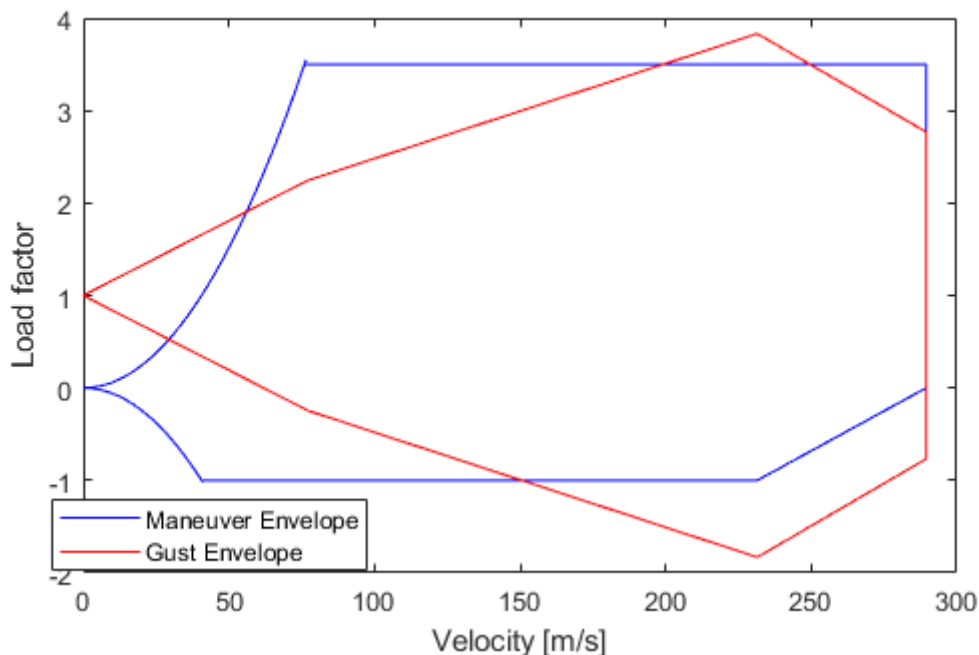
Figure 10.1: Flight Envelope Airplane Mode

Helicopters similarly have a V-n diagram, which looks similar to that of an airplane. However, the maximum load factor can be obtained already at zero velocity as the rotor produces its own forward velocity to produce lift. The customer requires a limit load factor of 3.5, so this is chosen as the maximum load factor for the helicopter flight phase up until the rotor is folded after transition.

The loads on helicopters however do not only depend on the load factor, but the critical loads for different components are obtained during different maneuvers. Especially the rotating components can be loaded up to multiple times the load factor during challenging maneuvers [61]. As an example, during a 2g maneuver of a helicopter the pitch links in particular can experience up to 3 times the steady state load. Thus, a set of maneuvers that the aircraft needs to be able to perform is selected, and typical loads on the rotating components for that maneuver are determined.

In addition, instead maintaining a constant load on the lifting surfaces during level flight independent of the velocity like aircraft, the loads of helicopter blades, hubs and pitchlinks can increase substantially during higher

velocity flying. This is due to the different velocity of the blades during their rotation as a combination of the forward flight speed and rotation, otherwise known as the advance ratio. This causes the rotor blades to flap, causing oscillating inertial forces in addition to the lift force, which is also oscillatory during forward flight. For example, at the expected maximum advance ratio of around 0.32 expected at 150 knots, the bending moment in the blades have been observed to approximately triple compared to hovering [61]. This flapping also introduces oscillating and vibratory loads into the hub and further into the entire aircraft.

10.2. Landing gear design

The landing gear is mainly designed to both support the aircraft on ground and to absorb the eventual shocks that occur during landing. Some of the less obvious, but just as critical functions of the landing gear is to provide ground maneuvering ability during taxi and take-off as well as braking after landing. Additionally, in conventional aircraft it is essential that it allows rotation during take-off. Due to the fact that the XV-25 shall be able to both take-off and land vertically not all conventional gear design applies. During normal operation the landing is vertical similar to helicopters, however for contingencies where the rotor system fails, it shall be able to land as an airplane would.

10.2.1. Landing Gear Configuration

There are multiple different choices to be made for the configuration of the gear design. These include both the retractability as well as the arrangement and location of the different landing gear, which influence the weight, and parasitic drag as well as ground maneuverability and stability.

Gear Retraction

The landing gear can be designed to be retracted or to stay in place during flight. There are advantages and disadvantages to each choice. The main advantage of the non-retractable landing gear is the light weight of the design as well as the simplicity and reliability of not using any mechanism for the landing gear. However, there is a large drag penalty due to the extra exposed surface area. The opposite is true for retractable landing gear. There is a large advantage in terms of drag performance, which comes at an increased weight and complexity. Additionally, the retraction mechanism can fail, leading to emergencies in flight and increased maintenance costs. Thus, for large aircraft that fly at elevated velocities, the designers usually choose retractable landing gear. A general rule is that for aircraft that fly at cruise speeds above 150 kts the cost penalty for the additional weight and maintenance of the retraction mechanism is outweighed by the reduction in drag [62]. Because the XV-25 cruise speed is required to be at least three times this value, no further trade-off is performed and a retractable gear system is chosen.

Gear Arrangement

There are multiple arrangements in which the landing gear can be attached to the aircraft. The main configurations used in aircraft are the tricycle, bicycle with outrigger and tail wheel configurations. Additionally, helicopters have the alternatives of skid based landing gear to their ability to vertically take-off. However, for the ability to take-off in heavy or hot conditions when vertical HOGE take-offs are infeasible wheeled landing gear is advantageous for the ability to perform roll-on take-offs [63]. Additionally, a horizontal flight landing in case the rotor system fails will also benefit from a wheeled landing gear. Thus the three configurations for the conventional aircraft are considered for a trade-off.

Trade-off for Gear Arrangement

The three arrangements will be traded off on multiple criteria. These are the weight, the stability during ground operations and landing as well as the ease of loading the landing gear allows on the ground. The weight is self explanatory for the flight performance, while the stability during ground operations and landing are important for the ability to land and take-off without tipping over. Finally, the ease of access to the cargo bay at the rear cargo ramp is considered, as different gear configurations might block the access to the ramp, while others enable easy access to the ramp.

The trade-off table is presented in Table 10.1, where the scores range from 1 (poor) to 3 (good), with the scores being adapted from Roskam [62]. The final scores for each arrangement are obtained by multiplying each score with the corresponding weight and finally dividing the sum of those scores by the sum of the weights.

Table 10.1: Landing gear arrangement trade-off table

	Weight	Tricycle	Bicycle	Tailwheel
Weight	3	2	1	3
Stability	2	3	2	1
Ease of loading	1	2	2	1
Final score		2.33	1.5	2

Additionally, a sensitivity analysis was performed, where a total of 16 weight combinations were chosen, in which the results only changed marginally and the tricycle wheel was the winner in almost all cases. Thus the selected gear arrangement is the tricycle arrangement.

10.2.2. Gear sizing

The gear sizing is based on the methods presented in [64] and it is assumed that the gear sizing will be comparable to a regional turboprop aircraft due to its similar size. Through this it can be determined that the number of wheels on the main landing gear will be 4, while there are two wheels on the nosegear. The inflation pressure of the wheels can be determined with methods from [64] as shown in Equation 10.1 using the lowest possible load classification number LCN of ten which is similar to aircraft carriers from which the aircraft shall operate.

$$p(kPa) = 430 \ln LCN - 680 = 310 kPa \tag{10.1}$$

For the relative sizing of the gear, it is assumed that the nosegear will carry at least 8% of the maximum takeoff weight according to [62] and the main gears would carry the remaining 92%.

To further specify the loads on the gears the disposition is determined in comparison to the center of gravity extremes. The disposition of the landing gear is dependent on the location of the center of gravity. The center of gravity for the aircraft needs to be between the two gear locations at all times. In contrast to conventional aircraft the rear landing gear can be placed further back, as no rotation during take-off is necessary due to the vertical take-off. Thus the disposition will be determined based upon the best packaging within the aircraft. Thus the nosegear is placed 1m behind the front of the aircraft, while the main gear is placed at 9.5m from the front. Thus the center of gravity is at all times contained between these two locations.

For this design stage the static load can be assumed to be sufficient for the main landing gear, while the braking loads is the most critical for the nose gear.

The braking loads are calculated as shown in Equation 10.2 with assumed values of 0.35 for $\frac{a_x}{g}$ [65] and l_n and l_m being the disposition of the respective landing gears from the center of gravity at the most forward center of gravity.

$$\frac{P_n}{W} = \frac{l_m + h_{cg}\frac{a_x}{g}}{l_m + l_n} = 0.297 \tag{10.2}$$

Thus the nose gear needs to carry 29.7% of the MTOW, with each tire of the nosegear carrying half that at the most forward location of center of gravity. The disposition results in the main gear carrying 84% of the weight at the most rearward center of gravity excursion, resulting in the static load on the nosegear to exceed the minimum of 8% needed to allow for steering.

Following this the tires will be selected according to diagrams obtained from [65] and using the previously obtained loads. These present different gear possibilities depending on the static load per wheel and the inflation pressure. From this the landing gear tires for both the front and rear landing gear are selected. This results in the main landing gear using 11.00 - 12 type III tires per strut with a 6 inch diameter and the nose gear using two 8.5 - 10 type III tires.

The strut of the landing gears shall be designed on the requirement to be able to land at 10 fps sink rate at structural design gross weight (SDGW) with 2/3 of rotor lift applied. However, due to the added requirement

of a gliding landing this will be the highest load on the landing gear. Thus, conventional aircraft sizing methods will be used for the strut and shock absorber sizing. It is assumed that the main landing gear will absorb the entirety of the landing forces. Thus, he stroke length is given by Equation 10.3 using the reaction factor λ of 2.5 for transport aircraft as well as the efficiency η_s of 0.8 for the energy absorbtion of an oleo-pneumatic shock absorber [65].

$$S = \frac{1}{\eta_s}\left(\frac{w^2}{1.84g\lambda}\right) \tag{10.3}$$

Here w is determined by $w = 0.9(\frac{W}{S})^{0.25}$ [65] at mid-cruise weight to arrive at the stroke length. Using these values the stroke length is determined to be 0.46m. This is a relatively large stroke length, which is results due to the high wing loading of the aircraft. Knowing the tire size, stroke length and the loads on the struts it is possible to determine the total length of the landing gear as well as the diameter of the struts.

The diameter is given by the empirical formula from [65] given in Equation 10.4 using the maximum applied load to each strut.

$$D_s = 1.3 + \sqrt{P_m} = 19.1 \text{ in cm} \tag{10.4}$$

For the length of the strut [65] provides a general rule that for landing gear with multiple tires, the total length is 3 times the stroke length, producing a total landing gear length of around 1.4m.

10.3. Hub design

The hub is a critical component that transmits the aerodynamic and inertial forces generated by the blades rotation through the air into the airframe to lift it. Thus, the entire aircraft is hanging off of this single part in between the blades and the airframe. Therefore, special attention needs to be paid to the design and reliability of this part. The type of rotor hub chosen is a fully articulated one, as it simplifies the already complex blade and hub design that already contains a blade retraction and hub lowering mechanism. Such a design is shown in
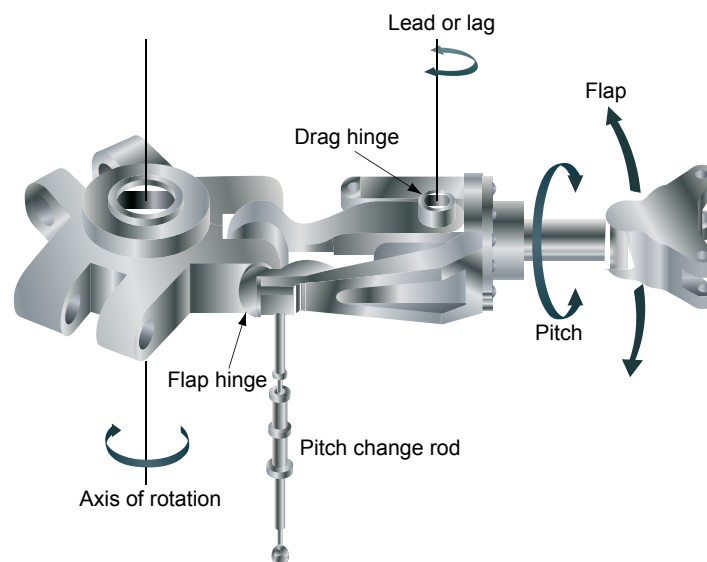
Figure 10.2: Fully Articulated Rotor Hub [1]

---

[1]https://commons.wikimedia.org/wiki/File:Fully_articulated_main_rotor_head.svg

10.3.1. Load determination

The hub is loaded in both a static and cyclic manner. In an idealized hover without forward velocity a constant force is transmitted through it to maintain the lift of the aircraft. Additionally, the rotating blades exert a constant centrifugal force in the plane of rotation on the hub. Apart from these constant forces in the most simplified case, there are cyclic forces that are applied on the blades when any flight speed or control is applied to the rotor through the pitch links that control the cyclical lift distribution. This leads to variations in the lift and inertial flap forces the blades apply on the hub. During maneuvers all these forces will be increased by the load factor of that maneuver.

Calculating the constant forces applied from each blade is possible from the calculations in Figure 8.1.2, where Equation 8.12 is integrated along the entire blade as shown in Equation 10.5.

$$F_L = \int_{r0}^{R} C_L \cdot \frac{1}{2} \cdot \rho \cdot (\Omega \cdot r)^2 \cdot cdr \tag{10.5}$$

However, due to the limiting loads on the rotating components typically being the fatigue life, the variation of the forces will need to be determined. For a preliminary analysis the flap loads will be determined using purely the aerodynamic forces depending on the advance ratio. The maximum absolute force and variation in force across the rotation will thus occur at the maximum flight velocity with the rotor working. The transition to horizontal flight begins at the stall speed and continues until the transition speed of 150 knots, so 150 knots will be the point at which the advance ratio is the greatest leading to the greatest force amplitudes. Thus, the lifting force can be written as a function of the advance ratio μ and ψ, being the position of the blade along its rotation, as shown in Equation 10.6.

$$F_L(\psi) = \int_{r0}^{R} C_L \cdot \frac{1}{2} \cdot \rho \cdot (\Omega \cdot r(1 + \mu sin(\psi))^2 \cdot cdr \tag{10.6}$$

Integrating this equation yields an estimate of the aerodynamic force the blade generates across a rotation in the maximum velocity forward flight, shown in Figure 10.3.
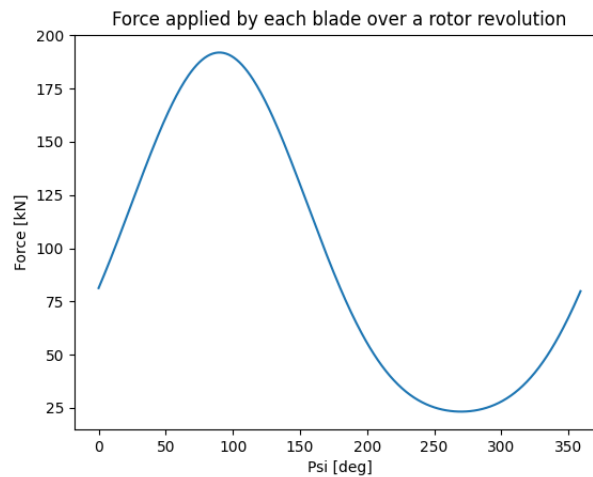
Figure 10.3: Variation of the Lift Force per Blade Along the Rotation Angle

This load is introduced through the flap hinges, and thus creates a large shear force and resulting moment across the hub from the hinges towards the center of rotation where the hub is attached to the mast.

The difference between the maximum and minimum of this curve will be the amplitude of the loading while the average is the steady state lift determined earlier using Equation 10.5. The amplitude will be crucial in determining the appropriate stress amplitude that is allowable for the determination of the fatigue life based on the stress amplitude in the hub.

It is important to note that this is a very preliminary analysis of the cyclical loads applied to the hub, as the determination of more accurate models is very complex due to the coupling of the flapping motion, lead-lag motion, the rotor's rotation as well as aeroelastic interactions. Thus, these calculations are regarded as a starting point for the analysis of the loads introduced into the rotating components and further analysis is recommended.

10.3.2. Material selection

Due to the very cyclical loading of the hub the limiting factor in selecting the material will be the fatigue life of that material compared to the weight requirements. The required cycle count can be calculated from the fraction of flight time with the rotor rotating in the typical flight profile. With 6 minutes of hover and 10 minutes of flight idle in a 2:55 hour mission. Thus around 9.2% of the flight hours include the rotor under load. With a typical operation of 2400 hours between replacement of the hub [66] this will result in 220 hours of rotor operation between replacements. With a rotor rotation rate of 187rpm and this results in $2.5 \cdot 10^6$ cycles for the required fatigue life of the rotor hub. At this number of cycles the ratio of stress amplitude σ_a obtained from Wöhler-curves to density ρ of three different possible materials will be compared. These three materials will be the common aerospace metals, Ti6Al4V, Al-7075-T6 and Stainless Steel 316L with surface treatment [67] [68] [69]. As this is a critical component with a relatively limited size the material is selected purely based on the performance instead of incorporating other parameters such as cost.

Table 10.2: Comparison of Different Materials Fatigue for the Hub

	σ_a at $2.5 \cdot 10^6$ cycles	density ρ	$\frac{\sigma_a}{\rho}$
Al-7075-T6	200 MPa	2.81 g/cm^3	71.4
Ti6Al4V	550 MPa	4.45 g/cm^3	123.6
SS316L	550 MPa	8.00 g/cm^3	68.9

The comparison of the values for the different materials is shown in Table 10.2. As can be seen, both stainless steel and titanium alloy have a vastly higher allowable stress amplitude at the reference cycle count compared to aluminum alloy. However, both of these materials also have a significantly higher density. Forming the ratio of the allowable stress amplitude and the ratio yields the selection criteria, in which the titanium alloy has the best performance. Both aluminum and stainless steel have similar performance, with aluminum being a little better. Thus, the final decision for the hub material is made in favor of the titanium alloy.

10.4. Blade Analysis & Design

This section will look at the Blade design. In order to determine the structural considerations an analysis of the loads experienced was required. The objective of the analysis was to determine the mass of the blades and establish the coning angle. For this, the case of hovering flight was considered. Once the loads have been characterized the layout of the structure can be detailed and materials traded off.

10.4.1. Blade Coning Angle

To analyze the blades we need to first assume they are rigid, or aero-elastically stiff. In hovering flight, the flow is directed down, and evenly distributed across the blades. This allows for an equilibrium state between the aerodynamic and centrifugal forces [70]. This equilibrium state will lift the rotor at the flapping hinge seen in Figure 10.2 and induce coning.
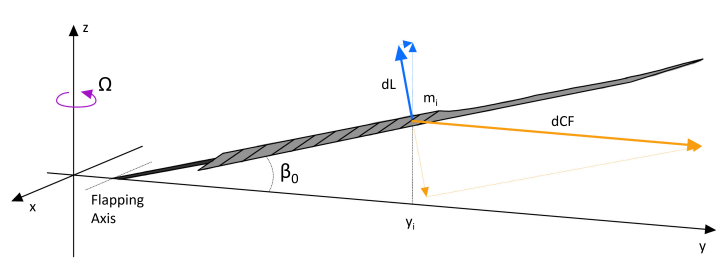
Figure 10.4: FBD of Rotor Blade

The coning angle β is set between the plane of rotation and the blade through the flapping hinge. CF is characterized as a function of the angular rotation, the radius and the mass, as seen in Equation 10.7. The Lift distribution across the rotor is derived in subsection 8.1.2. From each of these distributed forces the moments can be generated.

$$F_{CF}(y) = \int_0^R m_i \cdot \Omega^2 \cdot y \, dy \qquad (10.7) \qquad\qquad M_{CF}(y) = \int_0^R m_i \cdot \Omega^2 \cdot y^2 \, dy \qquad (10.8)$$

$$M_L(y) = -\int_0^R L \cdot y \, dy \qquad (10.9)$$

As the hinge by definition cannot carry any moment the blade will rotate, however as the blade cones the lift starts to compete with the centrifugal force. Illustrated in Figure 10.4. When the Blade rotates upwards the angle decreases the relative arm of each mass element in the blade by $Sin(\beta)$. Additionally, the hinge axis is generally offset from the hub by a factor e. As such the equation Equation 10.8 needed to be updated.

$$M_{CF}(y) = \int_{eR}^R m_i \cdot \Omega^2 \cdot y^2 \cdot sin(\beta) \, dy \qquad (10.10)$$

Balancing the moment by setting $Mhinge = M_{CF} - M_L = 0$ the two integrations can be seen in Equation 10.11.

$$M_{hinge} = \int_{eR}^R m_i \cdot \Omega^2 \cdot y^2 \cdot sin(\beta) \, dy - \int_0^R L \cdot y \, dy = 0 \qquad (10.11)$$

Applying the small angle approximation and solving for β yields the coning angle referred to as β_0 and can be seen in Equation 10.12. If we further simplify the model into a Riemann sum the equation can be seen in Equation 10.13.

$$\beta_0 = \frac{\int_0^R L \cdot y \, dy}{\int_{eR}^R m_i \cdot \Omega^2 \cdot y^2 \, dy} \qquad (10.12) \qquad\qquad \beta_0 = \sum_{i=1}^n \frac{L_i}{m_i \cdot \Omega^2 \cdot y_i} \qquad (10.13)$$

With the function, the coning angle and the mass can be compared with a fixed radius and angular velocity as well as a determined lift distribution. The plot in Figure 10.5 showcases the angles for different choices of mass per meter square. The right axis indicates the value in unit masses for this specific design. The dashed line indicates the chosen design point, with an angle of $\beta_0 = 4.989°$ and the mass per area of $\frac{M}{m^2} = 39.9 \frac{kg}{m^2}$ relating to a unit mass of $m_i = 3.92 \frac{kg}{n}$ derived from $n = 111$ sections across the radius of the blade. Resulting in a mass of 959 lbs (435 kg) per blade and a total mass of 2877 lbs (1305 kg) for the main rotors combined.

10.4.2. Blade Loads Analysis

Loads of the blades in flight are critical in the design of the structure. The initial and most important loads to consider are the lift distribution along the blade and the centrifugal forces, both generated when the blade is rotated. The forces will introduce an internal shear and moment. The internal shear is important as this characterizes the transfer of the lifting force into the hub from the blades, while the internal moments are important to determine the potential bending of the blade in flight. In Figure 10.7 these forces are plotted for the given lift distribution and set distributed mass determined in subsection 10.4.1. In order to understand the flow the coordinate system of the internal forces is defined in Figure 10.6.
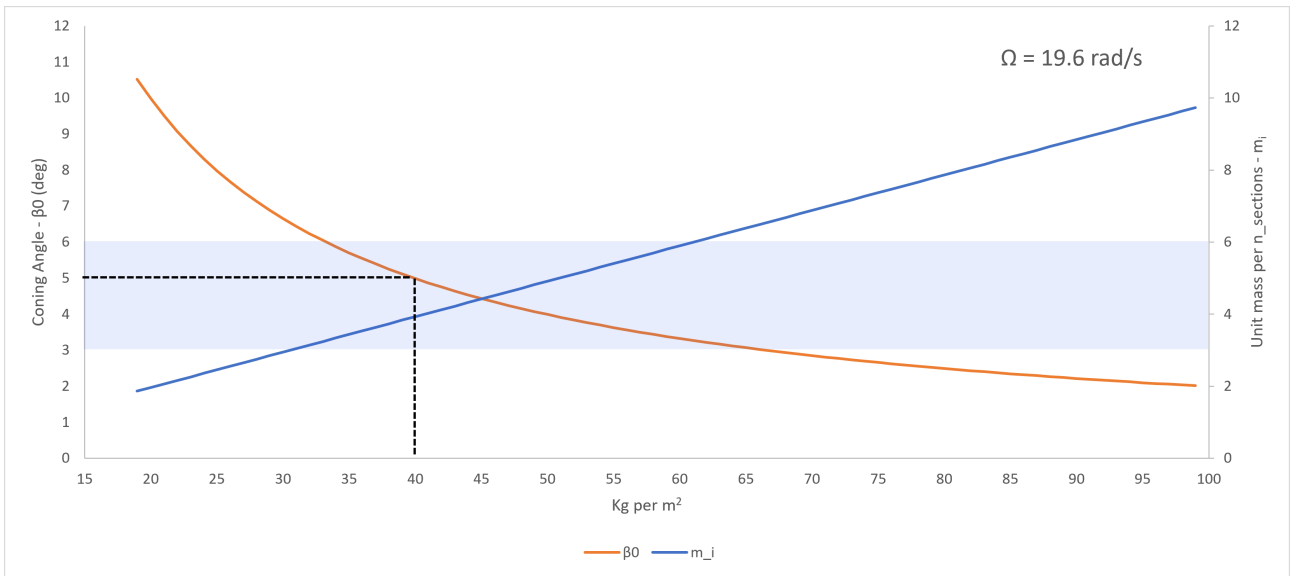
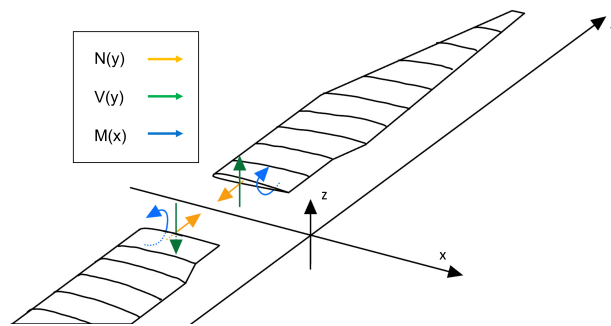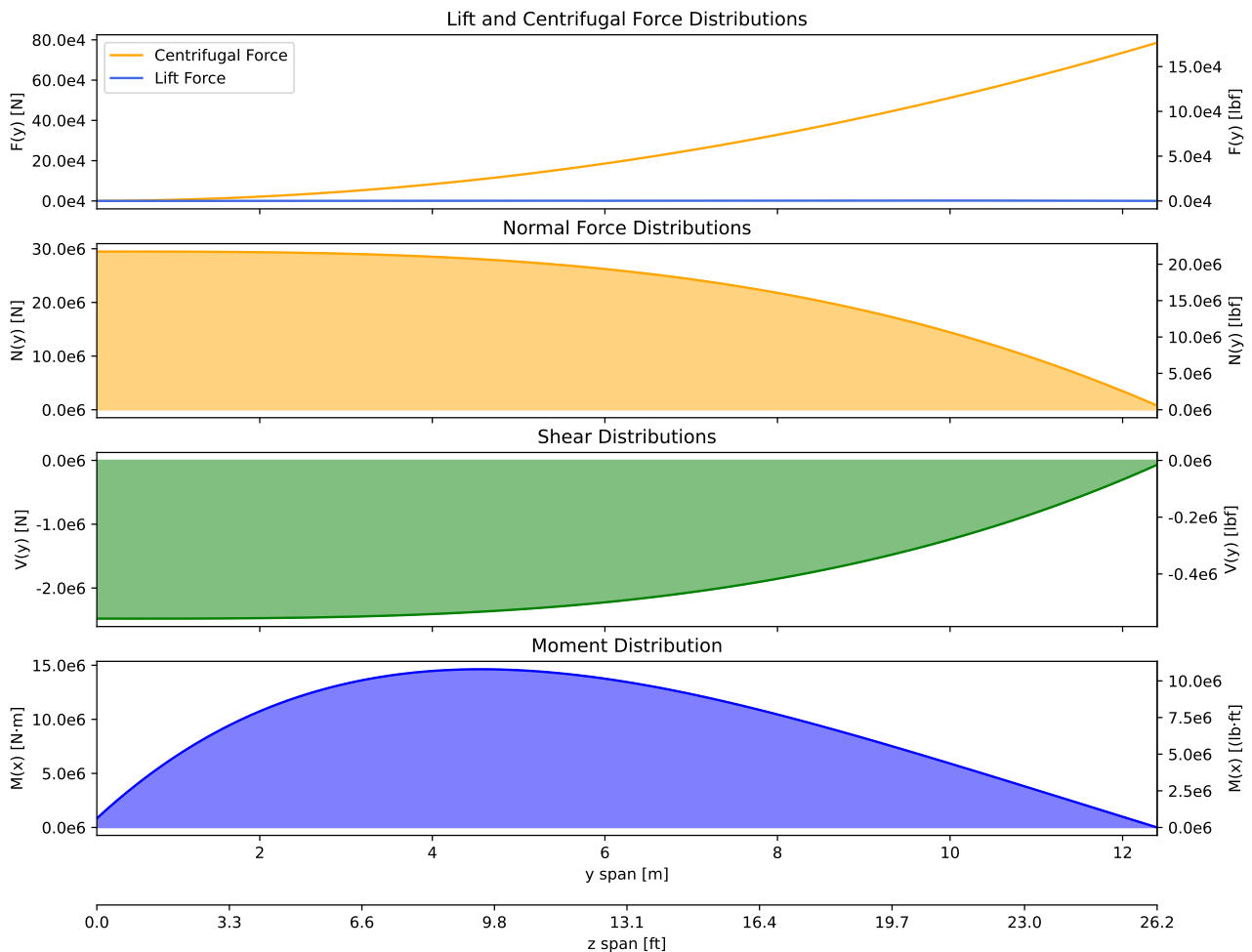**Figure 10.5:** Coning Angle with Change in Mass per m^2

Figure 10.6: Internal Force Coordinate System

The internal forces seen in Figure 10.7 allow for an understanding of the interaction of the blade in the hub and the potential bending across the blade. Looking at the Normal forces we can see that the hinges need to withstand around 30 MN of force while the blades are rotating. The lifting forces are translated to the hub in shear, generating approximately 2.4 MN of force in the hub. The moments are zero at the lift as the blade will be in equilibrium. In order to design the blade properly the aerodynamic and dynamic forces should be analyzed at different flight phases, with the range of lift distributions. Once the flight is no longer in hover, the velocities experienced change the lift distributions across the blade, this is seen in Figure 10.3. It is therefore recommended that further analysis looks at the cyclic behavior and conducts a modal analysis of the blades to better characterize the dynamic behavior of the blades in flight.

10.4.3. Blade Material

The blades for conventional helicopters are usually made from a number of different materials. A common combination is a metallic torque box in the leading edge to contain the loads, with the rest of the material mostly maintaining an airfoil shape. As previously explained, the blades of the XV-25 Griffin are required to house the mechanism for retracting the blade. Thus the internal volume can not be entirely used to retain structural strength. Instead, the skin will be constructed to maintain strength in both torsions as well as bending. Thus, a strong material, which has high strength is required that is readily shaped to the desired airfoil shapes. Thus, carbon fiber composite is selected for this part.

The internal centrifugal forces need to be carried from the tip towards the hub. These will partly be transmitted through the mechanism, containing a jackscrew carrying all the centrifugal loads. This will be required to maintain a high fatigue strength. However, due to the required weight in the blades to maintain a low coning angle the density of the material is not very important. Instead, a tradeoff will include the ease of manufacturing. The three materials considered here will be Ti6Al4V, Al-7075-T6 and Stainless Steel 316L with surface treatment [67]–[69]. The trade-off will include the fatigue strength at $2.5 \cdot 10^6$ cycles as well as the ease of manufacturing on a scale of 1-3. The weights chosen are 3 for the fatigue strength and 2 for the ease of manufacturing, with scoring on a range of 0-5.

Table 10.3: Comparison of Different Materials for the Blade Mechanism

	σ_a at $2.5 \cdot 10^6$ cycles	Ease of manufacturing	Score
Weights	3	2	
Al-7075-T6	2 (200 MPa)	5	16
Ti6Al4V	4 (550 MPa)	2	16
SS316L	4 (550 MPa)	4	20

As can be seen in Table 10.3, the mechanism elements shall use stainless steel for its ability to withstand the large fatigue loads as well as its ease of manufacturing.

10.5. Wing Box Analysis and Design

This section analyses the loads and requirements on the wing and determines the wingbox design. The methodology followed can be applied to the main wings of the aircraft, to the vertical and horizontal stabilizers, and to the rotor blades. The first step in the design process is characterizing the loads to which the wings are subjected. After that, the wing geometry will be introduced and a structural idealization performed. Finally, bending and torsion will be analyzed and the area of the skin, spar webs and stiffeners will be optimized to be within the material stress limits.

10.5.1. Analytical Load Analysis

The main force to which the wing is subjected is the distributed lift force that it produces. The lift distribution was assumed to be elliptical. For untwisted forward-swept wings, the typical lift distribution follows the elliptical pattern but with slightly more lift being generated towards the root of the wing. In section chapter 8, the twist of the wing was optimized to more closely match the ideal elliptical lift distribution. The lifting line method used for the optimization has been proven to work qualitatively, however, there have not been experimental

validations performed for multi-surface wings [38]. Therefore, the ideal elliptical distribution is assumed to conservatively size the wingbox. The ideal elliptical distribution is given by [16]:

$$L'(z) = \rho \cdot V_\infty \cdot \Gamma(z) \tag{10.14}$$

Where $\Gamma(z)$ is the circulation distribution and it is equal to:

$$\Gamma(z) = \Gamma_0 \cdot \sqrt{1 - \left(\frac{2z}{b}\right)^2} \tag{10.15}$$

The total lift can be found by integrating the lift distribution over the whole wing:

$$L = \int_{-b/2}^{b/2} L'(z)\, dz = \int_{-b/2}^{b/2} \rho \cdot V_\infty \cdot \Gamma_0 \cdot \sqrt{1 - \left(\frac{2z}{b}\right)^2}\, dz = \frac{\pi}{4} \cdot \rho \cdot V_\infty \cdot \Gamma_0 \cdot b \tag{10.16}$$

Γ_0 is obtained by setting the lift equal to half the MTOW of the aircraft - since the upper and lower wings carry half the weight each - and multiplying it by the maximum load factor of 3.8, taken from the load diagrams, as well a safety factor of 1.5 taken from the requirements. The drag distribution D' can be obtained analogously by employing the lift-over-drag ratio of $C_L/C_D = 10.2$.

An overview of both load distributions, as well as the wing geometry and the coordinate system used, can be found on Figure 10.8.
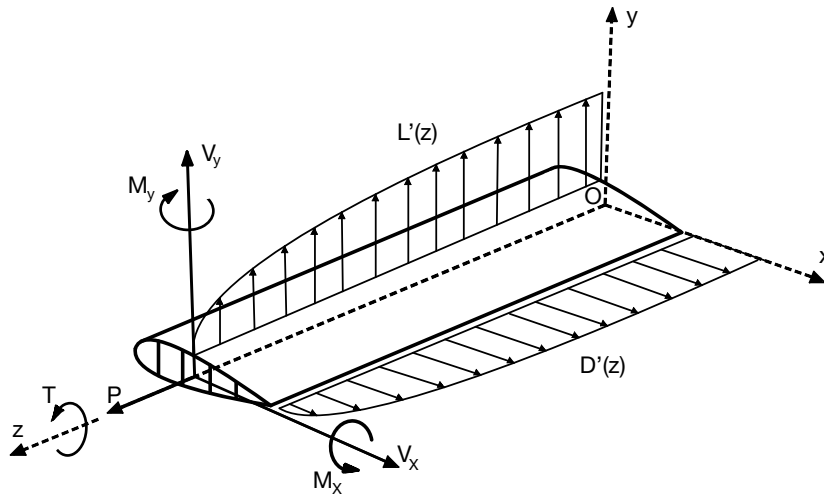
Figure 10.8: Lift and Drag Distributions, Coordinate System and Wing Geometry

The moment distributions are then found by integrating the force distributions multiplied by the along-span distance z with integration limits between the wing root and wing tip.

$$M_x(z) = \int_z^{b/2} L'(z) * -(\widetilde{z} - z)\, d\widetilde{z} \tag{10.17}$$

$$M_y(z) = \int_z^{b/2} D'(z) * -(\widetilde{z} - z)\, d\widetilde{z} \tag{10.18}$$

The shear distributions are the derivative of the moment distributions with respect to z.

$$V_y(z) = \frac{\partial M_x(z)}{\partial z} \tag{10.19} \qquad\qquad V_x(z) = \frac{\partial M_y(z)}{\partial z} \tag{10.20}$$

The torque distribution is found by integrating along the span the lift distribution multiplied by the x offset, which is caused by the sweep of the wing.

$$T(z) = \int_z^{b/2} L'(z) * (\widetilde{z} - z) * sin(\theta) \, d\widetilde{z} \tag{10.21}$$

An overview of the different distributions can be found in Figure 10.9.
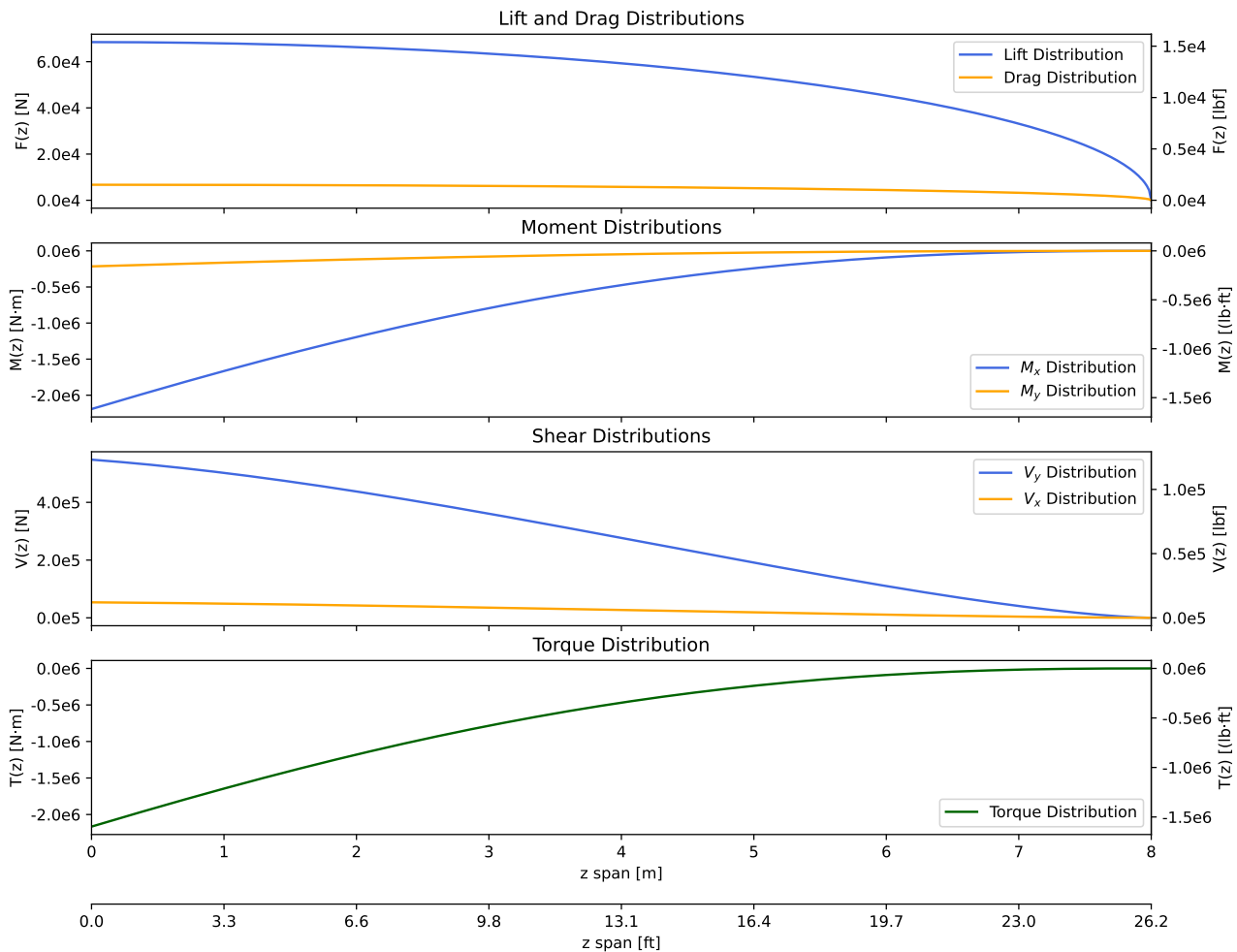
Figure 10.9: Lift and Drag Forces, Moments, Shear and Torque Distributions Along the Span of Half Wing z, from Wing Root, z=0, to Wing Tip, z=8. Blue Lines Show L, M_x, and V_y. Orange Lines Show D, M_y, and V_x.

Once the force, moment, and torque distributions were found, an internal load analysis was conducted using an idealized wing methodology in order to understand the stresses to which the wing is subjected. The critical cases analyzed were the bending and torsion of the wing, and how these forces influence the flow of stress and strain within the structure.

10.5.2. Structural Idealization

The structure of the wing was defined in chapter 8 where the airfoil, span, taper, and sweep were specified along with the chord lengths and thickness ratio across the span. From the wing platform, two cross-section idealizations were constructed. In the idealized structure, the stringers and spar flanges are assumed to act as concentrations of area, known as booms. The booms carry all the axial stresses and the skin carries the shear stresses. The wing profile shape and dimensions are fixed since they were optimized for aerodynamic performance. The number and area of stringers and flanges and the thickness of the skin can be chosen to be able to carry the stresses present in the most demanding situations while minimizing the weight of the structure. Most of the theory for this chapter was based on the textbook 'Aircraft Structures for Engineering Students [71].

The idealized cross sections are presented in figure 10.10. For both idealizations, a wing box was constructed going from 10% to 70% of the chord. In the idealization for the bending case, Figure 10.10a, the structure is divided into twenty booms along the exterior wing profile, ten on the upper side and ten on the lower. They represent the area of wing skin that resists bending as well as the area of the stringers. In Figure 10.10b the idealization for the torsion case is shown. In this case, the airfoil cross-section internal area is sectioned into three sections, with each wall given a certain thickness. The sections are non-symmetric and therefore no simplifying assumptions can be made in that regard.

(a) Bending Idealization - Boom Characterization

(b) Torsion Idealization - Area Sections
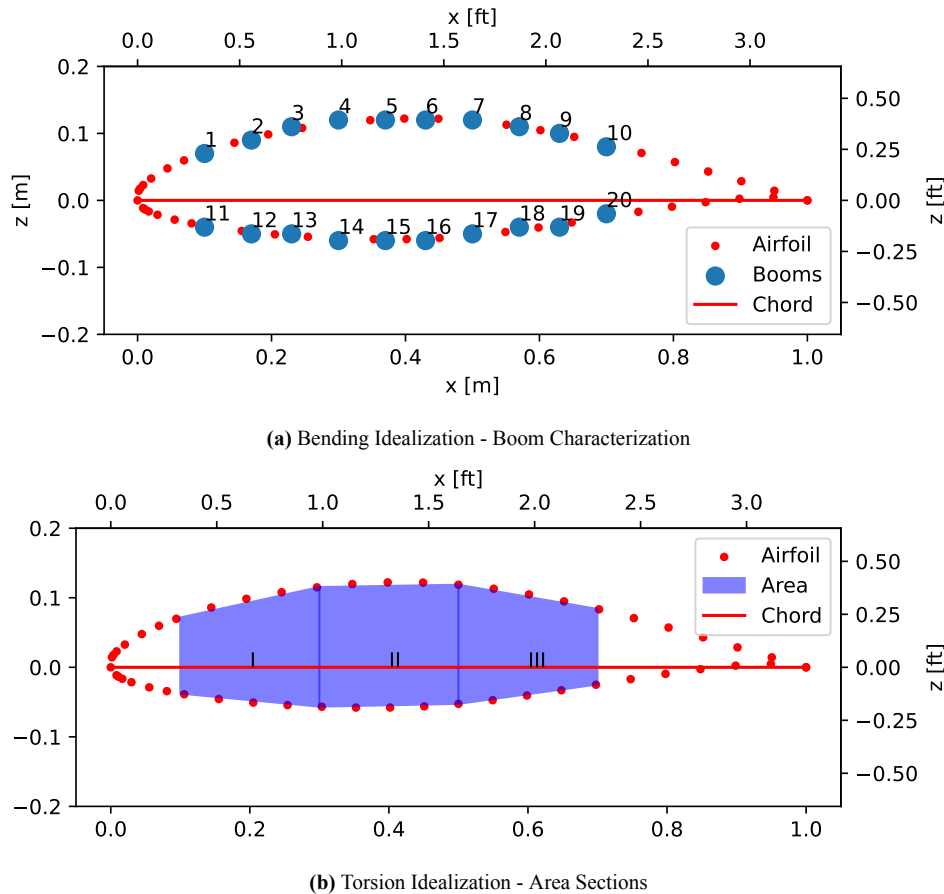
Figure 10.10: Wing Cross-Section Idealization

The procedure to idealize the wing was implemented in Python and, to completely characterize the wing, one hundred cross sections were generated along the span, one for every eight centimeters of the wing. Each cross-section took into account the local airfoil profile, twist and taper ratios, and the wing sweep. A similar methodology was followed for the torsion idealization, dividing the wing along the span into one hundred cross sections as well. It was decided to use a single material to build all elements of the wingbox, to simplify the manufacturing process and reduce the cost of the wings. After a material trade-off was performed, to be presented in subsection 10.5.5, it was decided to use aluminum 7075 as the material for the booms. It has a yield strength of 503 MPa, or 73 ksi, a Poisson's ratio of 0.33, and a density of 2.81 g/cm^3, or 0.102 lb/in^3. Although an analysis and figures were made for all materials considered, in the following subsection's plots only the results for Aluminum 7075 will be presented.

10.5.3. Bending

The objective of the section is to design the wingbox in order to be able to carry the stresses present due to bending while minimizing the weight of the structure. In order to do that, for each of the hundred sections into which the wing was divided, the stress was analyzed for each of the twenty booms. To calculate the direct stress, the bending moment distributions M_x and M_y previously obtained were used.

The first step was to calculate the centroid of each cross-section, taking into account only the booms, such that:

$$\overline{x} = \frac{\sum_{i=1}^{20} A_i \cdot x_i}{\sum_{i=1}^{20} A_i} \qquad (10.22)$$

$$\overline{y} = \frac{\sum_{i=1}^{20} A_i \cdot y_i}{\sum_{i=1}^{20} A_i} \qquad (10.23)$$

Where A_i are the areas of each boom and x_i and y_i are the distances from each boom to the coordinate axes. In the next step, for each cross-section, the moments of inertia were found. Only the Steiner terms of the booms were considered, making use of the parallel axes theorem. Each moment of inertia is then given by:

$$I_{xx} = \sum_{i=1}^{20} A_i \cdot (x - \overline{x})^2 \quad (10.24) \qquad I_{yy} = \sum_{i=1}^{20} A_i \cdot (y - \overline{y})^2 \quad (10.25) \qquad I_{xy} = \sum_{i=1}^{20} A_i \cdot (x - \overline{x}) \cdot (y - \overline{y})$$

$$(10.26)$$

For the whole analysis, the coordinate system established in Figure 10.8 was used. Once all the values are calculated, the bending stress in each boom is given by:

$$\sigma_z = \frac{I_{xx} \cdot M_y - I_{xy} \cdot M_x}{I_{xx} \cdot I_{yy} - I_{xy}^2} * x + \frac{I_{yy} \cdot M_x - I_{xy} \cdot M_y}{I_{xx} \cdot I_{yy} - I_{xy}^2} * y \qquad (10.27)$$

Furthermore, the location of the neutral axis, where the stress $\sigma_z = 0$, can be found with:

$$\tan \alpha = \frac{M_y \cdot I_{xx} - M_x \cdot I_{xy}}{M_x \cdot I_{yy} - M_y \cdot I_{xy}} \qquad (10.28)$$

By coding the procedure in Python, the stress for each location of the wing was found, assuming a constant boom area of 1000 mm^2, or 1.55 in^2. To calculate the stress, the worst case scenario with the highest wing loading was used, furthermore, a conventional 1.5 safety factor was applied. The results are presented in Figure 10.11.
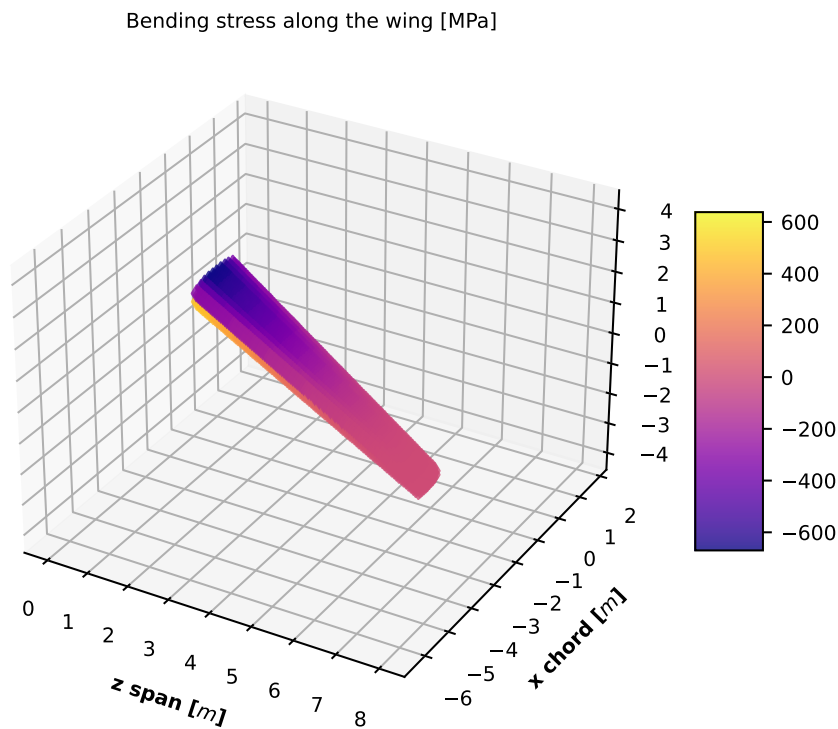
Figure 10.11: Normal Stress due to Bending Along the Wing

Positive stress represents tension and occurs on the lower half of the wing, while negative stress is compressive and occurs on the upper surface of the wing. To size the materials the absolute value of the stress is the driving consideration. It can be seen that the stress is a function of the span of the wing, decreasing towards the wing tip. It also depends on the distance to the neutral axis, being highest in the central portion of the chord. It can be

seen that the stress is above the material yield strength of 503 MPa at the root of the wing, so the wing would fail because the initial constant area was too small at the root of the wing. Furthermore, it can be seen that the stress is well below the yield strength for the sections of the wing closer to the wing tip, which means that the initial constant boom area was too high in those areas and it lowered to reduce the weight of the wingbox.

An optimization procedure was then developed to arrive at the optimal boom areas for each section of the wing. The objective was to homogenize the stresses along the span by progressively reducing the area of the booms to achieve a maximum stress of 90% of the material yield strength, fulfilling the load requirements while minimizing the weight.
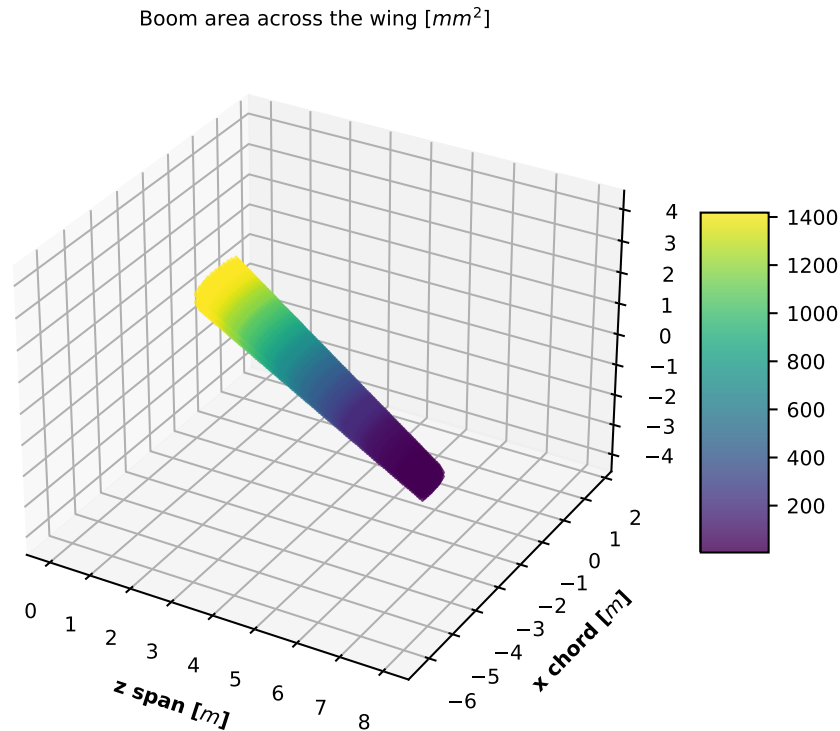
Figure 10.12: Optimized Boom Areas Across the Wing

Recalculating the normal stresses using the optimized boom areas results in the stress distribution presented in Figure 10.13. Comparing the results with those obtained previously it can be seen that the optimized areas better distribute the stress and achieve a maximum stress of 90% of the material yield strength all along the span.

Optimized bending stress along the wing [MPa]
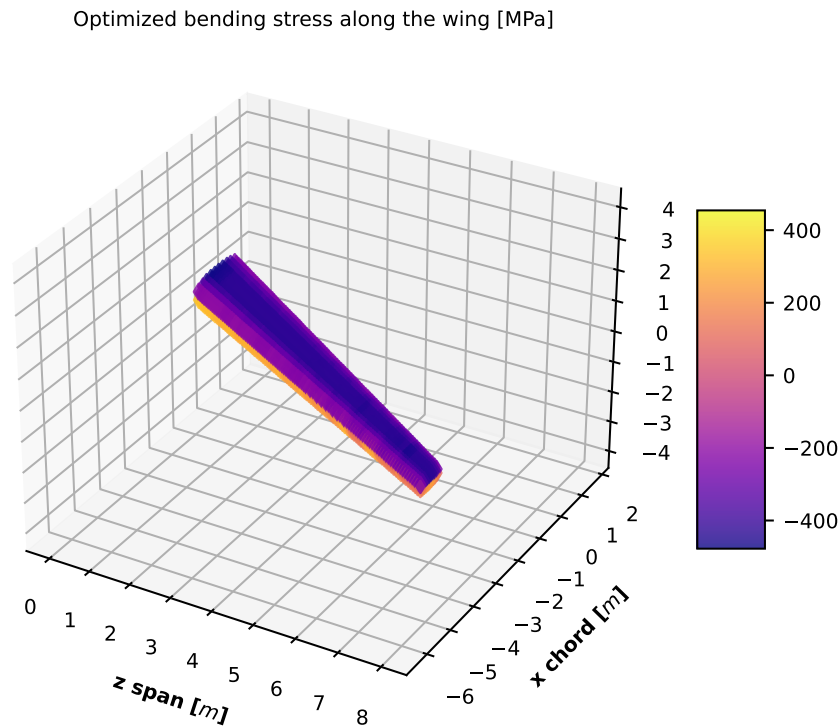
Figure 10.13: Normal Stress due to Bending Along the Wing with Optimized Boom Areas

The optimization procedure was an iterative process where the boom areas of a cross-section at a specific span location were slightly changed and the centroid, moments of inertia, and stress at each boom were recalculated. If the stress at any boom was higher than 90% of the yield strength, the areas of the booms at that location were increased. If, however, the stresses were lower than the objective, the boom areas at that location were decreased. The optimization ended when the maximum stress at that span location was equal to 90% of the yield strength. It must be kept in mind that the stresses are calculated for the worse case scenario to be encountered during flight and, as such, the actual stresses in the wingbox will be much lower for the majority of the time.

10.5.4. Torsion

The objective of this subsection is to optimize the thicknesses of the skin and spar webs in order to resist the shear flows induced by the torsion distribution characterized in Figure 10.9. For the torsion analysis, the idealization shown in Figure 10.10b was used. The wing cross-section was divided into three distinct cells with the use of two spar webs. The cells have been labeled I, II, and III in the figure. The software developed is capable of optimizing continuously changing thicknesses at each point of the wing. However, to simplify the manufacturing process, it was decided to use the same skin thickness for all the skin panels; a different thickness was calculated for the leading edge web of cell I and the trailing edge cell of section III; and lastly, a third thickness was optimized for the two spar webs dividing the cells.

For each section of the wing, the local thicknesses were optimized. The first step was to find the areas of the cells and the lengths of each wall based on the wing geometry, taking into account all wing parameters. The sum of the torques over each cell must then equal the total torque over the entire cross-section. The torque over each cell is equal to two times the area of the cell, A_i, multiplied by the shear flow, q_i, therefore:

$$T = 2A_1q_1 + 2A_2q_2 + 2A_3q_3 \tag{10.29}$$

We have then one equation with three unknowns. To obtain the remaining equations to be able to solve the system, compatibility is used, by setting that the angle of twist $d\theta/dz$ must be the same for all cells.

$$\frac{d\theta}{dz} = \frac{1}{2A_r} \oint_V \frac{q}{Gt} \, ds \tag{10.30}$$
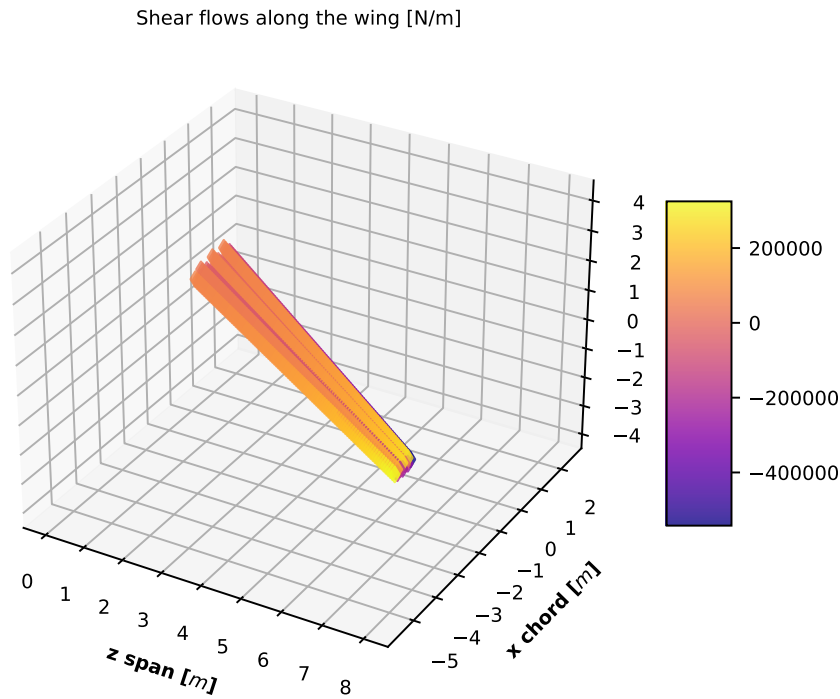
Figure 10.14: Shear Flows Along the Wing

We thus get four equations and four unknowns. Solving the system of equations results in the values of q_1, q_2, q_3, and $d\theta/dz$. The results for the shear flows are shown in Figure 10.14. It can be seen that the shear flows increase towards the wing tip since the areas of the cells are much smaller because of the taper ratio. The reduction in cell area more than offsets the decrease in torsion force due to the decrease in lift force arising from the lift distribution.

The minimum thickness for each wall at each section can then be obtained by dividing the shear flow at that wall by the maximum shear stress supported by the material.

$$\tau = \frac{q}{t} \rightarrow t_{min} = \frac{q}{\tau_{max}} \tag{10.31}$$

To find the shear flow in the webs, the shear flows of both surrounding cells were taken into account. The analysis was performed for each wing section to obtain the distribution of thicknesses required along the span of the wing. Furthermore, the required wing structural dimensions were calculated for each material considered, in order to aid in the material choice.

10.5.5. Material Trade Off

For the material trade-off, the main consideration was the weight of the structure. Several aerospace materials were considered in the analysis. The required areas of stringers and spar flanges were calculated to resist bending and the areas of the skin and spar webs were calculated to resist shear flows due to torsion. The area optimization occurred for each section of the wing along the span, one hundred sections overall. To calculate the weight, the areas were multiplied by the section length and the material density to obtain the section weight. The weights of all sections were then added up to arrive at the total weight of the wing. The results are presented in Table 10.4.

The table shows the weights of the structural elements of the wing, excluding mechanisms and any other components. As can be seen in the table, steel resulted in the highest structural weight, the reason being that steel alloys have high ultimate strengths but low yield strengths, which were the design criteria. Titanium performed well for the weight of stringers and spar flanges but not so much for the skin and spar webs. Titanium is furthermore significantly more expensive and hard to work with than the other materials. The lightest option would be the use of aluminum for the internal elements and magnesium for the skin. However, because of the poor corrosion properties of magnesium and to simplify the manufacturing process by using only one material, it was decided

Table 10.4: Wing Box Material Characteristics and Structural Weights

	Aluminum 7075	316 Stainless Steel	Titanium Ti-6AI-4V	Magnesium Alloy
Density [g/cm^3]	2.81	7.8	4.43	1.77
Yield strength [MPa]	503	290	880	200
Poisson ration	0.33	0.27	0.34	0.35
Total Weight Stringers and Spar Flanges [kg]	321	1423	378	463
Total Weight Skin and Spar Webs [kg]	299	831	472	189
Total Weight [kg]	620	2254	850	652

to build the whole wingbox out of Aluminum 7075. Aluminum is furthermore easy to manufacture and work with and presents good corrosion properties. The total structural weight of the wing is thus 620 kilograms or 1367 pounds. That's the weight for one wing, the weight of the total wing assembly, including both sides of the upper and lower wings, is, therefore, four times as high, for a total weight of 2480 kilograms, or 5468 pounds.

10.6. Fuselage

The fuselage is the largest part of the aircraft containing all the other systems. Multiple loads from different parts need to be carried which results in different loading cases, such as the bending loads introduced by the inertial forces and the landing gear when landing, or the lift forces of the wing and tail during a gust in cruise.

10.6.1. Bending loads

There are multiple sources of bending loads on the fuselage. These include forces introduced through the wing and stabilizer along both the z and y-axis, reacted by the inertial forces of the mass along the fuselage as well as different lift and rotor forces. Additionally, there will be the loads introduced by the rotor in helicopter mode, as well as from the gear when landing. The horizontal loads introduced into the tail causing a bending load are at their maximum when a gust is encountered in cruise. This changes the instantaneous angle of attack, causing a lift to act on the surface. This force can be calculated as given in Equation 10.32.

$$L_{VT} = \frac{1}{2}\rho V_{cruise}^2 C_{lVT} S_v = 36.34 kN \tag{10.32}$$

This lift introduces both a bending moment across the fuselage, while also applying an angular acceleration to the aircraft. However, the thrusters in the tail create a similar moment to counteract the torque of the rotor. This force of 58 kN as introduced in subsection 9.2.4 produced by the thrusters exceeds the maximum gust load and is thus used to calculate the moment distribution.
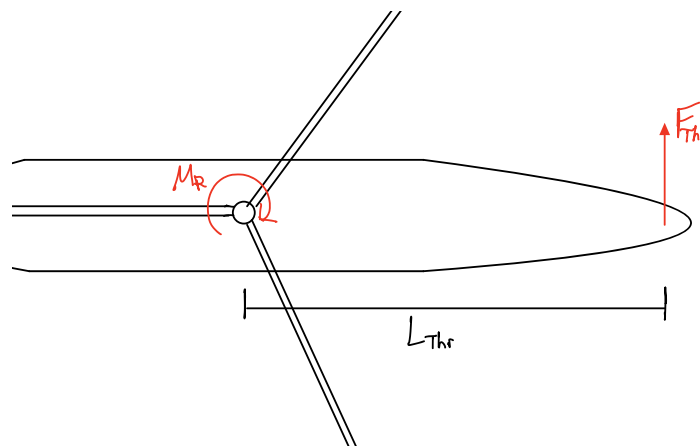
Figure 10.15: FBD of Bending About Z-Axis

This results in a linear moment distribution with a peak of $M = L_{Thr} \cdot F_{Thr} = 609kN$ at the point of where the rotor introduces its torque and linearly reducing to 0 at the point the thruster lies.

A more complicated loading occurs in the z axis, where loading for the maximum load factor during horizontal flight as well as the landing forces are considered. The freebody diagram for the landing case is shown in Figure 10.16.

The weight force distribution is obtained by using the masses from each component and distributing it across the length of that component, multiplied by the load factor of 2.5 as used in the gear sizing. As the landing occurs on the main gear only, that is the only force considered apart from gravity. As it is a dynamic event, there is an angular acceleration as well during the landing. This angular acceleration is given by $\alpha = \frac{F_{MG}l_{MG-CG}}{I_{yy}}$ where the moment of inertia is obtained from the CAD model. The landing gear force is calculated to be the maximum take-off weight times the load factor n.

(a) Landing Case - Free Body Diagram   **(b)** Landing Case - Kinetic Diagram
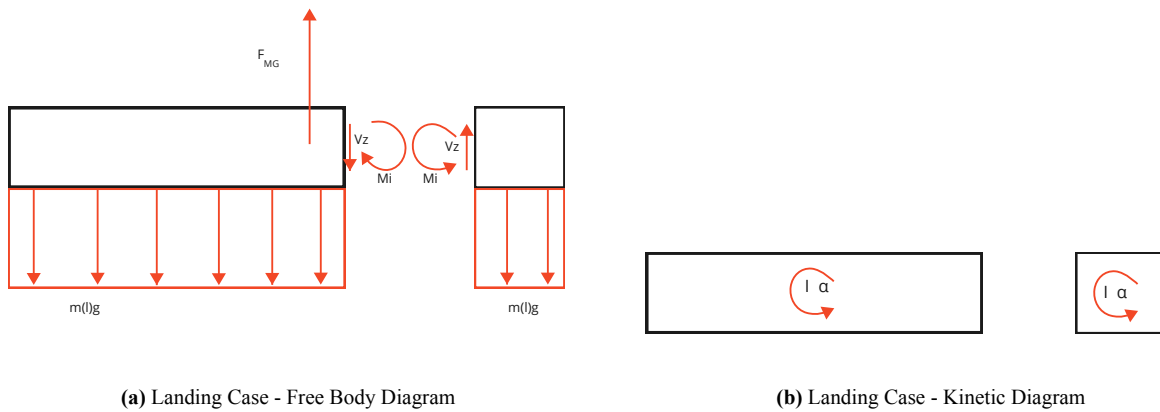
Figure 10.16: Fuselage Bending - Landing

Thus the shear force distribution and moment distribution can be calculated as shown in Equation 10.33, with the landing gear contributions only being considered when the cutting plane is rearwards of the landing gear.

$$Vz = \int_0^x nm(l)g - m(l) * \frac{\alpha l}{2} dl - F_{MG} \qquad My = \int_0^x nm(l)g - I_f(l)\alpha dl - F_{mg} \cdot (x - x_c g) \quad (10.33)$$

Here $m(l)$ and $I_f(l)$ represent the mass and inertia distribution across the front section of the aircraft up until the cutting plane. The maximum bending moment for this load case is $2.07MNm$ at the point where the landing gear touches down.
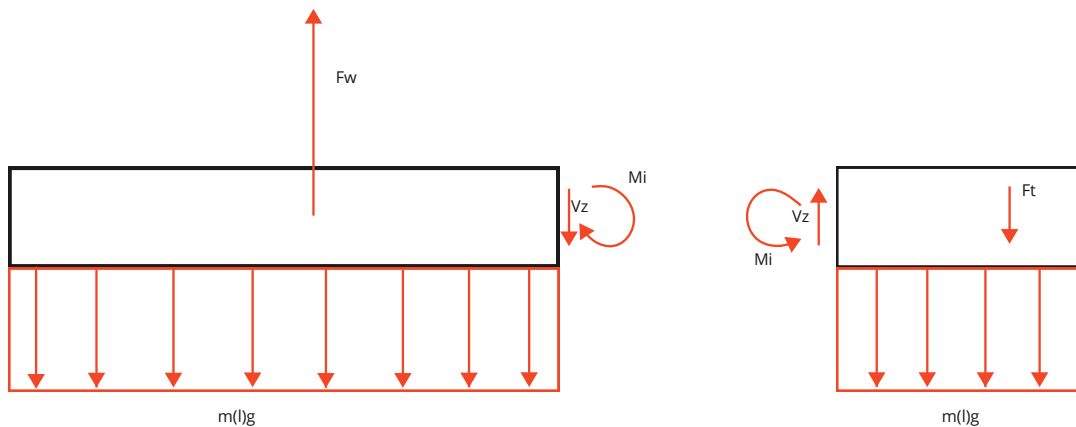
Figure 10.17: Fuselage Bending - Maximum Gust case

The second critical load case for the fuselage bending is a gust at MTOW flying at cruise speed. This is a conservative assumption, as the aircraft will have burnt at least some fraction of the fuel to arrive at cruise speed, thus reducing the loads. The free body diagram is shown in Figure 10.17. Here the same mass distribution as for the landing loadcase can be used. The equations for the shear and moment distribution are very similar to those of the landing case, however instead of a singular force from the landing gear and angular acceleration, in this case, there will be two distributed forces from the wing and the horizontal stabilizer. These forces from both the lift and weight will be multiplied by the maximum load factor $n = 3.8$ to reflect the maximum loading. Thus, the equations are the same, but instead of subtracting the gear contributions once the cutting plane is rearwards, the wing and stabilizer will only be considered once the cutting plane is alongside those surfaces. This results in Equation 10.34.

$$Vz = \int_0^x nm(l)g - F_w(l) - F_s(l)dl \qquad My = \int_0^x nm(l)gdl \qquad (10.34)$$

The maximum bending moment of this load case is $1.67MNm$, with the maximum occurring at the joint between the wing and the fuselage.

10.6.2. Internal Torque in Fuselage

The vertical tail serves to stabilize the aircraft around the yaw axis in flight. To do this, it will introduce a force at its aerodynamic center that acts perpendicular to the flight direction along the y-axis. As this aerodynamic center can be misaligned with regard to the center of gravity, it will introduce a torsion along the fuselage in addition to bending. Similarly, the thruster will also introduce a torsion load into the fuselage while hovering. This produces two different torque loads. The torque from the tail thruster will be reacted from the rotor introducing a rolling moment resulting in a constant torque across the fuselage between the tail and rotor with a magnitude of $T = F_{Thr} \cdot H_{ThrCG} = 87kNm$.

The horizontal force from the stabilizer will be reacted by inertial forces as the aircraft gains angular acceleration from the force as shown in Equation 10.35. The moments of inertia around the x-axis are estimated from the CAD model that was created for the aircraft.

$$\alpha = \frac{F_{Thr} \cdot H_{Thr}}{I_{xx}} \qquad (10.35)$$

With the angular acceleration, the free body diagram and torque along any position of the fuselage can be constructed as shown in Figure 10.18.
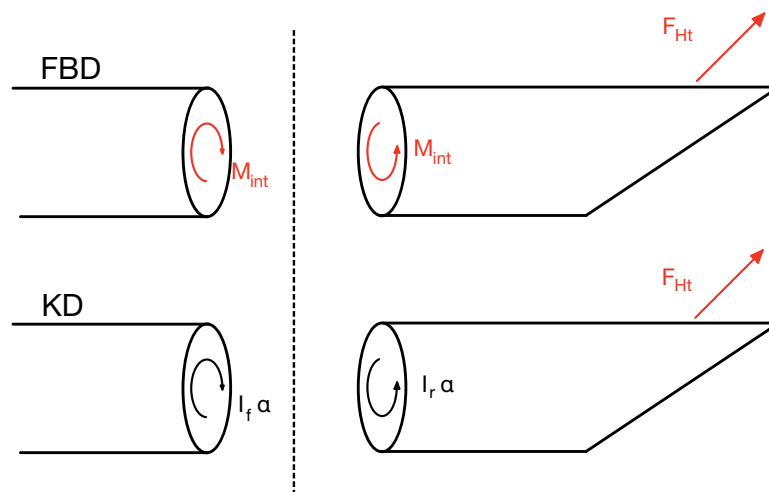
Figure 10.18: FBD of Horizontal Stabilizer Gust Loads

Using these diagrams the equation for the internal torque is calculated in Equation 10.36 using the left half of Figure 10.18 and Equation 10.35.

$$M_{int} = I_f \cdot \alpha = \frac{I_f}{I_f + I_r} F_{Ht} \cdot H_{Ht} \tag{10.36}$$

The front and rear moments of inertia are determined by measuring the moments of inertia of every component using the CAD model and distributing it evenly along the length of that component. Thus a moment of inertia per unit length can be constructed for each component, which is added from the front to the point at which the equation is evaluated. When this equation is evaluated along the length of the entire aircraft using the previously determined horizontal stabilizer force and a distance of the application of the force to the center of gravity of 1.5m the diagram shown in Figure 10.19 is obtained.
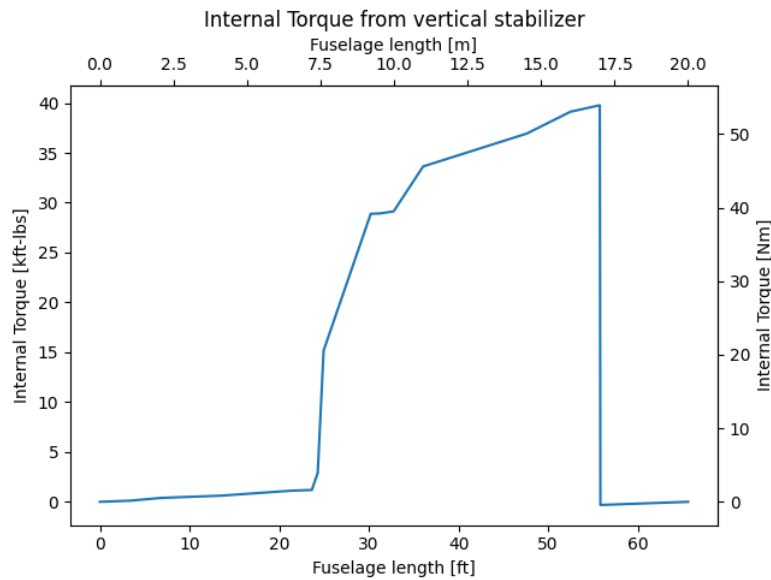
Figure 10.19: Fuselage Internal Torque

It can be observed that a large internal torque persists until around the midpoint of the aircraft. This is due to the fact that a large part of the moment of inertia of the aircraft is due to the wing and rotor, which have a large moment of inertia and are attached only to the center of the aircraft, resulting in a large drop in the internal moment around those attachments, while ahead of these components the fuselage, payload, and other systems are kept close to the center of gravity.

10.6.3. Design
As the aircraft is designated to carry cargo and three crew, an unpressurized fuselage with a small pressurized volume for the crew in the cockpit will be used. This enables a lower weight, due to the fuselage only having to carry the previously calculated loads. As the fuselage does not need to be a pressure vessel, the fuselage will be a rounded rectangle shape to reduce the frontal area while still allowing the required payload size to be accommodated. Similar to the wings, the fuselage will be constructed from skin with stringers and frames. These stringers are responsible for carrying the majority of the calculated bending loads, while the skin forms a closed section carrying the torsion through the fuselage. As no windows will be required along the payload bay, the only large cutout in the skin will be the payload ramp in the rear. Thus the majority of the fuselage can take advantage of the light and strong stringer on skin construction, with local reinforcements around the ramp, especially since the ramp is the location with the largest internal torque.

The material selected is based on the cost function ratio of strength to density. Comparing common materials that are used for aircraft structures, such as aluminum, carbon fiber and stainless steel. Of these, the strength-to-weight ratio of carbon fiber is the greatest, with possible weight savings of up to 30% possible compared to more traditional materials. This will enable large weight savings to increase performance.

10.7. Mechanisms

In this section, the design of the mechanisms needed is showcased. These mechanisms are conceptualized below in the following subsection. There are three key mechanisms, specifically the retracting rotors, the lowering of the main rotor and hub, and the stowing of the main rotor and hub in the body of the fuselage and wings.

10.7.1. Blades Retraction

The concept of retracting the blades in flight is not novel. In 1969 Sikorsky began wind tunnel testing on the "Telescopic Retracting Aircraft" rotor [72]. The development and testing of this concept came to light in order to make feasible the stored rotor in flight compound concept and increase the cruise speed capability of compound configurations. The principle employed is to store a jack-screw in the internal structure that connects the extended portion of the rotor to the fixed portion, through anchored nuts. The concept tested by Sikorsky lead to a number of benefits, including static and dynamic force reductions. Reducing the rotor radius also decreases the aeroelasticity problems at high speeds and increases the stability of the blade during the lowering phase of the transition.

In Figure 10.20 a top view cross section of a single blade can be seen. The concept retracts the final third of the rotor into the first two thirds. To do so each blade will contain a threaded titanium rod connected to an electric motor. The threaded rod will sit inside a threaded cylinder attached to the final section of the blade. Actuating the motor will extend or retract the blades. The final third of the blade will also extend inside the non-actuated part of the blade. This combined with the cylinder will add structural rigidity to the blades. For redundancy, the blades can be extended without the electric motor by disengaging the actuator gears and utilizing the centrifugal forces experienced when the rotor are rotated.
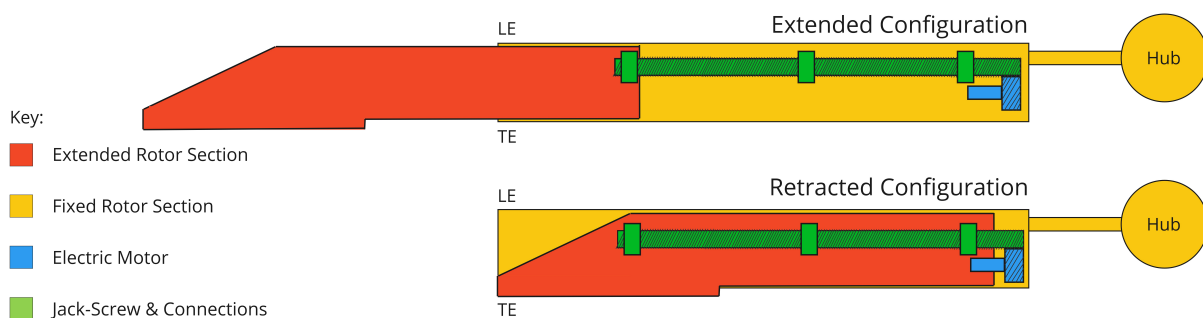
Figure 10.20: Blade Retraction Mechanism Design

A key consideration in the detailed design of the structure will be to account for the increase in chord at the rotor tip's. The tip trailing edge extends past that of the trailing edge of the fixed portion of the blades. To account for this the structure at the trailing edge of the fixed section of the blades will need to split along chord and open to accommodate the increased chord. This is not considered a problem as the structural component of conventional blades is housed in the forward half of the chord, with the aft half usually consisting of a foam or honeycomb structure. Additionally, the required hinge location is past the structural portion of the rotor and the deflection required would be a few degrees. The part of the fixed blade that needs to split and accommodate the extended chord can be latched mechanically by the portion of the extended section that remains within the fixed blade section. Further analysis should be conducted as to the material selection of the internal structure in the second third of the blade to optimize for structural rigidity of the entire blade while allowing for ease in storage.

10.7.2. Rotor Hub Lowering

The lowering of the hub requires a combination of mechanisms working in tandem, specifically a lowering mechanism, a breaking mechanism and locking mechanism. The process the mechanism will follow includes first disengaging the engines from the rotor and allowing it to windmill. Once the rotors are windmilling the breaks are engaged and the rotor is brought to a stop. Once the rotors are stopped, then the mechanism in subsection 10.7.1 can be activated. Then the lowering of the hub and rotors can begin, This will then bring the entire system into the fuselage and wings. When the rotors are close to the body, the mechanism in subsection 10.7.4

are actuated allowing access to the storage compartments and a mechanical groove will maintain the alignment of the rotors with the compartments. In Figure 10.21 a front view cross section can be seen of the concept.
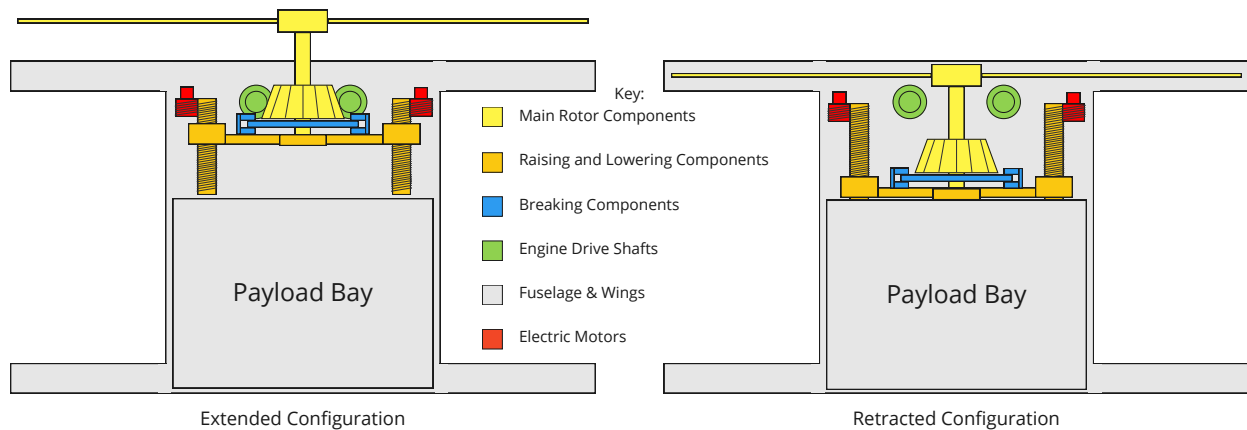
Figure 10.21: Hub Lowering Mechanism Design

The concept leverages the beveled gears connecting the engines to the main rotors and lowers the entire hub downwards physically disengaging the main rotor from the gears of the engines. The lowering is facilitated by jack screws mounted above the payload bay. Actuated by electric motors the jack screws connect to the hub through a bearing at the base of the mast. The braking mechanism sits above the bearing. In-flight the lift generated by the rotors will force the mast and hub to constrain between the engine gears and the bearing locking it in place for powered flight.

10.7.3. Rotor Brake Design

The aircraft design calls for the storage of the main rotor during cruise to increase the aerodynamic performance. In order to do so, the main rotor needs to be stopped in the correct orientation before it is lowered into the fuselage and upper wings. For safety reasons, the brake is sized so that it is able to stop the rotor while it is spinning at maximum rotational speed. That is the case when the rotor wing tips achieve Mach 0.92, which was the maximum design speed. For a speed of sound of 340 m/s at sea level conditions, the rotational speed is 24.5 rad/s, or 234 rpm, since the blade radius is 12.4 meters.

The moment of inertia of the rotating blade assembly, conservatively assuming a thin flat plate, is:

$$I = \frac{1}{2} \cdot M \cdot R^2 \tag{10.37}$$

The mass of the each blade is 186 kg, and the mass of the hub is 415 kg, which gives a total spinning mass of 972 kilograms. The moment of inertia is thus 74727 kg/m^2. The rotational kinetic energy of the system is given by:

$$E_{rotational} = \frac{1}{2} \cdot I \cdot \omega^2 \tag{10.38}$$

Using the values stated previously, the rotational energy comes out to be 23.83 MJ. All that kinetic energy needs to be absorbed and dissipated by the brakes in the form of heat. Since the brake operation occurs infrequently, only twice throughout the mission profile, active cooling of the brake won't be required and the brake will be cooled through cooling ducts with air-stream flow. Therefore, the brake will be sized to be able to initially absorb all the heat generated and slowly dissipate it after.

The usual brake system for aircraft landing gears consists of a closed system with a stack of static and rotating disks, to which a pressure force is applied to push the disks together. There are several options for the brake material, the most common among which are steel or carbon fiber-carbon composites, also known as C/C. The material properties of both materials are presented in Table 10.5.

Table 10.5: Brake Disk Material Characteristics

	Steel	C/C Composite
Specific Heat [J/g*K]	0.59	1.42
Thermal Conductivity [J/m*s*K]	59	100-150
Coefficient of Linear Expansion [1/K]	14e-6	5e-6
Upper Operating Temperature [ºC]	1500	2500
Density [g/cm^3]	7.8	1.7

Given the specific heat and the difference between the maximum operating temperature and the ambient temperature, the mass of brake material required to act as a heat sink for the total amount of rotational energy can be calculated. It comes out to be 14.9lbs (6.76kg) for C/C brakes and 35.89lbs (16.28kg) for steel brakes. It is thus decided to opt for carbon-carbon as the material of choice.

Additionally, carbon brakes are optimal for the system since carbon brakes wear out mostly based on the number of brake applications, whereas steel brakes wear out proportionally to the applied brake duration. To brake the rotor, only one long application is needed and so carbon maximizes the lifespan of the brakes.

Carbon disks wear out faster when cold; so to maximize the life of the component, the brake sequence will start by applying light pressure in order to heat up the brake until the optimal temperature is achieved, from which point onward higher brake pressures can be applied.

To minimize the weight of the system and improve safety, an electromechanical brake actuation system will be used, as opposed to a hydraulic system. Electromechanical actuators remove the need for complex hydraulic piping systems and avoid hydraulic fluid leaks, which jeopardize safety, pose fire dangers and are damaging to the environment.

10.7.4. Rotor Storage

The last key mechanism required to transition from hovering to forward flight mode is the storage compartment access doors. The fuselage and wings will contain doors that actuate along the skin and open to give access to the storage compartments below. The location of the storage compartments can be seen Figure 10.22, with each top wing and the fuselage aft of the rotor hub having storage space.

Redraw with Hub Doors also
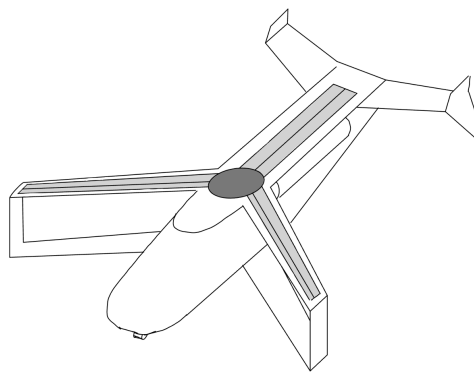
Figure 10.22: Storage Mechanism Locations

In figure Figure 10.22, the central section, seen as the dark oval where the hub is located will be closed by a skin that slides under the fuselage forward of the hub gap, closing the gap in forward flight and stowed out of the flow in hovering. This can be seen in seen in Figure 10.23, where the door is actuated forwards and aft to open and close the hub compartment. To counter the vortexes in hover that may be generated with the storage compartment being open, the mast and gap will be covered with a flexible material to close off the interior from the exterior, this material will deform to allow the storage and stretch to cover the gap when the mast is extended. To actuate the storage door, electric motors will be used.
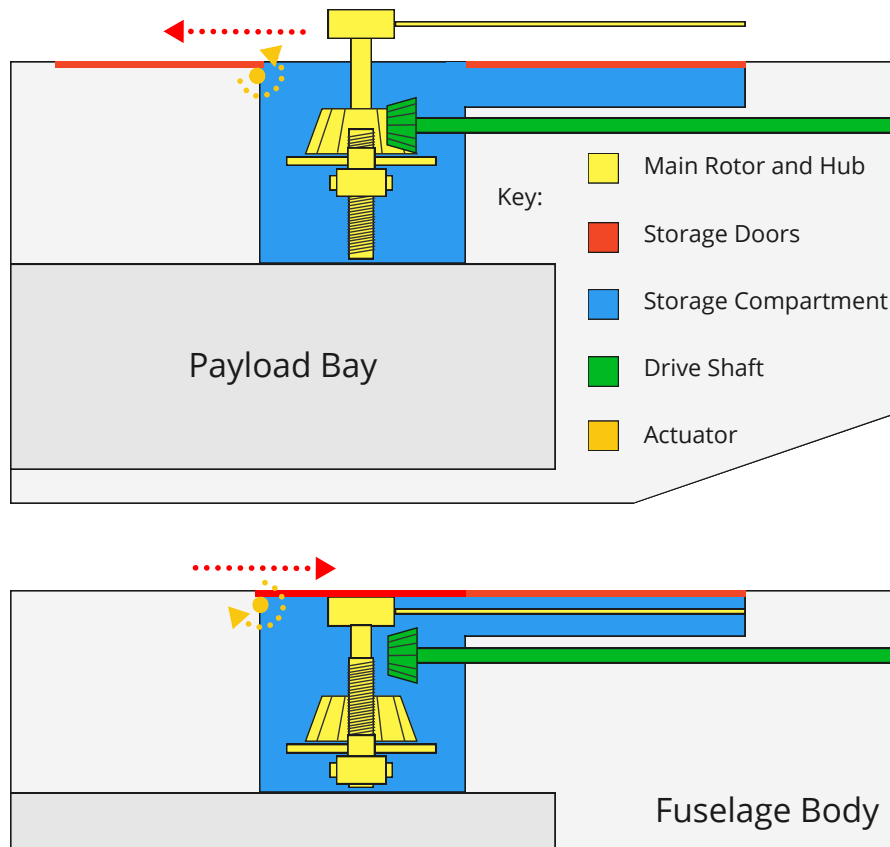
Figure 10.23: Hub Storage Mechanism

The wing and fuselage storage compartments work with two doors, with each door sliding open along the skin of the fuselage or wing. Electric motors will be positioned along the edges of the compartments to actuate the doors when the rotors are to be lowered or raised. A cross-section of the starboard wing compartment can be seen in Figure 10.24. Showcasing how the storage bays will open and close to house the rotors. The inner surface of the compartments will be lined with flexible material to both protect the blades but also allow for the pressure to assist in forming the blades into the space when lowered. This will likely be needed to counter any dynamic movements generated from the flow velocities during lowering.
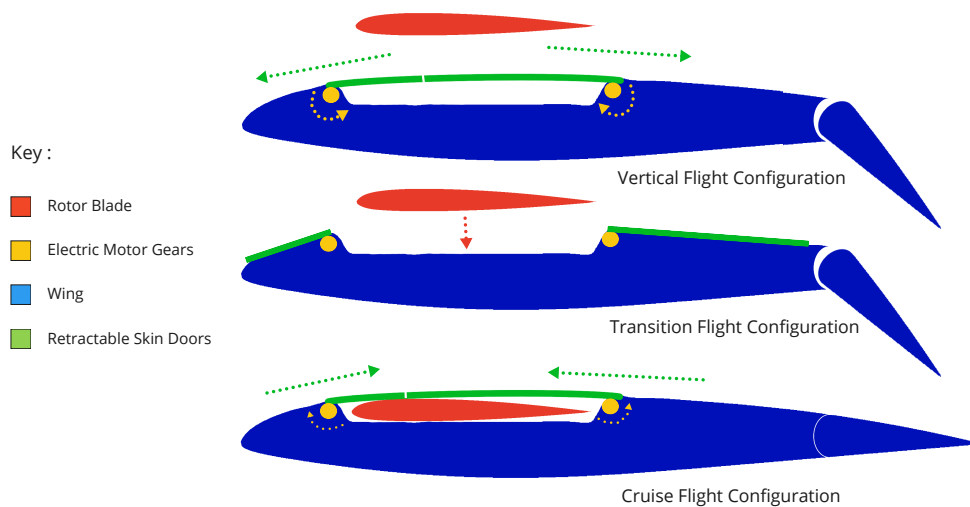
Figure 10.24: In-Wing Rotor Storage Mechanism

These mechanisms will work with the maneuvers characterized in Figure 7.2. There will need to be further structural and aerodynamic analysis to determine the exact behaviors of these mechanisms and their respective sizes and capabilities.

10.8. Loading Diagram

The loading diagram using the calculated empty, the payload and fuel weights and their respective location of the center of gravity a loading diagram is constructed. This illustrates the variation of the center of gravity depending on the loaded fuel and payload and is shown in Figure 10.25.
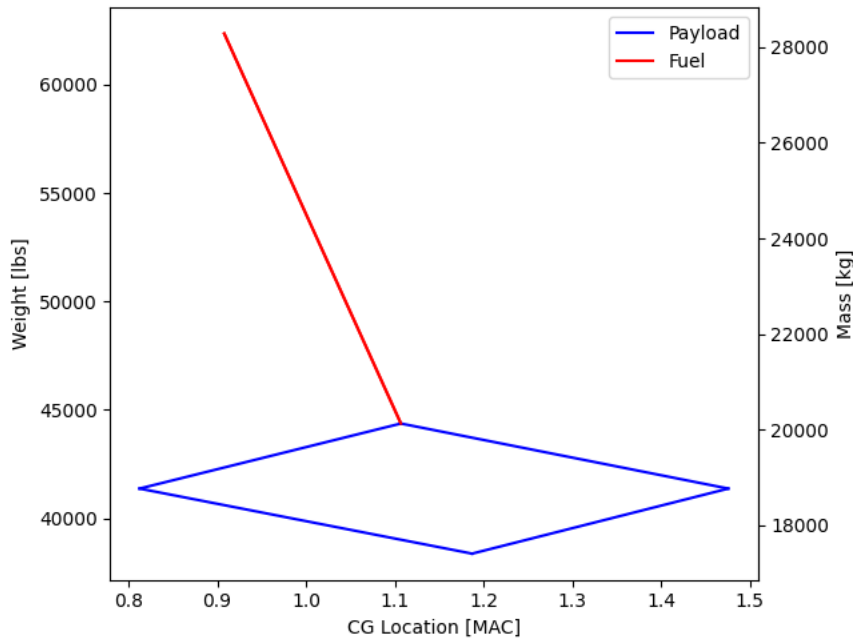
Figure 10.25: Loading Diagram

As can be seen the center of gravity excursion is located between around 0.8 to 1.45 around the mean aerodynamic chord's leading edge in units of the mean aerodynamic chord, which will be further used for the stability calculations. However, the center of gravity moves a large amount in the case of loading the payload only in the front or back. This is valuable to gain an understanding of how much the center of gravity moves during loading, thus giving the requirements for rear tip over on the ground. For this case, as mentioned earlier, this is not a large concern due to the large margin towards the gear afforded by the vertical take-off as mentioned in section 10.2. For stability, not the entire range of center of gravities will be considered, but only the most forward and rear that are found when fully loaded or empty, but no positions in between. This will place a constraint on the payload distribution in the cargo bay, but will allow for better stability and controllability.

10.9. Component and total weights

From the refined design for the XV-25 Griffin a Class II weight estimation for each component is produced. The method and equations for the estimation of each weight can be seen in the Baseline Report [5]. The values were updated with more accurate inputs given from the different departments after further and more in-depth analysis. Some components, for example, the engine, were sized with direct calculations and statistical analysis, while others were determined from commercial off-the-shelf components. To account for the estimation and snowball effect of changes all weights are inflated by 5%. The effect of this is not insignificant as all departments optimize their analysis based on these estimations. An overview of the different sub weight groups is seen in Table 10.6.

Table 10.6: Vehicle Weights (Components Inflated by 5%)

Component	[lbs]	[kg]
Blades Total	3,792	1,720
Hub	2,179	988
Wings Total	6,181	2,722
Gear	2,770	1,256
Fuselage	5,842	2,650
Horizontal Tail	272	123
Vertical Tail	121	55
Engine Intake	655	297
Fuel System	941	427
Drive System	6,925	3,141
Engines	4,396	1,994
Other Systems	4,384	1,988
Crew	750	340
Operating Empty Weight	38,457	17,444
Fuel	18,001	8,165
Payload	6,001	2,722
Maximum Take Off Weight	63,194	28,644

The total empty weight of the vehicle is estimated to be around 63.194 lbs (28.64 tons) with an empty weight of around 36'457 lbs (17.4 tons).

10.10. Verification & Validation

It is necessary to ensure the calculations performed, and thereby the results found, are rooted in reality and are not corrupted due to either errors performed in the implementation of the code or due to errors in the models used to calculate the results. Thus, verification is performed to ensure no errors were made in the implementation and calculation, while the results are validated with experimental data where available, or other means in case it is not.

Constant Loads and stresses

For the different load and stress calculations across the different parts of the aircraft, different types of programs were implemented. These were verified by using simple cases, such as simple beams with constant distributed loading, and computing the resulting loads both through the program and analytically.

Rotating Loads and Stresses

For the rotating components, a simple lift and centrifugal force distribution was calculated analytically to compare the results to verify the code. To validate it, the results from the final code were compared with the results from a study performed by Mikjaniec on the SHARCS rotor blades [73], which showed close resemblance to the results obtained by the code when using the same inputs..

Regarding fatigue, the material properties, and especially the Wöhler curves that were used are obtained by experiment, and thus are considered to be validated. However, the load determination on the hub is currently only verified through analytical checks but not verified. It is likely that it will also not hold up to validation, as it is known that the simplified model used here is not accurate for the flapping motion. This is a point of improvement that shall be considered in further development.

Component and Total weight calculations

The component and total weights calculations are verified by calculating sample components both analytically and using the code that was written. Once it is verified using that method, multiple example aircraft provided

by both [12] and [74] were used to compare the outputs of the weight estimations given the parameters of each aircraft to the actual weight of the aircraft. Comparing the weight estimates using the inputs from the V22-Osprey showed results that were within 5% of the weight of the real V22.

11
Control and Stability

11.1. Vehicle Description

The XV-25 Griffin Compound Aircraft is part of the truly niche industry of HS-VTOL. There, it is essential for the vehicle to be controllable in all phases of the mission profile. Due to the complexity of the vehicle control required for hover and cruise, a fly-by-wire system is adopted. The aircraft contains different controls for different phases of flights.

11.1.1. Rotary Wing Flight

In conformity with the mission profile, the vehicle initially takes off in a helicopter manner. The pilot manipulates the flight control to achieve and maintained controlled flight. Changes in the flight control system allows the aircraft to maneuver in the desired motion. The controls can be separate into cyclic (longitudinal and lateral), collective, throttle and anti-torque pedals. These controls will function similar to a conventional helicopter for simplicity and ease of pilot training.

A conventional swash plate is used to translate the pilot's collective and cyclic inputs to the main rotor and achieve the desired motion. The swash plate tilts the main rotor disk in order to match cyclic input. The swash plate simultaneously allows increase or decrease of the blade pitch angle, causing the aircraft's ascend or descend from collective input. The pilot is allowed the given range in which the vehicle is operational.

The anti-torque pedals control the yaw rate and direction the nose faces. This is linked to the pressured gas yaw control posts showcased in chapter 9. This is used similar as the F-35 does for roll control in VTOL. The Griffin redirects the engine bleed air to the tail in order to maximize the moment arm. Applying force on the pedals allows for the post to bleed air and control its heading and yaw rate.

11.1.2. Fixed Wing Flight

During fixed wing flight, the control surfaces of the aircraft translate pilot input to the desired maneuver. The control surfaces are placed along the wings and tail as per a traditional airplane. The aircraft possess an H-Tail in order to provide longitudinal and directional stability and control. Conventional ailerons are located on the main wing in order to provide roll control and maneuverability. Furthermore, the vehicle possesses plain flaps for additional lift during transition. The pilot controls the stick, throttle and rudder pedals. The stick allows for pitch and roll control by deflecting the elevator and ailerons using actuators. The throttle increases or decreases the thrust of the engines to the desired amount for the phase of the flight. The rudder pedals actuate the rudder for to change the heading and yaw.

Table 11.1: Compound Control Angles

	Minimum	Maximum
Longitudinal Cyclic [deg]	-11.0	+8.7
Collective [deg]	-0.5	10.0
Elevator (+ve up) [deg]	-15	10
Rudder [deg]	-15	15

11.2. Equations of Motion

In this section, the equations of motion for the Griffin are elaborated upon. This project will restrain to the longitudinal direction. The free body diagram for longitudinal equilibrium is presented in Figure 11.1. X_B points in the body's tangential direction, positive left, and Z_B points in the body's normal direction, positive downwards. Similarly, X_S and Z_S determine the stability axis. In the free body diagram showcasing the lateral

geometry, the main contributors to the forces are the upper and lower wings, the horizontal stabilizer, the rotor, and the forward propulsion unit.
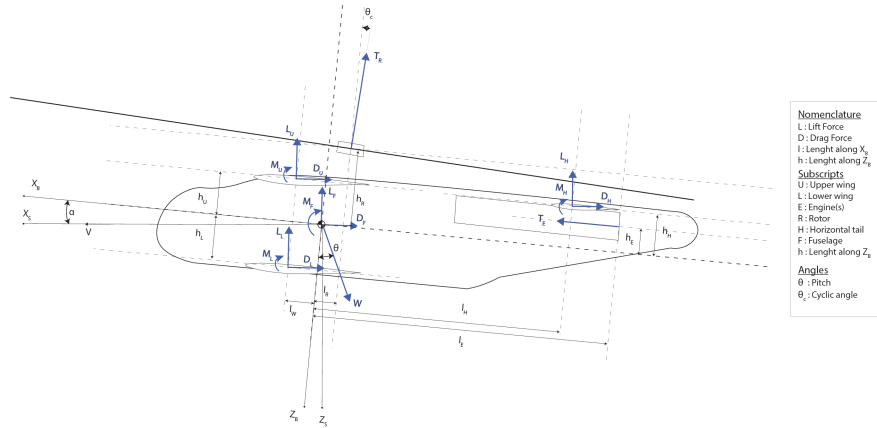
Figure 11.1: Geometry of the XV-25 Griffin

$$(\leftarrow_+) \sum F_{X_B} = T_E + (L_U + L_L + L_H)\sin\alpha - (D_U + D_L + D_H + D_F)\cos\alpha$$
$$- T_R \sin(\theta_c + a_1) - D_R \cos(\theta_c + a_1) - W \sin\theta_f \tag{11.1}$$

$$(\downarrow_+) \sum F_{Z_B} = -(L_U + L_L + L_H)\cos\alpha - (D_U + D_L + D_H + D_F)\sin\alpha$$
$$- T_R \cos(\theta_c + a_1) + D_R \sin(\theta_c + a_1) + W \cos\theta_f \tag{11.2}$$

$$(CW_+) \sum M_{Y_B} = M_F + M_U + M_L + M_H + \cos\alpha(L_U l_W + L_L l_w + D_U l_U - D_L h_L$$
$$- L_H l_H + D_H h_H) + \sin\alpha(-L_U h_U + L_L h_L - L_H h_H + D_U l_W - D_L l_W$$
$$- D_H l_H) - T_E h_E - T_R \cos(\theta_c + a_1)l_R + T_R \sin(\theta_c + a_1)h_R$$
$$+ D_R \cos(\theta_c + a_1)h_R + D_R \sin(\theta_c + a_1)l_R \tag{11.3}$$

Furthermore, the equations for translation, rotation, and Euler angle rates are established in Equation 11.4, Equation 11.5 and Equation 11.6 [75].

$$\begin{aligned} F_x &= m(\dot{u} + qw - rv) \\ F_y &= m(\dot{v} + ru - pw) \\ F_z &= m(\dot{w} + pv - qu) \end{aligned} \tag{11.4}$$

$$\begin{aligned} L_x &= I_x\dot{p} - I_{xz}\dot{r} + qr(I_z - I_y) - I_{xz}pq \\ M_y &= I_y\dot{q} - rp(I_x - Iz) + I_{xz}(p^2 - q^2) \\ N &= I_z\dot{r} - I_{xz}\dot{p} + pq(I_y - I_x) + I_{xz}qr \end{aligned} \tag{11.5}$$

$$\dot{\phi} = p + q\sin\phi\tan\theta + r\cos\phi\tan\theta$$
$$\dot{\theta} = q\cos\phi - r\sin\phi \tag{11.6}$$
$$\dot{\psi} = (q\sin\phi + r\cos\phi)\sec\theta$$

The report will focus on the longitudinal case in horizontal flight. The longitudinal components can be easily decoupled from the lateral and directional components. Therefore, in Equation 11.7 the following are neglected for symmetric aircraft in horizontal flight: $I_{xz} = 0, r = 0, p = 0, \cos\phi \approx 1$.

$$F_x = m(\dot{u} + qw)$$
$$F_z = m(\dot{w} - qu)$$
$$M_y = I_y \dot{q}$$
$$\dot{\theta} = q$$

(11.7)

These can be used to determine the static stability in section 11.3 and later to compute dynamic stability in section 11.5.

11.3. Static Stability

Achieving Static longitudinal stability with the Griffin led to major challenges. The challenge origins from the core of the compound, storing a rotor inside a wing. For this, the rotor center and blades must align with the wing. This therefore effects the method in which the wing and rotor hub are in place with respect to the aircraft. The aircraft must be statically stable during hover, yet it is desired to remain statically stable in flight. These are inherently conflicting in the way each are individually place for a conventional vehicle. As the aircraft makes use of a fly-by-wire system, the stability during cruise proved to be the lesser constraint. The first step is to achieve static stability for vertical flight and hover. Following, a preliminary sizing of the horizontal tail in order to achieve longitudinal static stability in horizontal flight, meanwhile compromising with the desired static stability for vertical flight.

11.3.1. Static Stability in Hover

The configuration of the Griffin proved to be challenging in order to achieve Static Stability in Hover. This is shown in Figure 11.2 and Equation 11.8.
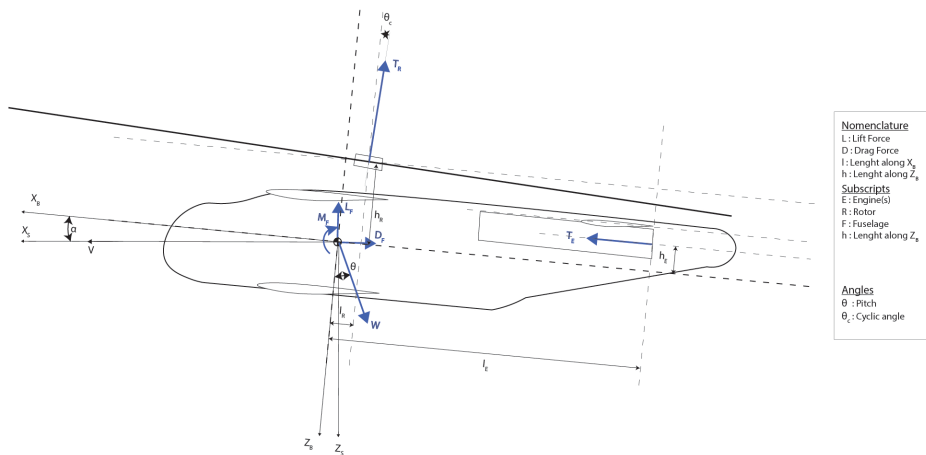
Figure 11.2: Aircraft Description in Hover and Vertical Flight

$$\sum F_x = T_R \sin \theta_f + \theta_c - T_E \cos \theta_f = 0$$
$$\sum F_z = T_R \cos \theta_f + \theta_c + T_E \sin \theta_f - mg = 0$$
$$\sum M_y = -T_E z_E + T_R \cos(\theta_c) l_R + T_R \sin(\theta_c) h_R = 0$$

(11.8)

with T_E the engine thrust non zero as the engines are on to provide rotor thrust T_R. The sum of forces is quite simple to fulfil, however, the sum of moments is difficult to meet. As θ_f is constraint by the blade clearance

and the engines must be sufficiently far away in order not to impact the down wash requirement. The sum of moment has proven to be most challenging, as it becomes clear that a significant amount of thrust is required to overcome the moment perceived from the rotor and vehicle cg off set. This further impacts the cyclic and pitch angle and required Engine Thrust. In order to overcome this issue, a trade-off was established in Table 11.2. The F-35 engine is already proven effective to allow thrust vectoring in VTOL. After preliminary sizing, this does come with significant weight impact to the weight budget, which can not be met at this step in the design without significant re-design of the rotor. Thrust Deflector are significantly lighter and the mechanism

Table 11.2: Thrust Dump Mechanisms Trade-Off Table

	Weight	Thrust Vectoring	Thrust Deflection
Weight	3	1	3
Complexity	1	1	2
Effectiveness	2	3	2
Final score	6	1.66	2.5

Thrust deflection in the form of thrust reversers are chosen. They are used to deflect the flow in the lateral direction in an equally distributed manner. This allows the engine thrust component to be neglected in the X and Z directions, along with the moment it would provide.

Furthermore, the Rotor Hub must be position in such manner to provide sufficient clearance with the utmost edges of the vehicle. The constraining elements are the utmost wing tips and the tail of the aircraft. Note that the pitch of the aircraft required for equilibrium is directly linked to

In order to minimize such cg offset and allow the aircraft to be statically stable at MTOW and OEW, The placement of key heavy components were revised. This is completed such that to minimize the cg range the aircraft may perceive. This cg range must be minimal, as the maximum and minimum pitch angles are constrained by the vehicle geometry in order to provide clearance to the forward swept wings and the tail. Therefore, fixed elements such as the gear-box and engines were placed as far away from the cg. On the other hand, elements such than cargo pay and fuel were placed as close to the determined cg. Then, the wing can be position along the fuselage. Note that in the compound case, the wing group is composed of the box wing itself, in-wing fuel storage and the entire rotor blades, hub and mechanisms. After numerous iterations, the placement leading to minimal cg range was determined. The distance from the nose to the leading edge mean aerodynamic chord is fixed to 16.4 ft (5.89m). This allows the computation of the constraining angles from vehicle geometry. Note that in operation, the blades showcase coning, allowing for further clearance and maneuverability. The following parameters were determined in Table 11.3.

Table 11.3: Clearance Angles for Aircraft Hover

	Forward Most	Aft Most
CG Location $\frac{x_{cg}}{\bar{c}}$	0.908	1.187
Resultant θ_f [°]	-4.52	7.46
Clearance [°]	6.58	3.68

Note the clearance is from the tail when the cg is most forward and from the wings when the cg is most aft. As seen from Table 11.3, the clearance allows sufficient margin for maneuverability in hover. In addition, the aft most cg is an extreme condition in case the aircraft carries no payload or fuel. Droop stops are used to ensure the rotor never comes in contact with each wing nor the tail.

The directional stability of the aircraft will function as per conventional helicopter described by Prouty [12]. Concerning the differences with traditional helicopters, the main rotor provides a torque which is counteracted using pressured gas and the flow deflectors during hover. The directional stability of the aircraft is mentioned for completeness and will not be elaborated further.

11.3.2. Static Stability in Forward Flight

The static stability is essential for forward flight and necessary for dynamic stability in section 11.5. The vehicle is first described in Figure 11.3 to be determined in the non-dimensional form in the body axis. In this section of the flight, the rotor has been stored, and its impact is neglected.
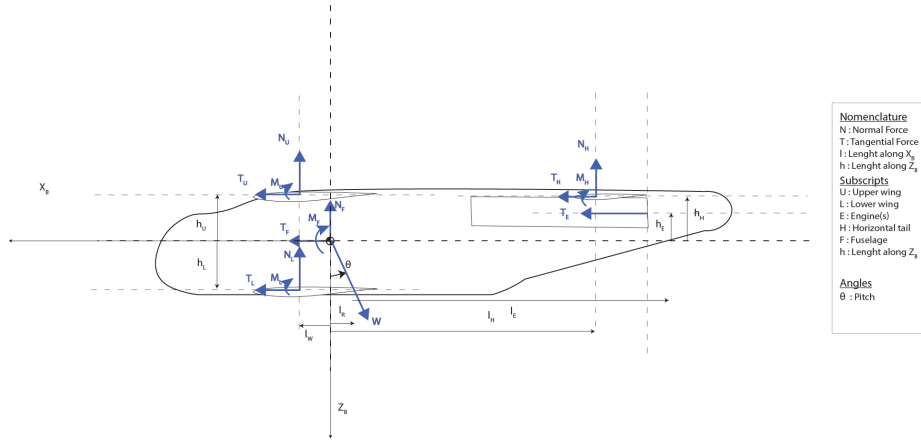
Figure 11.3: Fixed Wing Simplification

$$\sum F_x \cdot \frac{1}{\frac{1}{2}\rho V^2 S} = C_{T_w} + C_{T_h} \cdot \left(\frac{V_h}{V}\right)^2 \cdot \frac{S_h}{S} + \frac{T_E}{\frac{1}{2}\rho V^2 S} + C_{D_f} \cdot \frac{S_f}{S} + \frac{W}{\frac{1}{2}\rho V^2 S} \cdot sin(\theta) \qquad (11.9)$$

$$\sum F_z \cdot \frac{1}{\frac{1}{2}\rho V^2 S} = C_{N_w} + C_{N_h} \cdot \left(\frac{V_h}{V}\right)^2 \cdot \frac{S_h}{S} + \frac{T_E}{\frac{1}{2}\rho V^2 S} - \frac{W}{\frac{1}{2}\rho V^2 S} \cdot cos(\theta) \qquad (11.10)$$

$$\sum M \cdot \frac{1}{\frac{1}{2}\rho V^2 S \overline{c}} = C_{m_{ac_w}} + C_{N_w} \cdot \frac{x_{cg} - x_w}{\overline{c}} - C_{T_w} \cdot \frac{z_{cg} - z_w}{\overline{c}} + C_{m_{ac_h}} \cdot \left(\frac{V_h}{V}\right)^2 \cdot \frac{S_h}{S} \cdot \frac{\overline{c}_h}{\overline{c}}$$
$$+ C_{N_h} \cdot \left(\frac{V_h}{V}\right)^2 \cdot \frac{S_h}{S} \cdot \frac{x_{cg} - x_h}{\overline{c}} - C_{T_h} \cdot \left(\frac{V_h}{V}\right)^2 \cdot \frac{S_h}{S} \cdot \frac{z_{cg} - z_h}{\overline{c}} + \frac{T}{\frac{1}{2}\rho V^2 S} \cdot cos(\alpha_d) \cdot \frac{(z_{cg} - z_E)}{\overline{c}} \qquad (11.11)$$

The aircraft stabilizer is sized for forward horizontal fixed wing flight, and later discussed the effects of transition upon the stability of the aircraft.

For a given section of the horizontal flight, the compound can be visualized as a conventional aircraft, in which stick fixed static stability and the neutral point may be determined. Neutral point refers to an existing point at which the resultant of the lift forces variation when perturbation is applied [76]. If the aircraft is longitudinal statistically stable, it shall respond to perturbations in the lifting forces by an opposite moment. Therefore, an increase in angle attack should correspond to a pitch down moment:

$$\frac{dC_m}{d\alpha} < 0$$

As the flight conditions are numerous and vary during flight, longitudinal trim is obtained through variation of the horizontal tail lift. Furthermore, as the surface and airfoil section are fixed, this variation is done through

change in angle of attack α_h. This can be done through the use of control surfaces and the adjustment of the entire surface.

The following table Table 11.4 showcases the trade-off between different tail setting configurations. A fixed tail is fixed to the fuselage through joining techniques, unable to change its angle of attack. An adjustable tail allows minor adjustments in which a pilot may set its angle. Lastly, the all moving tail allows direct movement from pilot stick input.

Table 11.4: Tail Setting Configuration Trade-Off Table

	Weight	Fixed	Adjustable	All-moving
Weight	3	3	2	1
Simplicity	2	3	2	1
Maneuverability	1	1	2	3
Final score		2.66	2	1.33

As seen above in Table 11.4, the fixed tail is chosen. The absence of an additional rotation mechanism and its simplicity overcome its maneuverability benefit. Maneuverability can be achieved using an elevator later designed in section 11.4. Furthermore, the trim capability benefits of the adjustable are less significant due to the relatively short flight time of the compound.

The horizontal tail airfoil must generate the required lift with minimum drag and minimum pitching moment. Furthermore, as cg changes during flight from fuel consumption, the horizontal tail may require to generate positive and negative lift. Therefore, a symmetric airfoil is chosen. The NACA 0012 is chosen for its simplicity, trivial solution and thickness to provide structural capability for the vertical wings of the H-tail.

The horizontal tail does not perceive the same angle of attack as the main wing. This is due to tail incidence angle i_h and the down wash ϵ of the wing, which can be corrected using Equation 11.12 and Equation 11.13. At this preliminary stage of the design, the down wash from the rotor in the pre-transition phase is not accounted for. This will be corrected by ensure that the elevator offers a large range of deflection in section 11.4

$$\alpha_h = \alpha_w + i_h - \epsilon \tag{11.12}$$

$$\frac{d\epsilon}{d\alpha} = \frac{2C_{L_{\alpha_w}}}{\pi \cdot AR} \tag{11.13}$$

The aerodynamic center of the aircraft is a crucial point for static stability and controllability of the aircraft. This is essential, as the more aft $\overline{x_{ac}}$, the more stable the aircraft becomes. On the other hand, in the case of forward swept wing, the fuselage presents destabilizing effect due to the nose effect and lift loss at wing fuselage crossing. In conventional aircraft the nacelles also contribute to an effect, yet the engine is located within the fuselage the effect upon the aerodynamic center may be neglected. This point is therefore corrected to compute the wing-fuselage aerodynamic center in Equation 11.14. In addition, the moment around this point is also calculated in Equation 11.15 using parameters from Table 11.5

$$\left(\frac{x_{ac}}{\overline{c}}\right)_{wf} = \left(\frac{x_{ac}}{\overline{c}}\right)_w + \frac{1.8}{C_{L\alpha A-h}} \frac{b_f h_f l_f n}{s\overline{c}} + \frac{0.273}{1+\lambda} \frac{b_f c_g (b - b_f)}{\overline{c}^2 (b + 2.15 b_f)} \tan \Lambda_{1/4} \tag{11.14}$$

$$C_{m_{ac}wf} = C_{m_{oairfoil}} \frac{AR cos(\Lambda)^2}{AR + 2cos(\Lambda)} - 1.8(1 - \frac{2.5 b_f}{l_f}) \frac{\pi b_f h_f l_f}{4 S \overline{c}} \frac{C_{L_o}}{C_{L_{\alpha A-h}}} \tag{11.15}$$

As the H-Tail is fuselage mounted, the tail wing speed ratio $(\frac{V_h}{V})^2 = 0.85$ due to the perturbing presence of the fuselage.

Table 11.5: Aircraft Correction Parameters

Fuselage width	b_f	6.56ft (2.6m)
Fuselage height	h_f	9.84ft (3.4m)
Length nose to LE	l_{fn}	2.92ft (7.1m)
Mean geometric chord	c_g	6.56ft (2.6m)
Fuselage length	b	65.6ft (20.2m)
Aerodynamic center Aircraft less tail	$\left(\frac{x_{ac}}{\bar{c}}\right)_{wf}$	-0.30
Moment coefficient Aerodynamic center Aircraft less tail	$C_{m_{ac}wf}$	-0.814
Lift Slope tail	$C_{L_{\alpha_h}}$	4.324 1/rad
Lift Slope Aircraft less tail	$C_{L_{\alpha_{A-h}}}$	2.348 1/rad

$$C_{m_{ac}} + C_{L\alpha A-h}(\overline{x_{cg}} - \overline{x_{ac}}) = \frac{C_{L\alpha h}S_h l_h}{S\bar{c}}\left(\frac{V_h}{V}\right)^2 \tag{11.16}$$

$$\frac{S_h}{S} = \frac{1}{\frac{C_{L\alpha h}}{C_{L\alpha A-h}}\left(1-\frac{d\epsilon}{d\alpha}\right)\frac{l_h}{\bar{c}}\left(\frac{V_h}{V}\right)^2}\bar{x}_{cg} - \frac{\bar{x}_{ac} - S.M.}{\frac{C_{L\alpha h}}{C_{L\alpha A-h}}\left(1-\frac{d\epsilon}{d\alpha}\right)\frac{l_h}{\bar{c}}\left(\frac{V_h}{V}\right)^2} \tag{11.17}$$

With $C_{L\alpha A-h}$, the lift coefficient of the aircraft less tail of 2.348 [76], S.M. as the stability margin of 0.05.

Furthermore, the tail is simultaneously designed for controllability by rearranging the trim equation as seen in Equation 11.16.

$$\frac{S_h}{S} = \frac{1}{\frac{C_{L\alpha h}}{C_{L\alpha A-h}}\frac{l_h}{\bar{c}}\left(\frac{V_h}{V}\right)^2}\overline{x_{cg}} + \frac{\frac{C_{m_{ac}}}{C_{L\alpha A-h}} - \overline{x_{ac}}}{\frac{C_{L\alpha h}}{C_{L\alpha A-h}}\frac{l_h}{\bar{c}}\left(\frac{V_h}{V}\right)^2} \tag{11.18}$$

Here it is seen that elements conflict with stability and controllability, such as moving the aerodynamic center forward for trimmability yet impacts the stability.

It was determined that choosing the smallest surface ratio is convenient for cruise flight yet complicates static stability and control when the rotary wing is used. Furthermore, the cg range determined in subsection 11.3.1 is used to showcase static stability and controllability for cruise, transition, and hover. This is observed in Figure 11.4.
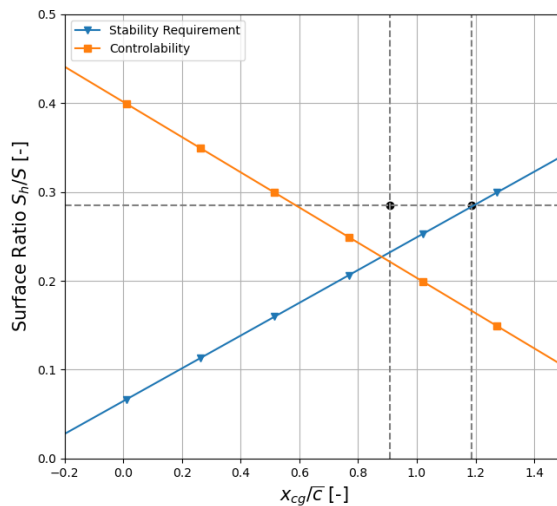
Figure 11.4: Scissor Plot for Static Stability and Controllability

Table 11.6: H-Tail Geometry

	Horizontal Tail	Vertical Tail
Surface Area $ft^2(m^2)$	171(15.96)	32.1(2.98)
Span $ft(m)$	27.4(8.35)	8.01(2.44)
Average Chord $ft(m)$	6.27(1.91)	4.00(1.22)
Aspect ratio	4.36	2.00
Sweep deg	35	35
$x - x_{c.g.}$ $ft(m)$	39.4(12.42)	45.9(14.72)

This leads to the following wing parameters determined using the same method as section 8.2.

11.3.3. Vertical Tail Sizing

The vertical tail is essential for directional stability. The Tail is designed to be efficient in cruise and should allow sufficient moment for one engine inoperative scenario. Similar to the horizontal tail, the vertical tail can be preliminarily sized through statistics [75] for transport jet. This lead to a tail volume coefficient of 0.090 shown in Equation 11.19.

$$\overline{V_v} = \frac{l_v S_v}{bS} \tag{11.19}$$

Similar to the vertical tail, $5[deg]$ of sweep may be added. In addition, the vertical tail is out of the wake of the horizontal stabilizer and therefore more effective. It is also important to note that the vertical tail is not symmetric with respect to the horizontal stabilizer, as it allows clearance with the rotor blades. In order to obtain directional trim, it is sized for one engine inoperative and cross wind landing. Note that the aircraft is capable of conventional landing using fixed wing only. However, this is not a driving parameter, as the tail is sized for effective control from stall speed and over. Furthermore, the sum of forces and moment shall be null for directional static stability.

$$\sum F_x = 0$$
$$\sum F_y = 0 \tag{11.20}$$
$$\sum N_z = 0$$

The vertical stabilizer will be fixed without an angle of incidence using the airfoil NACA0012 for similar reasons as the horizontal tail. This allows directional control using the rudder when in maneuvering operations such as turning flight and spin recovery. From there, a rudder may be sized.

11.4. Control Surface Sizing

Once the longitudinal forces and moments are in equilibrium, the aircraft is longitudinally trimmed. The elevator then plays a key role in order to trim the aircraft over the range of operational velocities.

In conventional aircraft, the elevator is sized for take-off rotation, as this is the critical point at which a minimum rotational acceleration is set according to Roskam [75] However, as the compound aircraft is designed for VTOL, this requirement will not be driving. The elevator is therefore sized for longitudinal trim across the velocity range. This is determined using Equation 11.21 in which the moment coefficient of the aircraft C_{m_o}

$$C_m = C_{m_o} + C_{m_\alpha}(\alpha - \alpha_o) + C_{m_{\delta_e}}\delta_e = 0$$
$$C_{m_o} = C_{m_{ac}} - C_{L_\alpha}(\alpha_o - ih)(\frac{V_h}{V})^2 \frac{S_h l_h}{S\overline{c}}$$
$$C_{m_\alpha} = C_{L_{w_\alpha}} \frac{x_{cg} - x_w}{\overline{c}} - C_{L_{h_\alpha}}(1 - \frac{\delta\epsilon}{\delta\alpha}(\frac{V_h}{V})^2 \frac{S_h l_h}{S\overline{c}} \tag{11.21}$$
$$C_{m_{\delta_e}} = -C_{L_{\alpha_h}} \frac{b_e}{b_h}\tau_e(\frac{V_h}{V})^2 \frac{S_h l_h}{S\overline{c}}$$

To evaluate the elevator sizing required for the vehicle, The method found in [77] is used to determine $C_{m_{\delta_e}}$. The tail configuration is an H-tail, therefore the ratio between the control surface and lifting surface $\frac{b_E}{b_h}$ is 1.

This also is done for ease of fabrication. Furthermore, the elevator effectiveness parameter τ_e is determined using Figure 11.5a. The elevator size is obtained in

(a) Control Surface Angle of Attack Effectiveness Parameter [77]

(b) Elevator Deflection Over Angle of Attack α
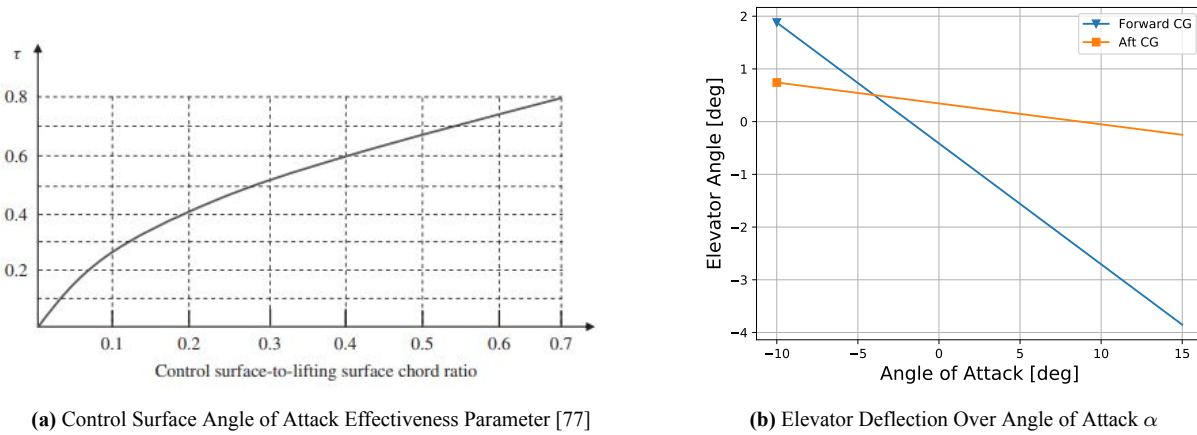
Figure 11.5: Elevator Sizing

Table 11.7: Elevator Parameters

Description	Subscript	Value	Range [75]
Surface ratio [-]	S_e/S_h	0.4	0.15 - 0.4
Span ratio [-]	b_E/b_h	1	0.8 - 1
Chord ratio [-]	c_E/c_h	0.4	0.2 - 0.4
Maximum Elevator Deflection [deg]	$\delta_{e_{max}up}$	-15	(-15) - (-25)
Maximum Elevator Deflection [deg]	$\delta_{e_{max}down}$	+10	(+10) - (+20)

It can be seen that a small elevator input is required for a large variation in angle of attack. This show that the aircraft is relatively unstable. This is accepted as the fly-by-wire system is used. Furthermore, the actuators require small distances and therefore can be executed faster. The elevator is set such that minimal elevator is required during cruise when the aircraft weight is between the MTOW and OEW. As previously mentioned, the effects of rotor down wash were not taken into account when designing the tail. As it is anticipated to reduce effectiveness along the horizontal tail, this given elevator size is expected to fulfill control and stability in the pre-transition stage.

11.5. Dynamic Stability
11.5.1. Setup of the State-Space System
To evaluate the longitudinal dynamic stability of the vehicle, a linear model of the equations of motion is created. This model takes a state-space format such that existing LTI (Linear Time Invariant) system solvers can simulate the characteristics of the vehicle.

The first step is to define the linear system. For that, a set of state and control variables needs to be defined. The set of state variables consists of u (velocity along the X_B axis), w (velocity along the Z_B axis), q (pitch rate) and θ_f (pitch angle). The set of control variables consists of θ (collective pitch angle), θ_{1_S} (cyclic pitch angle), δ_e (elevator deflection angle) and δt (throttle percentage). Reformulating Equation 11.1, Equation 11.2 and Equation 11.3 as seen on Equation 11.22 enables the separation between forces and moments generated by the aircraft (X, Z and M) and components of weight.

$$\Sigma F_{X_B} = X - mg\sin\theta_f = m(\dot{u} + qw)$$
$$\Sigma F_{Z_B} = Z + mg\cos\theta_f = m(\dot{w} - qu) \quad (11.22)$$
$$\Sigma M_{Y_B} = M = I_y\dot{q}$$

$$X = f(u, w, q, \theta_f, \theta, \theta_{1_S}, \delta_e, \delta_t)$$
$$Z = f(u, w, q, \theta_f, \theta, \theta_{1_S}, \delta_e, \delta_t)$$
$$M = f(u, w, q, \theta_f, \theta, \theta_{1_S}, \delta_e, \delta_t)$$

When the aircraft is trimmed for steady, symmetric flight, then the sum of all forces and moments is considered

to be zero. Additionally the pitch rate $q = 0$. Let then X, Z and M at the trimmed state to be denoted as X_0, Z_0 and M_0. At this condition the state variables are assumed to have values $u = u_0$, $w = w_0$, $q = 0$ and $\theta_f = \theta_{f_0}$. Similarly, the control variables have values $\theta = \theta_0$, $\theta_{1_S} = \theta_{1_{S_0}}$, $\delta_e = \delta_{e_0}$ and $\delta_t = \delta_{t_0}$.

Assuming there are small perturbations around that trimmed condition, the state and control variables can be denoted as:

$$u = u_0 + \Delta u$$
$$w = w_0 + \Delta w$$
$$q = q_0 + \Delta q$$
$$\theta_f = \theta_{f_0} + \Delta \theta_f$$

(11.23)

$$\theta = \theta_0 + \Delta \theta$$
$$\theta_{1_S} = \theta_{1_{S_0}} + \Delta \theta_{1_S}$$
$$\delta_e = \delta_{e_0} + \Delta \delta_e$$
$$\delta_t = \delta_{t_0} + \Delta \delta_t$$

(11.24)

Considering that the forces X and Z and moment M have a small deviation due to changes in the state and control variables, the forces on each axis can be approximated as seen on Equation 11.25, where ΔX, ΔZ and ΔM can be found on Equation 11.26.

$$X = X_0 + \Delta X$$
$$Z = Z_0 + \Delta Z$$
$$M = M_0 + \Delta M$$

(11.25)

$$\Delta X = X_u \Delta u + X_w \Delta w + X_q \Delta q + X_{\theta_f} \Delta \theta_f + X_\theta \Delta \theta + X_{\theta_{1_S}} \Delta \theta_{1_S} + X_{\delta_e} \Delta \delta_e + X_{\delta_t} \Delta \delta_t$$
$$\Delta Z = Z_u \Delta u + Z_w \Delta w + Z_q \Delta q + Z_{\theta_f} \Delta \theta_f + Z_\theta \Delta \theta + Z_{\theta_{1_S}} \Delta \theta_{1_S} + Z_{\delta_e} \Delta \delta_e + Z_{\delta_t} \Delta \delta_t$$
$$\Delta M = M_u \Delta u + M_w \Delta w + M_q \Delta q + M_{\theta_f} \Delta \theta_f + M_\theta \Delta \theta + M_{\theta_{1_S}} \Delta \theta_{1_S} + M_{\delta_e} \Delta \delta_e + M_{\delta_t} \Delta \delta_t$$

(11.26)

Finally, combining Equation 11.22, Equation 11.25 and Equation 11.26 and formulating in state-space form, the equations of motion of the linearized system can be expressed as seen on Equation 11.27 [78].

$$\begin{bmatrix} m\Delta \dot{u} \\ m\Delta \dot{w} \\ I_y \dot{q} \\ \Delta \dot{\theta}_f \end{bmatrix} = \begin{bmatrix} X_u & X_w & X_q - qw_0 & X_{\theta_f} - mg\cos\theta_{f_0} \\ Z_u & Z_w & Z_q + qu_0 & Z_{\theta_f} - mg\sin\theta_{f_0} \\ M_u & M_w & M_q & M_{\theta_f} \\ 0 & 0 & 1 & 0 \end{bmatrix} \begin{bmatrix} \Delta u \\ \Delta w \\ \Delta q \\ \Delta \theta_f \end{bmatrix} + \begin{bmatrix} X_\theta & X_{\theta_{1_S}} & X_{\delta_e} & X_{\delta_t} \\ Z_\theta & Z_{\theta_{1_S}} & Z_{\delta_e} & Z_{\delta_t} \\ M_\theta & M_{\theta_{1_S}} & M_{\delta_e} & M_{\delta_t} \\ 0 & 0 & 0 & 0 \end{bmatrix} \begin{bmatrix} \Delta \theta \\ \Delta \theta_{1_S} \\ \Delta \delta_e \\ \Delta \delta_t \end{bmatrix}$$

(11.27)

Where, for instance, $X_u = \frac{\partial X}{\partial u}$ and the other derivatives follow a similar pattern. For the sake of addressing the state-space representation of the equations of motion further on in this report in a more efficient manner, the equations of motion can be written in a shortened matrix equation format as $\dot{\mathbf{x}} = \mathbf{A}\mathbf{x} + \mathbf{B}\mathbf{u}$.

11.5.2. Representation of Aerodynamic Values in Terms of State and Control Variables

The state variables, as defined on subsection 11.5.1 are the key output where stability of the system is determined. However, it is more convenient for aerodynamic analysis to reformulate the state variables in a format that would make aerodynamic analysis more intuitive and convenient. For that reason, the translation between state variables and aerodynamic variables is centrally defined in this subsection for enhancing clarity and convenience.

$$V = \sqrt{u^2 + w^2} \qquad (11.28)$$

$$\alpha_0 = \arctan\frac{w}{u} \qquad (11.29)$$

From Equation 11.28, the free-stream velocity can be determined and from Equation 11.29, the vehicle angle of attack can be determined. Any local variations of V and α_0 will be discussed on their respective subsection.

11.5.3. Fixed-Wing Dynamics

First the fixed wing flight dynamics come into consideration. Starting with the equations of motion, the constituents of each force and moment have to be evaluated.

The lift, drag and moment of each aerodynamic component can be calculated using Equation 11.30, Equation 11.31 and Equation 11.32 respectively.

$$L = \frac{1}{2}C_L\rho S V^2 \quad (11.30) \qquad D = \frac{1}{2}C_D\rho S V^2 \quad (11.31) \qquad M = \frac{1}{2}C_m\rho S V^2 \quad (11.32)$$

To compute the effective angle of attack α of each component, Equation 11.33 is used, where α_0 is the free-stream angle of attack, ϵ is the downwash as indicated on subsection 11.3.2 and i is the installation angle of incidence of each component. The difference of angle of attack at each station to to the curvilinear flow field caused by pitching maneuvers, denoted as α_q, can be computed using Equation 11.34, where q is the pitch rate.

$$\alpha = \alpha_0 + \alpha_q + i + \epsilon \quad (11.33) \qquad\qquad \alpha_q = (x - x_{c.g.})\frac{q}{V} \quad (11.34)$$

Finally, to compute the lift, drag and moment coefficient of each component, Equation 11.35, Equation 11.36 and Equation 11.37 are used respectively. To compute the engine thrust, the maximum thrust of the engine $T_{E_{max}}$ is multiplied by δ_t as seen on Equation 11.38.

$$C_L = C_{L_0} + C_{L_\alpha}\alpha + C_{L_{\delta_e}}\delta_e \quad (11.35) \qquad\qquad C_D = C_{D_0} + k_1 C_L + k_2 C_L^2 \quad (11.36)$$

$$C_m = C_{m_0} + C_{m_\alpha}\alpha \quad (11.37) \qquad\qquad T_E = T_{E_{max}}\delta_t \quad (11.38)$$

11.5.4. Rotary-Wing Dynamics

The first step of evaluating the rotary-wing dynamics in order to calculate the rotor thrust and drag is to define some important aerodynamic parameters. Namely, the control plane angle of attack α_c is defined on Equation 11.39, the advance ratio μ is defined on Equation 11.40 and the rotor inflow λ_c is defined on Equation 11.41. Here, Ω is the rotational velocity of the rotor and R is the rotor radius [78].

$$\alpha_c = \theta_{1_S} - \alpha_0 \quad (11.39) \qquad \mu = \frac{V}{\Omega R}\cos\alpha_c \quad (11.40) \qquad \lambda_c = \frac{V}{\Omega R}\sin\alpha_c \quad (11.41)$$

In addition to aerodynamic parameters, it is important to define some rotor parameters, namely the blade moment of inertia I_b around its flapping hinge axis, the Lock number γ and the blade solidity σ. The three values can be computed using Equation 11.42, Equation 11.43 and Equation 11.44 respectively [79].

$$I_b = \frac{mR^2}{3} \quad (11.42) \qquad \gamma = \frac{\rho C_{L_{\alpha_R}} c_R R^4}{I_b} \quad (11.43) \qquad \sigma = \frac{Nc_R}{\pi R} \quad (11.44)$$

A very important parameter of the rotor dynamics is the induced velocity V_{ind_h} of the rotor. The induced velocity has its maximum value at hover and subsequently decreases with increasing vehicle velocity. In order to calculate the induced velocity, actuator disk theory is used. First the induced velocity at hover needs to be defined. V_{ind_h} can be calculated using Equation 11.45, where m is the vehicle mass and $S_{Disk} = \pi R^2$ is the rotor disk plane surface area.

$$V_{ind_h} = \sqrt{\frac{mg}{2\rho S_{Disk}}} \quad (11.45)$$

To calculate the induced velocity beyond hover, the Glauert's Formula [78] defined on Equation 11.46 is used, where α_d is the angle of attack of the disk plane. Both the forward and the induced velocity of the rotor are made non-dimensional using the induced velocity at hover as seen on Equation 11.47.

$$\overline{V_{ind}}^2 = \frac{1}{(\overline{V}\cos\alpha_d)^2 + (\overline{V}\sin\alpha_d + \overline{V_{ind}})^2} \quad (11.46)$$

$$\overline{V_{ind}} = \frac{V_{ind}}{V_{ind_h}}$$
$$\overline{V} = \frac{V}{V_{ind_h}} \quad (11.47)$$

When flying level at low speed, it is assumed that $\alpha_d \approx 0$. Using this assumption in Glauert's Formula, the value of $\overline{V_{ind}}$ can be found by solving $\overline{V_{ind}}^4 + \overline{V}^2\overline{V_{ind}}^2 - 1 = 0$. Similarly, when flying at high speed it is assumed

that $V \gg V_{ind}$. This $\overline{V_{ind}} = \frac{1}{\overline{V}}$. Therefore, the induced velocity can be obtained using Equation 11.48.

$$\overline{V_{ind}} = \begin{cases} \frac{\sqrt{\sqrt{\overline{V}^4+4}-\overline{V}^2}}{\sqrt{2}} & \text{for } \overline{V} < 2 \\ \\ 1/\overline{V} & \text{for } \overline{V} \geq 2 \end{cases} \tag{11.48}$$

Thereafter, the induced velocity is made dimensional and non-dimensional again, but this time using the rotor tip velocity ΩR. This form of the induced velocity is denoted λ_i and can be calculated using Equation 11.49.

$$\lambda_i = \overline{V_{ind}} \frac{V_{ind_h}}{\Omega R} \tag{11.49}$$

Having calculated the induced velocity, the flapping coefficients a_0 (coning angle), a_1 (longitudinal disk-tilt angle) and b_1 (lateral disk-tilt angle) can be computed using Equation 11.50, Equation 11.51 and Equation 11.52 respectively [79].

$$a_0 = \frac{\gamma}{8} \left[\theta(1 + \mu^2) + \frac{4}{3}(\lambda_c + \lambda_i) \right] \tag{11.50}$$

$$a_1 = \frac{\frac{8}{3}\mu\theta + 2\mu(\lambda_c + \lambda_i) - \frac{16q}{\gamma\Omega}}{1 - \frac{1}{2}\mu^2} \tag{11.51} \qquad b_1 = \frac{\frac{4}{3}\mu a_0 - \frac{q}{\Omega}}{1 + \frac{1}{2}\mu^2} \tag{11.52}$$

Using these, the thrust coefficient C_T and the drag coefficient C_H of the rotor can be calculated using Equation 11.53 and Equation 11.54[79].

$$C_{T_R} = \frac{\sigma C_{L\alpha_{rot}}}{4} \left[\left(\frac{1}{3} + \frac{\mu^2}{2} \right) \theta + \frac{\lambda_c - \lambda_i}{2} \right] \tag{11.53}$$

$$C_{H_R} = \frac{\sigma C_{D_{rot}}\mu}{4} + \frac{\sigma C_{L\alpha_{rot}}}{4} \left[\theta \left(\frac{a_1\mu^2}{2} + \mu(\lambda_c + \lambda_i) \right) + \frac{q}{\Omega} \left(\frac{b_1\mu}{4} - \frac{a_0}{3} \right) - \frac{a_0 b_1}{3} + \frac{(a_0^2 + a_1^2)\mu}{2} \right] \tag{11.54}$$

Finally, the total rotor thrust and drag can be calculated using Equation 11.55 and Equation 11.56. Having these values, the two forces can now be added to the equations of motion.

$$T_R = \frac{1}{2} C_{T_R} \rho S_{Disk} (\Omega R)^2 \tag{11.55} \qquad D_R = \frac{1}{2} C_{H_R} \rho S_{Disk} (\Omega R)^2 \tag{11.56}$$

11.5.5. Vehicle Parameters and Assumptions

When developing the flight dynamics model, it is important to mention the assumptions made in order to evaluate the dynamic stability of the XV-25. First, it is assumed that all aerodynamic forces on lifting surfaces are positioned at one quarter of the mean aerodynamic chord of each surface. All lifting surfaces and the fuselage are assumed to be infinitely stiff. Furthermore it is assumed that all aerodynamic forces on the fuselage act through the vehicle's center of gravity and that the lift of the fuselage is negligible. Regarding the main rotor, it is assumed that the blades are untwisted and infinitely stiff. The friction of the flapping hinges is assumed to be zero as well.

For the XV-25 Griffin, all the values needed to calculate the forces according to the formulae displayed on subsection 11.5.3 and subsection 11.5.4 are presented on Table 11.8.

Table 11.8: Vehicle Parameters Used for Stability Determination

	Upper Wing	Lower Wing	Horizontal Tail	Fuselage	Rotor Blade
$C_{D_0}\,[-]$	0.00229	0.00229	0.00102	0.00866	0.00733
$k_1\,[-]$	0	0	0	0	0
$k_2\,[-]$	0.02643	0.02643	0.09734	0	0.02567
$C_{L_0}\,[-]$ Flaps Down	0.232	0.232	0	0	0
$C_{L_0}\,[-]$ Flaps Up	1.44	1.44	0	0	0
$C_{L_\alpha}\,[1/rad]$ Flaps Down	5.16	5.16	4.00	0	7.12
$C_{L_\alpha}\,[1/rad]$ Flaps Up	5.116	5.116	4.00	0	N/A
$C_{L_{\delta e}}\,[1/rad]$	0	0	2.59	0	0
$C_{m_0}\,[-]$	-1.8	-1.8	0	0	0
$C_{m_{alpha}}\,[1/rad]$	0	0	0	0	0
$C_{m_{\delta e}}\,[1/rad]$	0	0	0	0	0
$V/V_\infty\,[-]$	1	1	0.85	1	N/A
$S\,[ft^2](m^2)$	631 (58.66)	631 (58.66)	158 (15.9)	2250 (209)	107 (9.92)
$\bar{c}\,[ft](m)$	6.00 (1.83)	6.00 (1.83)	6.27 (1.91)	N/A	2.62 (0.8)
$x - x_{c.g.}\,[ft](m)$	4.2 (1.27)	4.2 (1.27)	36.6 (11.15)	N/A	0.768 (0.234)
$z - z_{c.g}\,[ft](m)$	5.6 (1.708)	3.8 (1.147)	6.2 (1.877)	N/A	9.6 (2.924)
$i\,[deg]$	1	1	-4	N/A	N/A

11.5.6. Numerical Determination of Stability Derivatives

At the moment, there is no defined way of analytically deriving the stability derivatives for a compound vehicle such as the Griffin. For that reason, a numerical method of estimating the stability derivatives has been developed. The first step is determining the state of the vehicle at a specific velocity. This is done using defined values provided by the aerodynamics department, such as angle of attack at specific air-speeds.

For that condition, the forces and moments for flight are recorded, as well as the state and control variable values resulting in these forces. The pitch rate at this condition is assumed to be zero thus $q_0 = 0$ Therefore these forces are denoted as X_0, Z_0 and M_0 defined on Equation 11.57. Those values are placed in vector format and the vector containing the sum of forces for trimmed flight is denoted as $\mathbf{S_0}$ as seen on Equation 11.58.

$$
\begin{aligned}
X_0 &= X(u_0, w_0, 0, \theta_{f_0}, \theta_0, \theta_{1_{S_0}}, \delta_{e_0}, \delta_{t_0}) \\
Z_0 &= Z(u_0, w_0, 0, \theta_{f_0}, \theta_0, \theta_{1_{S_0}}, \delta_{e_0}, \delta_{t_0}) \quad (11.57) \\
M_0 &= M(u_0, w_0, 0, \theta_{f_0}, \theta_0, \theta_{1_{S_0}}, \delta_{e_0}, \delta_{t_0})
\end{aligned}
\qquad
\mathbf{S_0} = \begin{bmatrix} X_0 \\ Z_0 \\ M_0 \end{bmatrix} \qquad (11.58)
$$

Thereafter a small perturbation p is given for each state and control variable such that:

$$
\begin{aligned}
u_p &= u_0 + p_u \\
w_p &= u_0 + p_w \\
q_p &= 0 + p_q \\
\theta_{f_p} &= \theta_{f_0} + p_{theta_f}
\end{aligned}
\quad (11.59)
\qquad
\begin{aligned}
\theta_p &= \theta_0 + p_\theta \\
\theta c_p &= \theta_{1_{S_0}} + p_{\theta_{1_S}} \\
\delta_{e_p} &= \delta_{e_0} + p_{\delta_e} \\
\delta_{t_p} &= \delta_{t_0} + p_{\delta_t}
\end{aligned}
\quad (11.60)
$$

Using the pertubated values one by one, X, Z and M can be re-evaluated separately for each perturbation and are denoted, for instance, X_{p_u} for X evaluated at $X(u_p, w_0, 0, \theta_{f_0}, \theta_0, \theta_{1_{S_0}}, \delta_{e_0}, \delta_{t_0})$. Following the vectorization scheme described earlier, as an example, the vector containing X_{u_p}, Z_{u_p} and M_{u_p} is denoted as seen on Equation 11.61. Given that the pertubations are small enough, the stability derivatives can be approximated as seen on equation Equation 11.62

$$
\mathbf{S_{p_u}} = \begin{bmatrix} X_{p_u} \\ Z_{p_u} \\ M_{p_u} \end{bmatrix} \qquad (11.61)
\qquad
X_u = \frac{\partial X}{\partial u} \approx \frac{\Delta X}{\Delta u} = \frac{X_{p_u} - X_0}{p_u} \qquad (11.62)
$$

Now, using the vectorized format, vectorized stability derivatives can be arranged in such a way that a structured

set of them can be utilized as a base to construct the **A** and **B** matrices of the state-space system. The vectorized derivatives for a perturbation in u are denoted $\mathbf{S_u}$ and the set of all vectorized derivatives is denoted as $\mathbf{S}$. The calculation method can be seen on Equation 11.63 and Equation 11.64 respectively.

$$\mathbf{S_u} = \frac{\mathbf{S_{p_u}} - \mathbf{S_0}}{p_u} \tag{11.63}$$

$$\mathbf{S} = \{\mathbf{S_u}, \mathbf{S_w}, \mathbf{S_q}, \mathbf{S_{\theta_f}}, \mathbf{S_\theta}, \mathbf{S_{\theta_{1_S}}}, \mathbf{S_{\delta_e}}, \mathbf{S_{\delta_t}}\} = \begin{bmatrix} X_u & X_w & X_q & X_{\theta_f} & X_\theta & X_{\theta_{1_S}} & X_{\delta_e} & X_{\delta_t} \\ Z_u & Z_w & Z_q & Z_{\theta_f} & Z_\theta & Z_{\theta_{1_S}} & Z_{\delta_e} & Z_{\delta_t} \\ M_u & M_w & M_q & M_{\theta_f} & M_\theta & M_{\theta_{1_S}} & M_{\delta_e} & M_{\delta_t} \end{bmatrix} \tag{11.64}$$

Finally, the columns of **S** can be used to construct **A** and **B** and with that the system can be simulated. The explicit definition of **A** and **B** are found on subsection 11.5.1. The stability and control derivatives for various velocities up to transition can be found on Figure 11.6 and Figure 11.7.
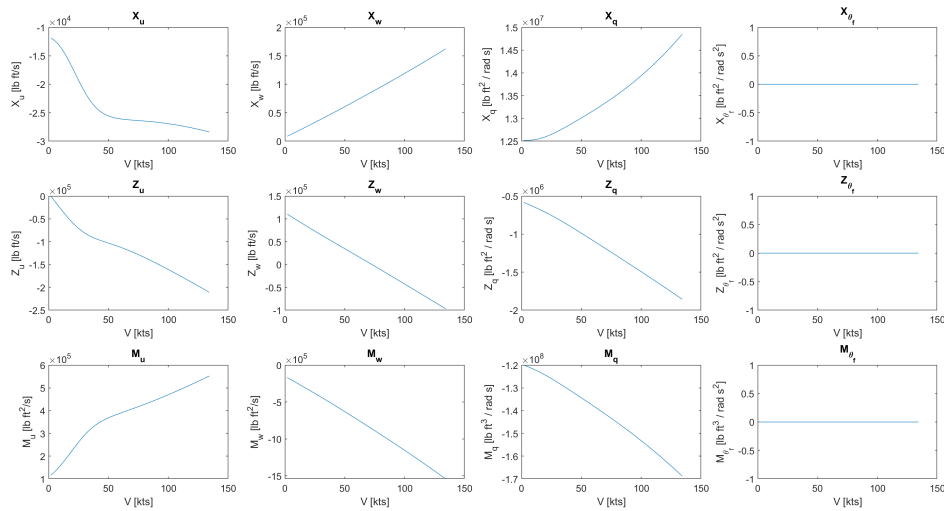
Figure 11.6: Stability Derivatives from 0 to 135kts
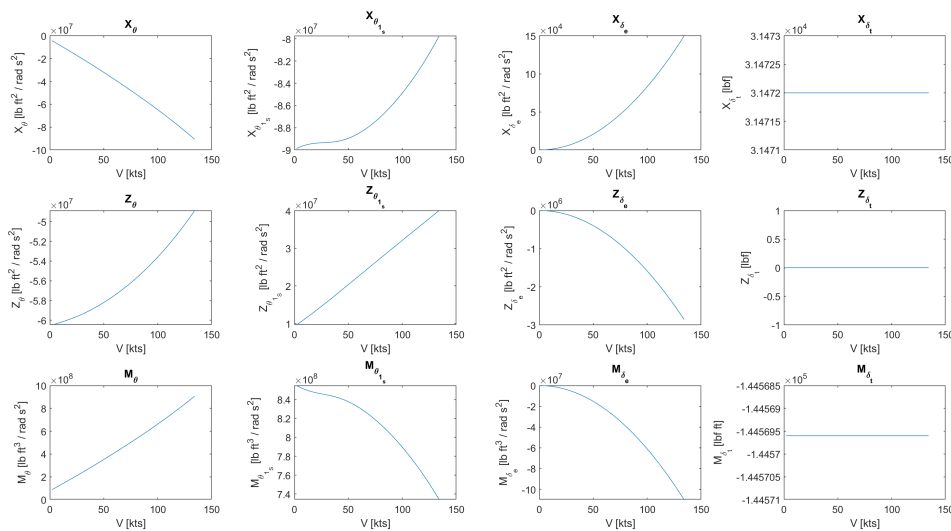
Figure 11.7: Control Derivatives from 0 to 135kts

Using a similar method for the aircraft with the rotor retracted (thus neglecting any contribution of the rotor), the stability and control derivatives can be found on Figure 11.8.
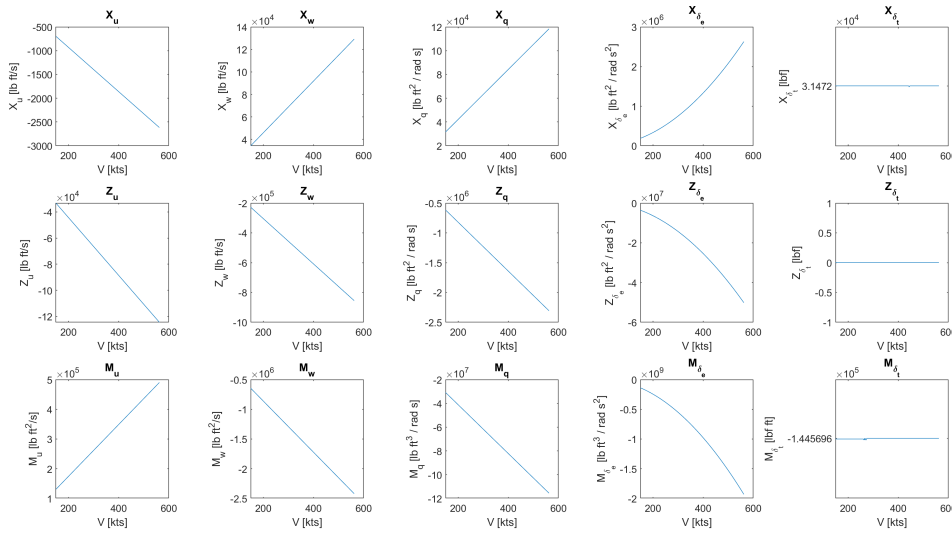
Figure 11.8: Stability and Control Derivatives at Fixed Wing Configuration

11.5.7. Dynamic Stability Characteristics

After constructing the state-space system for the XV-25, it is useful to also represent the system in the frequency domain. As a MIMO (Multi-Input, Multi-Output) system, the flight characteristics of the vehicle can be shown as a set of transfer functions from each input to the system output. One example set of these transfer functions can be found on Equation 11.65, describing the transfer functions of the linear system at $V = 65$kts from control variable θ (collective angle) to the output (in sequence, u, w, q and θ_f). As seen from the denominator of all the transfer functions, the compound helicopter is a fourth-order system. This information can be particularly useful for selecting a suitable controller for the system.

$$H_1(s) = \frac{-61.76s^3 - 42.55s^2 - 92.41s - 38.36}{s^4 + 2.892s^3 + 1.578s^2 + 0.2103s + 0.2784}$$

$$H_2(s) = \frac{-85.15s^3 + 66.25s^2 - 2.459s + 28.23}{s^4 + 2.892s^3 + 1.578s^2 + 0.2103s + 0.2784}$$

$$H_3(s) = \frac{8.905s^3 + 3.417s^2 - 0.1561s + 8.901 \times 10^{-17}}{s^4 + 2.892s^3 + 1.578s^2 + 0.2103s + 0.2784}$$

$$H_4(s) = \frac{8.905s^2 + 3.417s - 0.1561}{s^4 + 2.892s^3 + 1.578s^2 + 0.2103s + 0.2784}$$

(11.65)

In order to visualise the longitudinal stability characteristics of the system, the stability of the system is demonstrated using a disturbance of $1°$ of aft cyclic with a duration of $2s$ at time $t = 1s$ at various flight velocities. The behaviours of the compound from the mentioned input is shown on Figure 11.9a for hover, Figure 11.9b at 35kts, Figure 11.9c at 65kts and Figure 11.9d at 135kts when the rotor begins the power-down sequence. The Pole-Zero Map of each flight condition can be seen on Figure 11.10.

(a) Instability in Hover

(b) Instability at 35kts

(c) Instability at 65kts

(d) Marginal Instability at 135kts
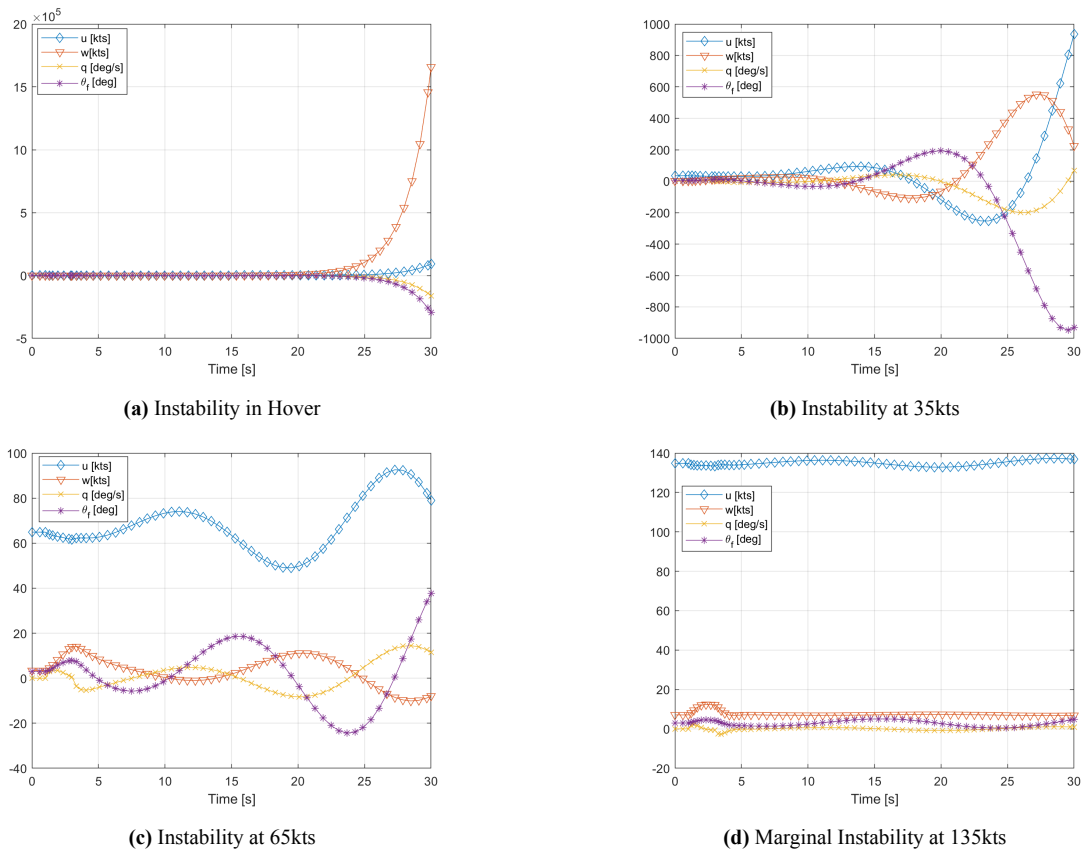
Figure 11.9: Stability Characteristics at Compound Configuration

(a) Pole-Zero Map at Hover

(b) Pole-Zero Map at 35kts

(c) Pole-Zero Map at 65kts

(d) Pole-Zero Map at 135kts
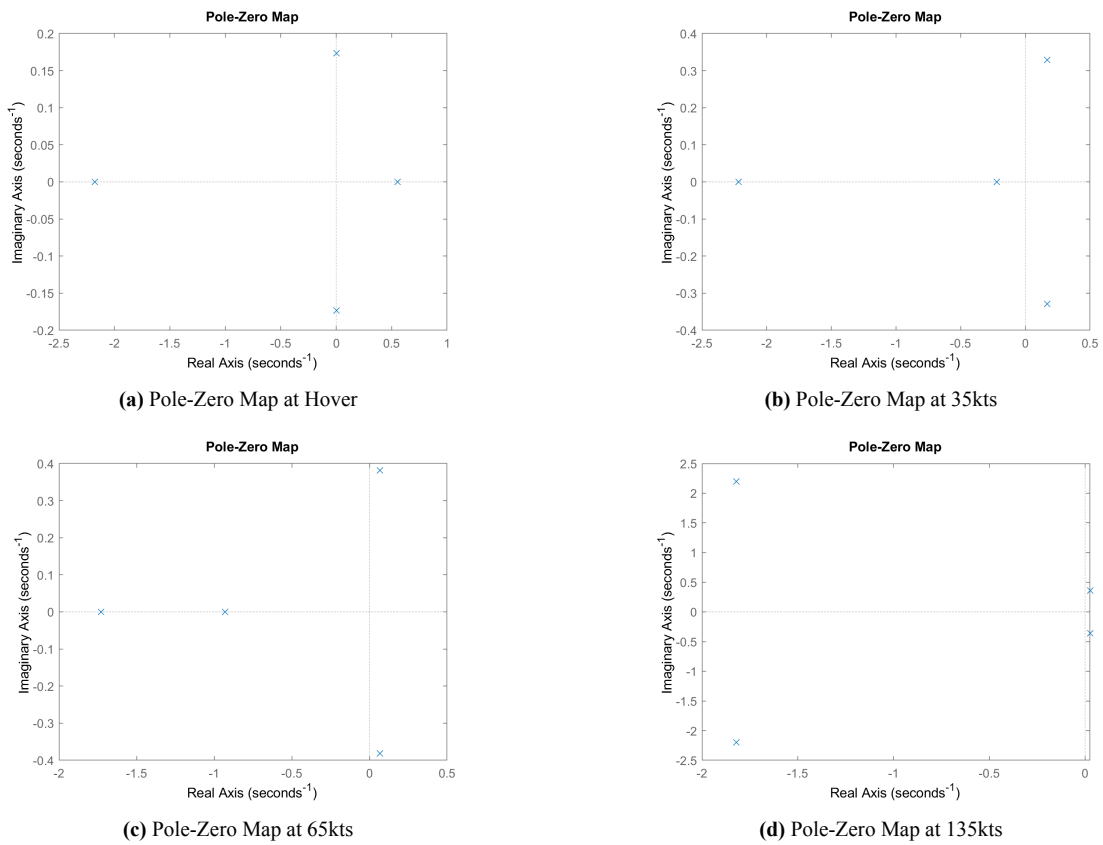
Figure 11.10: Pole-Zero Maps at Compound Configuration

11.5.8. Control Allocation

The XV-25 Griffin, due to the nature if its design, can be classified as an over-actuated system. That means that there are multiple ways of achieving control of the vehicle. It is therefore necessary to allocate in which way the vehicle is controlled while staying within the limits of the different control deflections. The control allocation is determined from the velocity of flight.

For speeds below 50 kts (25.7 m/s) the aerodynamic control surfaces are not effective enough to achieve any reasonable control authority. As such, the vehicle is operated as a pure helicopter below 50 kts.

For speeds between 50 kts (25.7 m/s) and the transition speed of 135 kts (69.4 m/s) aerodynamic surfaces start producing sufficient aerodynamic forces in order to start using them. Therefore the control authority of the rotor-based controls is linearly decreased as speed increases to the point that it is zero at the transition speed. This is done using a controls mixing factor denoted as CMF and can be calculated using Equation 11.66. This creates a control authority deficit which needs to be compensated using the throttle and elevator deflections to minimise the residuals of the deficit.

Finally for speeds above 135 kts (69.4 m/s) the aircraft is purely controlled as a fixed wing aircrft with throttle and elevator deflections, since the rotor is being stopped and any control outputs with decreasing rotor speed are unreliable.

$$CMF = \begin{cases} 1, \text{ for } V \leq 50\text{kts} \\\\ 1 - \frac{V-50}{135-50}, \text{ for } 50 \leq V \leq 135\text{kts} \\\\ 0, \text{ for } 135 \leq V \leq V_{max}\text{kts} \end{cases} \tag{11.66}$$

A problem that arises from over-actuation is control inputs being relayed from the pilot to the controls. Generally, there should only be one stick and throttle/collective at the cockpit. Therefore the transitioning of controls should happen through a control augmentation system that can either be mechanically or electronically (fly-by-wire) actuated. Since the controls of rotary and fixed wing aircraft are so drastically different, it is chosen to use a fly-by-wire system for control mixing. This has the additional benefit of simplifying the application of any controllers further on.

The method of allocating controls to different actuators by a single input system is performed by using a method called explicit ganging. With explicit ganging, there has to be a ganging matrix **G** that relates the existing control vector deflections to a pseudo-vector for control [80] . For instance, for the desired two-input control system of the XV-25 Griffin, the setup of the ganging matrix should be constructed as seen on Equation 11.67.

$$\mathbf{u} = \mathbf{G}\mathbf{u}_{pseudo} \Rightarrow \begin{bmatrix} \theta \\ \theta_{1_S} \\ \delta_e \\ \delta_t \end{bmatrix} = \mathbf{G} \begin{bmatrix} \delta_{stick} \\ \delta_{power} \end{bmatrix} \tag{11.67}$$

Since the control allocation has already been performed using the controls mixing factor, the ganging matrix can be defined as seen on Equation 11.68. Since the effectiveness of control deflections of cyclic with elevator and collective with throttle are not one-to-one, a deflection scaling factor should be introduced.

$$\mathbf{G}(V) = \begin{bmatrix} 0 & CMF \\ CMF & 0 \\ 1 - CMF & 0 \\ 0 & 1 - CMF \end{bmatrix} \Rightarrow \begin{bmatrix} \theta \\ \theta_{1_S} \\ \delta_e \\ \delta_t \end{bmatrix} = \begin{bmatrix} 0 & CMF \\ CMF & 0 \\ 1 - CMF & 0 \\ 0 & 1 - CMF \end{bmatrix} \begin{bmatrix} \delta_{stick} \\ \delta_{power} \end{bmatrix} \tag{11.68}$$

11.6. Stabilization and Controllers

As discussed in subsection 11.5.7, the vehicle demonstrates dynamic instability up to the transition speed of 135kts. This characteristic was deemed not acceptable by the design team and therefore it was decided to apply a controller in order to stabilize the vehicle. For the sake of simplicity, it was decided that a variant of a simple PID (Proportional-Integral-Derivative) controller would be investigated as a stabilization force for the system. Additionally, it was decided to apply the controller using pitch rate feedback, as it is seen that the compound demonstrates instability in pitch.

As seen on subsection 11.5.7, the XV-25 Griffin is a fourth order system. As rotary wing aircraft are characterised as relatively quick responding systems, having a derivative control is a logical step into choosing a controller, due to its trend based predictive control characteristics. This therefore limits the controller choice to either PD or PID. An integral controller would be beneficial as it can eliminate steady-state errors up to third order terms. However, due to the difficulty of tuning a PID controller, it is chosen to use a simpler PD controller to stabilise the system.

It is a characteristic of helicopters to be unstable up to specific speeds. Helicopters without a horizontal stabilizer generally remain unstable up to high speeds. However, helicopters that utilize a horizontal stabilizer are able to be stable at much slower speeds [81]. As the XV-25 Griffin has a horizontal tail with integrated elevators, it should be stable when the horizontal stabilizer is able to provide sufficient aerodynamic forces.

However, as indicated on subsection 11.5.7, the aircraft is aerodynamically unstable even with the horizontal tail present, due to the fact that the fixed wing system is mildly unstable by design. Hence, a stabilization strategy can be derived. Up to flight velocities of about 60kts, conventional helicopters are generally dynamically unstable, as the horizontal tail does not produce comparable aerodynamic forces to the main rotor. For the XV-25, as the elevators become relatively effective at 50kts, control authority starts being granted to the pilots. Adding a safety buffer of 15kts above that speed, the PD controller begins to stabilize the aircraft using elevator inputs. Therefore, for speeds up to 65kts, the XV-25 behaves like a pure helicopter and then after that the PD controller stabilizes the aircraft gradually so it is dynamically stable up to the transition speed. The architecture of the XV-25 Griffin's control system can be seen on Figure 11.11.
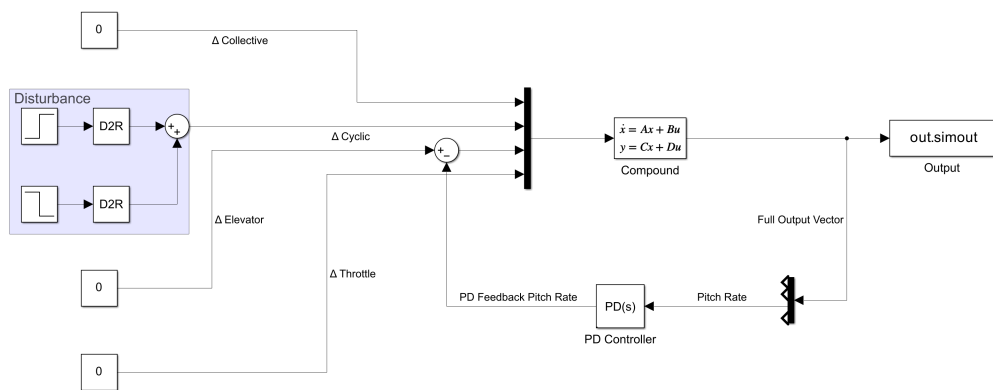
Figure 11.11: Architecture of the PD Controller System

The PD controller is tuned manually using a transfer function based compensator of the form seen on Equation 11.69, where K_p is the proportional gain, K_d is the derivative gain and N is a filtering coefficient. The controller was tuned to result in under-damped and marginally stable motion at a velocity of 65kts. The gains and filtering coefficient values can be found on Table 11.9.

$$K(s) = K_p + K_d \frac{N}{1 + N\frac{1}{s}} \qquad (11.69)$$

Table 11.9: P and D Gains and Filtering Coefficient

$\mathbf{K_p}$	-4.3156054
$\mathbf{K_d}$	-27.951217
$\mathbf{N}$	1.251914

Finally, for the system with the controller added, the stability characteristics for the same input and velocity as Figure 11.9c and Figure 11.9d can be found on Figure 11.12a and Figure 11.12b respectively.

(a) Stable Motion at 65kts

(b) Stable Motion at 135kts
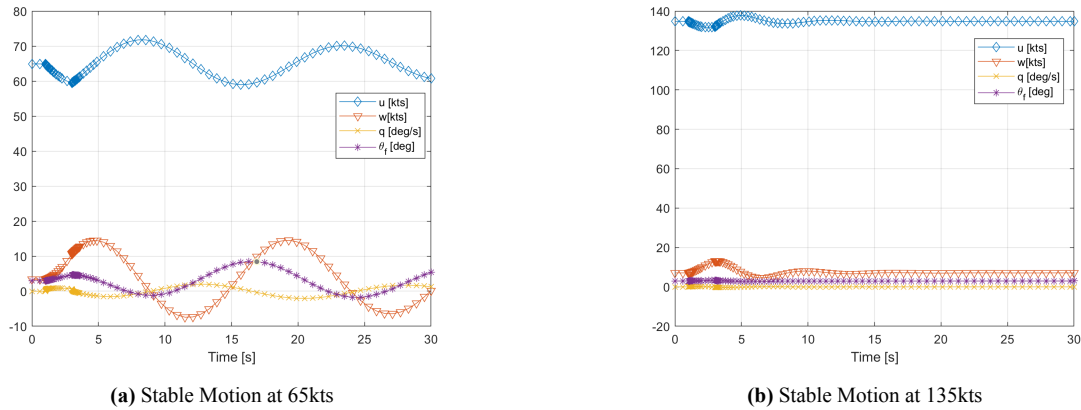
Figure 11.12: Stability Characteristics at Compound Configuration with Pitch Rate Controller

Similarly, when the aircraft is at cruise configuration, with the main rotor stowed, the same controller can be used to stabilize the oscillations from a disturbance. Here, a pull-up command of the aircraft using $5°$ of elevator deflection from $t = 1s$ until $t = 3s$ is performed at $V = 305kts$, which is the V_Y speed. The characteristics of the motion after the disturbance can be seen on Figure 11.13a for the free motion and Figure 11.13b for the stabilized motion. An important remark is that the stabilized aircraft velocity deviation at V_Y is less than $\pm10kts$ (namely $4kts$) in order to satisfy the CS-29 requirements set.

(a) Free Motion

(b) Stabilised Motion
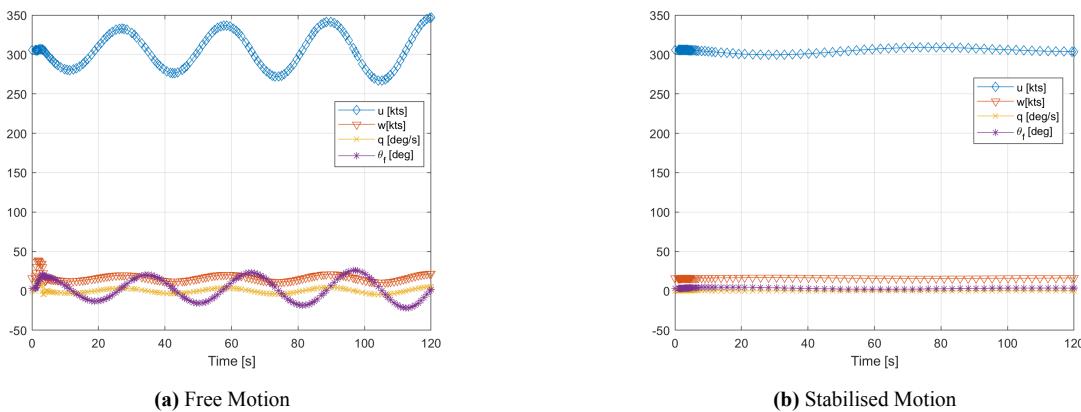
Figure 11.13: Comparison of Motion in Cruise Configuration of the Free and Stabilized Aircraft

11.7. Verification and Validation

Verification of the functions of the dynamic system was performed by feeding values of known helicopters and aircraft into separate functions and verifying that the results given corresponded with the actual values that arose from analytical solutions of the same problem.

Validation of the rotary wing model has been performed using data for the Bo-105 helicopter obtained from [79]. Using this data, the stability of the system compared to flight test data of the Bo-105 [82] were contrasted and found to be matching to a satisfactory level. However, as expected, differences were observed and can can be explained to the coupled nature of helicopter longitudinal and lateral modes.

Validation of the fixed wing model was performed by comparing with the scissor plot, this showcases that the aircraft is mildly unstable which is confirmed within the results.

12

Final System Overview

As individual subsystems have been analyzed thoroughly from Chapter 8 to Chapter 11, the XV-25 Griffin is now presented as a whole along with a complete CAD model. Typical characteristics of the aircraft such as performance usually involve two or more subsystems and generally cannot be assessed separately. The final design of the XV-25 Griffin is reported in section 12.1 while important details are outlined in section 12.2. An overview of the main vehicle parameters can be found on Table 12.1.

12.1. Final Vehicle Overview

Here a general overview of the vehicle will be given. The first section will describe the concept and the layout of the major components, followed by the internal layout of the different systems contained in the aircraft.

12.1.1. General Vehicle Overview
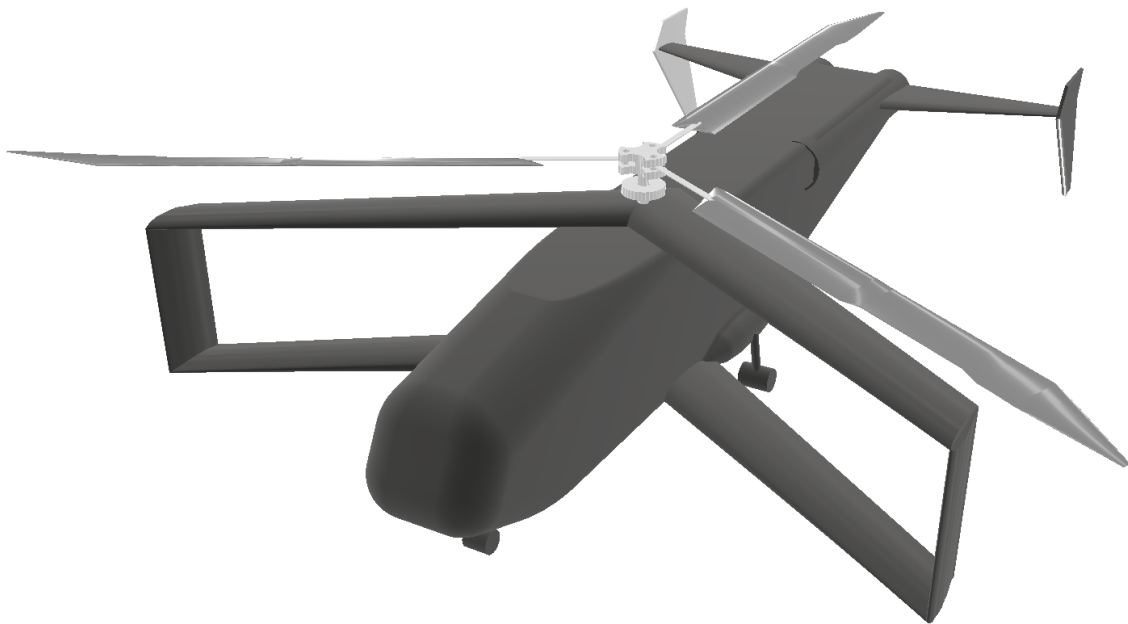
Figure 12.1: Overview of the XV-25 Griffin

Throughout the design, the team converged onto a final design of a stowed-rotor compound helicopter powered by two jet engines with auxiliary shaft output turbines to power the rotor. The design consists of a 20m long fuselage, with a rotor and forward swept wing mounted along each other in the center. This co-alignment and forward sweep allow the rotor to be lowered into the wings and rear fuselage. The rotor blades use an innovative rotor retraction mechanism that reduces the rotor radius from 12.4m to around 7.5m to allow the rotors to fit into the wings. To lower the rotor the entire mast and rotor assembly is attached to jack-screws, which can lower the rotor into the storage compartments in the wing and rear fuselage. The fuselage contains a payload bay 6.5 ft (1.98 m) high, 8 ft (2.43 m) wide, and 30 ft (9.14 m) long, which can be accessed through a ramp from the rear. This enables efficient loading and unloading of even the most bulky equipment. The tail is in H configuration, with the majority of the vertical stabilizer extending towards the ground to prevent collisions with the rotor. The tail also houses the two turbofan engines providing thrust for both forward flights as well as to counteract the torque from the rotor during hover. This is achieved using a nozzle using the redirected bypass flow.

Table 12.1: General Vehicle Overview

Variable	Value	Unit	Variable	Value	Unit
Weights			Speeds		
Maximum Take Off Weight	62,361	lbs	Cruise Speed	450	kts
Empty Weight	37,624	lbs	Transition Speed	150	kts
Operating Empty Weight	38,374	lbs	Stall Speed	121.6	kts
Fuel Mass	17,986	lbs	Rotor		
Crew Mass	750	lbs	Rotational Speed	19.6	rad/s
Payload Mass	6,001	lbs	Rotor Radius	40.68	ft
Wing			Collective Angle Hover	8.88	deg
Wing Area	631.4	ft^2	Max Collective Angle	10.25	deg
Wing Span	52.49	ft	Coning Angle Hover	5.02	deg
Wing Root Chord	7.43	ft	Max Rotor Lift	79,227.2	lbf
Wing Tip Chord	4.59	ft	Rotor Torque Hover	326,535.5	ft-lbs
Wing Aspect Ratio	8.72	-	Max Rotor Torque	391,259.4	ft-lbs
Thickness to chord ratio	0.15	-	L/D Blades Hover	17.58	-
Sweep Trailing Edge	-35.29	deg	L/D Blades Max Climb	16.08	-
Zero-lift angle of attack	-2.6	deg			
Horizontal Tail			Vertical Tail		
Horizontal Tail Area	171.79	ft^2	Vertical Tail Area	32.08	ft^2
Horizontal Tail Span	27.38	ft	Vertical Tail Span	8.01	ft
Horizontal Tail Average Chord	6.27	ft	Vertical Tail Average Chord	4.00	ft
Horizontal Tail Aspect Ratio	4.36	-	Vertical Tail Aspect Ratio	2.00	-

12.1.2. Internal configuration and layout
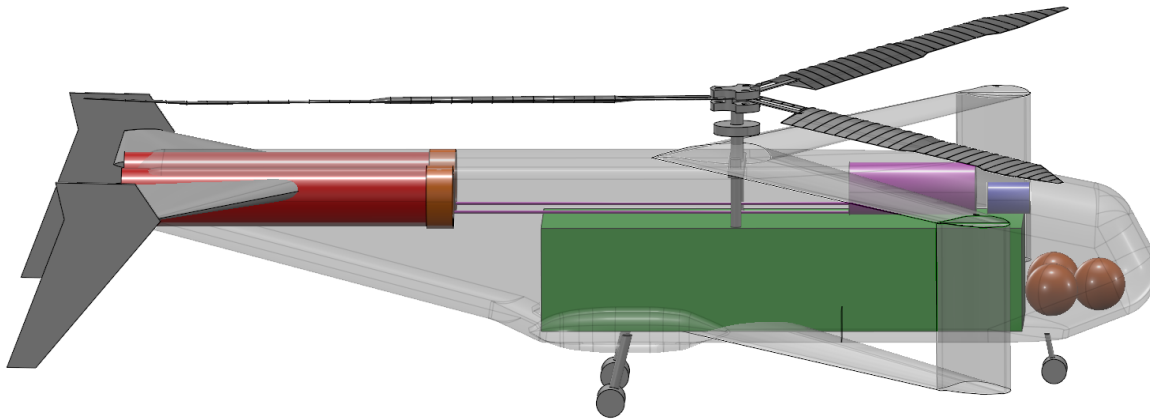
Figure 12.2: Side View of the Internal Layout of the XV-25 Griffin

The internal layout is largely determined by the payload, the need to lower the rotor as well as the mass distribution to ensure a manageable distribution of the center of gravity during flight for both forward flight and hover. The payload is placed centrally, with the fuselage built around it. The fuselage will allow for space above the payload to house the mechanism that lowers the rotor as shown in Figure 12.2. In addition to this mechanism, the space above the payload will house the gearbox along with its driveshaft to the engines. The gearbox is placed in front of the rotor to allow the aircraft to stay relatively balanced about the rotor and wing. The engines are placed in the rear of the fuselage, above the ramp accessing the payload bay. This allows great access to loading and unloading of the payload bay, while at the same time providing thrust and keeping the jet blast out of reach for the majority of ground equipment. Landing gear is arranged in a tricycle configuration, with the rear landing gear being behind the most aft possible center of gravity location to allow loading without tip over.

This limits the possibility of taking off horizontally as rotation becomes challenging, but still allows emergency landings as a glider. Fuel can be contained entirely in the lower wings, which allows the upper wings to act purely as the storage for the rotor blades. Additionally, the two engines are spaced apart to allow for the blade in the rear position to lower into the fuselage at that position as shown in Figure 12.3.
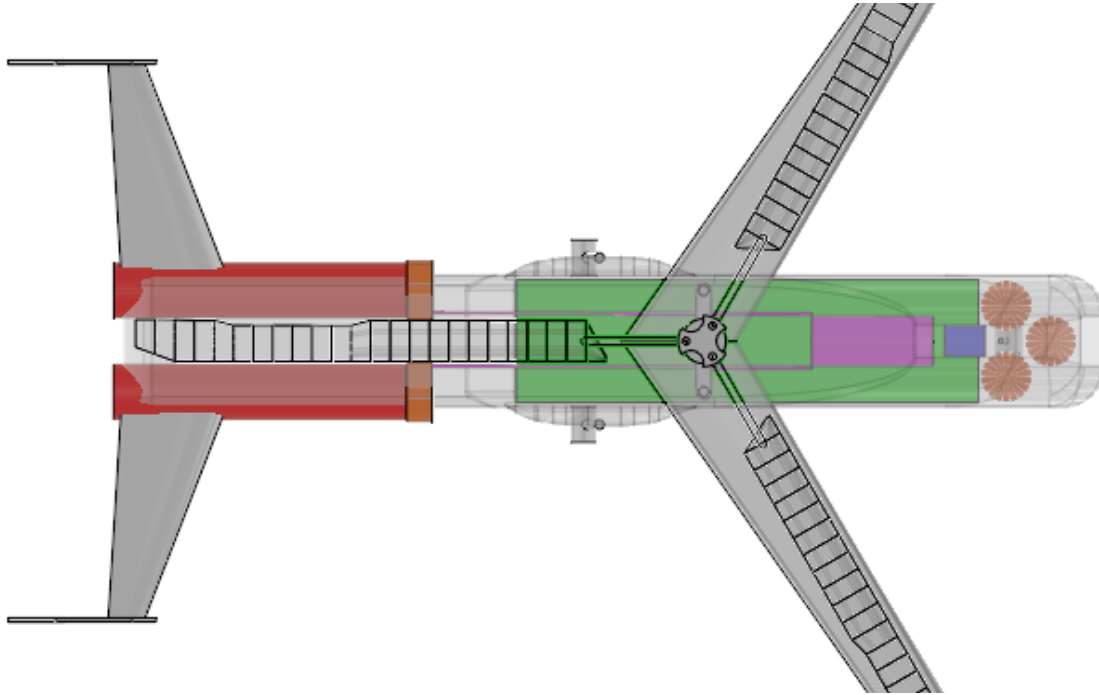
Figure 12.3: Top View of the Internal Layout of the XV-25 Griffin

12.2. Performance Analysis

12.2.1. Payload & Range

The payload-range relation can be described by the aforementioned list (repeated here for convenience).

- Missions range: 1852 km / 1150 miles + hover time, reserves.

- Continuous fixed-wing cruise starting at MTOW, maximum fuel and payload: 4309 km / 2678 miles taking 10.9 hours.

- Ferry (continuous fixed-wing cruise starting at MTOW, maximum fuel and zero payload): 4585 km / 2849 miles taking 12.4 hours.

- Ferry with range extender (extra fuel tank, same weight as maximum payload): 5698 km / 3541 miles taking 15.6 hours.

The available fuel for the range is heavily dictated by the design mission (payload). As can be seen from the list flying at optimal conditions greatly improves the possible range.

12.2.2. Climb performance

The climb characteristics of the XV-25 Griffin were calculated in section 9.5. A summary of the climb performance will be presented here. Due to the uniqueness of the vehicle, a climb performance analysis was performed on the vehicle when in two distinct mission phases; vertical flight (using the rotor) and forward flight (using conventional aircraft wings).

In hover, assuming take-off conditions, the XV-25 Griffin has a vertical rate of climb of 2.9m/s and a theoretical ceiling of approximately 1845m. Compared to conventional helicopters, these values are on the lower side but this can be explained by the fact that the rotor cannot produce a large thrust in excess to the thrust required to hover due to the stringent requirement of the vehicle having only 3 blades. These values rise up to 4.66m/s and 2750m, assuming end-of-mission conditions where most of the fuel has been expelled.

After the vehicle has transitioned and the rotor has been stored in the wings, a climb performance analysis will be performed assuming a conventional aircraft. In this mode, at take-off conditions, the XV-25 Griffin has a best rate of climb of 15.35m/s at a forward velocity of 157.2m/s (resulting in a climb angle of 5.58°) and it has a theoretical ceiling of 12100m. The variation of the best rate of climb and best rate of climb velocity can be found in section 9.5. In addition to this, at take-off conditions, the XV-25 Griffin has a maximum climb angle of 7.9° at a speed of 105.2m/s. This value can increase to 12.1° assuming end of mission conditions and no payload.

12.2.3. Noise characteristics

As earlier analyzed in chapter 8, Table 8.3 illustrated the estimated sound outcomes of the XV-25 Griffin in different flight phases. The actual EASA testing conditions defined in ICAO Annex 16 Volume I [83] are used to obtain the sound outputs, which provide more reasonable answers as the formulas take into account multiple aerodynamic factors rather than just the MTOW of the vehicle [4]. In comparison with other EASA-certified vehicles [1], the upper noise limit is set to be 100.5 dB for the Eurocopter EC225 and 101.5 dB for the Leonardo AW101. With a peak SPL of 97.8 dB at a distance of 150 ft (45.7 m) during take-off, the XV-25 Griffin is still a loud vehicle but it stays within the EASA certification range.

At this design phase, it is uncertain whether such noise would negatively affect the XV-25 Griffin's ability to properly execute the mission profile. If it is concluded that the noise is unacceptable for military purposes because it draws too much unnecessary attention, the team will consider multiple methods to reduce the noise. According to reference [18], the general advice is to reduce the rotor tip speed and use the lowest possible tip speed. Noise reduction from 7 to 10 dB can be achieved with this approach. It is also suggested to improve the blade design, possibly with a trapezoid tip shape to further decrease the vortex noise. Twists of the blade can be iterated to obtain an optimal distribution of the tip loading to minimize the local turbulence as a good aerodynamic design can lower the noise without a loss in efficiency.

12.2.4. Emissions

As explained in chapter 9, the team chose jet fuel (kerosene) as the fuel for the XV-25 Griffin due to storage constraints for hydrogen combustion in addition to mass constraints for fuel cells. With the fuel selected and the fuel mass having been calculated in chapter 9, an estimation of the emissions can be found.

Kerosene emits 3.16 kg of CO_2 per kilogram of kerosene combusted and the production of kerosene adds approximately another 0.5 kg of CO_2 per kg of kerosene [2]. Adding these up leads to a total value of 3.66 kg of CO_2 per kg of kerosene combusted. Multiplying this by the estimated fuel mass required leads to an average total amount of 29859.9 kg of CO_2 emitted during the course of a whole mission as prescribed in Figure 4.1. In addition to this, kerosene emits about 0.003 kg of nitrous oxides per kg combusted [3]. This results in a total nitrous oxide emission of 24.5kg per average mission of the XV-25 Griffin. Nitrous oxide is one of the most important greenhouse gasses after methane and carbon dioxide and hence must be taken into account when analysing the emission characteristics of the XV-25 Griffin.

Although this value is high due to kerosene having poor emission qualities, the team managed to reduce this value when compared to similar vehicles in production by reducing the weight of the vehicle due to the use of composites in the wing and the fuselage as explained in chapter 11. The use of composites does lead to an adverse effect in terms of sustainability due to it not being an ideal material for recycling although a lot of research is currently being done on the recycling of composites such as in [84]. In addition to this, sustainable, synthetic kerosene (SAF) could become a potential replacement for conventional kerosene in aviation leading to better emission characteristics. Countries like the Netherlands aim to have 14% of all aviation fuel be synthetic kerosene by 2030 [85] although costs are much higher when compared to conventional kerosene and are expected to stay high until at least 2050 [85]. In addition, as mentioned in subsection 9.4.3, hydrogen combustion could become a possibility throughout the next decade although the technology is not mature enough to be currently considered.

---

[1] https://www.easa.europa.eu/en/domains/environment/easa-certification-noise-levels
[2] https://www.offsetguide.org/understanding-carbon-offsets/air-travel-climate/climate-impacts-from-aviation/co2-emissions/
[3] https://www.engineeringtoolbox.com/nox-emission-combustion-fuels-d_1086.html

12.3. Compliance matrix

This section contains a compliance matrix of the XV-25 Griffin requirements, indicated by their ID for the sake of brevity. Full descriptions of each requirement can be found in the Baseline Report [5]. Because all of the stakeholder and mission requirements, as defined in chapter 4, were previously translated into direct technical requirements and constraints, only these are evaluated.

The compliance matrix is shown in Table 12.2. For the sake of brevity, each requirement is referred to by its ID. Full descriptions of each requirement can be found in the Baseline Report [5]. If compliance has been demonstrated, the cell is colored green and a reference to the relevant section of the report is given. Some requirements are colored grey, indicating that the requirement is not fulfilled. This happened for two reasons. On the one hand, some requirements related to subsystems that were still in consideration during earlier design phases but ultimately not chosen. Such requirements have been marked with **NA**. On the other hand, certain requirements needed a depth of analysis that was beyond the scope of this project, in which case they are marked with **OOS**. The unverified requirements are discussed in further detail below.

Unverified requirements

The non-applicable (NA) requirements were disqualified for reasons that are largely self-explanatory. When the choice was made to not use propellers for forward propulsion, as detailed in section 9.2, requirements SYS-TECH-PROP-1-1, SYS-TECH-PROP-6 and SYS-TECH-STRUC-4-1 became irrelevant. The decision to use two engines for purposes of redundancy eliminated SYS-TECH-ROT-2-4 as it only applies to single-engine vehicles. The options of intermeshing rotors as well as ducted fans were previously discarded for reasons explained in the [4], so the requirements under SYS-TECH-ROT-5 and SYS-TECH-ROT-6 were ignored.

Out-of-scope (OOS) requirements remain unverified because they required a detailed design or analysis that was too in-depth for the current project scope, or even needed testing of prototypes to be evaluated. SYS-TECH-PROP-2-2 and the requirements under SYS-TECH-PROP-5 would have required a vibrational analysis of the engine and design of the fuel pumping system, respectively. Under SYS-TECH-LG, the requirements on side loads could not be verified with the current landing gear model. The environmental hazards of SYS-TECH-SAFE-1 also require too much detail on the structures, electrical system and fuel system to be answered at this point in time. Similarly, SYS-TECH-SAFE-3 and SYS-TECH-SAFE-4 were disregarded as the fire extinguishing and cooling systems have not been designed yet. The structural attachments of different components are not set yet so SYS-TECH-SAFE-5-1, dealing with fasteners, could not be answered.

While several requirements dealing with engine failure could be answered on the basis that the aircraft is capable of both autorotation and gliding, SYS-TECH-ROT-2-1 and SYS-TECH-FLY-4-1 require substantive flight testing to be verified. SYS-TECH-STRUC-2-1-6 also requires testing of components and could thus not be done.

Many of the structural requirements remain unverified. chapter 10 outlines the reasons for this in great detail, but they will be summarized here for clarity. Load analysis was limited to the wings, rotor structure, fuselage, landing gear and tail. As such, SYS-TECH-STRUC-2-1-5 concerning the engine mount, SYS-TECH-STRUC-5-1 concerning control surfaces, SYS-TECH-STRUC-6-2 concerning fuel tanks and SYS-TECH-STRUC-7-3 concerning emergency exit doors, were beyond the scope of this project. Although the static as well as cyclic loads acting on the fuselage and rotor pylon have been quantified, these are not the critical loads as meant by SYS-TECH-STRUC-2-6 and SYS-TECH-STRUC-2-7, which have been identified as dynamic in nature. Similarly, the dynamic analysis of aerodynamic surfaces such as the wings needed to answer SYS-TECH-STRUC-3-1 has not been performed at this point.

In terms of stability and maneuverability, SYS-TECH-FC/HQ-1-2-5 is out of scope as the lateral flight modes have not been examined. The SYS-TECH-FC/HQ-4 requirements are not satisfied as they involve side-winds and therefore also lateral stability.

Table 12.2: Requirements compliance matrix for the XV-25 Griffin.

ID	Details	ID	Details	ID	Details
SYS-CO-RES-1	All	SYS-TECH-FC/HQ-1-2-5	OOS	SYS-TECH-FLY-2-1	Ch. 9
SYS-CO-RES-2-1	Ch. 3	SYS-TECH-FC/HQ-2	Ch. 11	SYS-TECH-FLY-2-2	Ch. 9
SYS-CO-RES-2-2	Ch. 3	SYS-TECH-FC/HQ-3-1	Ch. 11	SYS-TECH-FLY-3-1	Ch. 9
SYS-CO-RES-3-1	All	SYS-TECH-FC/HQ-3-2	Ch. 11	SYS-TECH-FLY-3-2	Ch. 9
SYS-CO-RES-3-2	All	SYS-TECH-FC/HQ-3-3	Ch. 11	SYS-TECH-FLY-3-3	Ch. 9
SYS-CO-SUS-1-1	Ch. 5	SYS-TECH-FC/HQ-4-1	OOS	SYS-TECH-FLY-3-4	Ch. 9
SYS-CO-SUS-1-2	Ch. 5	SYS-TECH-FC/HQ-4-2	OOS	SYS-TECH-FLY-4-1	OOS
SYS-CO-SUS-2	Ch. 5	SYS-TECH-FC/HQ-5-1	Ch. 11	SYS-TECH-FLY-4-2	Ch. 9
SYS-CO-LEG-1	All	SYS-TECH-FC/HQ-5-2	Ch. 11	SYS-TECH-FLY-5	Ch. 9
SYS-CO-LEG-2	All	SYS-TECH-FC/HQ-5-3	Ch. 11	SYS-TECH-FLY-6-1	Ch. 9
SYS-CO-LEG-3	All	SYS-TECH-FC/HQ-5-4	Ch. 11	SYS-TECH-FLY-6-2	NA
SYS-CO-LEG-4	All	SYS-TECH-LG-1	Ch.	SYS-TECH-FLY-7	Ch. 9
SYS-TECH-PROP-1-1	NA	SYS-TECH-LG-2	Ch. 10	SYS-TECH-PAY-1	Ch. 10
SYS-TECH-PROP-1-2	OOS	SYS-TECH-LG-3-1	Ch. 10	SYS-TECH-PAY-2	Ch. 9
SYS-TECH-PROP-2-1	Ch. 9	SYS-TECH-LG-3-2	Ch. 10	SYS-TECH-PAY-2-1	Ch. 10
SYS-TECH-PROP-2-2	OOS	SYS-TECH-LG-3-4	Ch. 10	SYS-TECH-STRUC-1-1	Ch. 10
SYS-TECH-PROP-3	Ch. 9	SYS-TECH-LG-3-5	OOS	SYS-TECH-STRUC-1-2	Ch. 10
SYS-TECH-PROP-4-1	Ch. 9	SYS-TECH-LG-4-1	Ch. 10	SYS-TECH-STRUC-1-3	Ch. 10
SYS-TECH-PROP-4-2	Ch. 9	SYS-TECH-LG-4-2	OOS	SYS-TECH-STRUC-1-4	Ch. 10
SYS-TECH-PROP-4-3	Ch. 9	SYS-TECH-LG-5-1	Ch. 10	SYS-TECH-STRUC-2-1-1	Ch. 10
SYS-TECH-PROP-4-4	Ch. 9	SYS-TECH-LG-5-2	Ch. 10	SYS-TECH-STRUC-2-1-2	Ch. 10
SYS-TECH-PROP-5-1	Ch. 9	SYS-TECH-LG-5-3	Ch. 10	SYS-TECH-STRUC-2-1-3	Ch. 10
SYS-TECH-PROP-5-2	OOS	SYS-TECH-LG-5-4	Ch. 10	SYS-TECH-STRUC-2-1-4	Ch. 10
SYS-TECH-PROP-5-3	Ch. 10	SYS-TECH-ELEC-1	Ch. 9	SYS-TECH-STRUC-2-1-5	OOS
SYS-TECH-PROP-5-4	OOS	SYS-TECH-ELEC-1-1	Ch. 9	SYS-TECH-STRUC-2-1-6	OOS
SYS-TECH-PROP-5-5	OOS	SYS-TECH-ELEC-1-2	Ch. 9	SYS-TECH-STRUC-2-1-7	Ch. 10
SYS-TECH-PROP-5-6	OOS	SYS-TECH-ELEC-1-3	Ch. 9	SYS-TECH-STRUC-2-2-1	Ch. 10
SYS-TECH-PROP-6	NA	SYS-TECH-ELEC-2-1	Ch. 9	SYS-TECH-STRUC-2-2-2	Ch. 10
SYS-TECH-ROT-1	Ch. 9	SYS-TECH-ELEC-2-2	Ch. 9	SYS-TECH-STRUC-2-3	Ch. 10
SYS-TECH-ROT-2-1	OOS	SYS-TECH-ELEC-3	Ch. 9	SYS-TECH-STRUC-2-4	Ch. 10
SYS-TECH-ROT-2-2	Ch. 10	SYS-TECH-ELEC-4	Ch. 9	SYS-TECH-STRUC-2-5	OOS
SYS-TECH-ROT-2-3	Ch. 10	SYS-TECH-ELEC-5-1	Ch. 9	SYS-TECH-STRUC-2-6	OOS
SYS-TECH-ROT-2-4	NA	SYS-TECH-ELEC-5-2	Ch. 9	SYS-TECH-STRUC-2-7	OOS
SYS-TECH-ROT-2-5	Ch. 9	SYS-TECH-SAFE-1-1	OOS	SYS-TECH-STRUC-3	OOS
SYS-TECH-ROT-3	Ch. 10	SYS-TECH-SAFE-1-2	OOS	SYS-TECH-STRUC-3-1	OOS
SYS-TECH-ROT-4	Ch. 10	SYS-TECH-SAFE-2-1	Ch. 10	SYS-TECH-STRUC-4	Ch. 10
SYS-TECH-ROT-5-1	NA	SYS-TECH-SAFE-2-2	Ch. 10	SYS-TECH-STRUC-4-1	NA
SYS-TECH-ROT-5-2	NA	SYS-TECH-SAFE-3-1	OOS	SYS-TECH-STRUC-5-1	OOS
SYS-TECH-ROT-6	NA	SYS-TECH-SAFE-3-2	OOS	SYS-TECH-STRUC-5-2	OOS
SYS-TECH-ROT-6-1	NA	SYS-TECH-SAFE-3-3	OOS	SYS-TECH-STRUC-5-3	OOS
SYS-TECH-ROT-6-2	NA	SYS-TECH-SAFE-3-4	OOS	SYS-TECH-STRUC-5-4	OOS
SYS-TECH-ROT-6-3	NA	SYS-TECH-SAFE-3-5	OOS	SYS-TECH-STRUC-5-5	Ch. 10
SYS-TECH-ROT-7	Ch. 9	SYS-TECH-SAFE-3-6	OOS	SYS-TECH-STRUC-5-6	Ch. 10
SYS-TECH-FC/HQ-1-1-1	Ch. 11	SYS-TECH-SAFE-4	OOS	SYS-TECH-STRUC-6-1	OOS
SYS-TECH-FC/HQ-1-1-2	Ch. 11	SYS-TECH-SAFE-5-1-1	OOS	SYS-TECH-STRUC-6-2	Ch. 10
SYS-TECH-FC/HQ-1-1-3	Ch. 11	SYS-TECH-SAFE-5-1-2	OOS	SYS-TECH-STRUC-7-1	Ch. 10
SYS-TECH-FC/HQ-1-1-4	Ch. 11	SYS-TECH-SAFE-5-2	Ch. 10	SYS-TECH-STRUC-7-2	Ch. 10
SYS-TECH-FC/HQ-1-1-5	Ch. 11	SYS-TECH-SAFE-5-3	Ch. 10	SYS-TECH-STRUC-7-3	OOS
SYS-TECH-FC/HQ-1-1-6	Ch. 11	SYS-TECH-SAFE-5-4	Ch. 10	SYS-TECH-STRUC-7-4	Ch. 10
SYS-TECH-FC/HQ-1-2-1	Ch. 11	SYS-TECH-FLY-1-1	Ch. 9	SYS-TECH-STRUC-7-5	Ch. 10
SYS-TECH-FC/HQ-1-2-2	Ch. 11	SYS-TECH-FLY-1-2	Ch. 9	SYS-TECH-STRUC-7-6	Ch. 10
SYS-TECH-FC/HQ-1-2-3	Ch. 11	SYS-TECH-FLY-1-3	Ch. 9	SYS-TECH-STRUC-7-7	OOS
SYS-TECH-FC/HQ-1-2-4	Ch. 11	SYS-TECH-FLY-1-3-1	Ch. 8		

13

Conclusion and Recommendations

The aim of this report was to take the final concept traded-off in the midterm and design it further in order to provide a detailed conceptual design to the subsystem level. To do so, the team split into subgroups per sub-system and performed a detailed design with the help of tools developed by the team.

To ensure the XV-25 Griffin meets all key requirements a detailed analysis was performed for each subsystem and the results were compared to the requirements with the use of a compliance matrix. Although some requirements were not met, these were either no longer considered applicable or were considered out of scope for our project giving the team a good idea that the final design of the XV-25 Griffin meets all the key requirements and can thus be considered a successful conceptual design. In addition to this, a market analysis was conducted to ensure that the XV-25 Griffin is a commercially viable design for the current market needs as well as a cost estimation coming in at approximately 50 million USD which is 20 million USD less than the cost of the main competition in today's market, the V-22 Osprey. An equally important aspect of the design process was the sustainability of the XV-25 Griffin. Although no driving requirements were provided on the sustainability of the vehicle, the team took it into account throughout the design process to ensure the basic standards were met. Namely, the weight was significantly reduced due to the high use of composite materials, and an investigation into the possibility of hydrogen combustion was conducted. Having said this, the team is confident in the ability of the XV-25 Griffin as a VTOL transport aircraft to revolutionize the market for small to medium-transport aircraft with its multitude of novel features leading to unique abilities.

With the initial conceptual design of the XV-25 Griffin having been completed, some future recommendations for the later design phases will be presented. For the propulsion sub-system, along with a more detailed engine sizing, the drive system connecting the engines to the rotor must be investigated in more detail as well as the free-spinning turbine driving the shaft. A further investigation into the viability of hydrogen combustion should also be performed. For the control sub-system, the lateral modes must be examined, and, potentially, the use of a more refined controller (LQR) should be considered. In addition, a more in-depth analysis of the drag estimation can be performed by testing a prototype in a wind tunnel and a further analysis of the rotating loads on the rotor must be performed. Optimization of the structures is required to decrease the weight of the vehicle as much as possible while facilitating the capabilities required, recommendations regarding novel materials and structures should be employed. Finally, the XV-25 Griffin has a high amount of novel mechanisms which, although have been proven to function individually, must be tested when integrated together on the vehicle. This further design will eventually lead to the first prototype's flight.

The vehicle produced by this team requires a substantial amount of further analysis to be deemed feasible for the prototype phase, however, the building blocks of this novel design have been provided and the theory organized and employed such that the team is confident to present this concept and the team working forward for continued design and analysis.

References

[1] Vertical Flight Society, "40th annual student design competition 2022-2023 request for proposals (rfp): High-speed vertical takeoff and landing (hsvtol) aircraft," Tech. Rep., 2022.

[2] Gilliland, J. J., "The establishment of helicopter subsystem design-to-cost estimates by use of parametric cost estimating models," Ph.D. dissertation, Denton, Texas, Aug. 1979.

[3] Stahl, J. W., Arena, J. A., and Knapp, M., "Cost-estimating relationships for tactical combat aircraft," Institute for Defence Analyses, Tech. Rep., 1984.

[4] Sanz-Gadea, E., Vasileiadis, E., Wegkamp, T., Holohan, D., Do, L., Gupta, K., Knöll, N., Coveliers-Munzi, U., Van den Bosch, J., and Faulquier, C., "Hs-vtol aircraft midterm report," TU Delft, Tech. Rep., 2022.

[5] Sanz-Gadea, E., Vasileiadis, E., Wegkamp, T., Holohan, D., Do, L., Gupta, K., Knöll, N., Coveliers-Munzi, U., Van den Bosch, J., and Faulquier, C., "Hs-vtol aircraft baseline report," TU Delft, Tech. Rep., 2022.

[6] *Certification specifications, acceptable means of compliance and guidance material for large rotorcraft cs-29*, English, European Union Aviation Safety Agency, May 2022. [Online]. Available: `https://www.easa.europa.eu/en/downloads/134339/en`.

[7] *14 cfr part 25 airworthiness standards: Transport category airplanes*, English, Federal Aviation Administration, Nov. 2022. [Online]. Available: `https://www.ecfr.gov/current/title-14/chapter-I/subchapter-C/part-25`.

[8] Chawla, V.K., Chanda, A.K., Angra, S., and Chawla, G.R., "The sustainable project management: A review and future possibilities," *Journal of Project Management*, pp. 157–170, 2018. DOI: `10.5267/j.jpm.2018.2.001`.

[9] International Civil Aviation Organization, "Report on the feasibility of a long-term aspirational goal (ltag) for international civil aviation co2 emission reductions," International Civil Aviation Organization, Tech. Rep., 2022.

[10] Zhao, D., Guo, Z., and Xue, J., "Research on scrap recycling of retired civil aircraft," *IOP Conference Series: Earth and Environmental Science*, vol. 657, no. 1, p. 012 062, Feb. 2021. DOI: `10.1088/1755-1315/657/1/012062`.

[11] Chen, C., Prasad, J.V.R., Basset, P.M., and Kolb, S., "Prediction of vrs boundaries of helicopters in descent flight," *Annual Forum Proceedings - AHS International*, pp. 1161–1179, Jan. 2006.

[12] Prouty, R., *Helicopter Performance, Stability, and Control*, 4th ed. Malabar, United States of America: Krieger Publishing Company, 1990.

[13] Thibert, J.J., and Pouradier, J.M., "Design and test of an helicopter rotor blade with evolution profile," ONERA, SNIAS, Tech. Rep. ICAS-80-10.3, 1974.

[14] Bousman, W. J., "Aerodynamic characteristics of sc1095 and sc1094 r8 airfoils," NASA, Tech. Rep. NASA/TP–2003-212265, 2003.

[15] Martin, P. B., "Rotor blade airfoil design for high-altitude, long-endurance vtol uavs," *31st European Rotorcraft Forum*, Jan. 2005.

[16] Anderson, J. D., *Fundamentals of aerodynamics*, 5th ed. McGraw-Hill, 2011.

[17] Lowson, M.V., and Ollerhead, J.B., "A theoretical study of helicopter noise," *Journal of Sound and Vibration*, vol. 9, no. 2, pp. 197–222, Mar. 1969. DOI: `10.1016/0022-460X(69)90028-5`.

[18] Schlegel, R. G. and King, R. J. and Mull, H. R., "Helicopter rotor noise generation and propagation," 1966.

[19] Hubbard, H. H., and Maglieri, D. J., "Noise characteristics of helicopter rotors at tip speeds up to 900 feet per second," *Journal of the Acoustical Society of America*, vol. 32, pp. 1105–1107, 1960.

[20] Hubbard, H. H., "Propeller-noise charts for transport airplanes," NACA, Tech. Rep. TN-2968, Jun. 1953.

[21] Ruijgrok, G. J. J., *Elements of Airplane Performance*. Delft University Press, 1990.

[22] Raymer, D. P., *Aircraft Design: A Conceptual Approach*, 2nd ed. Washington, D.C.: American Institute of Aeronautics and Astronautics, Inc. (AIAA), 1992.

[23] Abbott, I. H. A. and Von Doenhoff, A. E., *Theory of Wing Sections Including a Summary of Airfoil Data*, 1st ed. New York: Dover Publications, Inc., 1959, ISBN: 0-486-60586-8.

[24] Gudmundsson, S., *General Aviation Aircraft Design: Applied Methods and Procedures*. Boston: Butterworth-Heinemann, 2014.

[25] NLR Amsterdam, "Nlr 7301 airfoil," in *Experimental data base for computer program assessment - report of the fluid dynamics panel working group 04*, NATO Advisory Group for Aerospace Research and Development, Neuilly sur Seine, France, May 1979, App. A4.

[26] Chan, Y. Y., "Analysis of experimental data for cast-10-2/doa 2 supercritical airfoil at low reynolds numbers and application to high reynolds number flow," National Research Council Canada, Ottawa, Ontario, Tech. Rep. NRC NO. 80268, Jan. 1989.

[27] Middleton, D. B., Bartlett, D. W., and Hood, R. V., "Energy efficient transport technology - program summary and bibliography," Langley Research Center, Hampton, Virginia, Tech. Rep. NASA RP-1135, Sep. 1985.

[28] Somers, D. M., "Design and experimental results for a natural-laminar-flow airfoil for general aviation applications," Langley Research Center, Hampton, Virginia, Tech. Rep. NASA TP-1861, Jun. 1981.

[29] Drela, M., "Xfoil: An analysis and design system for low reynolds number airfoils," in *Low Reynolds number aerodynamics*, Mueller, T. J., Ed., Berlin, Heidelberg: Springer Berlin Heidelberg, 1989, pp. 1–12.

[30] Finck, R. D., "Usaf datcom," Tech. Rep., 1978.

[31] Prandtl, L., "Induced drag of multiplanes," NASA Scientific and Technical Information Facility, Tech. Rep., 1924, NASA-TN-182.

[32] Frediani, A., and Montanari, G., "Best wing system: An exact solution of the prandtl's problem," in *Variational Analysis and Aerospace Engineering*, New York, NY: Springer New York, 2009, pp. 183–211.

[33] Kroo, I. M., "Vki lecture series on innovative configurations and advanced concepts for future civil aircraft," in *Nonplanar Wing Concepts for Increased Aircraft Efficiency*, 2005.

[34] Demasi, L., "Investigation on conditions of minimum induced drag of closed wing systems and c-wings," *Journal of Aircraft*, vol. 44, no. 1, pp. 81–99, Jan. 2007. DOI: 10.2514/1.21884.

[35] Prandtl, L., "Applications of modern hydrodynamics to aeronautics," NASA, Washington D.C., USA, Tech. Rep. NACA Report No. 116, 1921.

[36] Glauert, H., *The elements of aerofoil and airscrew theory*, 2nd ed. Cambridge, England, UK: Cambridge University Press, 1959, pp. 142–145.

[37] Anderson, J. D., Corda, S., and Van Wie, D. M., "Numerical lifting line theory applied to drooped leading-edge wings below and above stall," *Journal of Aircraft*, vol. 17, no. 12, pp. 898–904, 1980. DOI: 10.2514/3.44690.

[38] Phillips, W. F., and Snyder, D. O., "Modern adaptation of prandtl's classic lifting-line theory," *Journal of Aircraft*, vol. 37, no. 4, pp. 662–670, 2000. DOI: 10.2514/2.2649.

[39] Demasi, L., "Minimum induced drag theorems for multiwing systems," *AIAA Journal*, vol. 55, no. 10, pp. 3266–3287, Oct. 2017. DOI: 10.2514/1.J055652.

[40] Kunze, P., and Wentrup, M., "Aerodynamic analysis and optimization of wings and tail surfaces of a compound helicopter with box wing," in *New Results in Numerical and Experimental Fluid Mechanics XII*, Dillmann, A., Heller, G., Krämer, E., Wagner, C., Tropea, C., and Jakirlić, S., Ed., Cham: Springer International Publishing, 2020, pp. 372–381.

[41] Goates, C. D., and Hunsaker, D. F., "Modern implementation and evaluation of lifting-line theory for complex geometries," *Journal of Aircraft*, vol. 0, no. 0, pp. 1–19, 2022. DOI: 10.2514/1.C036748.

[42] Hunsaker, D. F., "Post stall behavior of a lifting line algorithm," in *Rocky Mountain Space Grant Consortium Meeting Proceeding*, 2007.

[43] Jacobs, R. B., Ran, H., Kirby, M. R., and Mavris, D. N., "Extension of a modern lifting-line method to transonic speeds and application to multiple-lifting-surface configurations," in *30th AIAA Applied Aerodynamics Conference*, New Orleans, Louisiana, 2012.

[44] Oliviero, F., *Aircraft aerodynamic analysis - estimation of lift & drag*, PowerPoint slides, Oct. 2022.

[45] Torenbeek, E., *Advanced Aircraft Design: Conceptual Design, Analysis and Optimization of Subsonic Civil Airplanes*. John Wiley & Sons, 2013.

[46] Kroo, I. M., "Aircraft design: Synthesis and analysis," 1999.

[47] Sun, J., Hoekstra, J. M., and Ellerbroek, J., "Aircraft drag polar estimation based on a stochastic hierarchical model," 2018.

[48] Russo, L., Tognaccini, R., and Demasi, L., "Box wing and induced drag: Compressibility effects in subsonic and transonic regimes," *AIAA Journal*, vol. 58, no. 6, pp. 2398–2413, Jun. 2020. DOI: 10.2514/1.j059080.

[49] Lee, H., Viswamurthy, S. R., Park, S. C., Kim, T., Shin, S. J., and Kim, D., "Helicopter rotor load prediction using a geometrically exact beam with multicomponent model," *Journal of Aircraft*, vol. 47, no. 4, pp. 1382–1390, Jul. 2010. DOI: 10.2514/1.47608.

[50] McAlister, K. W., and Takahashi, R. K., "Naca 0015 wing pressure and trailing vortex 1991 measurements," Ames Research Center, Moffett Field, California, Tech. Rep. NASA TP-3151, Nov. 1991.

[51] Purser, P. E., and Spearman M. L., "Wind-tunnel tests at low speed of swept and yawed wings having various plan forms," Langley Aeronautical Laboratory, Langley Field, Virginia, Tech. Rep. NACA TN-1861, Dec. 1951.

[52] Thiemeier, J., Öhrle, C., Frey, F., Keßler, M., and Krämer, E., "Aerodynamics and flight mechanics analysis of airbus helicopters' compound helicopter RACER in hover under crosswind conditions," *CEAS Aeronautical Journal*, vol. 11, no. 1, pp. 49–66, Apr. 2019. DOI: 10.1007/s13272-019-00392-3.

[53] Quackenbush, T.R., Whitehouse, G.R., Danilov, P.V., and Solomon, C.L., "Analysis of rotor/airframe interaction in hover and near-hover flight conditions," Tech. Rep., 2019.

[54] Bevilaqua, P.M., "Future applications of the jsf variable propulsion cycle," Lockheed Martin Aeronautics Company, Tech. Rep., 2003.

[55] Wurth, S.P., and Smith M.S, "F-35 propulsion system integration, development, and verification," Lockheed Martin Aeronautics Company, Tech. Rep., 2018.

[56] Jachtenberg, M. H., "Development of a preliminary lifing analysis tool for the f135-pw-100 engine," Delft University of Technology, Tech. Rep., 2018.

[57] Rolls-Royce, "Rolls-royce liftsystem," Rolls-Royce, Tech. Rep., 2021.

[58] Pratt & Whitney, "F135 specs charts," Pratt & Whitney, Tech. Rep., 2012.

[59] Sheffield, J.W., Martin, K.B., and Folkson, R., "Electricity and hydrogen as energy vectors for transportation vehicles," in Woodhead Publishing Limited, 2014, pp. 117–137.

[60] European Union Aviation Safety Agency, "Type-certificate data sheet tp400-d6," European Union Aviation Safety Agency, Tech. Rep., 2021.

[61] Kufeld, R.M., and Bousman, W.G., "High load conditions measured on a uh-60 in maneuvering flight," 1995.

[62] Roskam, J., *Airplane Design Part IV: Layout Design of Landing Gear and Systems*. DARcorporation, 1989.

[63] Enciu, K., and Rosen, A., "Helicopter roll-on takeoff simulation," *Journal of the American Helicopter Society*, vol. 56, no. 1, 2011.

[64] Vos, R., and Melkert, J. A., "Aerospace and systems engineering elements i," Presentation Slides, 2022.

[65] Torenbeek, E., *Synthesis of Subsonic Airplane Design*. Delft University Press, 1982.

[66] Robinson Helicopter Company, *Robinson r44 maintenance manual: Chapter 3 life-limited components*, 2018.

[67] Janeček, M., Novy, F., Harcuba, P., Stráský, J., Trško, L., Mhaede, M., and Wagner, L., "The very high cycle fatigue behaviour of ti-6al-4v alloy," *Acta Physica Polonica A*, vol. 128, pp. 497–503, Oct. 2015. DOI: `10.12693/APhysPolA.128.497`.

[68] Zalnezhad, E., Ahmed, D., Sarhan, A., Abd Shukor, M., and Asri, B., "A fuzzy logic based model to predict the fretting fatigue life of aerospace al7075-t6 alloy," vol. 1, pp. 39–48, Jan. 2012.

[69] Uusitalo, J., Pentti Karjalainen, L., Retraint, D., and Palosaari, M., "Fatigue properties of steels with ultrasonic attrition treated surface layers," *Materials Science Forum*, vol. 604-605, pp. 239–248, Oct. 2008. DOI: `10.4028/www.scientific.net/msf.604-605.239`.

[70] Leishman, G.J., *Cambridge aerospace series: principles of helicopter aerodynamics series number 12*, 2nd ed. Cambridge, England: Cambridge University Press, Dec. 2016.

[71] Megson, T. H. G., *Aircraft Structures for Engineering Students*, Fifth Edition. Boston: Butterworth-Heinemann, 2013. DOI: `https://doi.org/10.1016/B978-0-08-096905-3.00065-6`.

[72] Fradenburgh, E A., Murrill, R. J., and Kiely, E. F., "Dynamic model wind tunnel tests of a variable-diameter telescoping-blade rotor system," United Aircraft Corporation, Tech. Rep. USAAMRDL TR-73-32, Jul. 1973.

[73] Mikjaniec, T., "The preliminary design of the sharcs rotor blade," Carleton University, Tech. Rep., 2006.

[74] Johnson, W., "Nasa design and analysis of rotorcraft," Ames Research Center, Tech. Rep., 2015.

[75] Roskam, J., *Airplane Flight Dynamics and Automatic Flight Controls* (Airplane Flight Dynamics and Automatic Flight Controls). DARcorporation, 1998.

[76] Oliviero, F., *Requirement analysis and design principles for a/c stability control*, PowerPoint slides, Oct. 2022.

[77] Sadraey, M. H, *Aircraft Design: A Systems Engineering Approach*. A John Wiley & Sons, Ltd., 2013.

[78] van Holten, T., and Melkert, J.A., *Helicopter performance, stability and control*, Delft University of Technology Faculty of Aerospace Engineering Course Readers, Nov. 2002.

[79] Simplicio, P. V. M., "Helicopter nonlinear flight control: An acceleration measurements-based approach using incremental nonlinear dynamic inversion," M.S. thesis, Delft University of Technology, Aug. 2011.

[80] Oppenheimer, M.W., Doman, D.B., and Bolender, M.A., "Control allocation for over-actuated systems," in *2006 14th Mediterranean Conference on Control and Automation*, 2006, pp. 1–6. DOI: `10.1109/MED.2006.328750`.

[81] Wittenberg, H., "The dynamic stability of the helicopter," Delft University of Technology, Tech. Rep. LR772, Apr. 1993.

[82] van Grünhagen, W., and Tischler, M.B., "Time and frequency-domain identification and verification of bo 105 dynamic models," *Journal of the American Helicopter Society*, Oct. 1989.

[83] International Civil Aviation Organization, *Environmental Protection*, 8th ed. Montreal, Quebec, Canada: International Civil Aviation Organization (ICAO), Jul. 2008, vol. I: Aircraft Noise.

[84] Yang, Y., Boom, R., Irion, B., van Heerden, D.J., Kuiper, P., and de Wit, H., "Recycling of composite materials," *Chemical Engineering and Processing: Process Intensification*, vol. 51, pp. 53–68, 2012.

[85] E4tech, "Decarbonisation potential of synthetic kerosene," Ministerie van Infrastructuur en Waterstaat, Tech. Rep., 2021.

A
Appendix

This appendix contains the supporting diagrams. The first diagram represents the Development Logic followed by the Work Flow and Work Breakdown Structure and finally the Gantt chart is presented.
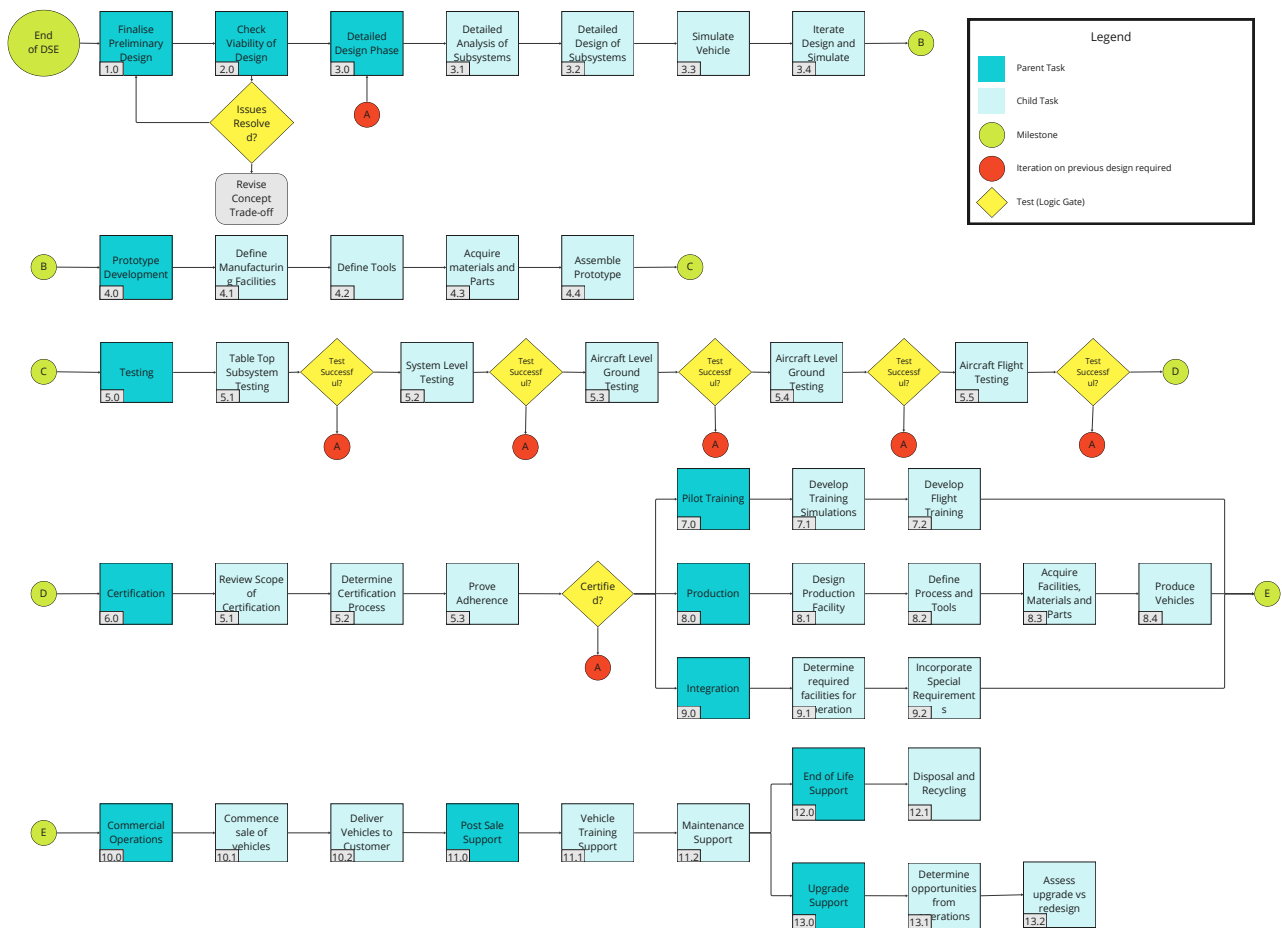
Figure A.1: Development Logic Diagram

WORK FLOW DIAGRAM

P1

Project Objective 1.1.1

Top Level Requirements 1.1.2

VFS Competition Requirements 1.1.3

Define team organization
Project Approach
Departments & Roles
Rules and Regulations
| 30 | 1.2 | 1 |

Define Tools
| 10 | 1.3 | 2 |

Determine Requirements
| 40 | 1.4 | 24 |

Define project
POS, MNS, WBS, WFD, Gantt
Design and Development Logic
| 66 | 1.5 | 14 |

Perform **Risk Assessment**
| 16 | 1.6 | 8 |

Perform **Quality Control**
| 4 | 1.7.2 | 4 |

Complete **Project Plan**
1.7

Determine Horizontal Flight Requirements
Determine Vertical Flight Requirements
Perform Class I Weight Estimation
Research 1.9
Determine MTOW for Horizontal Flight
Determine MTWO for Vertical Flight
Brainstorm configurations

P2

Define System Requirements
| 24 | 2.1.1 | 6 |

Define Mission Requirements
| 24 | 2.1.2 | 6 |

Define Sub-System Requirements
| 24 | 2.1.3 | 6 |

Generate Requirements Discovery Tree
| 8 | 2.2 | 2 |

Define system functionality
Functional Flow Diagram
Functional Breakdown Structure
| 20 | 2.3 | 2 |

Generate Design Option Tree
| 60 | 2.5 | 6 |

PROJECT MANAGEMENT DEVELOPMENT

Develop Contingency Management Plan
| 18 | 2.4.1 | 6 |

Assess Technical Risk
| 12 | 2.4.2 | 6 |

Perform Market Analysis
| 12 | 2.4.3 | 6 |

Develop Resource Allocation Budget
| 12 | 2.4.4 | 6 |

Define Sustainable Development Strategy
| 12 | 2.4.5 | 6 |

Perform **Quality Control**
| 6 | 2.6.2 | 6 |

Complete **Baseline Report**
2.6

P3

Develop **Analysis** Tools
| 48 | 3.2.1 | 16 |

Update **Project Definition**
| 4 | 3.1 | 4 |

Preliminary Sub-system/ Component **Design**
| 48 | 3.4 | 8 |

Analyse 3 Design Options
| 108 | 3.5 | 12 |

Perform Final Design **Trade-Off**
| 200 | 3.6 | 15 |

Design Sub-system & Components
| 160 | 3.7 | 16 |

Trade-off to arrive to 3 Design Options
| 200 | 3.3 | 16 |

Analyse Design Options
| 24 | 3.2.2 | 6 |

Perform **Verification & Validation**
| 0 | 3.2.3 | 4 |

Perform **Verification & Validation**
| 12 | | 4 |

Perform **Quality Control**
| 8 | 3.8.2 | 8 |

Complete **Midterm Report**
3.8

Perform Trade-off

Define trade method rationale and organisation
Define trade-off criteria
Weigh criteria factors
Complete N2 Chart
Develop trade-off summary table

Perform Sensitivity analysis
| 40 | 3.6.6 | 4 |

P4

Detailed **Analysis** of Sub-systems
| 40 | 4.2 | 20 |

Design Sub-systems in Detail
| 64 | 4.3 | 32 |

Conclude Final Design
| 70 | 4.5 | 7 |

Update Previous Deliverables
| 24 | 4.1 | 8 |

Perform **Quality Control**
| 16 | 4.6.2 | 16 |

Complete **Final Report**
4.6

Determine Vehicle Properties

Determine Conceptual Design Trade Studies
| 111 | 4.4.1 | 111 |

Determine Vehicle Description
| 111 | 4.4.2 | 111 |

Determine Propulsion System Data
| 111 | 4.4.3 | 111 |

Determine Mission Performance Data
| 111 | 4.4.4 | 111 |

Complete Air Vehicle Design & Subsystem Drawings
| 111 | 4.4.5 | 111 |

Determine Aerodynamic Data
| 111 | 4.4.6 | 111 |

Determine Loads & Criteria Data
| 111 | 4.4.7 | 111 |

Determine Mass Properties Data
| 111 | 4.4.8 | 111 |

Determine Manufacturing & Cost Data
| 111 | 4.4.9 | 111 |

Determine Operational Description
| 111 | 4.4.10 | 111 |

WORK BREAKDOWN STRUCTURE

Project Initiation

Project Organisation

- **1.2** Define Team Organisation
  - **1.2.2** Departments and Roles
  - **1.2.3** Rules and Regulations
  - **1.2.1** Project Approach
- **1.3** Define Tools
  - **1.3.1** Coding: Python & Matlab
  - **1.3.2** Modeling: 3dx & Blender
  - **1.3.3** Simulation & Analysis: Ansys, Simscale, Open Vsp & Open Foam

Project Definition

- **1.1** Gather Information
  - **1.1.1** Gather Project Objective
  - **1.1.3** Gather VFS Competition Requirements
  - **1.1.2** Gather Top Level Requirements
- **1.5** Define POS, MNS, WBS, WFD, Gantt Chart
- **1.5.5** Determine Design and Development Logic
- **1.6** Perform Risk Assessement

Project Requirements

- **2.2** Generate Requirements Discovery Tree
  - **2.1.1** System Requirements
  - **2.1.2** Mission Requirements
  - **2.1.3** Sub-System Requirements
  - **2.1.4** CS29 Requirements
- **2.5** Generate Design Option Tree

System Functionality

- **2.3.1** Functional Flow Diagram
- **2.3.2** Functional Breakdown Structure
- **2.4** Project Management Development
  - **2.4.1** Develop Contingency Management Plan
  - **2.4.2** Assess Technical Risk
  - **2.4.3** Perform Market Analysis
  - **2.3.4** Develop Resource Allocation Budget
  - **2.3.5** Define Sustainable Development Strategy

Research

- **1.9.7** Research Rotorcraft Concepts
- **1.9.4** Perform Class I Weight Estimation
- **1.9.1** Read Helicopter Literature

Perform Quality Control

- **1.7** Ensure Report Quality
- **1.9.8** Compound Vehicles
- **1.9.9** Tilt Rotor Vehicles
- **1.9.5** MTOW for Horizontal Flight
- **1.9.6** MTOW for Vertical Flight
- **1.9.1.2** General Operation
- **1.9.1.4** Rotorcraft Performance
- **1.9.1.3** Rotorcraft Design

Project Completion

Analyse

- **3.2.1** Develop Analysis Tools
  - **3.2.1.1** Aerodynamic Analysis Tool
  - **3.2.1.2** Weight Estimation Tool
  - **3.2.1.3** Propulsive Performance Tool
  - **3.2.1.4** Structural Analysis Tool
- **3.5** Preliminary Analysis of top 3 Configurations for Trade-Off
- **4.4** Determine Aircraft Properties
  - **4.2** Analysis of Sub-Systems
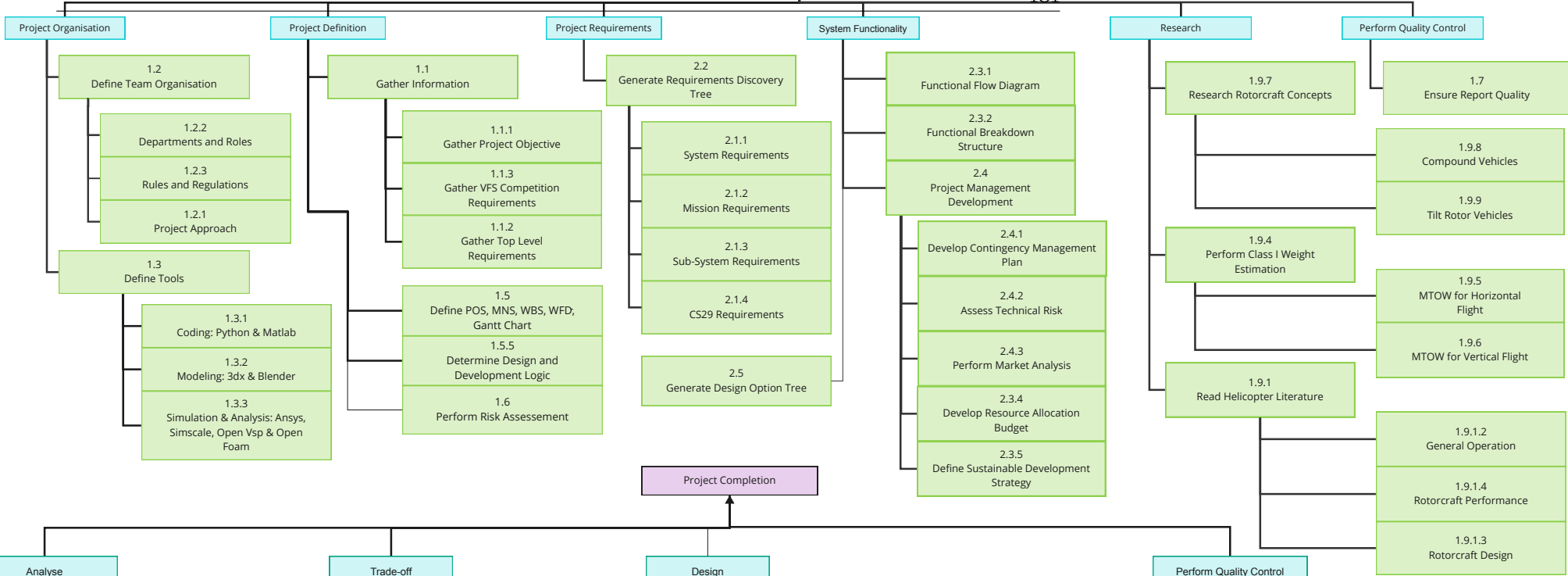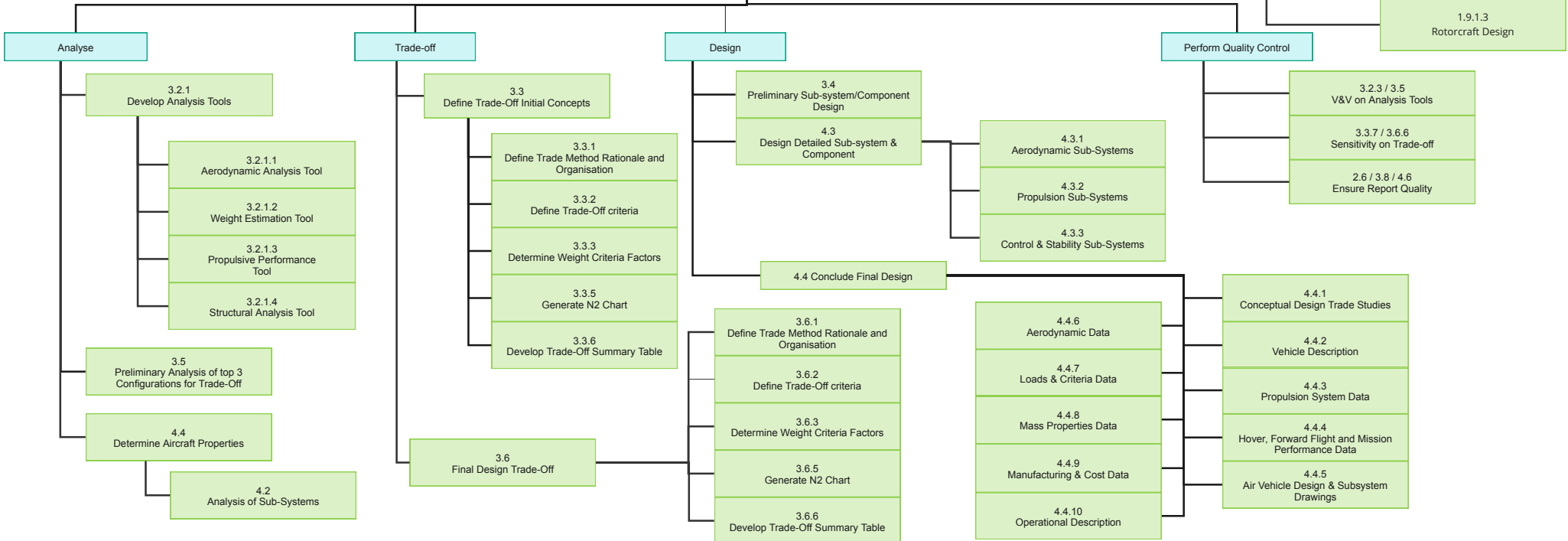
Trade-off

- **3.3** Define Trade-Off Initial Concepts
  - **3.3.1** Define Trade Method Rationale and Organisation
  - **3.3.2** Define Trade-Off criteria
  - **3.3.3** Determine Weight Criteria Factors
  - **3.3.5** Generate N2 Chart
  - **3.3.6** Develop Trade-Off Summary Table
- **3.6** Final Design Trade-Off

Design

- **3.4** Preliminary Sub-system/Component Design
- **4.3** Design Detailed Sub-system & Component
  - **4.3.1** Aerodynamic Sub-Systems
  - **4.3.2** Propulsion Sub-Systems
  - **4.3.3** Control & Stability Sub-Systems
- **4.4 Conclude Final Design**
- **3.6.1** Define Trade Method Rationale and Organisation
- **3.6.2** Define Trade-Off criteria
- **3.6.3** Determine Weight Criteria Factors
- **3.6.5** Generate N2 Chart
- **3.6.6** Develop Trade-Off Summary Table
- **4.4.6** Aerodynamic Data
- **4.4.7** Loads & Criteria Data
- **4.4.8** Mass Properties Data
- **4.4.9** Manufacturing & Cost Data
- **4.4.10** Operational Description
- **4.4.1** Conceptual Design Trade Studies
- **4.4.2** Vehicle Description
- **4.4.3** Propulsion System Data
- **4.4.4** Hover, Forward Flight and Mission Performance Data
- **4.4.5** Air Vehicle Design & Subsystem Drawings

Perform Quality Control

- **3.2.3 / 3.5** V&V on Analysis Tools
- **3.3.7 / 3.6.6** Sensitivity on Trade-off
- **2.6 / 3.8 / 4.6** Ensure Report Quality

GANTT CHART

[Derived in Notion]